SPECTROSCOPY AND KINETICS OF ATMOSPHERIC RESERVOIR SPECIES: $HOONO$, $CH_3C(O)OONO_2$, CH_3OOH, AND $HOCH_2OOH$

Thesis by

Juliane Loraine Fry

In Partial Fulfillment of the Requirements

for the Degree of

Doctor of Philosophy

California Institute of Technology

Pasadena, California

2006

(Defended December 15, 2005)

I dedicate this thesis to

David L. G. Fry and Ludwig Waldmann,

from whom I inherited my love of science

ACKNOWLEDGEMENTS

I have had an incredibly rich graduate school experience at Caltech because of wide-ranging contributions to my education and personal growth from a wonderful group of coworkers, collaborators, and friends. I was extremely lucky the day Drs. Mitchio Okumura and Paul Wennberg agreed to jointly advise my Ph.D. I had no idea then what an enormous advantage it would be to work with two advisors looking at the same scientific problems with different, complementary perspectives. With their guidance I have combined diverse approaches into a thesis project that I truly enjoyed every step of the way. I am deeply grateful to them both for many scientific insights and personal lessons.

In the laboratory, I had more good fortune. I have been mentored by three excellent teachers and coworkers: Drs. Sergey Nizkorodov, Coleen Roehl, and Brian Drouin. In addition to teaching me how to be a laboratory spectroscopist and kineticist, they made long days in the lab fun. Sergey in particular is responsible for helping me get a good start in lab, and taught me how to approach problems as a scientist. I have also enjoyed working with and learning from fellow graduate students and visitors in the lab: John Crounse, Andrew Mollner, Francis Pope, Zsuzsa Marka, Susanna Widicus Weaver, and Jamie Matthews.

The broader circle of students and post-docs with whom I interacted supplied many valuable discussions, from science to politics to anything else. My great officemates David Shuster, Julie O'Leary, and John Crounse were constant sources of amusement, help, and coffee breaks. Lunch dates, science ideas, and supportive friends were always to be found

in the Okumura and Wennberg groups. I enjoyed sharing the Caltech experience with Rebecca Washenfelder, Zhonghua Yang, Gretchen Aleks, Alan Kwan, David McCabe, Andrew Mollner, David Robichaud, Aaron Noell, Kana Takematsu, and Laurence Yeung.

Collaborations have been an educational and enjoyable part of my thesis work. I have particularly benefited from working with Brian Drouin and Chip Miller at NASA JPL, Joe Francisco (Purdue) and Anne McCoy (Ohio State) over email, and Henrik Kjaergaard and Joseph Lane at the University of Otago in Dunedin, New Zealand. In addition to these formal collaborations, I have learned much from conversations with John Barker (U Michigan), David Golden (Stanford), Marsha Lester and her research group (U Penn), John Stanton (U Texas at Austin), and Geoff Blake and John Seinfeld (Caltech). I am indebted to my thesis committee for helpful feedback at my Candidacy and Proposals exams: Mitchio Okumura, Paul Wennberg, Pat Collier, Rudy Marcus, and Geoff Blake.

Life outside of lab has been very good to me as well. I have met too many fascinating people in California to mention here, but a few have had particularly profound influences on my life. Dave Michalak started as a friend from the Catalina apartments, became a hiking buddy, then a travel buddy, and has been my partner-in-crime ever since we stole one of the Caltech carts and got it stuck in the Millikan rock garden. Dave has taught me how to love life even more than I already did, and he has been a great companion throughout graduate school. The last stretch of thesis writing has been pretty intense, but going through it with him has made it manageable, and even fun. And with whom else would I have had the chance to act in a TV show about detectives on skateboards?

Two incredibly interesting, powerful, and fun women have also shared many great experiences and intense conversations: Maria Campa and Libby Mayo. These women are both role models to me and riotous entertainment. Great friends have also come in the form of housemates: my first year roomie Catharine Larsen showed me the ropes at Caltech, shared a lot of quotable moments, and is responsible for my addiction to banh tet trung thu. My housemates for the next three years - at our Altadena bungalow with the sweet swimming pool and questionable black shag carpet, and our Los Robles slum mansion with the occasional sound of gunshots and the fabulous lemon tree - were great friends and crucial support throughout graduate school. Wendy Belliston Bittner, Garrett Bittner, Christine Ueda, Dave Michalak, and I shared Thanksgivings, Easters, trips to the LA Phil or McCormick & Schmicks happy hour, fondue nights, movies on a big green TV, and all the trials and tribulations of the Caltech experience. My mom referred to them as my California "familia." True. Wendy, Maria, Libby, and I were also often the "Mission Impossible" quartet, finding ways to turn the simplest night out into a complex adventure.

Life in SoCal was also made more fun by my favorite co-pilot and the person who introduced me to general aviation, Fred Romberg, and my teammates in the Caltech Ice Hockey Club, the Panorama City Iceoplex women's hockey league, and the West L.A. College women's hockey program, especially the "Pylons" and the fun women I played tournaments with in Vancouver, L.A., and Las Vegas.

In addition to these great local friends, I am very grateful to my wonderful friends from earlier stages in life, who were always ready to talk on the phone or be the destination of a get-away weekend, and whose visits to California provided the impetus to get out and

see more of the area. My lovely friends Amber Ahmad, Becky Yingst, Meredith Dank, Kristin Rollins, and Ina Kinski have been constant inspiration and loving support to me.

Lastly, I am extremely grateful to my family. My parents, Claudia and David Fry, have consistently given me love, challenge, and encouragement. They worked very hard to provide me with an excellent education and to teach me the personal ethic to take full advantage of the opportunities that would follow. Throughout my time at Caltech, my parents have provided continual support, understanding, care packages, and good advice. I cannot possibly acknowledge their contributions to my education enough. I will be forever grateful and will endeavor to pay it forward. My brother Daniel, who is beginning a career as an automotive engineer to build the cars that will generate the emissions that my colleagues and I will worry about, is also a great supportive friend and confidant. My grandparents, Magda Waldmann and Alma and David Fry, continually supply active encouragement and enjoyable family visits on breaks from study.

My two grandfathers, David L.G. Fry and Ludwig Waldmann, had distinguished careers as physicists, one at General Motors and one in German academia. The family joke is that science/engineering interest is a skipped-generational trait, since my parents are business and finance professionals and my brother and I chose science and engineering majors. My Grandpa Fry and I have wonderful discussions about science: what he did at GM, what I am doing at Caltech, and what we read about in Physics Today or Scientific American. Unfortunately, I did not have the chance to know my Grandfather Waldmann, but we would have undoubtedly enjoyed similar discussions. Because of this shared love of science, I dedicate this thesis to my grandfathers.

ABSTRACT

This thesis reports experimental and theoretical studies of the spectroscopy and kinetics of four atmospheric reservoir species: peroxynitrous acid (HOONO), peroxyacetyl nitrate (PAN, $CH_3C(O)OONO_2$), methyl hydroperoxide (MHP, CH_3OOH), and hydroxymethyl hydroperoxide (HMHP, $HOCH_2OOH$). Reservoir species are so named because they temporarily or permanently sequester reactive radicals (such as OH, HO_2, or NO_2), reducing the oxidative strength of the atmosphere and allowing transport of pollutants to remote regions.

Two conformers, *cis-cis* and *trans-perp* HOONO, are identified in the $2\nu_{OH}$ region by vibrational overtone initiated photodissociation spectroscopy, and the isomerization barrier from the less stable *trans-perp* to *cis-cis* HOONO is determined experimentally, statistically, and *ab initio* to be ~ 40 kJ/mol. This low barrier indicates that only *cis-cis* HOONO is atmospherically important. The complex vibrational spectroscopy of *cis-cis* HOONO is assigned with the aid of a simple two-dimensional OH-stretch/torsion coupling model of the planar, partially hydrogen-bound molecule. Combined with nonuniform quantum yield, this model explains the major features in the *cis-cis* HOONO spectrum. Its application to the fundamental region suggests an upward adjustment of the atmospherically important $HOONO/HONO_2$ product branching ratio in the $OH + NO_2$ association reaction. The rotational spectrum and dipole moment of *cis-cis* HOONO and DOONO are measured in the submillimeter region to characterize the molecular structure of HOONO and enable a quantitative atmospheric search.

The overtone initiated photodissociation of PAN is studied in the $3\nu_{CH}$ and $4\nu_{CH}$ regions. No photodissociation is observed experimentally; statistical modeling is employed to estimate the importance of this process in PAN.

The UV photodissociation of MHP and HMHP is studied in the 300 – 350 nm region and extrapolated to 400 nm to calculate total UV photolysis rates.

The overtone initiated photodissociation of HMHP is studied in the $4\nu_{OH}$ and $5\nu_{OH}$ regions. The rich spectroscopy of this two-OH-chromophore molecule is assigned with the help of a one-dimensional anharmonic oscillator model on each OH stretch of three *ab initio* identified HMHP conformers. This modeling allows estimation of the (unknown) dissociation threshold for HMHP.

Lastly, an atmospheric search for HOONO, likely the most atmospherically important of the four molecules studied herein, is proposed and outlined.

TABLE OF CONTENTS

LIST OF FIGURES

LIST OF TABLES

NOMENCLATURE

ASUR. Airborne submillimeter radiometer

BBO. β-BaB_2O_4

CCSD(T). Coupled cluster singles and doubles with perturbative triples model

DFG. Difference frequency generation

FTIR. Fourier transform infrared

HMHP. Hydroxymethyl hydroperoxide

HOONO. Peroxynitrous acid

IUPAC. International Union of Pure and Applied Chemistry

IVR. Intramolecular vibrational redistribution

LIF. Laser induced fluorescence

MHP. Methyl hydroperoxide

OPO. Optical parametric oscillator

PAN. Peroxyacetyl nitrate

RRKM. Rice-Ramsperger-Kassel-Marcus

SHG. Second harmonic generation

SLS. Submillimeter limb sounder

SZA. Solar zenith angle

THG. Third harmonic generation

VOC. Volatile organic compound

CHAPTER 1

INTRODUCTION TO ATMOSPHERIC RESERVOIR SPECIES

Chapter 1

1. INTRODUCTION TO ATMOSPHERIC RESERVOIR SPECIES

1.1. HO_x and NO_x chemistry in the Earth's atmosphere

Knowledge of gas-phase chemical reactions in the Earth's atmosphere is critical to understanding such diverse phenomena as ozone formation and depletion, air quality, and climate. The presence of highly reactive radical species in the atmosphere and very efficient radical-radical reactions leads to a coupled system with strong interdependence of the reactive chemical species. In particular, the HO_x and NO_x families of radicals ($HO_x \equiv OH + HO_2$, $NO_x \equiv NO + NO_2$) are of critical atmospheric importance in the formation of photochemical smog and ozone in the troposphere (~ 0 – 10 km altitude) and ozone depletion in the stratosphere (~ 10 – 50 km altitude). Ozone is a powerful phytotoxic oxidant implicated in increased incidence of asthma in children, making its increasing concentration at ground level the foremost air quality concern in polluted urban areas. In the stratosphere, however, ozone absorbs harmful UV radiation, making its depletion in the upper atmosphere another process of critical interest.

The centrality of HO_x and NO_x in determining ozone concentrations throughout the atmosphere, as well as the high oxidative reactivity of these radicals towards volatile organic compounds (VOC), motivates the pursuit of a detailed understanding of the chemical processes that determine HO_x and NO_x atmospheric concentrations. Production of HO_x and NO_x in the troposphere is a signature of a polluted region because HO_x is produced by the photolysis of O_3 in the presence of water and NO_x is emitted as a

byproduct of combustion. Atmospheric dynamics and the transport of these species from their sources to more pristine regions of the atmosphere determine the regional and global distribution of the HO_x and NO_x pollutants.

1.2. Reservoir species

The short atmospheric lifetime of HO_x and NO_x radicals (in the troposphere, $\tau_{HOx} \sim 1 - 100$ s and $\tau_{NOx} \sim 1$ day – 1 week)[1] prevents them from being transported large distances in their radical form. However, reaction of these radicals with each other or with volatile organic compounds in the atmosphere can form more stable molecular species that serve as "reservoirs" for the reactive radicals. These reservoir species, such as HNO_3, formed by reaction of OH with NO_2 in the presence of a stabilizing third-body collision partner, can serve as either permanent sinks or temporary reservoirs for the radical species, depending on the subsequent chemistry of the reservoir species. For example, a long-lived reservoir species with a large uptake coefficient may be most likely to be absorbed by a raindrop and ultimately deposited via rainfall, permanently removing the initial radicals from the atmosphere. On the other hand, a weakly-bound reservoir species may exist as a stable molecule for days or weeks, allowing transport to another region of the atmosphere before thermal or photolytic re-dissociation into the original radicals. This latter case is the primary source of NO_x to remote regions of the troposphere.

A schematic of several important atmospheric radical and reservoir species is shown in Figure 1-1. The reactions after photooxidation (i.e., reaction with OH) are shown for a generic volatile organic compound. The important radicals are circled: peroxy (RO_2), alkoxy (RO), and acyl peroxyacyl (RC(O)OO), and the product radical sinks or reservoirs

are boxed: alcohols and ketones (ROH and RC(O)R′), organic hydroperoxides (ROOH), organic nitrates and peroxynitrites ($RONO_2$ and ROONO), aldehydes (RCHO), peroxyacids and carboxylic acids (RC(O)OH and RC(O)OH), and peroxyacyl nitrates ($RC(O)OONO_2$).

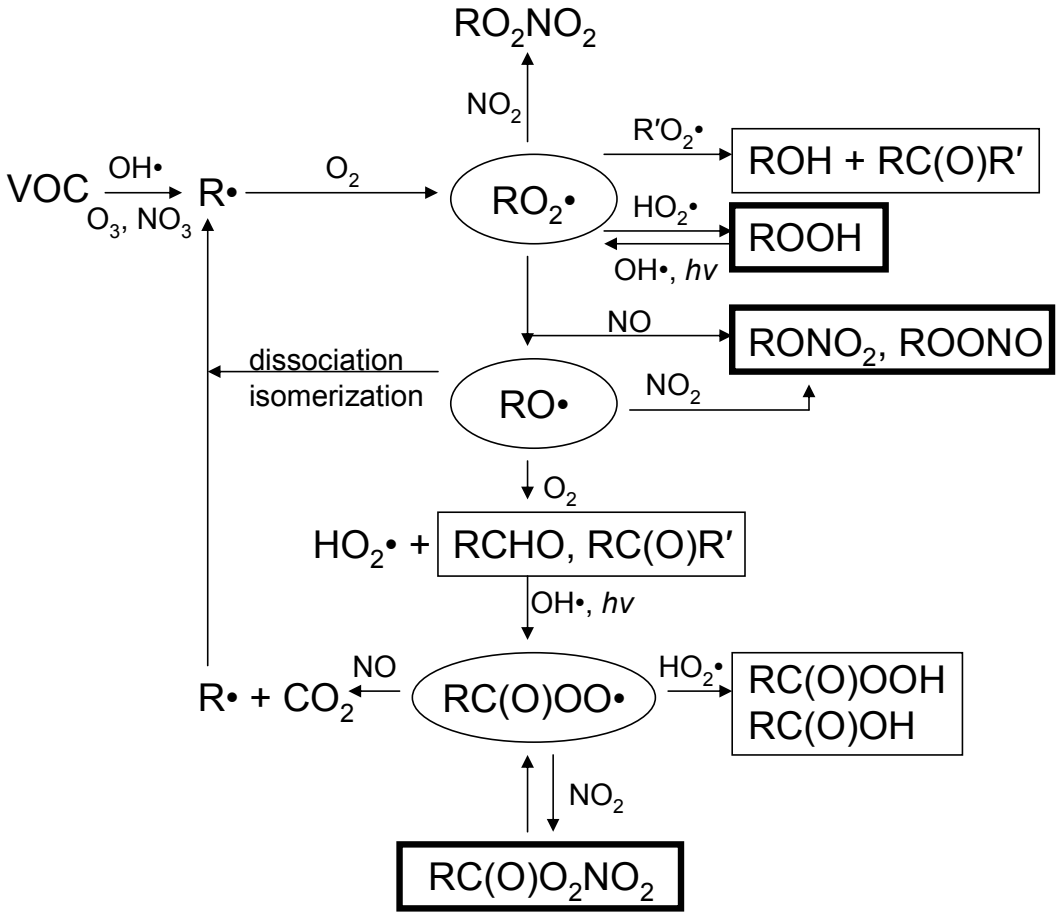

Figure 1-1. Radicals and products of photooxidation of a generic volatile organic compound (VOC). Adapted from Seinfeld and Pandis.[1]

The three classes of reservoir species boxed with a heavier line are those considered in this thesis. Specifically, the hydrogen peroxynitrite *peroxynitrous acid* (HOONO), the

organic nitrate peroxyacetyl nitrate (PAN, $CH_3C(O)OONO_2$), and the organic hydroperoxides methyl hydroperoxide (MHP, CH_3OOH) and hydroxymethyl hydroperoxide (HMHP, $HOCH_2OOH$) are discussed in the following chapters. The weaker peroxide bonds (an average O-O bond has $E_{O\text{-}O} \sim 197$ kJ/mol, while $E_{C\text{-}H} \sim 439$ kJ/mol, $E_{O\text{-}H} \sim 464$ kJ/mol, and $E_{C\text{-}C} \sim 347$ kJ/mol)[2] lead to shorter atmospheric lifetimes in these molecules, making them radical reservoirs more often than permanent sinks. For this thesis research I have focused on the processes by which these molecules dissociate, returning the reactive HO_x and NO_x radicals to the atmosphere.

A recent special issue of Chemical Reviews highlighting atmospheric chemistry shows the diversity of chemical processes of importance in the Earth's atmosphere.[3] Great progress has been made in understanding the gas-phase chemistry of the atmosphere through a combination of field measurements, controlled laboratory experiments, and atmospheric chemistry modeling.[4] The current version of the Master Chemical Mechanism (MCMv3), a comprehensive mechanism of known chemical and photochemical reactions in the troposphere maintained by the University of Leeds, contains over 4500 chemical species and over 12600 reactions.[5,6] Nevertheless, discrepancies remain between measured and modeled concentrations of HO_x[7] and NO_x,[8] and particularly in terms of transport of pollutants to remote areas, the dissociation of reservoir species could provide a significant and geographically distinct atmospheric source of HO_x and NO_x.

1.2.1. Peroxynitrous acid (HOONO) in the atmosphere

HOONO in the atmosphere is formed as one of two product channels in the three-body recombination reaction of OH and NO_2 radicals:

$$OH + NO_2 + M \rightarrow HNO_3 + M \quad \text{(R1)}$$

$$\rightarrow HONO_2 + M \quad \text{(R1a)}$$

$$\rightarrow HOONO + M \quad \text{(R1b)}$$

The more stable nitric acid isomer (1a) is formed as the dominant product channel and is observed with much higher concentration in the atmosphere due to its greater stability and hence longer atmospheric lifetime.[1] The less stable HOONO isomer (R1b) is predicted to have a short atmospheric lifetime (~ seconds) before thermal decomposition to OH and NO_2 fragments.[9] Based on the relative energies and densities of states of OH + NO_2 and HOONO and $HONO_2$, a statistical RRKM (Rice-Ramsperger-Kassel-Marcus) theory model can be used to determine the percent yield of HOONO as a function of altitude. Using the IUPAC data evaluation[4] pressure- and temperature-dependent rate constant for reaction R1, Golden et al. calculated a vertical profile of percent yield of HOONO in the OH + NO_2 reaction.[9] Multiplying these percent yields with a typical vertical profile of HNO_3 (this one from the subarctic winter),[10] a predicted vertical profile of HOONO can be calculated, as shown in Figure 1-2. The maximum predicted HOONO mixing ratio of ~ 1 ppb (parts per billion, 10^{-9}) occurs at approximately 20 km altitude, in the lower stratosphere.

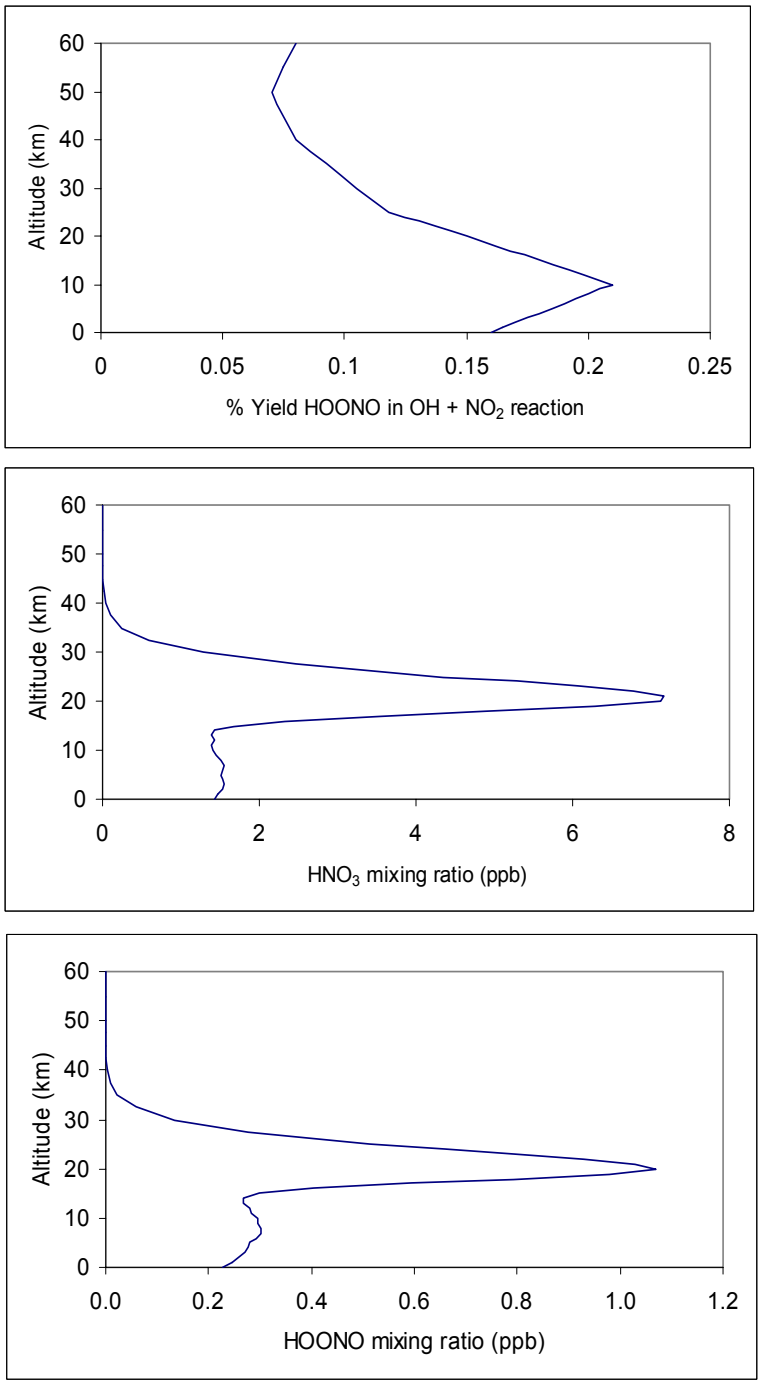

Figure 1-2. Vertical profiles of % yield of HOONO, HNO_3 mixing ratio in parts per billion, 10^{-9} (ppb), and HOONO mixing ratio in ppb. Percent yield and HNO_3 mixing ratio data used to generate these plots are from Golden et al.[9] and Kleinböhl,[10] respectively.

The formation of the short-lived HOONO molecule, rather than $HONO_2$, has important implications for the atmospheric budget of HO_x and NO_x. To the extent that HOONO is formed rather than $HONO_2$, reaction R1 recycles OH + NO_2 rather than serving as a permanent sink. Hence, the greater the branching ratio to HOONO, the weaker the sink of OH and NO_2 provided by this reaction. With HOONO formation, more OH and NO_2 reactive remain available for photochemical smog and ozone formation. Hence, quantifying the HOONO channel is an important component of understanding tropospheric ozone formation and air quality.

1.2.2. Peroxyacetyl nitrate (PAN) in the atmosphere

Peroxyacetyl nitrate (PAN) is formed in hydrocarbon-rich regions of the atmosphere by oxidation of acetaldehyde:

$$CH_3CHO + OH \xrightarrow{O_2} CH_3C(O)OO + H_2O \qquad (R2)$$

$$CH_3C(O)OO + NO_2 + M \rightarrow CH_3C(O)OONO_2 + M \qquad (R3)$$

The main sink of PAN throughout the troposphere is thermal decomposition, regenerating NO_2:

$$CH_3C(O)OONO_2 + M \rightarrow CH_3C(O)OO + NO_2 + M \qquad (R4)$$

The timescale of this reaction (the lifetime against thermolysis, $\tau_{thermolysis}$) determines the degree to which PAN contributes to long-range transport of NO_x to pristine regions of the atmosphere. At 295 K, $\tau_{thermolysis} \sim$ 1 hour, but at 240 K $\tau_{thermolysis} \sim$ several months.[11]

PAN accounts for a large fraction of all odd-nitrogen compounds ($NO_y \equiv NO + NO_2 + NO_3 + N_2O_5 + HNO_3 + HONO$ + peroxynitrates + alkyl nitrates) in most regions of the atmosphere, particularly at high latitudes and in polluted regions.[12,13] It has been suggested that long-range transport of PAN at high altitudes (lower temperature = longer lifetime) is a major source of NO_x in the remote troposphere.[14]

1.2.3. Methyl hydroperoxide (MHP) and hydroxymethyl hydroperoxide (HMHP) in the atmosphere

Organic hydroperoxides are formed in the atmosphere by RO_2-HO_2 radical-radical association reactions:

$$RO_2 + HO_2 \rightarrow ROOH + O_2 \qquad \text{(R5)}$$

This makes organic peroxides important temporary reservoirs or sinks of HO_x and RO_x species, depending on the subsequent chemistry of the ROOH. The peroxides can be photolyzed, releasing the radicals, or they can react with OH or be adsorbed on atmospheric droplets and be washed out permanently.[15] Analagous to PAN for NO_x, the transport of peroxides has been proposed to provide a significant HO_x source to remote regions of the troposphere.[16]

In the case of methyl hydroperoxide (MHP, CH_3OOH), the RO_2 radical (CH_3O_2) can be formed from OH reaction with many hydrocarbons, including methane:

$$OH + CH_4 \rightarrow CH_3O_2 + H_2O \qquad \text{(R6)}$$

This results in RO_2 sources not only in urban areas where multiple organic compounds are present, but also in the remote atmosphere where long-lived CH_4 is the

dominant hydrocarbon. In fact, formation of hydroperoxides is more efficient in the absence of NO_x, because of the competing reactions:

$$CH_3O_2 + NO \rightarrow NO_2 + HCHO + HO_2 \quad \text{(R7)}$$

$$HO_2 + NO \rightarrow OH + NO_2 \quad \text{(R8)}$$

This suggests that MHP will be a dominant HO_x reservoir species in the remote atmosphere. In fact, a recent field study found that over the tropical Pacific at an altitude of 8 – 12 km, photolysis of MHP accounts for 12 – 18% of the HO_x source.[17]

In the case of hydroxymethyl hydroperoxide (HMHP, $HOCH_2OOH$), in addition to $RO_2 + HO_2$ association reactions, another possible source exists in the ozonolysis of alkenes in the presence of water vapor:[15]

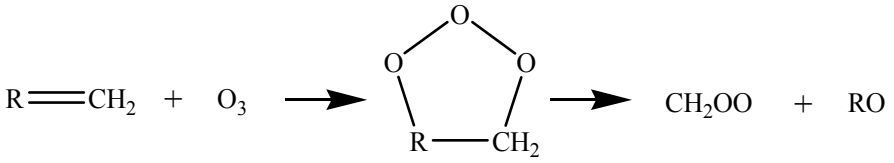

$$CH_2OO + H_2O \rightarrow HOCH_2OOH \text{ (HMHP)} \quad \text{(R9)}$$

This source of HMHP is distinct in that it does not involve HO_2. Hence, the dissociation of HMHP formed via reaction R9 results in a net formation of HO_x, rather than simply regeneration of HO_x from a reservoir.

Both MHP and HMHP have been detected in the atmosphere, and they are widely believed to be the two most abundant organic hydroperoxides.[18,19] Average measured atmospheric concentrations are in the tens of pptv to a few ppbv range for both peroxides.[19]

Thus, these two molecules are important to understand in the context of global transport and concentrations of HO_x.

1.3. Photochemistry in Earth's atmosphere

The reservoir species discussed in the previous sections, HOONO, PAN, MHP, and HMHP, all can be converted back to their constituent HO_x, NO_x, and RO_x radicals by thermal decomposition or by photochemical dissociation. Any thermal dissociation process with activation energy greater than about 100 kJ/mol will occur extremely slowly if at all in the Earth's atmosphere. The absorption of incoming solar radiation is an efficient alternate mechanism by which dissociation can be promoted when the bond dissociation energies are too high to allow thermolysis. Upon absorption of a solar photon, a molecule is deposited into a higher energy state than the local thermal equilibrium. The excess energy may be collisionally redistributed to return the molecule to Boltzmann equilibrium, or it may cause bond cleavage, resulting in *photodissociation* of the molecule.

This photodissociation process can be initiated by excitation of the molecule to an electronically excited state by absorption of UV radiation (200 – 400 nm). These transitions (300-600 kJ/mol) correspond to energies comparable to or in excess of most bond energies. For more weakly bound molecules, ground state processes may also promote dissociation. Absorption by a vibrational overtone may couple sufficient energy into the molecule to lead to photodissociation. The absorption cross sections for such vibrational overtone processes (~600 – 1500 nm) tend to be smaller than UV cross sections, and generally decrease one order of magnitude for each additional vibrational quantum. Some examples are shown in Table 1-1.

Table 1-1. Absorption cross sections in the UV and at specific vibrational overtones for some representative atmospheric molecules. Units are cm^2 $molecule^{-1}$ for UV absorption cross sections at 250 nm, and cm^2 $molecule^{-1}$ cm^{-1} for integrated absorption cross sections in the vibrational overtone bands. These overtone bands have linewidths on the order of 100 cm^{-1}.

Species	**σ(250nm) 298 K cm^2**	**σ($2\nu_{OH}$) cm^2 $molecule^{-1}$ cm^{-1}**	**σ($3\nu_{OH}$) cm^2 $molecule^{-1}$ cm^{-1}**	**σ($4\nu_{OH}$) cm^2 $molecule^{-1}$ cm^{-1}**
$HONO_2$	2.0×10^{-20} [a]		2.9×10^{-20} [c]	2.8×10^{-21} [c]
HO_2NO_2	4.1×10^{-19} [a]	9.5×10^{-19} [b]	3.8×10^{-20} [c]	3.0×10^{-21} [c]
H_2O_2	8.3×10^{-20} [a]		7.0×10^{-20} [c]	4.5×10^{-21} [c]

[a]Experimental cross sections from Sander et al.[20]
[b]Experimental cross sections from Roehl et al.[21]
[c]Experimental cross sections from Zhang et al.[22]

Because of the low cross sections in higher vibrational overtones, this process only need be considered for molecules with relatively low dissociation thresholds that will dissociate after excitation in a first or second overtone. OH-stretch vibrational modes are good candidates for vibrational overtone dissociation because of the generally large absorption cross sections and the high energy (~ 3500 cm^{-1} = 42 kJ/mol) of the mode.

In each individual case, a photolysis rate can be calculated for the UV photodissociation process and for vibrational overtone photodissociation to compare the magnitudes of the processes. This photolysis rate (J) incorporates the absorption cross section ($\sigma(\lambda)$), quantum yield of photodissociation ($\varphi(\lambda)$), and intensity of solar radiation at

that wavelength ($I(\lambda)$), and is integrated over some wavelength range of interest (i.e., UV or vibrational bands):

$$J = \int (\sigma(\lambda)\phi(\lambda)I(\lambda))d\lambda \quad (1)$$

The solar radiation term in equation 1 results in an altitude and solar zenith angle dependence of the UV photolysis rate because UV radiation is screened out by O_2 and O_3 absorption in the atmosphere. The solar zenith angle (SZA) is the angle between the sun's position in the sky and the normal to the surface, i.e., at daybreak and twilight, SZA = 90°. The solar spectrum as a function of altitude from the Earth's surface and solar zenith angle is shown in Figure 1-3. Because of the SZA dependence, overtone (near-IR) photodissociation processes, which occur in a region of the solar spectrum less attenuated at high SZA (> 600 nm), have been suggested to be responsible for an observed "burst" of HO_x at daybreak, when little UV radiation penetrates the atmosphere.[23] The observed OH and HO_2 diurnal variation is shown in Figure 1-4. The best model agreement to the field measurements requires including near-IR photolysis processes as well as the hydrolysis of bromine nitrate with reaction probability 0.8.

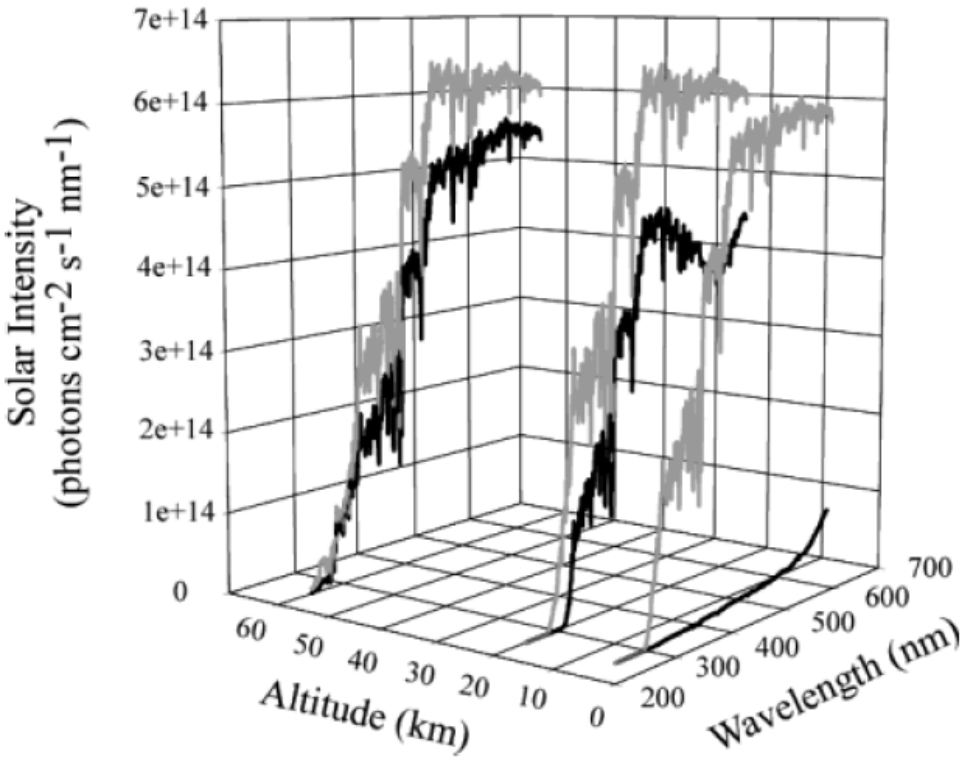

Figure 1-3. Altitude and solar zenith angle (SZA) dependence of the solar actinic flux (solar intensity). Black: SZA = 90°, gray: SZA = 0°. Reprinted with permission from Donaldson et al.[24] Copyright 2003 American Chemical Society.

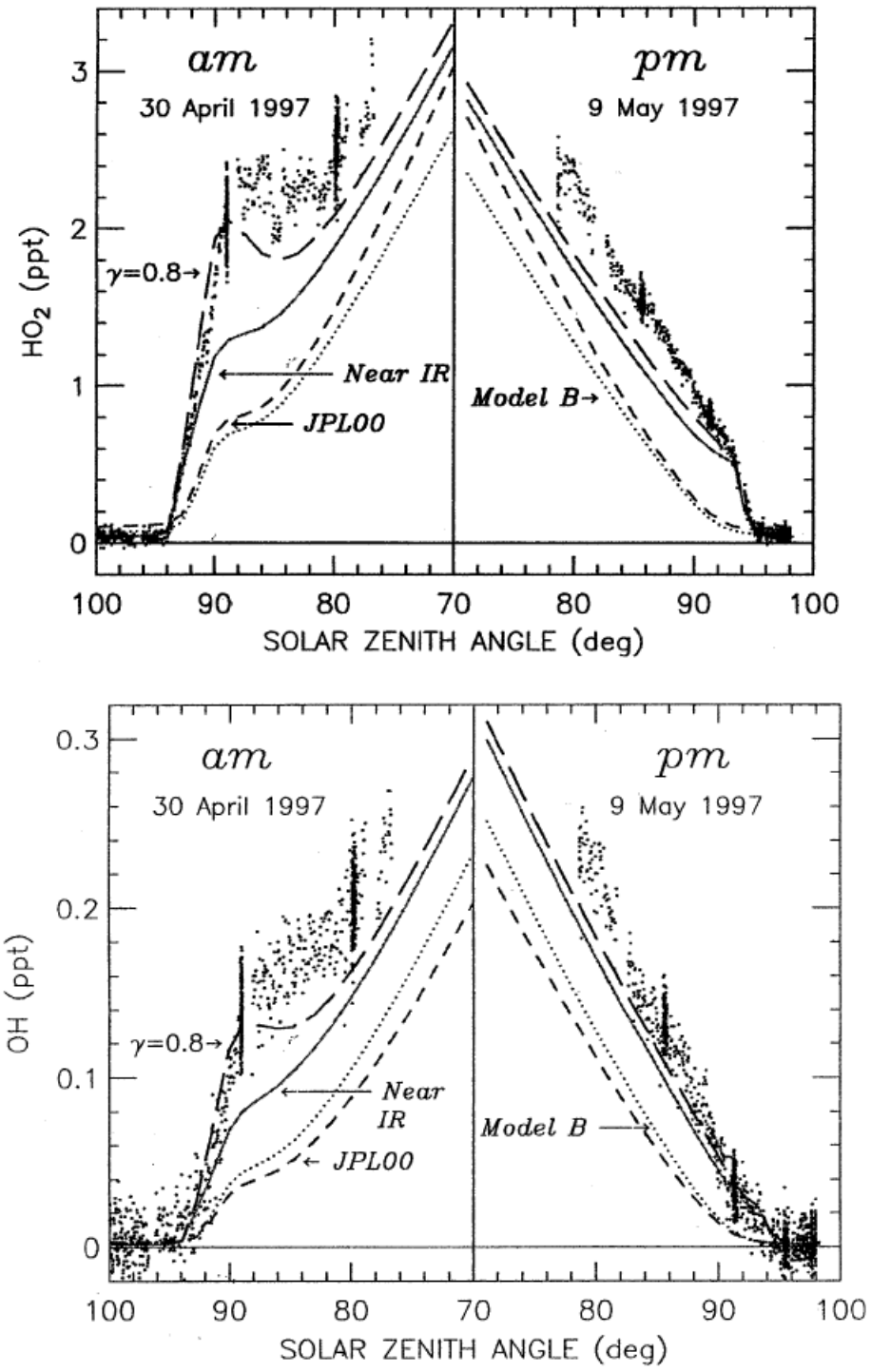

Figure 1-4. Comparison of observed OH and HO_2 concentrations with predictions from models of the HO_x chemistry. The best agreement (long dashed line) requires inclusiong of near-IR photodissociation processes and bromine nitrate hydrolysis. Reprinted with permission from Salawitch et al.[23] Copyright 2002 American Geophysical Union.

This thesis research includes investigation of several photodissociation processes for various atmospheric reservoir species and in various wavelength regions. These are summarized in Table 1-2.

Table 1-2. Summary of photodissociation processes studied in this thesis. Dissociation energies for the bond broken in these dissociation processes (in all cases listed here, an O-O bond) are also shown.

Atmospheric reservoir molecule	**Photodissociation processes studied**	D_0
cis-cis HOONO	$2\nu_{OH}$ region, multiple spectral bands (6200-7400 cm^{-1})	6860 cm^{-1} = 82 kJ/mol (Konen, et al.[25] with ΔE(cc-tp) from Bean et al.[26])
trans-perp HOONO	$2\nu_{OH}$ (6971 cm^{-1})	5670 cm^{-1} = 68 kJ/mol (Konen, et al.[25])
Peroxyacetyl nitrate ($CH_3C(O)OONO_2$, PAN)	$3\nu_{CH}$ (8550 cm^{-1}) and $4\nu_{CH}$ (11,100cm^{-1}), neither observed	9930 ± 330 cm^{-1} = 119 ± 4 kJ/mol (Bridier et al.[27]); 9470 ± 210 cm^{-1} = 113 ± 2.5 kJ/mol (Zabel[28])
Methyl hydroperoxide (CH_3OOH, MHP)	UV, 300 – 400 nm[a] (25,000 – 33,000 cm^{-1})	14880 ± 350 cm^{-1} = 178 ± 4 kJ/mol (Matthews et al.[29])
Hydroxymethyl hydroperoxide ($HOCH_2OOH$, HMHP)	UV, 300 – 400 nm[a] (25,000 – 33,000 cm^{-1}), $4\nu_{OH}$ (multiple bands 13,000 – 13,800 cm^{-1}), $5\nu_{OH}$ (multiple bands 15,900 – 16,700 cm^{-1})	14,050 ± 50 cm^{-1} = 168 ± 1 kJ/mol (Fry et al.[30])

a. For the MHP and HMHP UV photodissociation studies, photodissociation cross sections were measured in the range 300 – 350 nm and extrapolated to 400 nm.

In addition, the complex vibrational spectroscopy of HOONO and HMHP were investigated in greater detail and compared to theoretical models, and the rotational spectroscopy of *cis-cis* HOONO was studied. It is hoped that this rotational spectroscopic signature of HOONO will enable future atmospheric detection and quantification of this important molecule to allow better constraint of the OH + NO_2 + M reaction that serves as the major atmospheric sink of HO_x and NO_x.

1.4. Outline of thesis

The organization of the remainder of this thesis is outlined in this section. In the paragraphs below, I attempt to make clear the collaborative nature of these projects. While each chapter represents either research that I spearheaded or a project in which I was actively involved, I would certainly not have been able to have the breadth of experience and gain such diverse insights into the chemistry of atmospheric reservoir species without the opportunity to work with many wonderful collaborators. I mention them below in brief descriptions of each individual chapter. I am deeply grateful for the very educational and scientifically exciting experience of working with each of them.

Chapter 2 is an overview of the action spectroscopy experiment in the 063 South Mudd laboratory for the study of IR and UV photodissociation of molecules. The goal of this chapter is to provide a useful laboratory guide for future students, so I include detailed descriptions of the day-to-day operations and some troubleshooting tips. This was the laboratory for which I was primarily responsible. I do not include any operational details on the JPL and Caltech Blake Group submillimeter spectrometers that were used for rotational spectroscopy studies or on the UCSD photodissociation experiment, since those

instruments are managed by other groups and more expertise can be found with Dr. Brian Drouin (JPL), Susanna Widicus Weaver and Prof. Geoff Blake (Caltech), or Jamie Matthews and Prof. Amit Sinha (UCSD).

Chapter 3 presents a detailed study of the near-IR vibrational overtone photodissociation spectroscopy (also called action spectroscopy) of peroxynitrous acid, HOONO, in the $2\nu_{OH}$ region. With excellent mentoring from Dr. Sergey Nizkorodov, who first detected gas-phase HOONO in the laboratory,[31] I found that this molecule has two stable conformers, *cis-cis* and *trans-perp* HOONO. With our kinetics flow tube we were able to directly measure the isomerization from *trans-perp* to the more stable *cis-cis* HOONO, and we studied the action spectrum of both species experimentally and theoretically. It was found that *cis-cis* HOONO is the only atmospherically relevant conformer. This work was published in the Journal of Chemical Physics in July 2004 (Fry, Nizkorodov, Okumura, Roehl, Francisco, and Wennberg[32]), and the text of chapter 3 is taken directly from that paper.

Chapter 4 is a discussion of the physical basis for the complex vibrational spectroscopy of HOONO. In collaboration with Prof. Anne McCoy (Ohio State University) and Prof. Joe Francisco (Purdue University), we developed a simple 2-dimensional model incorporating the OH stretch and the HOON torsion modes with statistical quantum yield which describes the majority of the vibrational spectrum. Cavity ringdown experiments were done in our laboratory to verify this model, in collaboration with graduate student Andrew Mollner, who brought his ringdown cell across campus for the experiments. This work was published in the Journal of Chemical Physics in March

2005 (McCoy, Fry, Francisco, Mollner, and Okumura[33]) and is included as Appendix I. The text of chapter 4 is an original description of this collaborative project.

Chapter 5 presents a discussion of the rotational spectroscopy of *cis-cis* HOONO. The millimeter-wave and submillimeter-wave spectroscopy of *cis-cis* HOONO was measured in Prof. Geoff Blake's laboratory at Caltech and (primarily) in the Jet Propulsion Laboratory (JPL) submillimeter spectroscopy group with Dr. Brian Drouin and Dr. Chip Miller. It is hoped that the known submillimeter spectroscopic signature of HOONO will aid in its detection in the atmosphere (Chapter 9). Comparison of the rotational spectra of HOONO and its deuterated isotopomer, DOONO, provides structural information about the molecule. Stark effect measurements were also applied to experimentally determine the dipole moment of HOONO for the first time. The knowledge of this dipole moment makes quantitative spectroscopic investigations of HOONO possible, and will also allow any future spectroscopic detection of HOONO in the atmosphere to be expressed in terms of an absolute column abundance. These results were published in two papers, in a March 2004 Journal of Chemical Physics paper (Drouin, Fry, and Miller[34]) and in a forthcoming Journal of Chemical Physics paper (Fry, Drouin, and Miller[35]). The former publication is included as Appendix II, and the text of chapter 5 is taken directly from the latter.

Chapter 6 discusses the near-IR photodissociation of peroxyacetyl nitrate (PAN, $CH_3C(O)OONO_2$), to assess whether infrared radiation converts this reservoir species back to reactive NO_x. Attempts to measure this photodissociation process in the laboratory employing chemical ionization mass spectrometry (CIMS) are described. These experiments were unsuccessful, likely due to the large binding energy of PAN. Statistical

modeling was used to interpret this system, with the help of measured (FTIR) relative intensities of the ν_{CH}, $2\nu_{CH}$, and $3\nu_{CH}$ bands. These latter experiments and calculations are described in a paper published in February 2005 (Nikorodov, Crounse, Fry, Roehl, and Wennberg[36]), which is included as Appendix III. The text of chapter 6 outlines these results, focusing on the portion of the work that I was primarily responsible for, the (failed) attempt to observe PAN photodissociation in the laboratory.

Chapter 7 describes photodissociation action spectroscopy experiments on two organic hydroperoxides using tunable UV radiation. The additions to the laser system required to generate tunable UV were designed by Dr. Coleen Roehl and implemented by her and by Dr. Zsuzsa Marka, while my contribution to this work was to assist them in the maintenance and calibration of the system and data collection and analysis (calculations presented in this chapter). The study of the wavelength dependent UV photodissociation cross section of methyl hydroperoxide (MHP, CH_3OOH) and hydroxymethyl hydroperoxide (HMHP, $HOCH_2OOH$), the two most atmospherically abundant organic hydroperoxides, is presented here. Total UV photolysis rates are calculated by summing the product of solar photon flux with photodissociation cross section over this entire band for both peroxides, with extrapolation used for wavelengths at which measurement was not possible. The text of chapter 7 briefly describes these experiments and calculations. A publication on this work is forthcoming (Roehl, Marka, Fry, and Wennberg[37]).

Chapter 8 is a discussion of near-IR and visible photodissociation action spectroscopy experiments on the more weakly bound of the two organic peroxides discussed in chapter 7: hydroxymethyl hydroperoxide (HMHP). The goal of this

experiment was to determine if vibrational overtone excitation could cause dissociation of HMHP and be a significant atmospheric source of HO_x. The spectroscopy and dissociation kinetics of HMHP are interesting due to the two distinct OH stretches and the dissociation threshold falling within one of the OH bands. The spectra in the $4\nu_{OH}$ and $5\nu_{OH}$ region were measured in the laboratory of Prof. Amit Sinha at UCSD, in collaboration with Dr. Coleen Roehl (Caltech) and graduate student Jamie Matthews (UCSD). Analysis of these spectra by *ab initio* spectral modeling was also a collaborative effort, with Prof. Henrik Kjaergaard and graduate student Jo Lane (University of Otago, New Zealand). I was responsible for the analysis and write-up of the spectroscopy portion of this work, and the paper soon to be submitted to the Journal of Physical Chemisry A (Fry, Matthews, Lane, Roehl, Sinha, Kjaergaard, and Wennberg[30]) is the text of chapter 8. A subsequent paper on the dissociation dynamics of HMHP is forthcoming (Matthews, et al.[38]).

Chapter 9 discusses the possibility of looking for HOONO in the atmosphere using the recently established rotational spectroscopic signature. I propose an atmospheric search for HOONO using the Universität Bremen Airborne Submillimeter Radiometer (ASUR) and/or the NASA Jet Propulsion Lab Submillimeter Limb Sounder (SLS). The expected signal from atmospheric HOONO has been predicted for both platforms. Helpful discussions with Armin Kleinböhl and Bob Stachnik contributed to this chapter. Both instruments are described briefly, and the feasibility of in situ atmospheric measurement of HOONO is discussed.

Appendices I-III are the related publications mentioned in the paragraphs above, and Appendix IV is a list of all papers published in conjunction with this Ph.D. thesis.

CHAPTER 2

ACTION SPECTROSCOPY INSTRUMENTATION AND CHEMICAL SYNTHESES

Chapter 2

2. ACTION SPECTROSCOPY INSTRUMENTATION AND CHEMICAL SYNTHESES

2.1. Introduction

The experimental apparatus used to study near-IR and UV photodissociation processes is located in the Wennberg Group Atmospheric Spectroscopy and Kinetics Laboratory in 063 South Mudd Building at Caltech. This technique is referred to as *action spectroscopy* because the laser light affects a chemical change when it leads to dissociation of the molecule.

The action spectroscopy experiment consists of two lasers: a pump pulse that is tuned over vibrational overtone resonances (for near-IR overtone photodissociation) or over the continuum of an electronically excited state (for UV photodissociation); a probe pulse that is tuned to excite a resonant electronic transition of a product fragment (in all experiments discussed here the fragment probed is OH radical); a kinetics flow cell in which reactants are generated or mixed and chemically evolve; a detection chamber where the laser pulses and gas flow intersect; and a photomultiplier tube (PMT) detects laser induced fluorescence (LIF) of the product fragment. For selected experiments, the gas mixture downstream of the action spectroscopy experiment is sampled into a long-path Fourier transform infrared (FTIR) spectrometer for characterization. A schematic of this action spectroscopy instrument is shown in Figure 2-1.

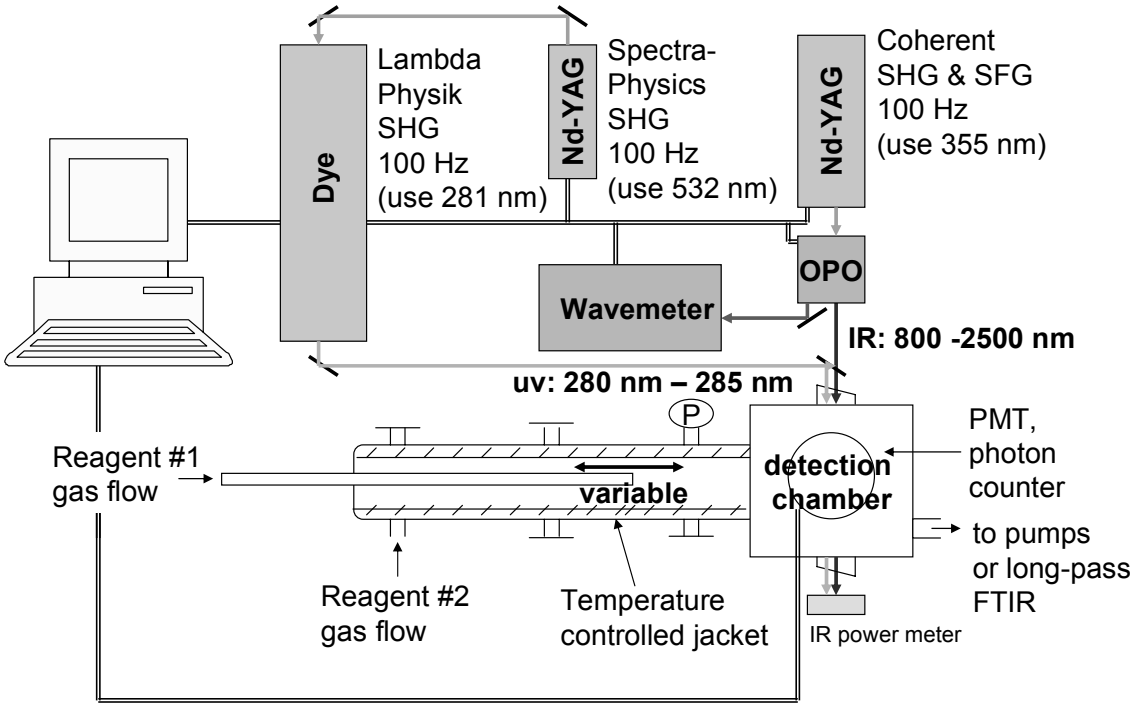

Figure 2-1. Schematic of action spectroscopy experiment apparatus in the Wennberg Atmospheric Spectroscopy and Kinetics Lab in 063 S. Mudd.

The experiment is run by LabView programs which control pump-probe delay and pump pulse wavelength, monitor pump laser power and wavelength, and gate and average the PMT signal. Three possible types of experiments are categorized in Table 2-1.

Table 2-1. Overview of three types of experiments possible with the action spectroscopy instrument.

Experiment type	Pump wavelength	Probe wavelength	Pump-probe delay
Spectroscopy	Varied	Constant	Constant
Product state	Constant	Varied	Constant
Kinetics	Constant	Constant	Varied

In sections 2.2 – 2.9 below, I describe each of the components of the action spectroscopy instrument in detail, including an overview of each software program used routinely in our lab (2.9). In the final section (2.10) I list a series of tips and troubleshooting hints for the lab.

2.2. Optical parametric oscillator (OPO) generation of tunable radiation

2.2.1. OPO

The optical parametric oscillator (OPO) used in our experiment is a novel design by Wu et al.[39,40] in Geoff Blake's research group at Caltech. The OPO used in this research is also described in Dr. Hui Zhang's 2001 California Institute of Technology Ph.D. thesis.[41]

The principle of optical parametric oscillation is the nonlinear difference frequency generation (DFG) caused by the incidence of a high-power laser pulse on a birefringent crystal. The angle of the crystal with respect to the incident light (φ) determines how the photon energy is split between the energies of the two DFG beams produced, referred to as the signal (higher energy) and idler (lower energy) beams:

$$\omega_{input} = \omega_{signal}(\phi) + \omega_{idler}(\phi) \qquad (2)$$

In this case two crystals are employed to allow compensation for beam walk-off, so that the output beam has the same Poynting vector regardless of wavelength. The crystals are type-II (signal and idler beam have opposite polarization) phase matched β-BaB_2O_4 (BBO), an improvement made by Wu et al. over the type-I (signal and idler same polarization) phase-matching used in earlier OPOs. These type-I BBO OPOs were

inherently more efficient because of larger nonlinear coefficients; however, they suffered from inconsistent linewidth as a function of operating wavelength.[42] This next-generation type-II BBO OPO has a low lasing threshold, high efficiency, and covers the same desirable tuning range as OPOs based on type I interactions. Improvements in cavity design and crystal coatings have made this new type of OPO efficient enough to be preferable to older designs, and we were fortunate to have one of the first type-II BBO OPOs to use in our laboratory.

The simple two-crystal, planar mirror OPO cavity is shown in Figure 2-2. The OPO is pumped at 100 Hz by 355 nm light that is the tripled output of a Nd:YAG laser (described below). The cavity consists entirely of planar mirrors. M1 and M2 are standard 45° high reflectors for *p* polarized 355 nm light. The output coupling mirror, M3, is a normal-incidence Nd:YAG 355 nm high reflector. The rear mirror, M4, is a standard metallic reflector in the near-IR. A Schott RG715 long-pass glass filter (shown as a gray bar in Figure 2-2) is placed at a 45° angle in the output beam, which consists of the three wavelengths ω_{input}, ω_{signal}, and ω_{idler}. This filter reflects the visible signal beam and passes the near-IR idler beam.

The two BBO crystals are mounted on actuator stages with digital stepping motors for precise rotation and are calibrated with the help of a LabView program that gives very reproducible scanning. Mirrors M1, M4, and M3 are finely tunable to align the cavity for optimum lasing. The two BBO crystals measure ~ 6 mm × 12 mm × 12 mm and are cut for type-II phase matching with a high damage threshold (>500 MW/cm^2 and 355 nm for nanosecond pulses) protective and antireflective dielectric coating.

We have purchased two sets of crystals from the CASIX and Kaston suppliers,[*] so that when the crystal coating gets damaged (this happens approximately every 6 months with regular use of the OPO at pump pulse energy of ~ 225 mJ/pulse), the crystals can be swapped out while the damaged pair gets sent in for recoating. This necessitates finding lasing and from scratch calibration of the OPO, which can be challenging. Some tips on this process are given in section 2.10.1.

The data for the two sets of crystals are given in Table 2-2. They are slightly different in cut angle, resulting in overlapping but slightly different usable ranges. The relevant equation for determining the idler wavenumber from the measured signal wavelength, using the pump laser third harmonic of 354.92 nm, is

$$Idler[cm^{-1}] = 10^7 \times \left(\left(\frac{1}{354.92} \right) - \left(\frac{1}{\lambda_{signal}[nm]} \right) \right) \quad (3)$$

[*] CASIX, Inc.: http://www.casix.com; Kaston Optronics Manufacturing, Ltd.: http://www.kaston.net.

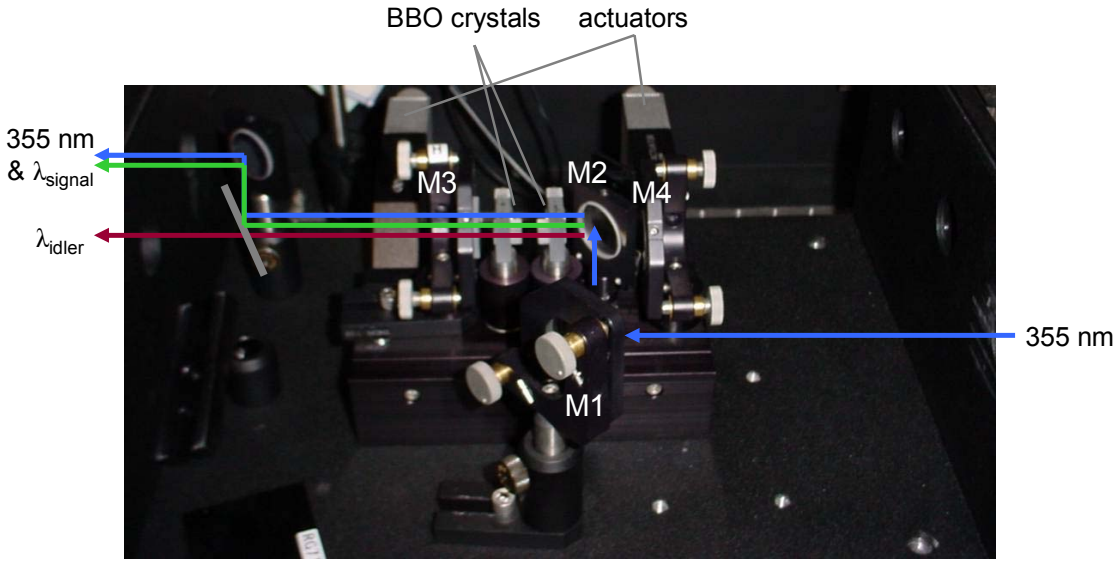

Figure 2-2. Custom-built type-II β-BaB_2O_4 optical parametric oscillator used for generation of tunable near-IR and visible radiation.

Table 2-2. Usable range for the two sets of crystals used in the OPO.

	CASIX	**Kaston**
Cut angle θ	28.5°	36.8°
Cut angle φ	30°	30°
Optimum signal range	420–550 nm 18,000–24,000 cm^{-1}	477–620 nm 16,000–21,000 cm^{-1}
(Corresponding) optimum idler range	1000–2300 nm 4900–10,000 cm^{-1}	800–1400 nm 7200–12,000cm^{-1}

The reported usable efficiency of this OPO is up to 30%.[39] With our ns pump laser running at the maximum pulse energy possible without fast damage to the BBO crystals (225 mJ/pulse at 1064 nm gives ~ 0.7 W at 10 Hz at 355 nm), we get an average of 2-3 mJ/pulse in the idler beam. We routinely use the idler beam in the range 1300-1700 nm

(5900-7700 cm^{-1}) to study OH first overtones ($2\nu_{OH}$), in the range 1100-1200 nm (8200-900 cm^{-1}) to study OH second overtones ($3\nu_{OH}$), and have looked for CH second and third overtones ($3\nu_{CH}$ & $4\nu_{CH}$) around 1800 nm (5500 cm^{-1}) and 1300 nm (7800 cm^{-1}). For tunable UV generation, the *signal* output is used in a subsequent frequency mixing step. For these experiments, we use signal output in the range 420 – 560 nm. The relevant formula for calculating the UV wavelength in nm from the second mixing stage between the measured OPO signal output and the pump laser fundamental at 1064 nm is:

$$Mixed\ UV[nm] = 1/\left(\left(\frac{1}{\lambda_{signal}[nm]}\right)+\left(\frac{1}{1064}\right)\right) \quad (4)$$

All calibrations are catalogued in the Infinity + OPO Logbook. This gives a good overview of all the ranges accessible with each set of crystals.

2.2.2. Coherent Infinity 40-100

The pump laser used for this OPO is a 100 Hz 3 ns pulse width Q-switched Coherent Infinity 40-100 Nd:YAG laser, shown in Figure 2-3. The manual for the Infinity laser is surprisingly comprehensive and quite good, including excellent descriptions of the scientific principles involved. I recommend any new student in the lab spend an afternoon reading it. The description of that laser here is brief. Through the use of phase conjugate optics, the Infinity laser system outputs a beam of excellent mode quality (TEM_{00}) at high repetition rates, making it ideally suited as an OPO pump beam. The 1064 nm pulses are doubled in type-I second harmonic generation (SHG) in BBO, to generate 532 nm. A waveplate is used to rotate the 1064 nm polarization onto the 532 nm polarization, and a

second type-I stage in BBO generates 355 nm. This second nonlinear stage is referred to as third harmonic generation (THG) because by adding 1064 nm + 532 nm it produces the third harmonic of 1064 nm, 355 nm. The measured 355 nm pulse energy that we use to pump our OPO is 0.6 – 0.8 W at 10 Hz, with the IR power set to 225 mJ/pulse. This power is measured at 10 Hz because at 100 Hz the power in this beam would burn the power meter.

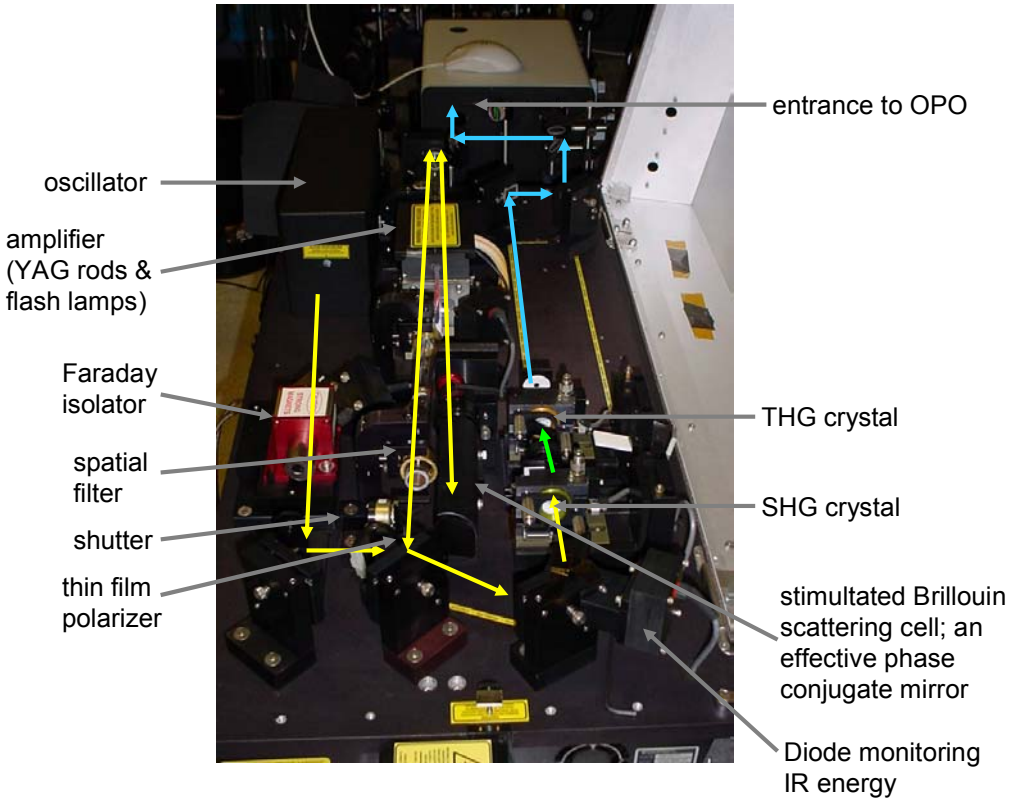

Figure 2-3. Coherent Infinity 40-100 laser used to pump the OPO. Beam path is indicated: yellow: 1064 nm light, blue: 355 nm light.

The recommended start-up procedure is to turn on the Neslab water circulator (mounted high on the south wall of the lab) and put the laser in "standby" mode at least 30

minutes before starting the flashlamps. The laser has an interlock that will not allow it to start before the resistivity of the water in the flow system goes above a threshold value, by circulating through the deionization filter. If this seems to take too long, the valve on the water flow can be opened slightly (see Infinity manual). If it still seems to take too long, the water and/or filter may need to be replaced.

The Infinity laser system is quite robust. Routine maintenance includes occasional replacement of the flash lamps (described in detail in the manual), occasional replacement of the cooling loop water and/or deionization filter, and more frequent "tune-ups" involving cleaning of the optics with MeOH on lens paper (wearing gloves to avoid getting any oils on the optics) and tweaking up the power by adjusting the SHG and THG crystal alignment. All maintenance and repairs are recorded in the Infinity & OPO Log Book. As marked inside the laser cover, it is recommended to only adjust the horizontal axis on the SHG crystal and the vertical axis on the THG crystal to avoid beam walk-off. This adjustment is done with an Allen wrench. Adjust these crystals while looking at the output of the OPO, not the Infinity alone, as the optimum alignment of the Infinity for best coupling into the OPO may not be identical to the optimum alignment for maximum 355 nm power output.

In addition to this routine maintenance, we have over the past few years made two more substantial repairs. We replaced the back window on the THG crystal mount in March 2003 because the coating had become damaged over time. A detailed description of how to remove the THG crystal is found in the log book. We also replaced the SBS (stimulated Brillouin scattering) cell in July 2003, after a hole was drilled in the front

window of it by accidentally running the laser at 3600 Hz for a few minutes. TRY NOT TO DO THIS! The Infinity has no guard against triggering externally at too high a repetition rate, so if you trigger off the probe laser at 6400 Hz and don't have the timing electronics set to divide the trigger pulse train frequency by 64 (see section 2.4 below), you WILL run the Infinity at 6400 Hz and will almost certainly damage the optics. Both of these repairs were relatively easy to do because the components are easy to remove and replace. However, since this laser has been discontinued and is no longer supported by Coherent, I recommend extreme caution with any repairs. A stockpile of flashlamps and spare parts is in the laser drawer in 063 S. Mudd.

2.2.3. Wavelength monitor: Burleigh Pulsed Wavemeter

A Burleigh Pulsed Wavemeter (Figure 2-4) is used to monitor the wavelength output of the OPO. A portion of the visible (λ_{signal}) output of the OPO is directed into the Wavemeter. Inside the wavemeter, the OPO laser light is passed through two Fabry-Perot interferometers (etalons) calibrated against an internal HeNe reference laser to generate interferograms which are detected by a CCD array and analyzed by the instrument to return to the experimenter the wavelength of the visible light. The operating wavelength of the Wavemeter is 400 – 1100 nm, and a gradient ND filter on the input to the instrument allows attenuation of incident light to an intensity tolerable to the instrument.

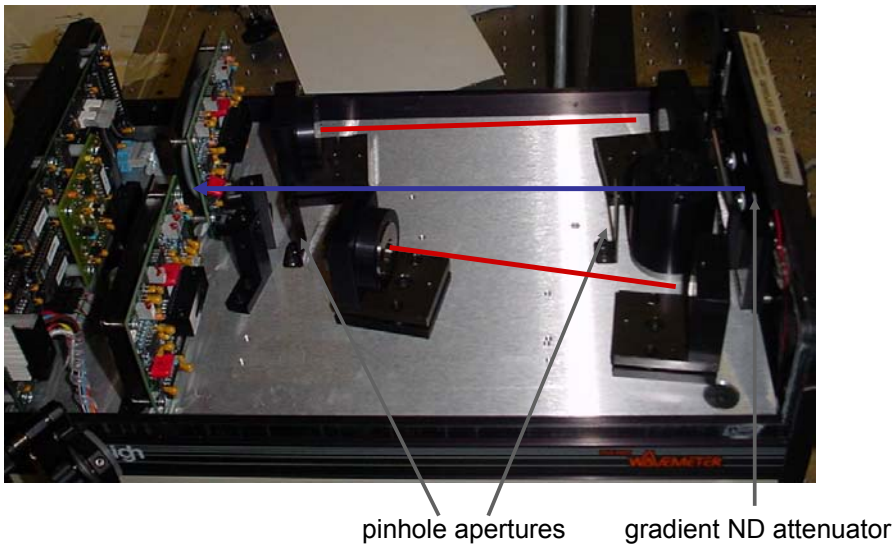

Figure 2-4. Burleigh Pulsed Wavemeter used to monitor the wavelength of the OPO signal output. The two pinhole apertures are used for alignment and the gradient ND attenuator is used to reduce input laser light intensity. Beam path is indicated, blue: visible incident beam from OPO, red: two etalon paths.

The alignment of the Wavemeter can be a bit tricky. Open the ND attenuator fully, then use two adjustable mirrors to direct the signal beam into the wavemeter, first ensuring by looking at a large distance that the beam is parallel to the laser table. Adjust the first of these two mirrors to align the signal beam into the first pinhole aperture, then use the second mirror to align onto the back aperture, and then iterate until maximum signal light is getting through behind the second pinhole. Last, use the attenuator to achieve nice Gaussian peaks in the interference pattern shown on the monitor. The horizontal axis can then be tweaked up slightly to achieve a symmetric interferogram pattern. As you make these last adjustments, you will notice that the output wavelength depends on the symmetry

of the pattern, so it's important to check this anytime you make changes elsewhere in the optics.

To calibrate the Wavemeter reading against an absolute standard, we have employed photoacoustic spectroscopy of water vapor. A 5 cm long cell with quartz windows containing 12 Torr H_2O vapor and a hearing aid microphone was inserted into the OPO idler beam path. The microphone voltage output was monitored by oscilloscope, and the peak voltage of the acoustic signal was recorded as a function of OPO idler wavenumber in the range 7100 – 7300 cm^{-1}, where well-known water transitions are found. Calibrating to the intense features found in this region, we found that a correction of + 4 cm^{-1} should be applied to Wavemeter derived readings. It is not clear to me why this is the case, and I would recommend repeating this calibration experiment to see if there is any change over time. This photoacoustic calibration was most recently done in September 2004, when the + 4 cm^{-1} correction was confirmed.

2.3. Laser-induced fluorescence (LIF) detection of OH radical

2.3.1. OH LIF theory

In all of the experiments described in this thesis, the action spectroscopy dissociation results in the formation of OH fragments, which are well-suited to detection by laser induced fluorescence (LIF). The 282 nm UV output of a second laser system is employed to excite the OH fragment to a vibrationally excited state on an excited electronic surface ($A^2\Sigma$ (v=1) ← $X^2\Pi$(v=0)). Collisional relaxation brings the OH fragments down to

$A^2\Sigma$ (v=0), from where they fluoresce near 309 nm ($A^2\Sigma$ (v=0) → $X^2\Pi$(v=0)). This process is illustrated schematically in Figure 2-5.

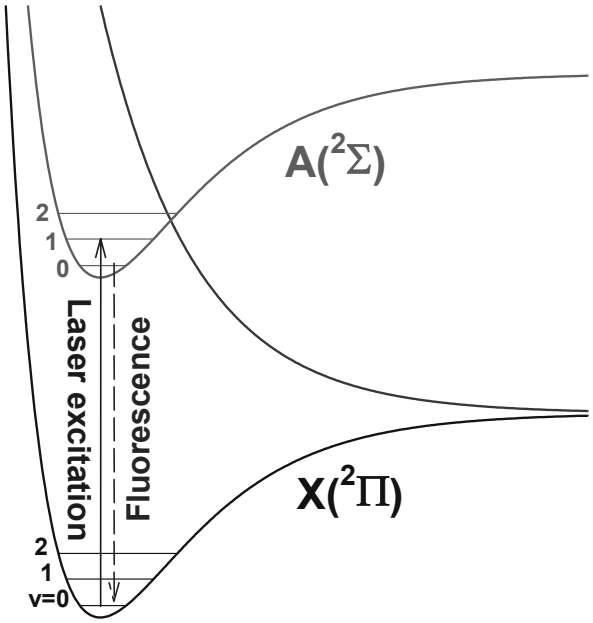

Figure 2-5. Schematic of OH electronic spectroscopy relevant to LIF detection. Laser excitation is around 282 nm and fluorescence is around 308 nm. Figure courtesy of Sergey Nizkorodov.

This LIF process depends sensitively on the presence of collision partners for relaxation to the v = 0 state, and hence on pressure. It has been demonstrated that for pressures above a few Torr, ~ 75% of excited OH molecules undergo vibrational energy transfer to v = 0.[43] The demonstrated detection threshold of this LIF instrument is on the order of 10^5 molecules cm^{-3} of OH.[43]

2.3.2. Spectra-Physics Nd:YAG and Lambda Physik dye laser

The laser used to generate the OH LIF UV excitation pulse is a Spectra Physics T40-532Q Nd:YAG pumped Lambda Physik dye laser. The Spectra Physics Nd:YAG laser generates 30 ns pulses of a few Watts of 532 nm light at repetition rates up to 10 kHz (most recently measurement: 0.85 W at 1000 Hz). This beam is directed into the Lambda Physic dye laser (Figure 2-6). The dye laser circulates Rhodamine 6G to generate tunable laser light in the range 550 – 590 nm. This visible, red dye beam is doubled in a KDP crystal (Lambda Physik FL30) to generate tunable UV in the range 275 – 295 nm with pulse energy < 1 μJ. A beam walk-off compensator crystal immediately after the KDP crystal ensures that the UV beam does not change direction with changing wavelength.

The primary maintenance need of this laser system is occasional replacement of the motor brushes in the dye circulator. This will be apparent in the terrible sound the motor makes. It is very important that this problem not be allowed to persist, because if the dye is not circulating, local heating in the dye solution can destroy the dye and potentially cause damage to the cuvet in the beam spot. The Spectra-Physics (SP) YAG laser is a hands-off system, not designed to be optimized in any way by the user. After a building power surge in S. Mudd in October 2003, we needed to replace one of the two diodes in the laser power supply. This required sending in the entire power supply (box under the laser table). Trouble with one of the diodes can be easily diagnosed: in the software running the SP YAG, the current can be independently adjusted for the two diodes. By turning them off sequentially, it is possible to ascertain that both are operational. The SP YAG is generally run with both diode currents set to 19.0 Amps. The power output can be optimized

somewhat by adjustment of the diode temperatures and crystal temperature (this is the temperature of the doubling crystal) in the software window. The SP YAG + Lambda Physik Dye Log book contains descriptions of past optimizations. The R6G dye is extremely long-lived, but it will need to be replaced occasionally. This will be apparent in a gradual decrease in power of the dye output.

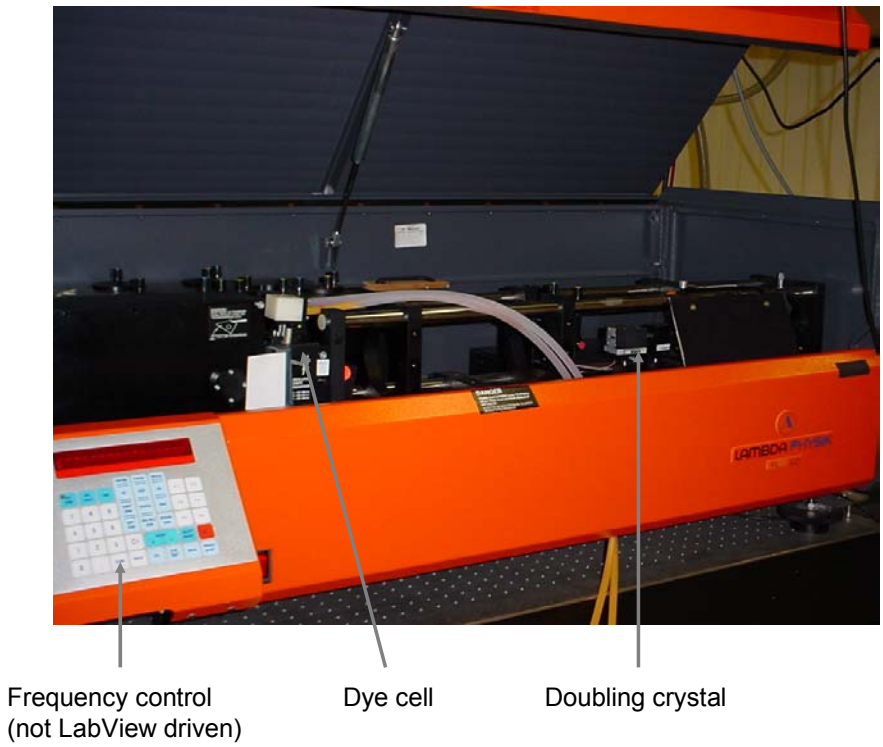

Figure 2-6. Lambda Physik dye laser and doubling crystal for generation of tunable UV laser light for OH LIF.

2.3.3. Photomultiplier tube detection of OH fluorescence

The fluorescence signal is focused onto a bialkali photomultiplier tube (PMT) mounted at 90° to both laser beams and the gas flow. A narrow band filter centered at 310

nm with 6 nm transmission bandwidth is used to reject scattered UV and visible light from the PMT. The signal from this PMT is amplified and directed into a Stanford Research Systems (SRS) model SR400 Gated Photon Counter. This instrument times the laser delay and gates the LIF signal to acquire only the actual OH LIF signal. This is described in more detail below. The SRS photon counter has two adjustable gates (Gate A and Gate B) to apply to the input signal, and can set a delay and send an output trigger pulse as well. This capability is exploited in the pump and probe laser timing.

2.4. Laser triggering and timing electronics

Timing is controlled in this experiment via the SRS photon counter, with one of the two pump Nd:YAG lasers serving as the master. Two possible triggering schemes are shown schematically in Figure 2-7. "Vic's box" is the historical name for a piece of electronics hardware that is used to divide the frequency or switch the polarity of the signal directed through it, depending on the triggering scheme in use. The operation of Vic's box is outlined in Figure 2-8.

The output of Gate A is used to control the pump-probe delay of the system. Gate B is optimized to reject the UV LIF probe pulse scatter, but to collect the maximum amount of OH LIF signal. The gate delays and widths (for A and B) can be adjusted in the SRS by touching "COM," then selecting A or B, using the up and down arrows to select gate delay or width, and then using the black turning knob to change the value.

For the 100 Hz mode, the Infinity laser is the master trigger. The Infinity software must be set on triggering "internal," and the SP YAG on trigger pulse repetition frequency

(PRF) = 0. This is its default setting for accepting an external trigger. The Infinity Q-switch sync is input to the SRS, and the Gate A output is channeled into Vic's box. The Channel 1 output with up polarity (the right Channel 1 BNC port in Figure 2-8) is sent to the SP trigger in. No delays or frequency dividing are used on Vic's box.

For the mode with 100 Hz pump and a 6400 Hz "comb" of probe pulses, the SP YAG is the master trigger. The Infinity software must be set on "external" (be careful not to trigger at too high a repetition rate! There is no guard against this!), and the SP YAG trigger PRF = 6400. The SP YAG sync out is directed into *both* Vic's box and into the SRS. Vic's Channel 2 out with down polarity (the left Channel 2 BNC in Figure 2-8), which generates the division to 100 Hz repetition rate, is sent to the Infinity lamp trigger in. Check this rep rate with the oscilloscope before triggering the Infinity off it. The SRS timing can be adjusted such that Gate A is zero and Gate B comes just after the probe laser pulse. Vic's box delay is used to move Gate B so that it does not include the pump laser pulse.

The most common experiment done in this thesis was the 100 Hz experiment with the Infinity as the master trigger. For these experiments, good initial settings for the SRS are Gate A and Gate B delays separated by about 1.1 μs to reject UV scatter from Gate B and gate widths on the order of 2 – 10 μs. The relative delays can be optimized by observing PMT signal in "free run" mode, scanning Gate B delay upwards from a value equal to Gate A delay, and looking for the cutoff where Gate B drops to much lower counts than Gate A. The widths can be optimized by reducing them until signal starts to be

diminished strongly. These widths should be set at the minimum possible to avoid averaging in noise but collect all signal.

The *absolute* pump-probe delay can be set to any value desired. A good setting is to arrange that at Gate A delay = 0 (i.e., the minimum setting for the triggering electronics), so that the probe pulse actually occurs slightly *before* the pump pulse. This way the delay can be scanned through zero to obtain a true baseline for any dissociation kinetics scans. This absolute pump-probe delay can be measured by a photodiode each collecting scattered OPO output and the SP YAG scattered light (fed into Channel 1 and 2 of the oscilloscope). These are normally left set up on the laser table so that the delay can be checked at any time by turning on the scope.

The pump-probe delay can be varied via the Infinity laser software. In the Infinity Application Interface window are two variable settings with scroll bars under High-precision Trigger: the coarse and Vernier scales. One count on the Vernier scale corresponds to approximately 0.5 ns, and the coarse scale is very coarse. It is likely only the Vernier scale will need to be varied. With Gate A delay = 0, the Vernier scale setting can be adjusted while observing the delay on the scope to set the delay for probe preceding pump. Then the absolute values of Gate A and Gate B can be set for the pump-probe delay appropriate for a given experiment.

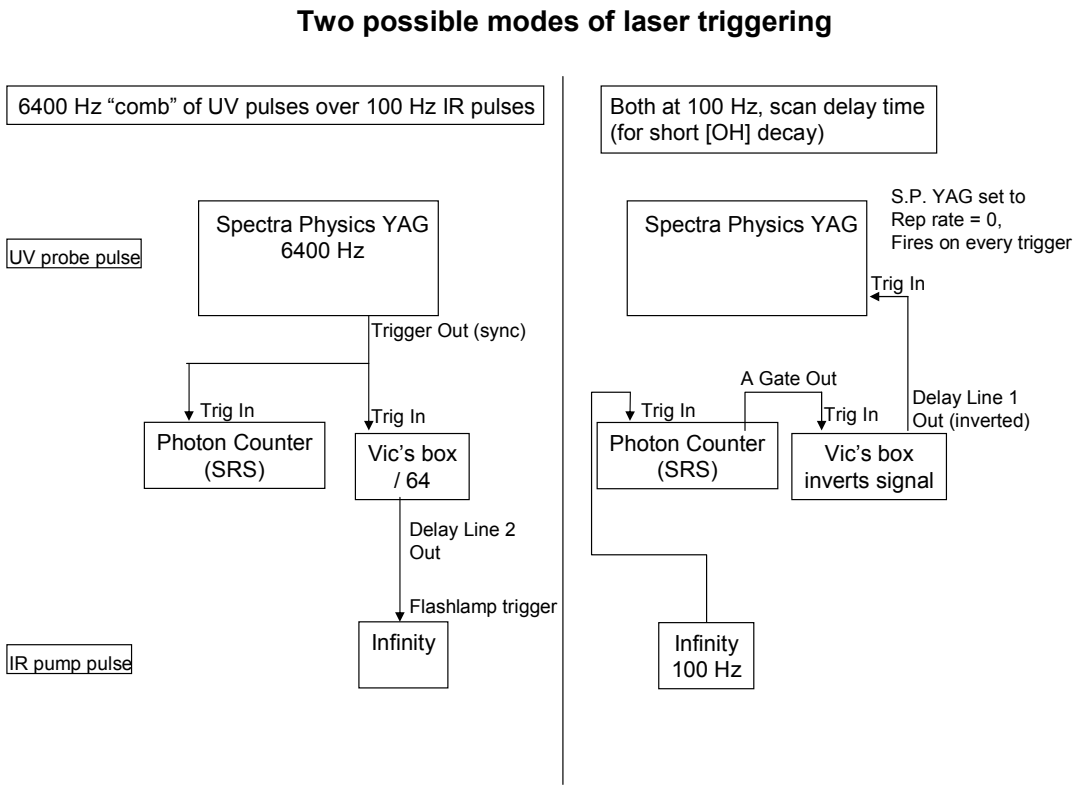

Figure 2-7. Diagram of the two possible modes of laser triggering.

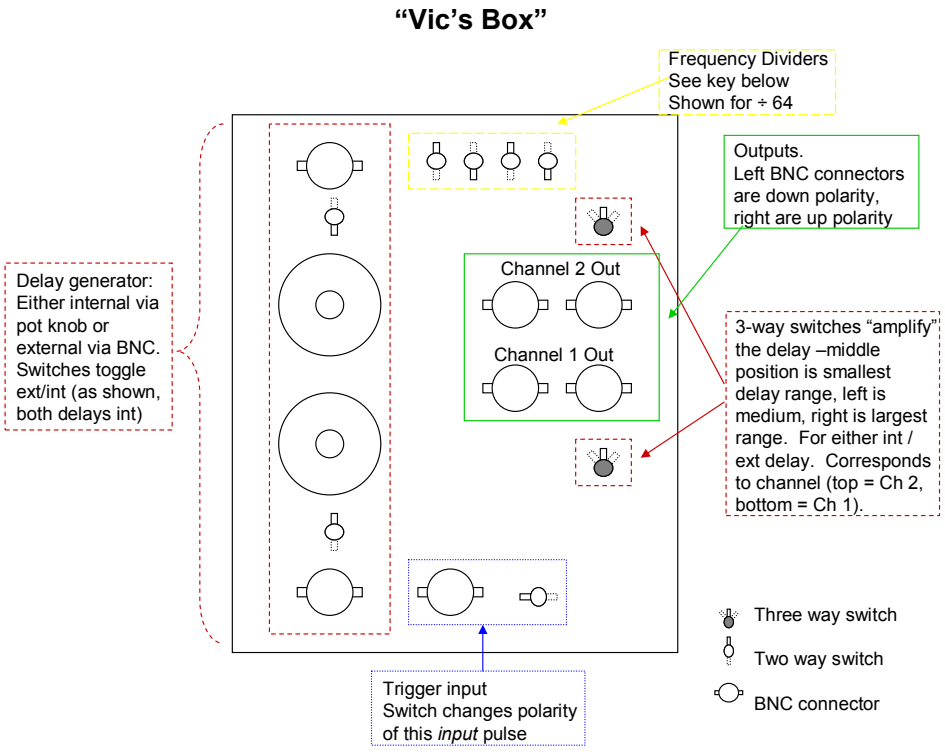

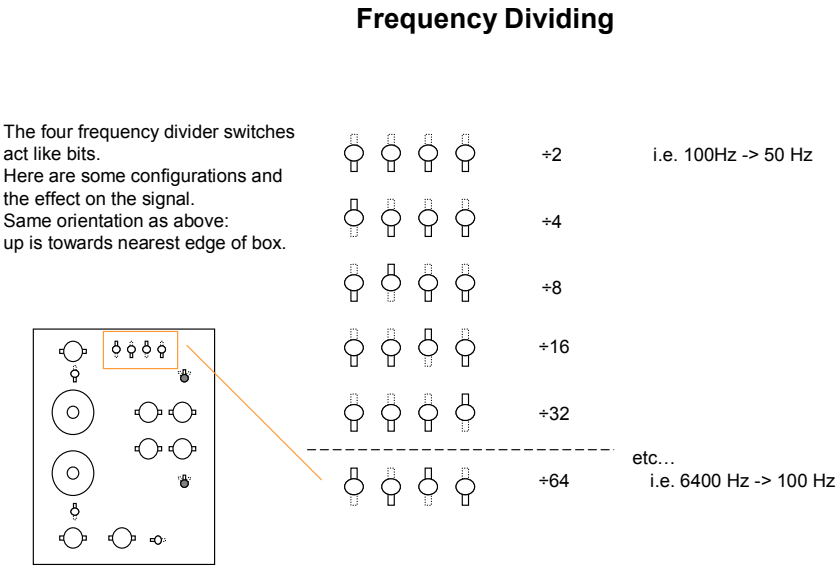

Figure 2-8. "Vic's box" signal processing electronics used for laser triggering and timing schemes.

2.5. Kinetics flow tube

The kinetics flow tube used for mixing and residence time variation of reagent gases is an approximately 1 meter long, 5 cm internal diameter, jacketed glass flow tube, with 6 side ports, o-ring coupling to the reaction chamber, and an end port with UltraTorr fitting for use of a variable position injector. This can be seen schematically in Figure 2-1. The interior of the flow tube is coated to minimize wall reactions. Earlier experiments used a halocarbon wax coating on the interior of the flow tube to minimize wall reaction, but more recently we have moved to a superior Teflon coating, deposited from FluoroPel solutions.[†]

The cooling jacket of the flow tube is circulated with a MeOH / ethylene glycol mixture capable of being cooled to – 80°C. A Neslab cooler/circulator (model ULT-80, 2 refrigerant stages) is used to control the temperature with high precision. A trick for faster cooling of the circulator fluid: pour some liquid N_2 into the reservoir to shock cool it, breaking up the ice formed with a screwdriver. This fluid will need to be replenished occasionally as the MeOH evaporates. The exact MeOH / ethylene glycol ratio is not critical. Add MeOH first and then ethylene glycol as required to prevent icing over at low temperatures.

2.6. Online Fourier-transform IR spectroscopy

In order to improve the detection threshold of our commercial Fourier transform IR spectroscopy (Nicolet Magna-IR 560 E.S.P. FTIR spectrometer, 800 – 12,000 cm^{-1} with

[†] Cytonix Corporation: http://www.cytonix.com/fluoroproducts.html.

various beamsplitters), we constructed a 1 meter external double-pass cell (shown in Figure 2-9) to increase the IR path length in the sample. This increases the path length from 15 cm to 2 m. The cell is constructed of glass, with six ports to allow for flowing sample or static and a pressure gauge. The major inlet and outlet ports are 3/4" diameter to allow for large flow rates, and the outlet port has a mounted 3/4" ball valve to the main vacuum manifold.

The back reflector is a 1 meter focal length gold mirror that is commercially produced for telescopes (hence the, in our case, unnecessarily large size). The cell windows, mounted with O-rings to the tube in Teflon machined cuffs to avoid gluing the windows directly to the glass tube, are 2" diameter wedged CaF_2 windows. The wedging eliminates etalon interferences in the FT spectrum. The side of the commercial FTIR spectrometer is visible at left in the photo, with the liquid N_2 cooled MCT-A detector visible in its externally mounted position (silver cylinder). The jumpering of the detector electronics must be changed to identify it in the external position, and in the FTIR software (see section 2.9.4) the "right microscope" geometry is selected to call this detector. This is described in the FTIR manual in lab. Reflected light is directed into the detector by a small parabolic gold mirror, cut to occlude the minimum possible amount of light entering the external cell from the spectrometer. Also visible in the photograph (black cylinder) is the Baratron pressure gauge.

The entire external cell and detector is enclosed in Plexiglass purge box to allow CO_2 – free dry air purging of the system to prevent CO_2 and water line absorption in the spectra. The purge gas flows through the FTIR spectrometer interferometer housing and

then out into the external cell box where a slight positive pressure is built up and the purge gas leaks out through the seams.

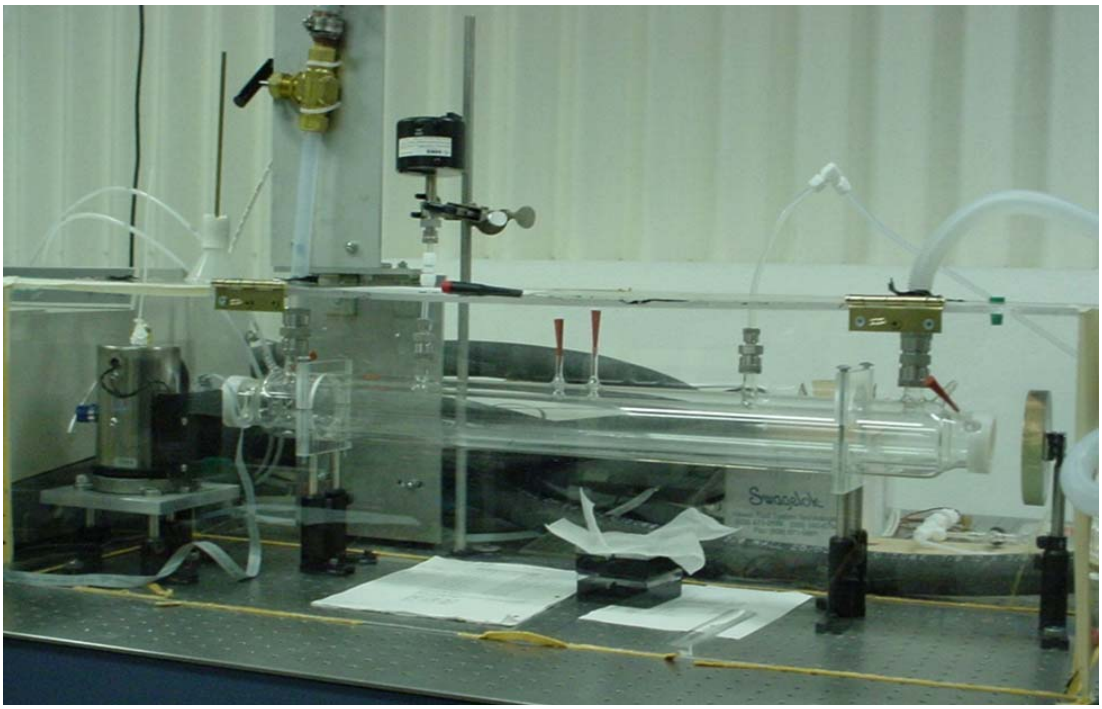

Figure 2-9. Long-path external cell with FTIR spectrometer.

2.7. Vacuum pumps

The vacuum pump used for these experiments is housed in room 0050, "Mechanical Equipment Room," in the subbasement of the South Mudd building. The main pump is a large water-cooled Edwards E2M275S Rotary Vane Vacuum pump with a displacement of 170 ft^3 min^{-1} and specified ultimate vacuum of ~ 10^{-4} Torr. A positive displacement Roots vacuum pump (Edwards EH1200 Mechanical Booster) is coupled to the inlet of the rotary vane pump to improve pumping speed.

In practice, the lowest background pressure we can achieve in our LIF chamber is on the order of 10^{-2} Torr. This is likely due to the limitation on the pumping speed imposed by our tubing and flow manifold and by any leaks in the system.

2.8. Syntheses

2.8.1. Peroxynitrous acid (HOONO)

More time has been spent on HOONO than on the other three molecules discussed in this thesis combined, and a correspondingly large number of synthetic routes have been tested in an effort to find the synthesis generating the highest concentration of HOONO. The lab notebooks document the successful generation of HOONO via OH + NO_2 (+ Ar), H_2O_2 + $NOBF_4$, H_2O_2 + $NOHSO_4$, H_2O_2 + $NOHSO_4/H_2SO_4$, and HO_2-CH_3COOH + NO, as well as unsuccessful attempts to generate HOONO via HO_2-HCOOH + NO. The most robust synthetic routes yielding the most sustained HOONO signal are OH + NO_2 (+ Ar) and H_2O_2 + $NOBF_4$, and these two will be described in detail below.

The generation of HOONO via HO_2-CH_3COOH + NO is an interesting indirect probe of the existence of the HO_2-CH_3COOH complex because HO_2 + NO does not generate HOONO in the absence of the acetic acid. Hence, the HOONO signal could be used as a proxy for the complex for kinetics studies or as a probe to determine if other HO_2-complexes formed. This can be understood in terms of the chaperone role of the acid. Based on calculations by Aloisio and Francisco,[44] the formation of the HO_2-HCOOH complex stabilizes the HO_2 radical by 54 kJ/mol and the HO_2-CH_3COOH complex by 78 kJ/mol. The argument against direct formation of HOONO via HO_2 + NO is that the HO_2

+ NO is 29 kJ/mol more energetic than OH + NO_2, so that the energetically slightly downhill two-body HO_2 + NO → OH + NO_2 is the favored pathway over the too-energetic HO_2 + NO + M → HOONO + M, where the third body must carry away much excess energy. With complexation, however, the HO_2-acid complex is lowered below the energy of the OH + NO_2, closing off this channel, so that now HO_2-acid + NO → HOONO is favored, with the acid chaperone carrying away the excess energy. It is interesting that in our laboratory experiments, acetic acid complexes worked while formic acid complexes did not. This may be worthy of further investigation. In addition, the atmospherically very interesting HO_2-H_2O complex[45] could be searched for in an analogous way.

The reagents and optimal flow conditions for the HO_2-CH_3COOH + NO synthesis of HOONO are shown in Figure 2-10.

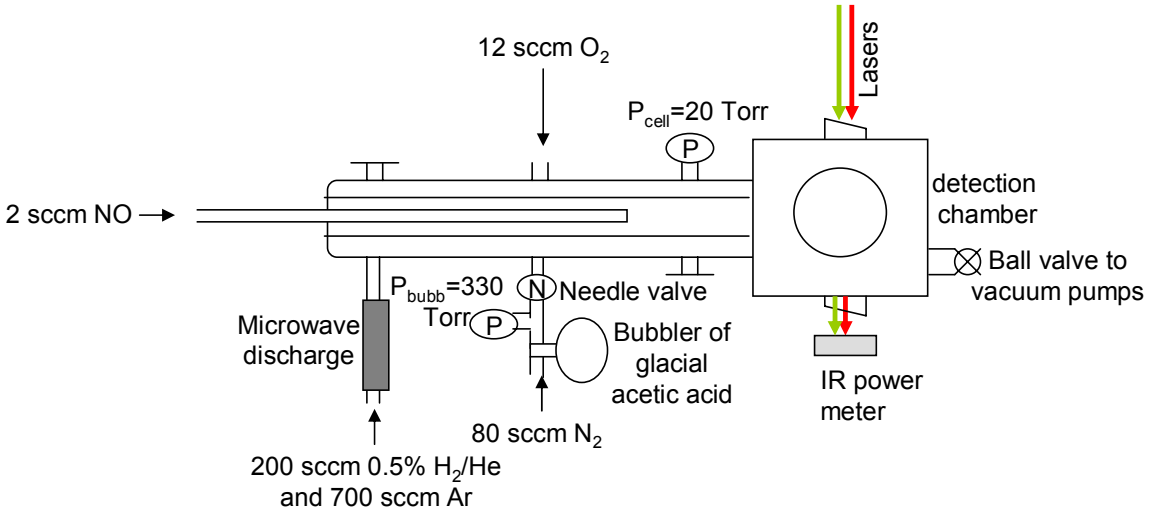

Figure 2-10. Optimal flow conditions and pressures for generation of HOONO via HO_2-CH_3COOH + NO.

The discharge OH + NO_2 (+Ar) synthesis was employed for the kinetics studies on *cis-cis* and *trans-perp* HOONO (Chapter 3) and the cavity ringdown spectroscopy of *cis-cis* HOONO (Chapter 4). This synthesis is shown in Figure 2-11.

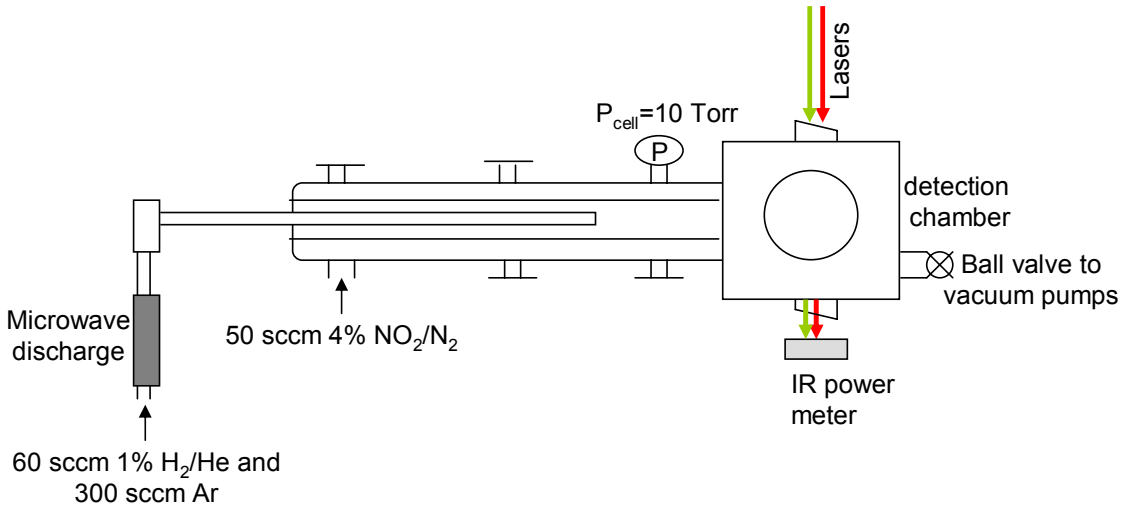

Figure 2-11. Optimal flow conditions and pressures for generation of HOONO via OH + NO_2.

The H_2O_2 + $NOBF_4$ synthesis of HOONO was used for verification in the cavity ringdown spectroscopy of *cis-cis* HOONO (Chapter 4) and for the rotational spectroscopy studies of *cis-cis* HOONO (Chapter 5). Because of the chaperone effect of the BF_4 group, this synthesis only produces HOONO in its most stable *cis-cis* structure. This synthesis has been used in various geometries for flow cell pressures in the 20 mTorr – 30 Torr range (Jet Propulsion Laboratory (JPL) submillimeter spectrometer and our 063 S. Mudd spectroscopy and kinetics flow cell), as well as in the supersonic pulsed expansion of the Caltech Fourier transform microwave spectrometer. The basic synthesis is to flow

concentration H_2O_2 vapor (with some minimized H_2O contribution) over the $NOBF_4$ crystals. Optimum HOONO concentrations are observed with a flow rate optimized to balance interaction time between the H_2O_2 and $NOBF_4$ with the gas-phase lifetime of HOONO. This varies with spectrometer system, but it is optimal to have the $NOBF_4$ crystals either directly in the detection region or as close as possible, and to have minimum water in contact with the crystals, as they are very hydroscopic. After significant hydrolysis, increased $HONO_2$ and HO_2NO_2 will be observed from this synthesis, and only replacement of the $NOBF_4$ crystals with a fresh, dry sample will regenerate the HOONO signal.

2.8.2. Peroxyacetyl nitrate (PAN)

Peroxyacetyl nitrate was synthesized in the fume hood following the method of Gaffney et al.[46] and Talukdar et al.[47] with slightly modified reagent amounts. PAN is extremely reactive; as a precaution, cool all glassware and reagents before using, add reagents slowly dropwise, and avoid shaking the mixture.

First, bubble 20 mL n-tridecane (n-$C_{13}H_{28}$) with high purity N_2 for ~ 30 minutes. Combine degassed tridecane with 5 mL peracetic acid ($CH_3C(O)OOH$) in a roundbottom flask with a Teflon coated stir bar in an ice bath. Slowly add 5 mL concentrated H_2SO_4, stirring slowly. Add 2.6 mL concentrated HNO_3 dropwise at a rate of about 2 drops per second. Allow mixture to stir vigorously for 15 minutes. Add ~ 50 mL ice water to a separatory funnel, and pour the contents of the roundbottom flask carefully into the separatory funnel on top of the water. DO NOT SHAKE the separatory funnel. Drain the aqueous (lower) layer in the separatory funnel (it will be strongly acidic). Wash the

organic layer three times with 50 mL cold water, gently rocking the separatory funnel but not shaking. Discard the interface layer to insure pure tridecane. Discard all aqueous separations, and dry the tridecane solution over $MgSO_4$. Transfer the filtered solution to a bubbler / sample container for use in experiments. We generally bubbled N_2 through this solution to generate a gas phase flow of PAN. The shelf life of PAN in the freezer is reasonable; we have used a sample that was 1 year old and still seen PAN signal. However, Talukdar et al.[47] recommend synthesizing fresh PAN samples immediately before use, and this was our common practice.

2.8.3. Methyl hydroperoxide (MHP)

Methyl hydroperoxide is synthesized in the fume hood following the method described by Vaghjiani and Ravishankara.[48] A mixture of 20 g (~ 15 mL) dimethyl sulfate ($(CH_3)_2SO_4$), 30 mL 30% H_2O_2 in H_2O, and 50 mL H_2O in a roundbottom flask submerged in an ice bath is stirred continuously while adding 25.2 mL 40% potassium hydroxide (KOH) dropwise over a period of 10 minutes. Dimethyl peroxide will escape as a gas during this reaction. Next, acidify the mixture by adding 40 mL 50% H_2SO_4, then extract the peroxide into diethyl ether in a separatory funnel (three extractions of about 50 mL diethyl ether). Discard the aqueous (bottom) layer, and dry the ether solution over anhydrous sodium sulfate (Na_2SO_4) overnight. Filter this mixture and put into a warm water bath (~308 K) to boil off excess ether. The concentrated mixture is then further dried over anhydrous copper sulfate ($CuSO_4$) for about 10 minutes and vacuum distilled on the Schlenk line in the hood. For this vacuum distillation, the reaction mixture is maintained in a warm water bath (~320 K) and a liquid N_2 trap is employed to trap reaction products. We

have found that vacuum distillation should be run at a pressure > 100 Torr, contrary to the Vaghjiani and Ravishankara paper.[48]

The collected methyl hydroperoxide should be a colorless liquid, stable at ambient conditions. As with any peroxide, there is an explosion hazard, so caution should always be exercised. The peroxide should be stored in the freezer in a container with a pop-top rather than a screw cap. For experiments, a specially designed Plexiglass box and sample quenching apparatus is used (described in the next section).

2.8.4. Hydroxymethyl hydroperoxide (HMHP)

Hydroxymethyl hydroperoxide was generally synthesized overnight immediately prior to use. It can also be stored in the freezer, but degradation is likely in older samples. The simple synthetic method is to blow N_2 over a heated sample (~100 °C) of paraformaldehyde and bubble that flow through warm (~60 °C) concentrated 90-95% H_2O_2/H_2O. Optimal HMHP generation in the liquid sample was achieved for bubbling ~ 15 hours and using approximately stoichiometric amounts of paraformaldehyde and H_2O_2 (5 grams paraformaldehyde to 7 mL 95% H_2O_2/H_2O). A schematic of the synthesis apparatus is shown in Figure 2-12.

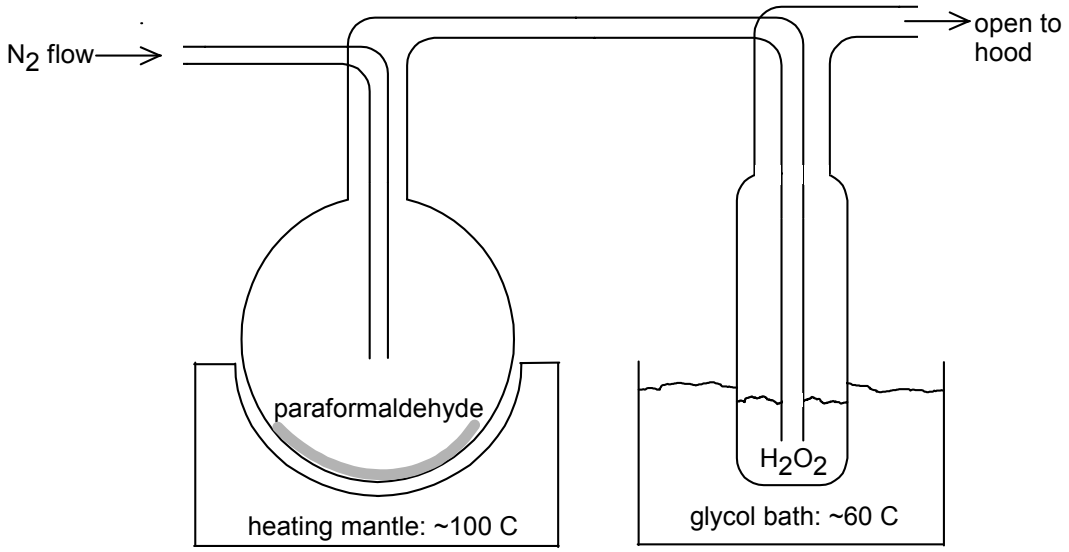

Figure 2-12. Setup for synthesis of hydroxymethyl hydroperoxide.

The resulting liquid sample contains the contaminants H_2O_2, H_2O, HCOOH, and $HOCH_2OOCH_2OH$ (*bis*-HMHP), which must be pumped off before HMHP begins to appear in the gas phase. The concentrated peroxide residue that is left after pumping off all impurities is optimum for experiments, but is also a serious explosion hazard. **Exercise extreme caution when handling concentrated peroxides!** An explosion occurred in our lab when a very small amount of peroxide residue was brought quickly up to atmospheric pressure. We developed a Plexiglass box to contain the peroxide bubbler, with an additional port on the top of the bubbler. A bulb of water with a needle valve is attached to this extra tube which sticks through the top of the Plexiglass box. The valve can be opened outside the box to allow water quenching before handling the peroxide glassware. A photograph of this peroxide bubbler is shown in Figure 2-13.

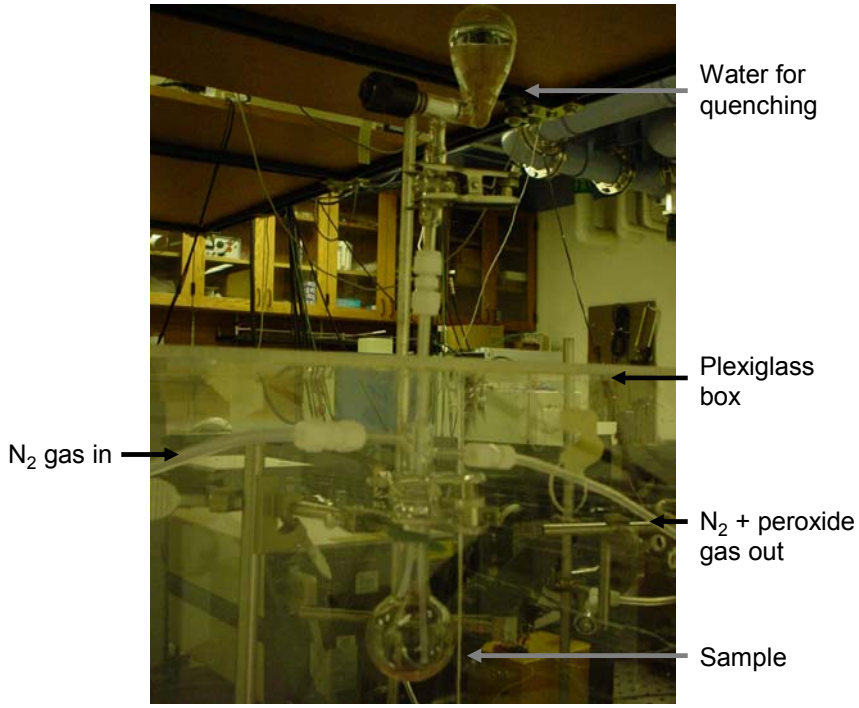

Figure 2-13. Specialized peroxide bubbler, with Plexiglass box and external water bulb to allow quenching before the box is opened.

2.9. Computer programs

2.9.1. Spectroscopy experiments: Scanner_program.vi

The screen capture below (Figure 2-14) shows the user interface for the scanning program, Scanner_program.vi, designed by Sergey Nizkorodov. This shows the parameters used for a high-resolution scan over the *trans-perp* HOONO $2\nu_{OH}$ peak, revealing rotational structure in that band. The two usable modes of this program, selected in the "Scanning mode" menu, are "Scan OPO" and "Free run." The former scans the OPO wavelength up from the current value in the increment chosen (here, 0.010 nm). The "Xtal settle time" is the delay after sending the signal to move the crystals to the next wavelength step before the signal is collected (here, 800 ms). In "Free run" mode, the

program simply collects data at a single wavelength. The "GOTO" button is used to jump to a new starting wavelength. "Rep rate" must be set to the data collection rep rate (100 Hz or 6400 Hz in the two triggering schemes described in section 2.4), and "Periods/scan" and "Triggers/period" determine the number of shots averaged per data point recorded. In the sample below, signal is added up over 100 shots, added up over the next 100 shots, then averaged and displayed, and moved to the next wavelength step.

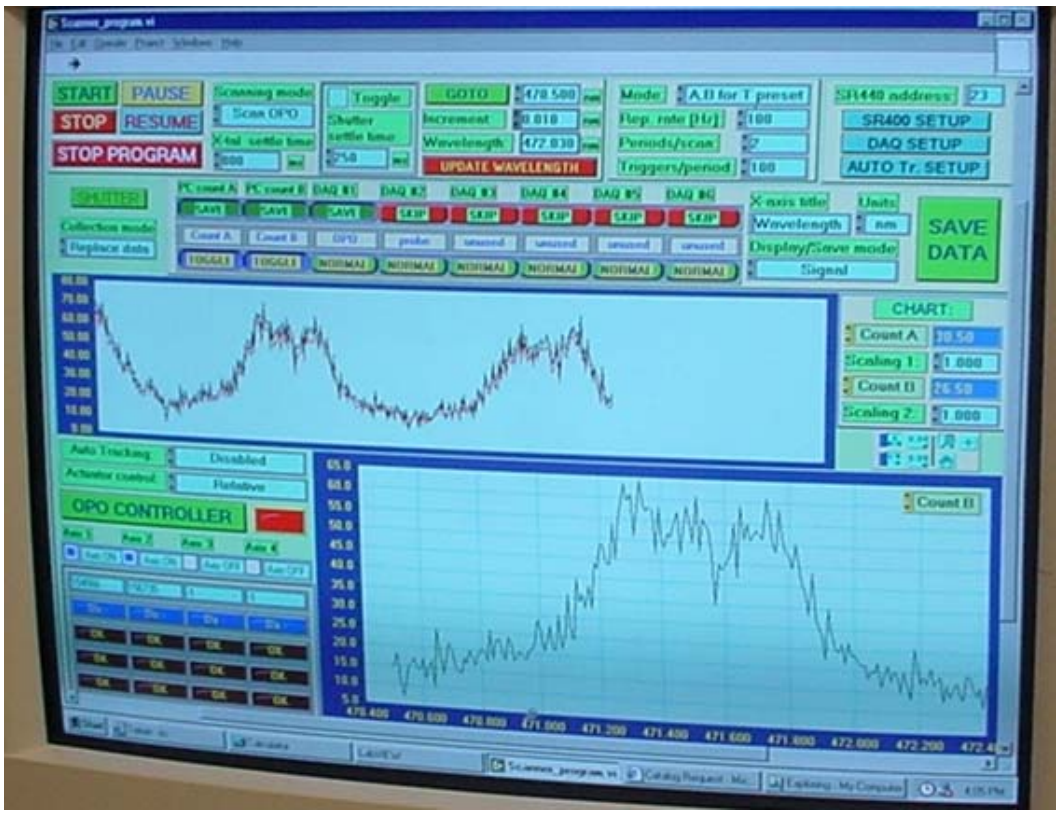

Figure 2-14. Scanner_program.vi user interface.

2.9.2. Kinetics experiments: Kinetics.vi

The screen capture below (Figure 2-15) shows the user interface for the kinetics program, Kinetics.vi, also designed by Sergey Nizkorodov. This program is used to scan the pump-probe delay in order to access photodissociation kinetics information. Many of the parameters are the same as for the scanning program, with the exception of the delay settings. The Vic's box settings are unimportant, as they simply shift the x axis. The start delay, increment, and end delay are used to define the range of the kinetics scan. For fast dissociation kinetics such as observed for OH, a good range is 0 to 0.7 ms in .01 ms increments. As discussed in section 2.4, the zero on this scale can be manually set to a negative delay, i.e., probe before pump pulse, to investigate both the (very fast) rise time and (~100s of μs) decay of the OH signal.

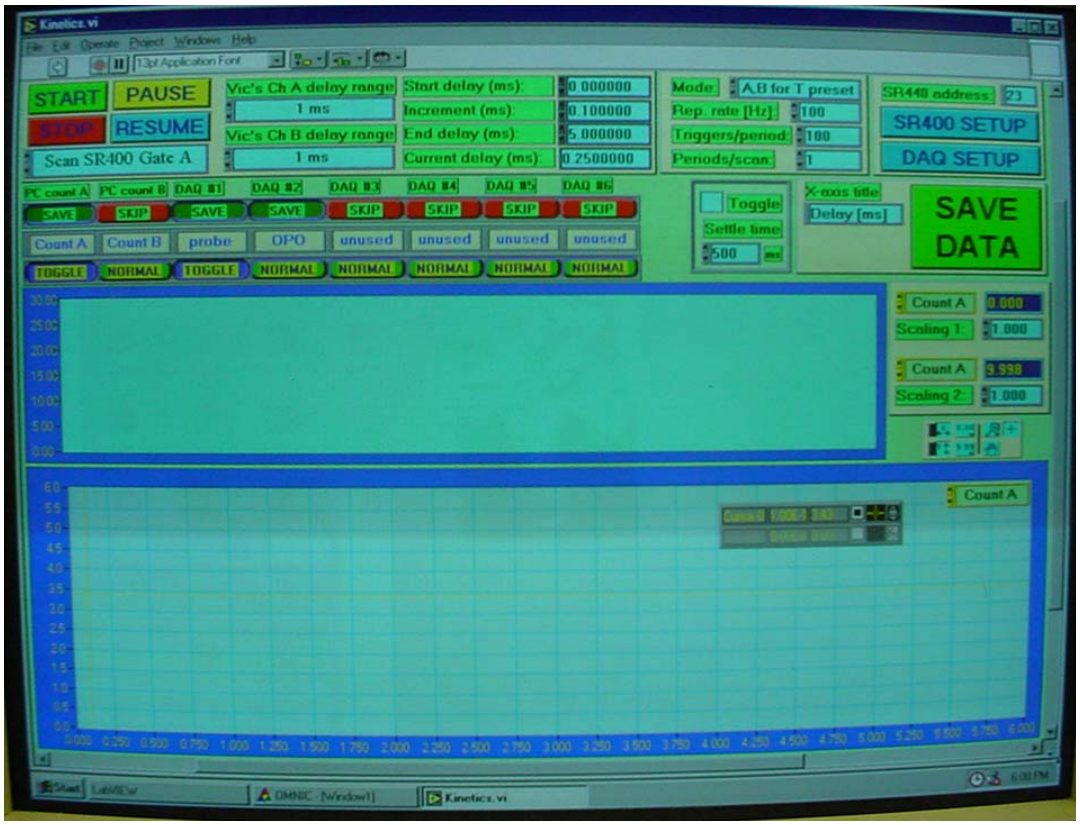

Figure 2-15. Kinetics.vi user interface.

A kinetics scan using this program can be used to distinguish dissociation processes producing OH (such as from HOONO) from those producing HO_2 (such as HO_2NO_2, a molecule previously studied in our lab). The OH signal will have an essentially instantaneous rise time since it is the direct product, while OH signal from HO_2 formation in the dissociation process requires the chemical step $HO_2 + NO \rightarrow OH + NO_2$, making OH signal rise time slower.

This program is not used for chemical kinetics studies such as those on *trans-perp* to *cis-cis* HOONO isomerization reported in chapter 3. Those studies employ the varying

position of the injector of one of the reactants to determine a kinetics time base and use the Scanner_program.vi in "Free run" mode to determine an average OH signal at each position.

2.9.3. Calibrating OPO: Calibrator_program.vi

In order to reproducibly scan the near-IR OPO idler beam (and the mixed UV beam) wavelength, the OPO must be calibrated. This is accomplished by scanning the crystal positions and optimizing signal intensity at a series of wavelengths (see section 2.10.1 for the details of the calibration process). The Calibrator_program.vi (Figure 2-16), designed by Sergey Nizkorodov, is used to record the stepper motor positions and the user-determined (read from Burleigh wavemeter) signal wavelength. The "Advance all" button advances each active axis the amount (user entered) in the "Advance to," and the "OPO controller" button can be subsequently used to optimize OPO output power. For mixing calibration, the optimum "Advance to" settings are: Axis #1, 10,000; Axis #2, 10,000; Axis #3, 3,700; Axis #4, 325 (~ 2 nm steps in signal wavelength). Once optimized, the "Add calibration point" button will prompt the user for the wavelength (read out of wavemeter) and plot and save the points. All data is saved at the end of the calibration by the "Save data" button. The resulting calibration curves for each crystal are obtained by plotting each of 2 or 4 "axes" versus wavelength (the motor on each is called an "Axis" by the program). Axes #1 and #2 are the two OPO crystals, and in the case of UV generation, the mixing crystal is Axis #3 and compensator prism is Axis #4.

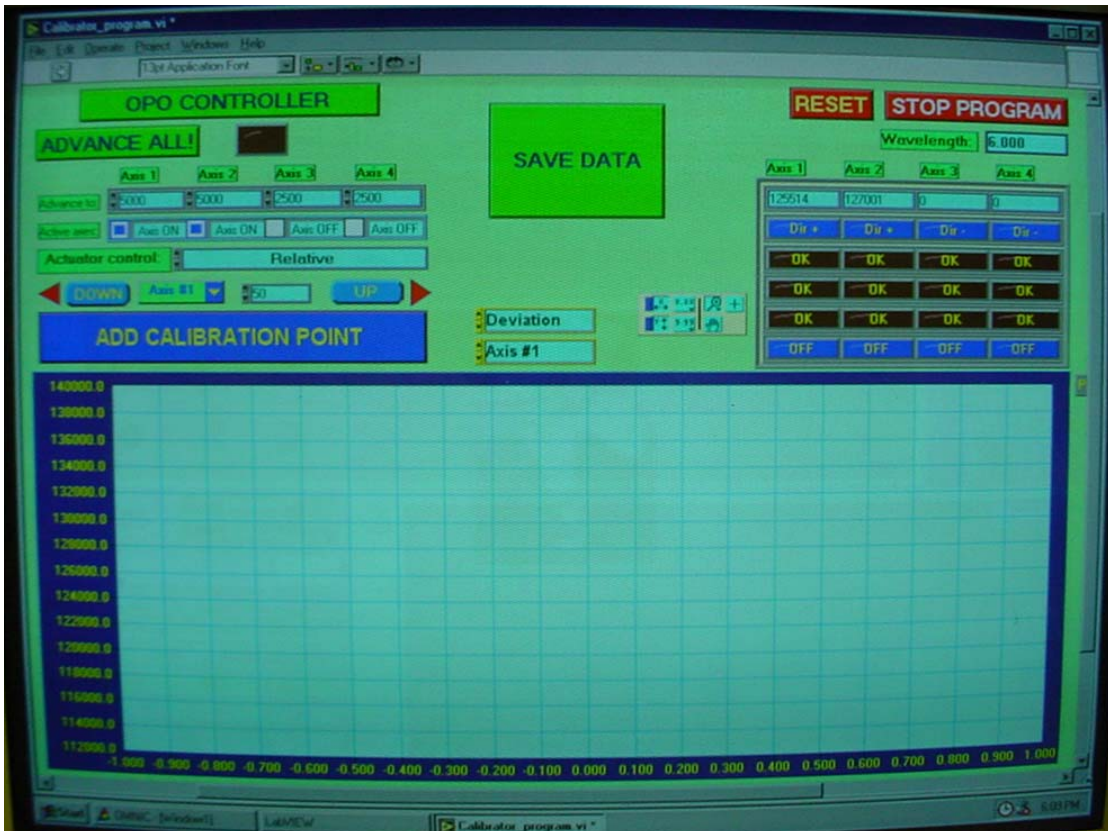

Figure 2-16. Calibrator_program.vi user interface.

2.9.4. FTIR spectrometer: Omnic

The Omnic software has excellent documentation, so the discussion here is limited to a few tips. The Omnic user interface is shown in Figure 2-17 in "bench not ready" status, meaning either that the detector is not yet cooled or the bench is out of alignment. The MCT-A detector requires a large amount of liquid N_2 and approximately 30 minutes cooling time. The settings shown are for the external long-path arrangement: the "Right μScope" compartment must be selected. When the detector is sufficiently cooled and the

alignment is optimized, at a gain setting of 1 and aperture of 13, you should see around "Max: 6.18," with a single clear peak in the preview window.

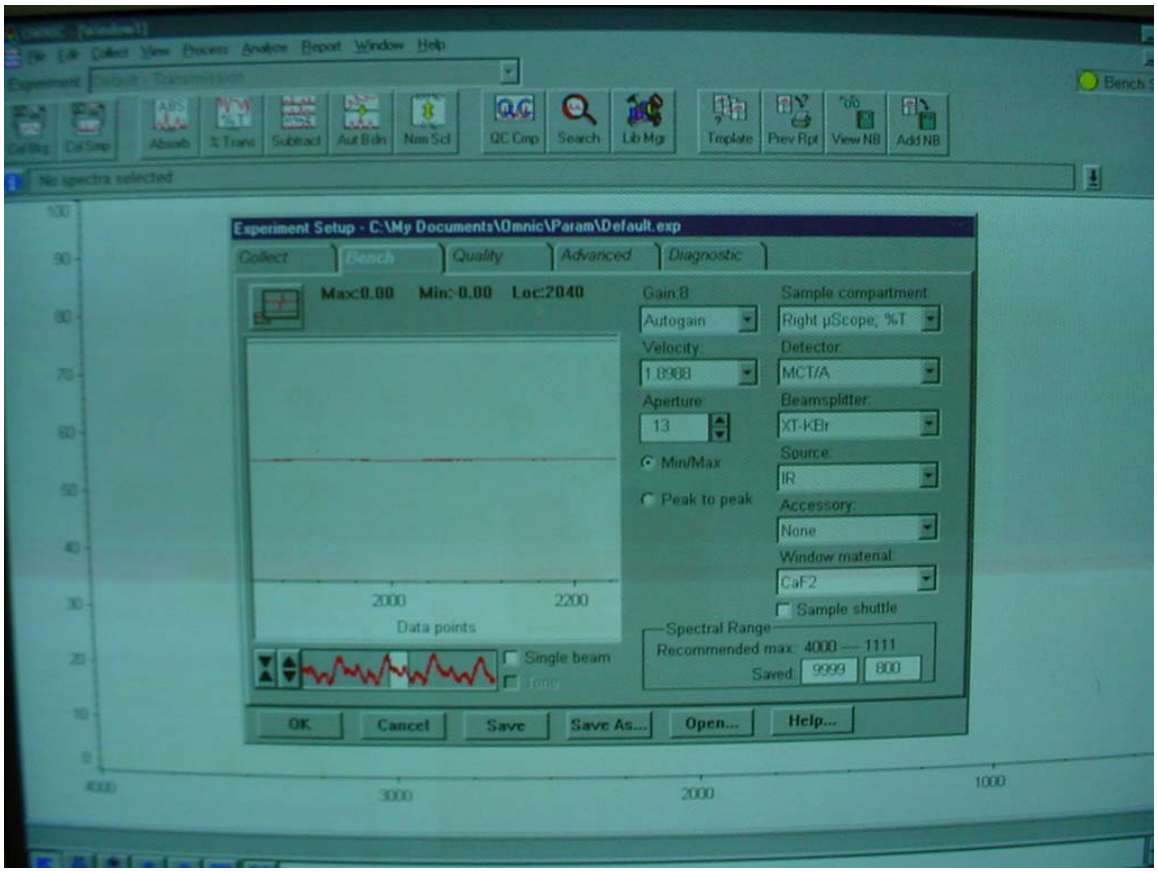

Figure 2-17. Omnic FTIR software user interface.

2.10. Some additional lab tips and troubleshooting

2.10.1. Getting the OPO lasing from scratch with new crystals

When the power output of the OPO begins to decline rapidly and there is a visible round burn in the coating on one or more faces of the crystals (most often these burns occur on the outside faces of both crystals concurrently), it is time to swap out the crystals for the

other pair. Use an Allen wrench to release the posts on the crystal mounts, and work carefully with gloves and over a layer of lens paper with the crystals. The mounts use springs to hold the crystals into place so they can fall out somewhat easily. In the past we have sent the burned crystals to Lambda Research Optics[‡] in Costa Mesa, CA for recoating.

Secure the new crystals in the mounts such that the birefringence appears on opposite sides of the crystals, as you look down the beam path. This is shown schematically in Figure 2-18. Set the actuators to the halfway point on their screws before inserting crystals. Ensure that the crystals are parallel to the laser table and put them in the post holders at the same height (marked on the posts) with their faces parallel as best as you can judge it by eye. This initial OPO arrangement was shown above in Figure 2-2, where the white crystals are visible sticking out of the silver mounts on the inside edges.

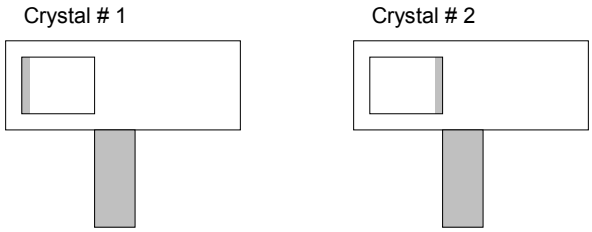

Figure 2-18. Orientation of BBO crystals in mounts, looking along the beam path through crystal #1 then #2. Birefringence should appear on opposite sides of the crystals.

With the crystals in place, the next step is to align the output coupling mirror, M3, with the Infinity Nd:YAG 355 nm input beam. This is accomplished by opening the

[‡] Lambda Research Optics: http://www.lambda.cc/.

Infinity (you need to defeat the interlock with the screw included for that purpose) so that the back reflection of the 355 nm beam from M3 through all the optics and back into the Infinity can be seen. With the laser goggles on, a glowing white spot (the 355 nm back-reflection) will be visible on the large round white aperture immediately after the THG crystal in the Infinity. This back-reflected beam must be blocked by the aperture, but the efficiency of the OPO is greatest when the alignment directs the beam almost directly back into the Infinity. We have found optimum OPO performance with the spot horizontally displaced just to one side of the hole in the white aperture plate. Make this adjustment with the controls on mirror M3, recalling that due to the two vertically mounted mirrors flipping the polarization between the Infinity and the OPO, the horizontal adjust on M3 will move the back-reflection spot vertically, and the vertical adjust on M3 will move it laterally. Once this spot is aligned, turn off the Infinity laser for the next step.

This next step is to ensure that mirrors M3 and M4 are parallel. Set up the Helium Neon (HeNe) laser to enter the OPO optics from the output side, with a large distance between the HeNe and OPO for maximum precision in back-reflection alignment. This is best accomplished with two turning mirrors in the HeNe path to allow easy alignment without moving the cumbersome HeNe laser mount itself. First, check reflection off the back of mirror M3 with the RG715 filter mounted to the back of M2 in place. Adjust the HeNe beam to achieve overlap of the back-reflection directly onto the HeNe source aperture. Then remove the M2 RG715 filter to find the reflection off the front of mirror M4, and adjust this mirror to achieve overlap of that reflected beam with the one from M2 onto the HeNe aperture.

Replace the RG715 filter on the back of M2, remove the HeNe laser, and turn on the Infinity. With maximum IR power (225 mJ/pulse), scan one of the crystals relative to the other until you see a flash of blue lasing. Adjust until you get maximum brightness of that flash, and then "zero" the positions of the actuators. Now you can always come back to the zeros if you lose lasing. Scope out the range of the crystals by scanning them in increments (you will need to occasionally re-optimize because the motors don't turn precisely in step with each other), re-zero the actuator positions at one end of the range, and then calibrate the wavelength to the actuator positions, in increments of ~ 10,000 units on Axes 1&2 (~ 2 nm signal wavelength), 3700 units on Axis 3, and 325 units on Axis 4, recording the wavelength and axis position for each axis (#1 and #2 are the OPO crystals in the LabView programs, #3 and #4 are the mixing crystal and compensator prism in the UV generation setup). The Calibrator_program.vi LabView program (shown in section 2.9.3) is designed to allow easy scanning and recording of the signal wavelength, which you read out from the Wavemeter, for each point. These points are then fit to an 8^{th} order polynomial, using a graphing program such as Kaleidograph. Check the goodness of the fit (recommend <200 difference between fit and exact position of each axis for each point). Save these fit parameters in the appropriate numerical format into the Geo_actuator.ini file in the c:/winnt/ directory. This is the file that the scanner program looks up to scan wavelength. The format of the numbers is critical; be sure to double check the number of significant figures and format of the exponents. If a number is formatted incorrectly, one crystal may be sent off to the end stop on the motor and you'll lose your calibration.

2.10.2. Things to try when the subbasement vacuum pumps quit

There are two trivial things that could have gone wrong if the vacuum pumps in the basement shut down. First, check that the water cooler (to the right on the north wall as you walk into the subbasement pump room, 0050 S. Mudd) is full to within one inch of the top of the reservoir. Add water and cycle it on and off again. Second, check that both circuit breakers on the side of the pump housing (in a grey box with a door, facing north) are in the "on" position, with the white buttons depressed. After resolving either of these problems, you'll need to have someone upstairs press the on button to see that the pump starts and runs smoothly.

To avoid bigger problems, check the pump oil on occasion. Open the valve on the front (west face) of the pump and let a little oil drain out. If it is black, change the pump oil entirely. The blue drum is our pump oil supply. This is a messy job, but will hopefully alleviate needing to send the pump in for a complete overhaul, as we did in 2004. The frequency with which it will be necessary to change the pump oil is sensitively dependent on what you are running through it, so the best rule is to check the oil color to see when a change is needed.

CHAPTER 3

CIS-CIS AND *TRANS-PERP* HOONO ISOMERIZATION KINETICS

This chapter was published as:

Fry, J.L., Nizkorodov, S.A., Okumura, M., Roehl, C.M., Francisco, J.S., and Wennberg, P.O., "Cis-cis and trans-perp HOONO: Action spectroscopy and isomerization kinetics," Journal of Chemical Physics ***2004,*** *121, 1432-1448.*

Chapter 3

3. *CIS-CIS* AND *TRANS-PERP* HOONO ISOMERIZATION KINETICS

3.1. Abstract

The weakly-bound HOONO product of the OH + NO_2 + M reaction is studied using the vibrational predissociation that follows excitation of the first OH overtone ($2\nu_1$). We observe formation of both *cis-cis* and *trans-perp* conformers of HOONO. The *trans-perp* HOONO $2\nu_1$ band is observed for the first time under thermal (223 – 238 K) conditions at 6971 cm^{-1}. We assign the previously published (warmer temperature) HOONO spectrum to the $2\nu_1$ band at 6365 cm^{-1} and $2\nu_1$–containing combination bands of the *cis-cis* conformer of HOONO. The bandshape of the *trans-perp* HOONO spectrum is in excellent agreement with the predicted rotational contour based on previous experimental and theoretical results, but the apparent origin of the *cis-cis* HOONO spectrum at 6365 cm^{-1} is featureless and significantly broader, suggesting more rapid intramolecular vibrational redistribution (IVR) or predissociation in the latter isomer. The thermally less stable *trans-perp* HOONO isomerizes rapidly to *cis-cis* HOONO with an experimentally determined lifetime of 39 ms at 233 K at 13 hPa (in a buffer gas of predominantly Ar). The temperature dependence of the *trans-perp* HOONO lifetime in the range 223 – 238 K yields an isomerization barrier of 33 ± 12 kJ/mol. New *ab initio* calculations of the structure and vibrational mode frequencies of the transition state *perp-perp* HOONO are performed using the coupled cluster singles and doubles with

perturbative triples (CCSD(T)) model, using a correlation consistent polarized triple zeta basis set (cc-pVTZ). The energetics of *cis-cis*, *trans-perp*, and *perp-perp* HOONO are also calculated at this level (CCSD(T)/cc-pVTZ) and with a quadruple zeta basis set using the structure determined at the triple zeta basis set (CCSD(T)/cc-pVQZ//CCSD(T)/cc-pVTZ). These calculations predict that the *anti* form of *perp-perp* HOONO has an energy of ΔE_0= 42.4 kJ/mol above *trans-perp* HOONO, corresponding to an activation enthalpy of $\Delta H^{\ddagger 0}_{298}$ = 41.1 kJ/mol. These results are in good agreement with statistical simulations based on a model developed by Golden, Barker, and Lohr. The simulated isomerization rates match the observed decay rates when modeled with a *trans-perp* to *cis-cis* HOONO isomerization barrier of 40.8 kJ/mol and a strong collision model. The quantum yield of *cis-cis* HOONO dissociation to OH and NO_2 is also calculated as a function of photon excitation energy in the range 5500 – 7500 cm^{-1}, assuming D_0=83 kJ/mol. The quantum yield is predicted to vary from 0.15 to 1 over the observed spectrum at 298 K, leading to band intensities in the action spectrum that are highly temperature-dependent; however, the observed relative band strengths in the *cis-cis* HOONO spectrum do not change substantially with temperature over the range 193 K to 273 K. Semi-empirical calculations of the oscillator strengths for $2\nu_1$(*cis-cis* HOONO) and $2\nu_1$(*trans-perp* HOONO) are performed using (1) a one-dimensional anharmonic model and (2) a Morse oscillator model for the OH stretch, and *ab initio* dipole moment functions calculated using Becke, Lee, Yang and Parr density functional theory (B3LYP), Møller-Plesset theory truncated at the second and third order (MP2 and MP3), and quadratic configuration interaction theory using single and double excitations (QCISD). The QCISD level calculated ratio of $2\nu_1$ oscillator strengths of *trans-*

perp to *cis-cis* HOONO is 3.7:1. The observed intensities indicate that the concentration of *trans-perp* HOONO early in the OH + NO_2 reaction is significantly greater than predicted by a Boltzmann distribution, consistent with statistical predictions of high initial yields of *trans-perp* HOONO from the OH + NO_2 + M reaction. In the atmosphere, *trans-perp* HOONO will isomerize nearly instantaneously to *cis-cis* HOONO. Loss of HOONO via photodissociation in the near-IR limits the lifetime of *cis-cis* HOONO during daylight to less than 45h; other loss mechanisms will reduce the lifetime further.

3.2. Introduction

Knowledge of the concentrations and chemistry of the HO_x (OH + HO_2) and NO_x (NO + NO_2) families of radicals is central to understanding global atmospheric chemistry. Both families are involved in tropospheric ozone production and stratospheric ozone loss. Hydroxyl radical (OH) has extremely high reactivity with many atmospheric trace gases, and is referred to as an atmospheric detergent because it cleanses the atmosphere of pollutants. NO_x is a major component of photochemical smog.

As the major sink of both HO_x and NO_x, the radical termination reaction

$$OH + NO_2 + M \rightarrow HONO_2 + M \qquad (R1)$$

is of critical importance in atmospheric chemistry. The rate constant of this reaction has been the topic of some controversy until recently,[9,49-54] because the high and low pressure rate constants could not be reconciled with a single termolecular rate expression. This discrepancy can be resolved by the inclusion of a second minor channel

forming a more weakly bound isomer of nitric acid, peroxynitrous acid, or HOONO, as first predicted by Robertshaw and Smith[55]:

$$OH + NO_2 + M \rightarrow HONO_2 + M \quad \text{ca. 90-95\%} \qquad \text{(R1a)}$$

$$\rightarrow HOONO + M \quad \text{ca. 5-10\%} \qquad \text{(R1b)}$$

The energetics of the $OH + NO_2 \rightarrow HOONO$ and $HONO_2$ are shown in Figure 3-1, with relative *cis-cis*, *trans-perp*, and *perp-perp* HOONO energies from CCSD(T)/cc-pVQZ//CCSD(T)/cc-pVTZ level calculations reported in this paper. The energies of $OH + NO_2$ and $HONO_2$ relative to *cis-cis* HOONO are taken from Bean, et al.[26] The formation of HOONO instead of $HONO_2$ has very different implications for the atmospheric concentrations of OH and NO_2. Since HOONO is more weakly bound than $HONO_2$ (Figure 3-1), it will have a short lifetime (~ seconds at 300 K) in the lower atmosphere due to efficient thermal dissociation back to OH and NO_2. No evidence has yet been found for direct isomerization of HOONO into $HONO_2$,[54] and it is likely to be prevented by a high reaction barrier.[56] A majority of previous kinetics studies of reaction (1) were done via observation of OH decay in the presence of excess NO_2 without taking the HOONO channel into consideration. At some conditions, these experiments measured the total reaction rate coefficient, $k_1=k_{1a}+k_{1b}$, while assuming the observed decay was due only to k_{1a}. Recent measurements [26,31,50] have found that HOONO is indeed formed in reaction (1) with a measurable yield of $k_{1b}/(k_{1a}+k_{1b}) \approx$ 5-10% at low pressures (27 hPa) and room temperature. Thus, to the extent that HOONO is formed, the total rate of reaction (1) overestimates the net loss of HO_x and NO_x to HNO_3.

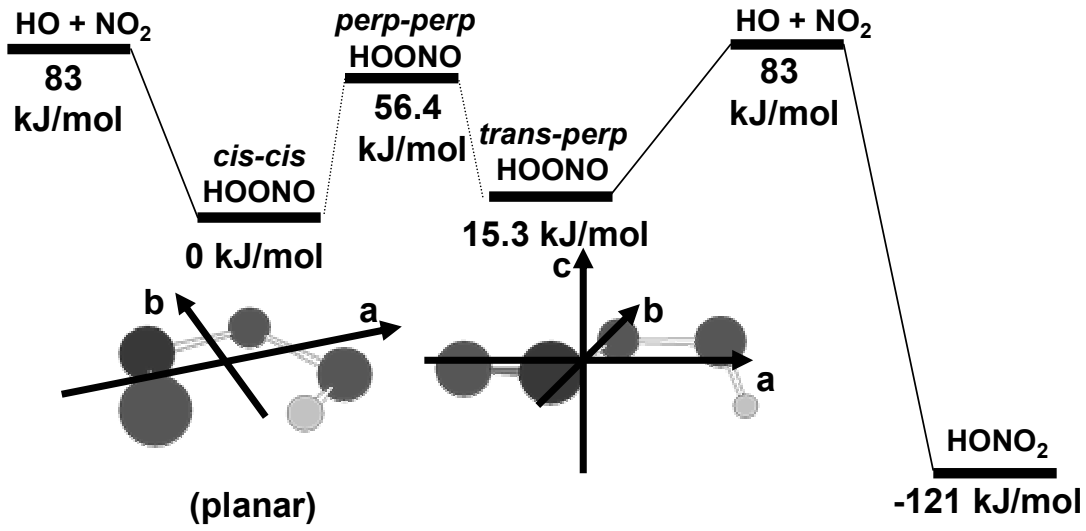

Figure 3-1. Energy level diagram for the OH + NO_2 reaction, with structures of *trans-perp* and *cis-cis* HOONO shown. HOONO energy levels are from present work; $HONO_2$ energy relative to *cis-cis* HOONO are from Bean, et al.[26], and OH + NO_2 energy relative to *cis-cis* HOONO is from Hippler, et al.[50] and Dixon et al.[56] Pathways for direct isomerization from HOONO into $HONO_2$ are not shown because they have substantially higher barriers compared to dissociation into OH and NO_2.

The OH + NO_2 system is complicated by the existence of several distinct conformers of HOONO.[49,57-59] The predicted lowest energy conformers are *cis-cis* and *trans-perp* HOONO (Figure 3-1), wherein the first and second prefixes refer to the conformations of the ONOO and NOOH dihedral angles, respectively. The planar *cis-cis* conformer has a weak internal hydrogen-bond and is stabilized relative to the open *trans-perp* conformer by 15.3 kJ/mol. A third conformer, *cis-perp* HOONO, was identified in early *ab initio* calculations of McGrath and Rowland[57] and calculated to be 1.7 – 2.5 kJ/mol above *cis-cis* HOONO. Tsai et al.[59] and Jin et al.[58] have calculated *cis-perp* HOONO

energies (relative to *cis-cis* HOONO) of 3.8 – 5.4 kJ/mol and -5.1 – 5.9 kJ/mol, respectively. Recent higher-level calculations indicate that the *cis-perp* conformer may not be a stationary point on the HOONO potential energy surface.[9,56]

Isomerization between the *trans-perp* and *cis-cis* conformers of HOONO occurs by rotation about the N-O bond. This transition state was first termed *perp-perp* HOONO by McGrath and Rowland,[57] because the OH and NO bonds are nearly perpendicular to the O-O-N plane. They calculated a transition state energy of 52.3 kJ/mol above the *cis-cis* conformer of HOONO. There are predicted to be two *perp-perp* conformers, encompassing two transition states of nearly identical energies and similar structures and frequencies. In the *anti* configuration, the OH and NO bonds lie on opposite sides of the NOO plane, in the *syn* conformation, they are on the same side. Golden, et al.[9], Jin et al.[58] and Tsai, et al.[59] have found that the two *perp-perp* HOONO conformers have nearly identical energies. This has led Golden et al.[9] to treat the isomerization from *trans-perp* to *cis-cis* HOONO as occurring by a single pathway with a degeneracy of two in statistical calculations.

Vibrational frequencies of various conformers of HOONO have been predicted at several levels of theory. MP2/6-31G(d) calculations of the harmonic vibrational frequencies and infrared intensities of eight conformational structures of HOONO were carried out by McGrath and Rowland.[57] Li and Francisco[60] later calculated vibrational frequencies for *cis-cis* HOONO at the QCISD(T)/cc-pVTZ level, and Jin et al.[58] reported vibrational frequencies for nine structures of HOONO (including the two *perp-perp* conformers) at the B3LYP/6-311+G(d,p) and MP2/6-311+G(d,p) levels. Bean et al.[26]

reported vibrational frequencies for both *cis-cis* and *trans-perp* HOONO at the CCSD(T)/cc-pVTZ level.

Estimates of the dissociation energy of *cis-cis* HOONO are converging on a value between 76 and 84 kJ/mol. Among the most recent *ab initio* calculations of the dissociation energy, Li and Francisco calculate D_0(*cis-cis* HOONO) = 78.7 kJ/mol at the QCISD(T)/cc-pVQZ level, and Dixon et al. calculate two values for D_0(*cis-cis* HOONO): first, 82.9 kJ.mol, a strictly *ab initio* number calculated at the CCSD(T)/CBS level with core/valence corrections to the dissociation energy and molecular scalar relativistic corrections accounting for the change in relativistic contributions to the total energy of the molecular or radical species versus the constituent atoms; second, 76.6 kJ/mol, using an experimental value for $\Delta H_f(NO_2)$. These calculations give a 6 kJ/mol wide bracket for the value of D_0(*cis-cis* HOONO), the width of which demonstrates the uncertainty of the *ab initio* calculations. Hippler et al. report the only experimental value, D_0(*cis-cis* HOONO) = 83 kJ/mol, from a third-law analysis of the equilibrium constants over 430-490 K.[50] A refinement of the evaluation of this data is underway, and reanalysis of the high temperature data now gives D_0(*cis-cis* HOONO) = 80.5 kJ/mol.[61] Pollack et al.[62] have set an experimental upper limit on the *trans-perp* HOONO binding energy of 70.3 kJ/mol from the product internal energy distribution of the vibrational predissociation of jet-cooled *trans-perp* HOONO. From this limit and the well-converged *ab initio* energy difference between *cis-cis* and *trans-perp* HOONO (14.2 kJ/mol), they find an upper limit for the *cis-cis* HOONO dissociation energy, D_0(*cis-cis* HOONO) $\leq$ 84.6 kJ/mol.

There have been several statistical calculations modeling the pressure and temperature dependence and HOONO/$HONO_2$ branching ratio of this reaction.[51,52,63] In the most recent study, Golden et al.[9] have published a thorough multi-well, multi-channel master equation model of the OH + NO_2 system. Their modeling is consistent with previous experimental results, but all such calculations still rely on experimental constraints, and cannot predict the behavior of this reaction from first principles.

The first spectroscopic observation of HOONO was a matrix study by Lee et al.[64] identifying several fundamental bands (700 – 3600 cm^{-1}) of both *cis-cis* and *trans-perp* HOONO after photolysis of $HONO_2$ in an Ar matrix. The first observation of HOONO in the gas phase was the action spectroscopy experiment reported by Nizkorodov and Wennberg[31] in 2002. In this method, HOONO is excited in the first overtone region by near-IR photons to predissociating states; absorption is monitored by LIF detection of OH products formed upon dissociation to OH and NO_2. They observed a series of vibrational bands in the first OH overtone spectral range from products of reaction (1) occurring in a flowing discharge cell, and provided tentative assignments of the bands in terms of the three conformers of HOONO.

This report was followed by observation of the OH stretching fundamental of *cis-cis* HOONO at 3306 cm^{-1} in direct absorption by cavity ring down spectroscopy.[26] Bean et al. determined the yield of HOONO in reaction (1) by directly measuring the integrated vibrational bands of *cis-cis* HOONO and $HONO_2$; however, they were unable to detect *trans-perp* isomer because its spectrum would be obscured by the strong nitric acid band. They assumed, with support from statistical calculations, that any *trans-perp* HOONO

formed in reaction (1) had isomerized to *cis-cis* HOONO in their experiment. Subsequently, Pollack et al. definitively identified the first OH stretching overtone of supersonically cooled *trans-perp* HOONO from the rotational band contours detected with photodissociation action spectroscopy.[62] Though the band origin at 6971.4 cm^{-1} lies close to the strongest band seen by Nizkorodov and Wennberg, the band is expected to be substantially narrower even at room temperature.

Several key issues remain unresolved, chief among them the question of whether *trans-perp* HOONO is produced in reaction (1) under thermal conditions. Statistical calculations indicate that this isomer will be formed in a high, nonthermal yield from this reaction; if so, then what is its spectroscopic signature, and how rapidly does it isomerize to *cis-cis* HOONO? The assignment of the bands seen in the HOONO overtone action spectrum reported by Nizkorodov and Wennberg remains unclear, especially given the new spectroscopic studies and recent *ab initio* studies suggesting that *cis-perp* HOONO structure is not stable.[9,56] If the spectrum is assigned to the *cis-cis* HOONO conformer, then the dissociation energy D_0 of this conformer is critical for interpreting the action spectrum, since the action spectrum requires that the molecule undergo vibrational predissociation to OH + NO_2 after absorption of a near-IR photon. Current estimates of the dissociation energy are greater than the photon energy for most of the observed bands, implying that the quantum yield is less than unity for much of the spectrum.

In this work, we re-examine the spectroscopy and isomerization kinetics of HOONO conformers in a discharge flow cell using the predissociation action spectroscopy approach of Nizkorodov and Wennberg. The goal of this study is to reconcile all of the

spectroscopic measurements and to provide new experimental and theoretical results on the relative energies and reaction barriers on the HOONO potential energy surface. Specifically, we seek to detect the isomers of HOONO by action spectroscopy, and to measure directly the rate and activation energy for isomerization of *trans-perp* HOONO to *cis-cis* HOONO. We apply statistical RRKM theory to calculate the isomerization rates, for comparison to the experimental data, and to predict photodissociation quantum yield of *cis-cis* HOONO to OH + NO_2. We perform CCSD(T) calculations to improve on predictions of the structure, energy, and frequencies of the isomerization transition state (*anti* configuration of the *perp-perp* HOONO structure), and refine the relative energetics of the *cis-cis, trans-perp*, and (*anti-*)*perp-perp* HOONO conformers. Finally, we calculate the oscillator strengths of both stable conformers, *cis-cis* and *trans-perp* HOONO. The calculated intensities allow us to estimate the *cis-cis* and *trans-perp* HOONO yields in our experiment, and to predict the lifetime of HOONO in the atmosphere due to predissociation by near IR radiation.

3.3. Experimental details

3.3.1. Action spectroscopy

We investigate the spectroscopy and isomerization kinetics of HOONO conformers using photodissociation action spectroscopy. In this method, HOONO undergoes vibrational predissociation upon absorption of a near-IR photon. The excitation is to the first overtone of the OH stretch vibration ($2\nu_1$), and the resulting OH fragment is detected via Laser Induced Fluorescence (LIF). This technique combines molecular selectivity with very high sensitivity: The more stable isomer of nitric acid, $HONO_2$, will not dissociate at

this energy, and the LIF method is sensitive to as few as 10^4 OH molecules/cm^3.[43] The experimental apparatus consists of two synchronized lasers to produce the pump (IR) and probe (UV) pulses, a flow cell and reaction chamber, and a photon-counting PMT detector mounted above the gas flow and lasers. A schematic overview is shown in Figure 3-2.

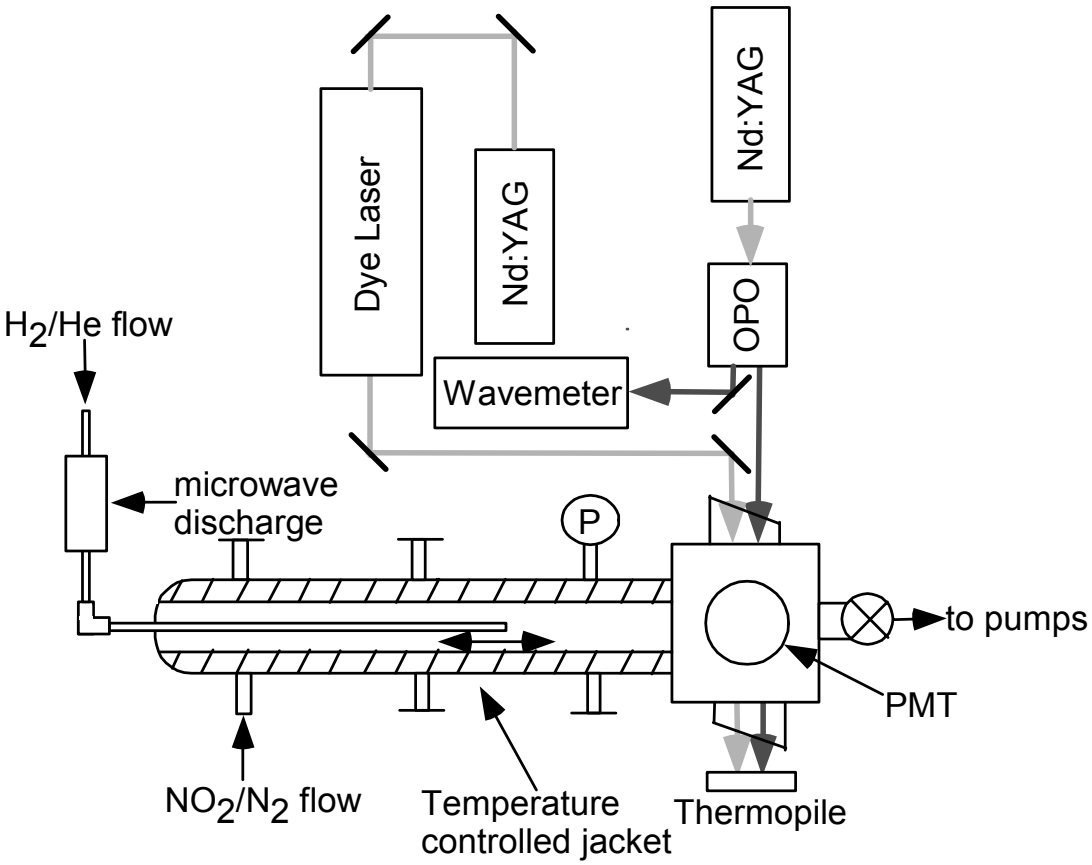

Figure 3-2. Schematic of the experimental apparatus. The pulsed (100Hz) tunable infrared (1.3 – 1.6 μm) for photolysis of HOONO and pulsed tunable ultraviolet (280-285 nm) for OH LIF enter the detection chamber perpendicular to the gas flow. A PMT detector, behind a 311 nm bandpass filter, at 90º to the flows and the lasers, detects the OH LIF. HOONO is produced in a temperature controlled (200 – 280 K) flow cell via gas-phase chemistry. The time delay between the formation of HOONO and its detection can be varied by adjusting the flow rate and position of the H-atom injector.

3.3.2. Flow cell and generation of OH radicals and HOONO

Gases are mixed in a 50 cm temperature controlled jacketed glass flow cell of 25 mm internal diameter. The flow cell has a movable injector, and the interior is coated with Teflon to minimize the occurrence of heterogeneous chemistry on the walls.

In a 2450 MHz McCarroll cavity microwave discharge, H_2 gas is converted to H atoms in the presence of buffer Ar. The H atoms react to form OH radicals rapidly upon mixing with flow containing NO_2:

$$H + NO_2 \rightarrow OH + NO \qquad \text{(R10)}$$

The OH quickly reacts with another NO_2 molecule, forming nitric acid and HOONO conformers (reactions 1a and 1b). Under optimized conditions, the flow cell pressure is 13 hPa and the flow consists of 300 sccm Ar and 60 sccm 1% H_2 in He through the discharge mixed with 50 sccm 4% NO_2 in N_2. This corresponds to 1.5% H_2, 0.5% NO_2, 72% Ar, 14% He, and 12% N_2.

The reaction $OH + NO_2 + M \rightarrow HNO_3 + M$ occurs on a microsecond timescale in the temperature range 200 – 280 K of the flow cell. At the injector port, however, the local temperature of the mixing gases is higher than the controlled flow cell wall temperature due to the highly exothermic reactions (R10) and (1). We cannot, therefore, quantitatively treat the formation kinetics of HOONO. This is not a concern in the experiments reported here, since the isomerization kinetics take place on a longer timescale (60-90 ms).

3.3.3. Lasers and detection

Reaction products are probed in a laser interaction region downstream from the injector at a distance which varies from 20 to 40 cm. The flowing gas is crossed by two lasers, an infrared laser for vibrational overtone excitation followed by a UV laser to probe OH products by laser induced fluorescence.

The tunable near-IR is generated in a type II BBO optical parametric oscillator (OPO) pumped by the 355 nm third harmonic of a pulsed Nd:YAG laser (3 cm^{-1} bandwidth). This OPO[39] outputs 2-3 mJ/pulse in the idler beam, tunable in the range 800 nm – 2500 nm (4000 – 12,5000 cm^{-1}) by rotation of the BBO crystals. The frequency of the signal beam is continuously monitored by a pulsed wavemeter. The wavemeter calibration is verified using photoacoustic spectroscopy of the well-known water transitions in the 7000 – 7200 cm^{-1} region.[65]

The IR pump beam passes through the detection chamber via Brewster-angle CaF_2 windows, perpendicular to the gas flow, and is measured by a thermal power meter after exiting the chamber for calibration of laser power fluctuations. It is overlapped spatially with the UV output of a second laser system, the second harmonic of a Rhodamine 6G dye laser pumped by a frequency doubled Nd:YAG laser (~0.2 cm^{-1} bandwidth).

The UV beam (< 1 μJ, tunable 280-282 nm) excites OH in the $A^2\Sigma$ (v=1) ←$X^2\Pi$ (v=0) band. The $A^2\Sigma$ (v=1) OH relaxes via collisions to the v=0 state and fluorescence is observed at 309 nm ($A^2\Sigma$ (v=0) → $X^2\Pi$ (v=0)). The LIF signal is focused onto a bialkali photomultiplier tube mounted above the detection region, at right angles to both the laser

beams and the gas flow. A 6 nm width narrow-band interference filter centered at 310 nm is employed to reject scattered UV and visible laser light.

For the data reported here, several modes of data acquisition are used. In the pump scanning mode, the IR pump beam is scanned over the $2\nu_1$ region of the HOONO spectrum, while the UV probe beam is maintained tuned on the strongest OH LIF feature ($Q_{21}(1)+Q_{11}(1)+R_{22}(3)$ unresolved triplet of lines). This yields action spectra, such as Figure 3-3 to Figure 3-5, in which the signal at each wavelength is proportional to the product of the absorption cross section and the quantum yield for photodissociation. In this mode, the pump-probe delay is set to 1 μs. This ensures a thermalized OH distribution, so that relative quantum yields from different bands are unaffected by differences in initially formed OH rotational state distribution. In the probe scanning mode, used to measure OH product state distribution shown in Figure 3-6, the IR pump beam is tuned to a wavelength corresponding to a particular overtone band of the molecule of interest, and the UV LIF probe beam is scanned over several OH features corresponding to different *N*-states of the photolysis product OH. In this mode, the pump-probe timing is set to the minimum possible delay, 50 ns, to capture the nascent OH rotational state distribution. Because of the 50 ns delay between pump and probe beams and the relatively high flow cell pressure, 13 hPa, the measured OH product state distribution is somewhat relaxed by rotational energy transfer from the nascent OH distribution produced in photodissociation. However, qualitative differentiation between chemical species is still possible. In the flow kinetics mode, used to generate Figure 3-7, the IR pump beam is toggled between three wavelengths of interest corresponding to various combinations of the two conformers. The

subsequent data analysis to obtain isomerization lifetimes is described below in section 3.4.3. Again, the UV probe beam is tuned on the strongest OH LIF feature. Results of all three modes of operation described above will be reported below.

3.4. Experimental results

3.4.1. New transient trans-perp HOONO spectrum

At room temperature, we observe the same spectrum previously reported by Nizkorodov and Wennberg.[31] However, upon cooling the flow cell to below 243 K, a new spectral feature emerges on top of the earlier spectrum (Figure 3-3). The feature is centered at 6971 cm^{-1} with a width of ~ 30 cm^{-1}, substantially narrower than the bands seen in the room temperature spectrum. Figure 3-3 shows an averaged spectrum of HOONO at 213 K. With decreasing temperature, this band rapidly grows in intensity relative to the other observed bands. The relative intensity of this feature also depends on the time delay between mixing H and NO_2 inside the flow cell and detection of HOONO in the main chamber. The apparent lifetime of the narrow band at this temperature is in the 100 millisecond range (Figure 3-4). The transient nature of this feature is consistent with a less stable conformer of HOONO, which isomerizes to a more stable conformer or undergoes some other reaction on a millisecond timescale. The peak position is consistent with the overtone frequency predicted for the free OH bond in *trans-perp* conformer of HOONO and the overtone band recently fit as *trans-perp* HOONO in a pulsed supersonic expansion (5 K) by Pollack, et al.[62] We therefore assign this new spectrum to the *trans-perp* conformer of HOONO.

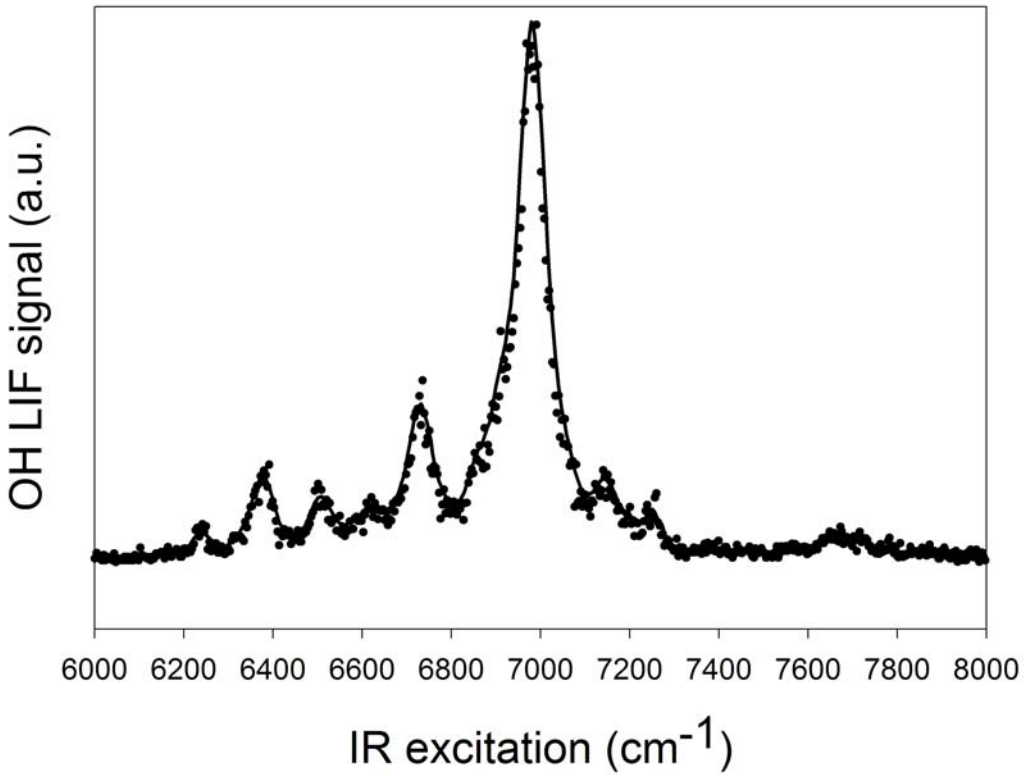

Figure 3-3. Averaged HOONO action spectrum obtained at T = 213 K, P = 13 hPa. Previously unobserved features at 6250 cm^{-1}, 6971 cm^{-1}, and 7700 cm^{-1} are seen in the spectrum.

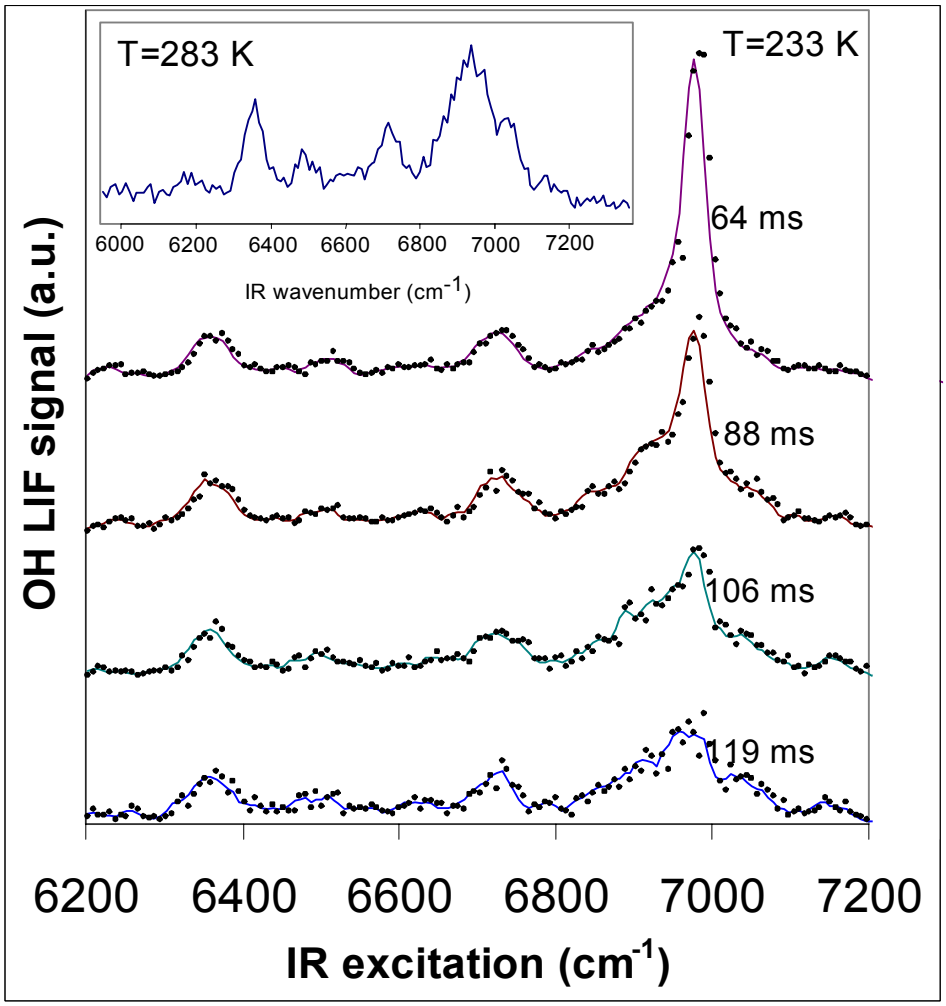

Figure 3-4. HOONO action spectra at various flow cell residence times obtained at $T = 233$ K, $P = 13$ hPa. Three spectra have been averaged at each residence time, and all spectra are scaled to the same 6365 cm^{-1} peak intensity. The prominent band at 6971 cm^{-1} is assigned to *trans-perp* HOONO. The *trans-perp* HOONO band decays relative to the *cis-cis* HOONO band on the ~ 100 ms timescale. **Inset:** 283 K spectrum of the same region contains *cis-cis* HOONO bands only. This spectrum was obtained with flow conditions and averaging identical to the $T = 233$ K spectra.

This assignment can be confirmed by examination of the observed bandshape. Figure 3-5a shows a 3 cm^{-1} resolution action spectrum of the 6971 cm^{-1} peak at 213 K along with rotational band contour simulations performed with the AsyRotWin program.[66] We used the calculated rotational constants shown in Table 3-1 and assumed the same constants for upper and lower states, in a mixed *a*-type and *c*-type hybrid band. The first simulation (dark line, Figure 3-5a), which used the *a*-type to *c*-type ratio of 1.7 derived from *ab initio* calculations of the *trans-perp* HOONO overtone transition moments discussed in section 3.5.4, matches our 213 K flow cell spectrum very well. Also shown for comparison is a simulation with an *a*-type to *c*-type band ratio of 1, a ratio which Pollack, et al.[62] found to give the best representation of their 5 K spectrum of *trans-perp* HOONO.

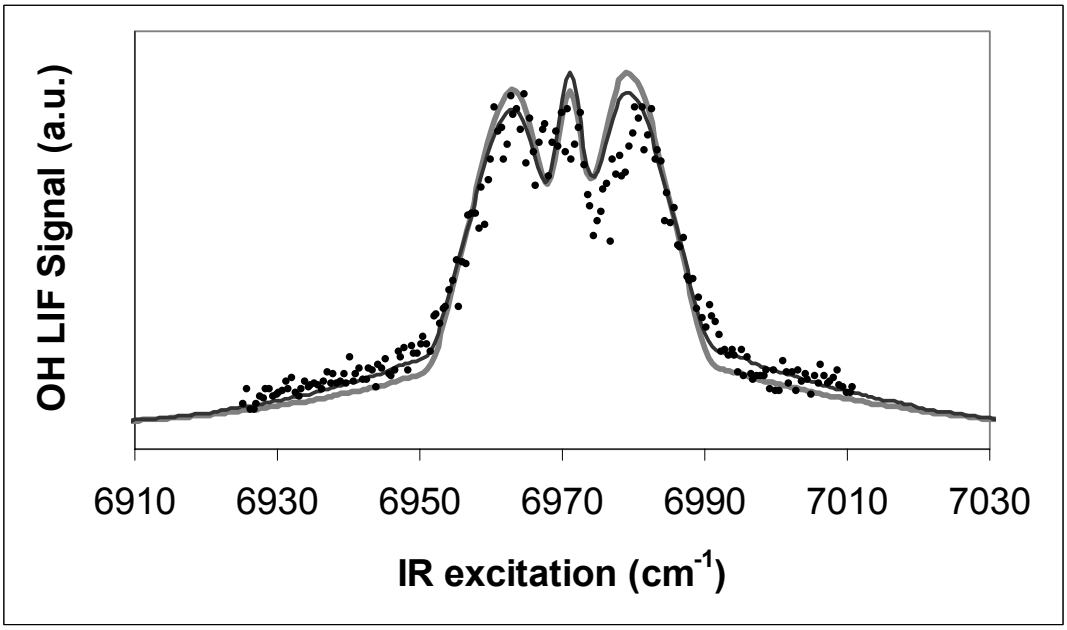

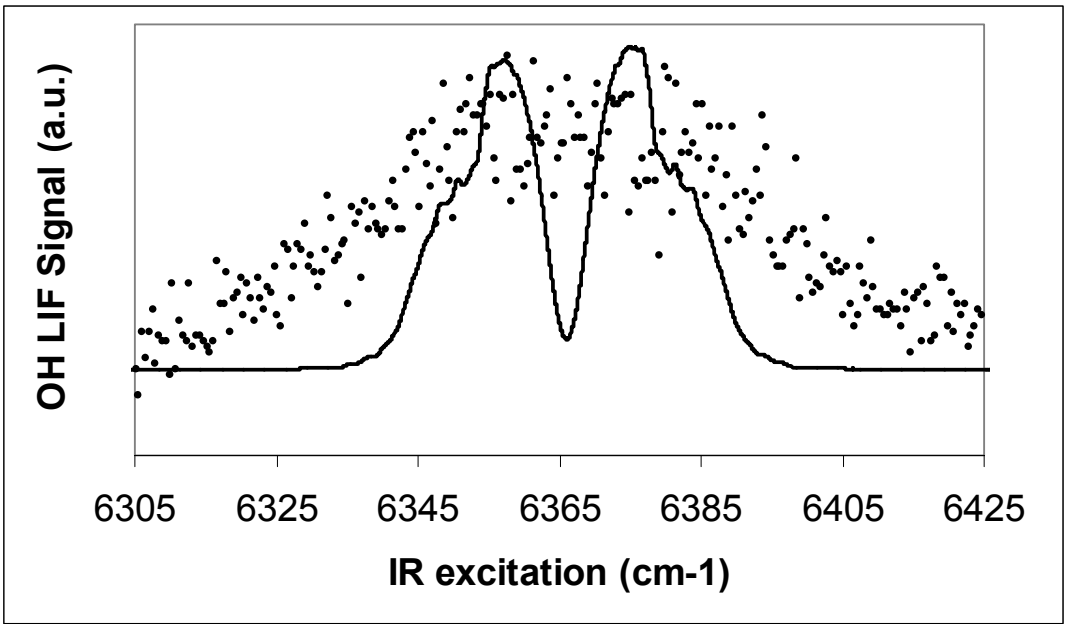

Figure 3-5. **(a)** Action spectrum of trans-perp HOONO at 213 K. A slow scan (0.05 cm^{-1} step size; 3 cm^{-1} resolution) over the narrow peak in Figure 3-3 reveals band structure. Smooth lines are simulations from the program AsyRotWin66 using molecular parameters from Table 3-1. Black and gray solid lines are band simulations for an *a*-type to *c*-type ratio of 1.8 and 1, respectively. The *a*-type/*c*-type ratio of 1.8 is the hybrid band type calculated in this paper; while the a-type/c-type ratio of 1 is the

approximate band type for trans-perp HOONO found by Pollack et al. to best represent their experimental spectrum in a supersonic expansion. **(b)** Action spectrum of $2\nu_1$ band of cis-cis HOONO at 273 K. A slow scan (points) reveals no resolvable structure. Line is a simulation of a pure *b*-type transition, using the program AsyRotWin66 with *cis-cis* HOONO molecular parameters from Table 3-1.

Table 3-1. Molecular constants for the *cis- cis, trans-perp,* and *perp-perp* conformers of HOONO computed at the CCSD(T)/cc-pVTZ level, except for energies, which are reported at both the CCSD(T)/cc-pVTZ and CCSD(T)/cc-pVQZ//CCSD(T)/cc-pVTZ levels, relative to the *cis-cis* HOONO energy at each level of theory.

	cis-cis **HOONO**	***trans-perp*** **HOONO**	***anti-perp-perp*** **HOONO**
Geometries[a]			
R(HO1) (Å)	0.9823	0.9663	0.9662
R(O1O2)	1.4332	1.4314	1.4384
R(O2N)	1.3845	1.4681	1.607
R(NO3)	1.1917	1.1692	1.1512
θ(HO1O2)	99.80°	100.75°	100.57°
θ(O1O2N)	112.98°	105.50°	100.33°
θ(O2NO3)	114.39°	108.75°	109.74°
ϕ(HO1O2N)	0°	176.83°	82.65°
ϕ(O1O2NO3)	0°	97.59°	97.00°
A (MHz)	21310	54127	24782
B	8081	4977	5896
C	5859	4627	5326
Energetics[b]			
CCSD(T)/cc-pVTZ			
E_{el} (hartrees)	-280.4736515	-280.4674707	-280.4503806
ΔE_{el} (kJ/mol)	0	16.2	61.1
ΔE_0 (kJ/mol)	0	14.6	56.9
ΔH^o_{298} (kJ/mol)	0	15.9	57.0
CCSD(T)/cc-pVQZ//CCSD(T)/cc-pVTZ			
E_{el} (hartrees)	-280.5603706	-280.5544193	-280.5373081
ΔE_{el} (kJ/mol)	0	15.6	60.5
ΔE_0 (kJ/mol)	0	13.7	56.1
ΔH^o_{298} (kJ/mol)	0	15.3	56.4
Harmonic frequencies[c]			
ν_1 (cm^{-1})	3521(a′)	3780	3774
ν_2	1630(a′)	1736	1794
ν_3	1458(a′)	1412	1374
ν_4	969(a′)	992	906
ν_5	838(a′)	816	702
ν_6	723(a′)	497	468
ν_7	419 (a′)	366	384
ν_8	523 (a″)	302	288
ν_9	383 (a″)	211	-233

a. Atom labels are assigned as HO1O2NO3

b. Zero point and enthalpy corrections to E_{el} are determined from CCSD(T)/cc-pVTZ frequencies
c. Vibrational frequencies of *cis-cis* and *trans-perp* HOONO from Bean, et al.[26]

In the room temperature spectrum, all of the sub-bands behave similarly with respect to changes in chemistry and temperature. This multiple-band spectrum is present without the 6971 cm^{-1} *trans-perp* HOONO feature at room temperature, and decays much more slowly than *trans-perp* HOONO does at colder temperatures. We therefore assign all of the bands in the room temperature spectrum to the lowest energy conformer, *cis-cis* HOONO.

A 3 cm^{-1} resolution action spectrum of the 6365 cm^{-1} *cis-cis* HOONO band is shown in Figure 3-5b, along with a rotational band shape simulation from the AsyRotWin program.[66] The upper and lower state rotational constants are taken from Table 3-1, and a *b*-type band is assumed, based on calculations in section 3.5.4. The simulated *cis-cis* HOONO band has the pronounced *P* and *R* bands of a *b*-type transition, and is slightly broader than the *trans-perp* HOONO band, but the experimentally measured *cis-cis* HOONO band is significantly broader than predicted and has no resolvable structure. We conclude that some dynamical process, either IVR or dissociation, is leading to the broadening and absence of rotational structure.

The *cis-cis* HOONO spectrum becomes progressively weaker at lower temperatures, most likely due to rapid wall loss. To observe the temperature dependence of the *cis-cis* HOONO spectrum over a larger temperature range, we employ an alternate synthesis of HOONO which does not require discharge chemistry (eliminating the need for long reaction times in the flow cell) and produces no detectable amount of *trans-perp*

HOONO. HOONO is prepared by reacting H_2O_2 vapor with solid $NOBF_4$ *in situ*, analogous to the production of HO_2NO_2 from NO_2BF_4 described in Kenley, et al.[67] Using this preparation method, we observe no temperature dependence of the relative peak intensities in the *cis-cis* HOONO spectrum in the range 193-273 K (Figure 3-9).

Weaker new bands are observed in the discharge HOONO synthesis at 6250 cm^{-1} and 7700 cm^{-1} (Figure 3-3). The peak at 6250 cm^{-1} is only observed at cold temperatures, coincident with the *trans-perp* HOONO peak at 6971 cm^{-1}, and is hence assigned to *trans-perp* HOONO. The temperature dependence of the 7700 cm^{-1} band was not studied systematically, therefore, this band cannot be assigned to either *trans-perp* or *cis-cis* HOONO.

3.4.2. OH product state distributions

The large differences in the structure and binding energy of *cis-cis* and *trans-perp* HOONO suggest that these two conformers should have distinct vibrational predissociation dynamics. The dynamical differences in the quantum state distribution of OH photofragments can be used to assist in spectroscopic assignment of various HOONO bands and provide other useful information. Pollack et al. analyzed the OH state distribution from the photolysis of supersonically cooled HOONO in the 6971 cm^{-1} band to constrain its binding energy to $D_0 < 70.3$ kJ/mol, consistent with an assignment of the band to the *trans-perp*, but not *cis-cis*, conformer of HOONO.[62]

In our experiment, the nascent energy distribution of the product OH fragments can be estimated by scanning over various OH lines with the LIF probe laser while the

pump laser is fixed on a chosen OH overtone resonance of one of the HOONO conformers. To minimize thermalization of the OH prior to detection, the cell pressure and the pump-probe delay must be kept at their lowest possible values. The minimal pump-probe delay in this experiment is 50 ns, limited primarily by jitter in the pump-probe separation (10 ns) and by temporal width of the UV probe laser pulse (20 ns). In Ar bath gas, the average rotational energy transfer (RET) rate constant for OH $^2\Pi_{3/2}$(v"=0), in N"=1-5, is 2.3×10^{-11} cm^3 $molecule^{-1}$ sec^{-1}.[68] At a pressure of 13 hPa, this corresponds to ~0.5 effective collisions between pump and probe pulses.

Despite this partial thermalization, a significantly different energy distribution in the OH photofragments is observed for the *cis-cis* and *trans-perp* conformers of HOONO. Figure 3-6 shows the observed distributions within the corresponding $^2\Pi_{3/2}$-(N) rotational manifolds obtained from analysis of $Q_{11}(N)$ branch of the $A^2\Sigma$ (v=1) ←$X^2\Pi$ (v=0) band. The OH fragments from the photodissociation of *trans-perp* HOONO are rotationally excited, while the OH fragments from *cis-cis* HOONO are concentrated more heavily in the lowest N states, even though the *cis-cis* HOONO spectrum is recorded at a higher temperature. This distribution is consistent with the larger energy release (hv-D_0) expected for *trans-perp* than for *cis-cis* HOONO based on the laser excitation energy and the empirically determined dissociation energies, providing further evidence that the transient feature observed is *trans-perp* HOONO.

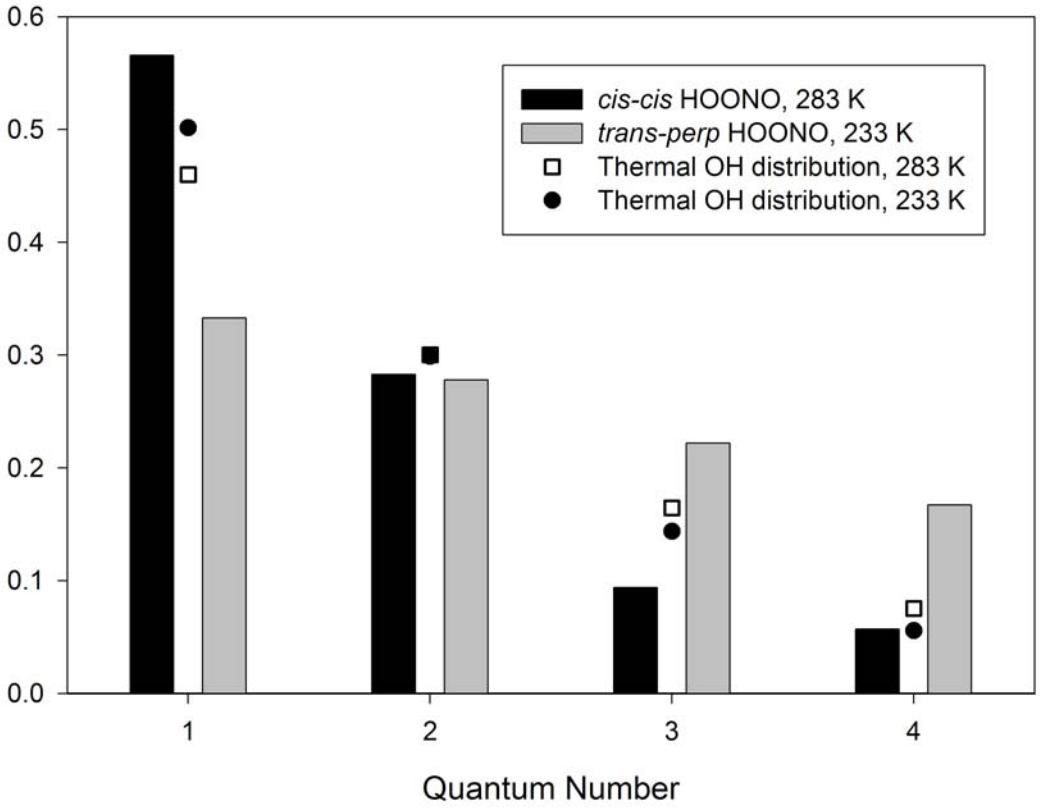

Figure 3-6. Relative populations of the first few OH $^2\Pi_{3/2}^-(N)$ rotational states, N = 1-4. Black bars represent normalized population of the lowest quantum states after IR photodissociation on a *cis-cis* HOONO band at 6365 cm^{-1} at 283 K; grey bars, after photodissociation on a *trans-perp* HOONO band at 6970 cm^{-1} at 233 K. Both *cis-cis* and *trans-perp* HOONO measurements were conducted at 13 hPa, 50 ns pump-probe delay. Symbols indicate thermal OH distribution at the two temperatures. Large difference in the OH fragment internal energy reflects the difference in the photon energy available for dissociation.

3.4.3. Trans-perp to cis-cis HOONO isomerization rate

Flow cell kinetics experiments have been employed to measure the lifetime of *trans-perp* HOONO. At low temperatures, the signal from both conformers decays with

residence time (distance from injector), but the *trans-perp* HOONO signal at 6971 cm^{-1} decays faster. The loss of *cis-cis* HOONO only occurs at temperatures below about 270 K, and the loss rate increases with decreasing temperature. We therefore conclude that the *cis-cis* HOONO decay is due to diffusion to the walls and subsequent uptake or reaction, while the faster decay of the *trans-perp* HOONO signal is due to isomerization. If we assume that both conformers of HOONO have the same wall loss rates in the flow cell, then the ratio of the *trans-perp* to *cis-cis* HOONO signals gives the *trans-perp* HOONO decay due to isomerization alone.

The relative ratio of intensities I_{tp}/I_{cc} of *trans-perp* to *cis-cis* HOONO signal is monitored at a series of injector positions (residence times) in the flow cell at several temperatures by measurement of signal intensity I at three wavelengths: one where both *trans-perp* and *cis-cis* HOONO absorb (6971 cm^{-1}), one which determines the baseline absorption by *cis-cis* HOONO underneath the 6971 cm^{-1} signal (6950 cm^{-1}), and one where only *cis-cis* HOONO signal is present (6365 cm^{-1}).

$$\frac{I_{tp}}{I_{cc}} = \frac{I(6971cm^{-1}) - I(6950cm^{-1})}{I(6935cm^{-1})} \tag{5}$$

In addition, we assume that the increase in *cis-cis* HOONO signal due to the isomerization is negligible, since the number density of *trans-perp* HOONO is significantly lower than that of *cis-cis* HOONO, and since the spectrum is spread over a broad 1000 cm^{-1} wavelength range compared to the spectrally narrow 30 cm^{-1} *trans-perp* peak. A plot of $\ln(I_{tp}/I_{cc})$ versus residence time has a slope that is the unimolecular rate of *trans-perp* to *cis-*

cis isomerization. Temperature-dependent isomerization rates are shown in Figure 3-7 in the range 223 K < T < 238 K.

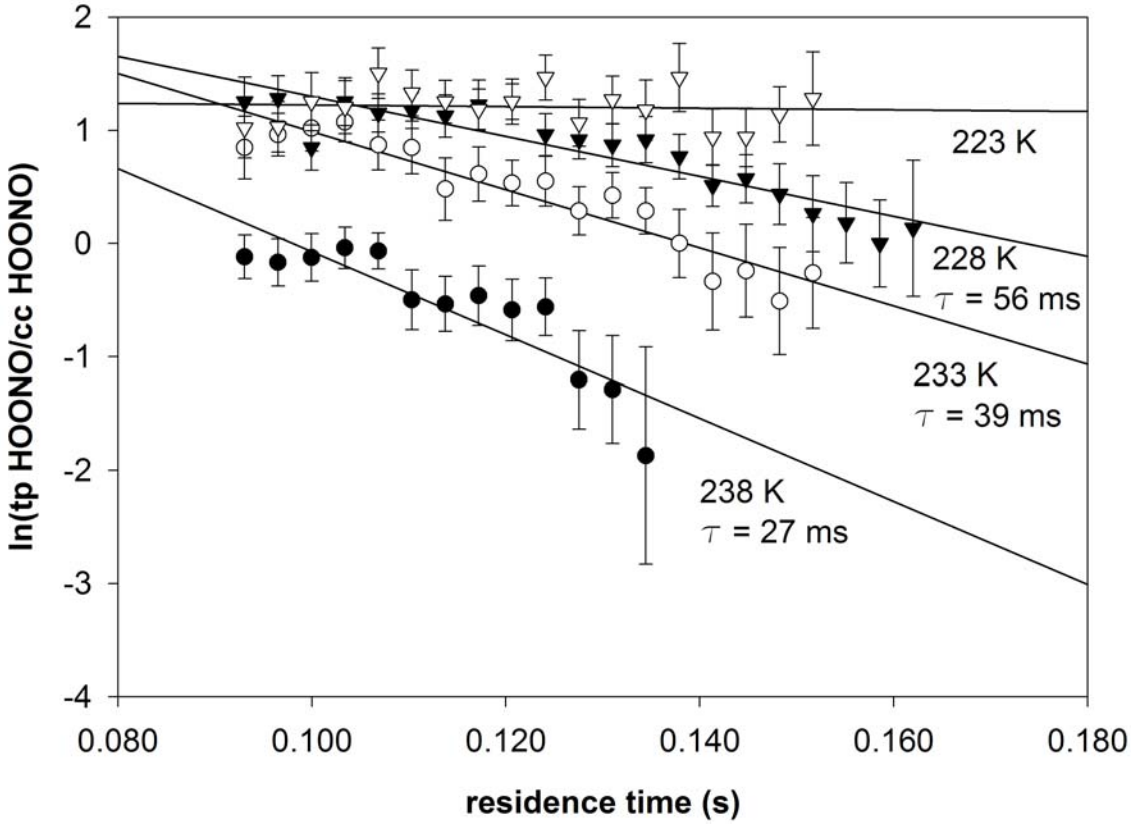

Figure 3-7. Measurement of lifetimes of *trans-perp* HOONO in the flow cell at various temperatures. The measurement is done by monitoring the ratio of the relative intensities of the *trans-perp* HOONO to *cis-cis* HOONO overtone bands as a function of the flow cell residence time. The slope of each line is the decay rate in s^{-1}.

The lifetimes of *trans-perp* HOONO at 238 K, 233 K, and 228 K, are estimated to be 27 ± 4 ms, 39 ± 3 ms, and 56 ± 6 ms, respectively, at 13 hPa of predominantly Ar. Unfortunately, we cannot probe the isomerization over a broader temperature range,

because only one conformer can be detected with sufficient precision at colder and warmer temperatures. The data at 223 K show a very small slope and significant error; no accurate lifetime can be determined. The Arrhenius ln(k) vs. 1/T relationship (Figure 3-8) gives an activation energy for isomerization of E_{act} ~ 33 ± 12 (1σ) kJ/mol. The large uncertainties stem from the narrow temperature range used to determine E_{act}.

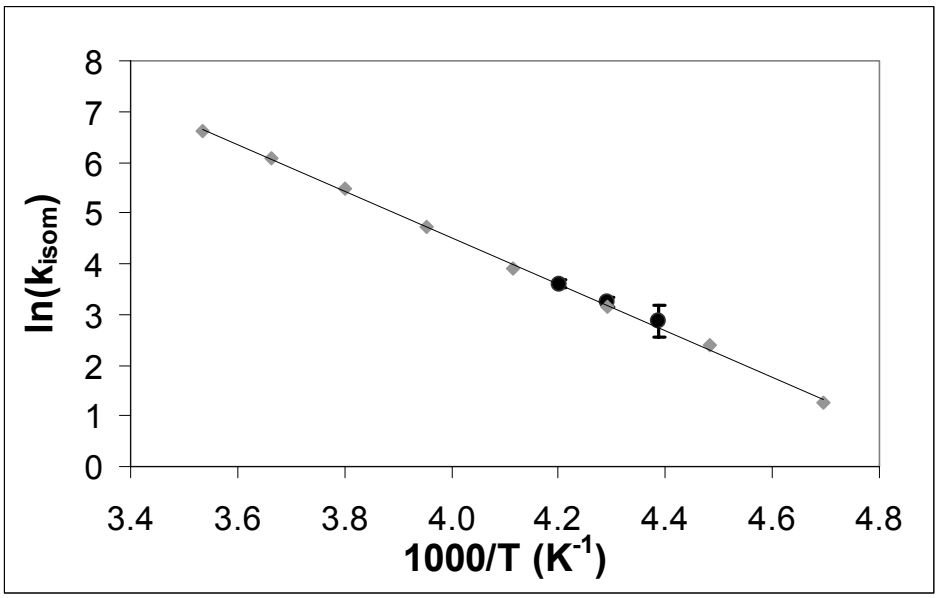

Figure 3-8. *Trans-perp* to *cis-cis* HOONO isomerization rate as a function of temperature. Grey diamonds represent the results of a MultiWell simulation with an isomerization barrier of 40.8 kJ/mol at 8.7 hPa. Black circles are experimental data. Fit to the experimental data gives an isomerization activation barrier of E_{act} (230 K) = 33 ± 12 kJ/mol.

3.5. Computational results

3.5.1. Ab initio calculations of cis-cis, trans-perp, and perp-perp HOONO structure, energetics, and frequencies

The structures, energies, and vibrational frequencies of the *cis-cis*, *trans-perp*, and (*anti*-) *perp-perp* HOONO conformers have been calculated by electronic structure theory using the program Gaussian98.[69] For these calculations we use coupled cluster theory[70] with single and double excitations, with perturbative estimates of connected triples CCSD(T). The calculations employ the Dunning correlation-consistent polarized valence basis sets. The two basis sets used in this study are the cc-pVTZ basis set (4s3p2d1f for C, N, and O; 3s2p1d for H) and the cc-pVQZ basis set (5s4p3d2f1g for C, N, and O; 4s3p2d1f for H).[71,72]

Optimized structures and vibrational frequencies of the three isomers are computed at the CCSD(T)/cc-pVTZ level. The *perp-perp* isomer possesses one imaginary frequency, corresponding to torsion of the heavy atoms (OONO). Energies at these geometries are computed at the CCSD(T)/cc-pVTZ and CCSD(T)/cc-pVQZ levels. Table 3-1 lists the structures, energies, rotational constants and vibrational frequencies of the three conformers, with *perp-perp* HOONO computed in the *anti* configuration. The normal modes of the *trans-perp* and *perp-perp* isomer are ordered in descending frequency, while the modes of the *cis-cis* isomer, which has C_s symmetry, are ordered based on the symmetry, a' and then a''. The CCSD(T)/cc-pVQZ//CCSD(T)/cc-pVTZ energies are consistent with QCISD and CCSD(T)/cc-pVTZ results reported previously.[26]

3.5.2. Statistical (RRKM) calculations of isomerization rate

To better understand the observed temperature dependence of HOONO action spectra, we model the isomerization rates of HOONO conformers using the program MultiWell,[73] which uses a stochastic approach to solving RRKM master equations. The main goal of these simulations is to confirm that the experimentally determined rates of isomerization from the *trans-perp* conformer to the lower energy *cis-cis* conformer are consistent with the *ab initio* energetics of HOONO. We adopt the required RRKM parameters from the model developed by Golden et al.,[9] which successfully reproduced the extensive kinetic data on the OH + NO_2 reaction (Hippler, et al.,[50] and others). The dissociation energy of *cis-cis* HOONO is fixed at 83 kJ/mol and the energy separation between *trans-perp* and *cis-cis* conformers is set to 15 kJ/mol. The average internal energy transferred per collision is chosen to be $\alpha = 500$ cm^{-1}. The height of the *trans-perp* $\rightarrow$ *cis-cis* HOONO isomerization barrier (treated as a single transition state energy for both *perp-perp* states) is varied to reproduce the experimentally observed *trans-perp* isomerization rates. Because the reaction is in the low pressure limit, isomerization rates and collision parameter (α) are linearly related, and the *trans-perp* $\rightarrow$ *cis-cis* HOONO isomerization barrier determined is inversely correlated to the choice of $\alpha = 500$ cm^{-1}. The simulation starts with the *trans-perp* conformer in an internally thermalized state, from which it can either reversibly isomerize into the *cis-cis* well or irreversibly dissociate into OH and NO_2. For the range of probed barrier heights (15 – 55 kJ/mol), the rate of dissociation into OH and NO_2 is negligibly small compared to the rate of equilibration between *cis-cis* and *trans-perp* conformers of HOONO. Therefore, the simulated time-dependence for the *trans-perp*

concentration can be directly fitted to an exponential decay to extract the effective equilibration rate ($= k_{tp\rightarrow cc} + k_{cc\rightarrow tp} \approx k_{tp\rightarrow cc}$).

The RRKM simulations of *trans-perp* to *cis-cis* HOONO isomerization presented here were performed assuming a bath gas of N_2. Our experimental gas mixture, however, consists of small amounts of H_2 and NO_2, 72% Ar, 14% He, and 12% N_2. Donahue, et al.[74] have shown that relative to a collisional efficiency of $\beta = 1$ for nitrogen, $\beta(Ar) = 0.61 \pm 0.03$ and $\beta(He) = 0.48 \pm 0.03$, in the OH + NO_2 system. For the gas mixture used in these experiments, then, the collisional efficiency is approximately $\beta = 0.65$. In the low pressure limit, which is applicable to these experiments at 13 hPa, this lower collision efficiency is equivalent to a lower pressure. Our gas mixture at 13 hPa behaves equivalently to pure N_2 at 8.7 hPa.

Figure 3-8 displays the calculated $k_{tp\rightarrow cc}$ isomerization rates at 8.7 hPa of N_2 as a function of temperature. The calculation uses the *trans-perp* $\rightarrow$ *cis-cis* HOONO isomerization barrier of $\Delta E_0 = 40.8$ kJ/mol (corresponding to an energy of $\Delta E_0 = 55.8$ kJ/mol for the *perp—perp* isomer relative to the *cis-cis* HOONO energy). The modeled *trans-perp* to *cis-cis* HOONO barrier height is in excellent agreement with the energy computed here at the CCSD(T)/AUG-cc-pVQZ //CCSD(T)/cc-pVTZ level, $\Delta E_0 = 42.4$ kJ/mol, and is also consistent with the energy computed by Golden et al.[9] at the QCISD(T)/cc-pVDZ level, 45.3 kJ/mol, for *perp-perp* HOONO relative to *trans-perp* HOONO.

The predicted temperature dependence of the isomerization rates compares favorably with the experimental results (black points in Figure 3-8, derived from Figure 3-7). The value suggested by our Multiwell simulations (40.8 kJ/mol) is within the error limits of the experimentally determined activation energy (E_{act} = 33 ± 12 kJ/mol).

3.5.3. Calculated photodissocation quantum yields and temperature dependence of relative band intensities in cis-cis HOONO

We also use MultiWell to predict the effective photodissociation quantum yields for the overtone transitions of *cis-cis* HOONO. The results of these simulations are shown in Figure 3-9 (a) and (b). In these simulations, the internal energy distribution for thermalized *cis-cis* HOONO is abruptly shifted upward by the photon energy. The fraction of HOONO conformers and $OH+NO_2$ products formed after 100 collisions following the excitation is taken as the yield. We use D_0(*cis-cis* HO-ONO) = 83 kJ/mol (6940 cm^{-1}), which represents the best *ab initio* estimate from Dixon et al.[56] as well as the empirical value determined by extrapolation to 0 K from high-temperature data from Hippler, et al.[50]

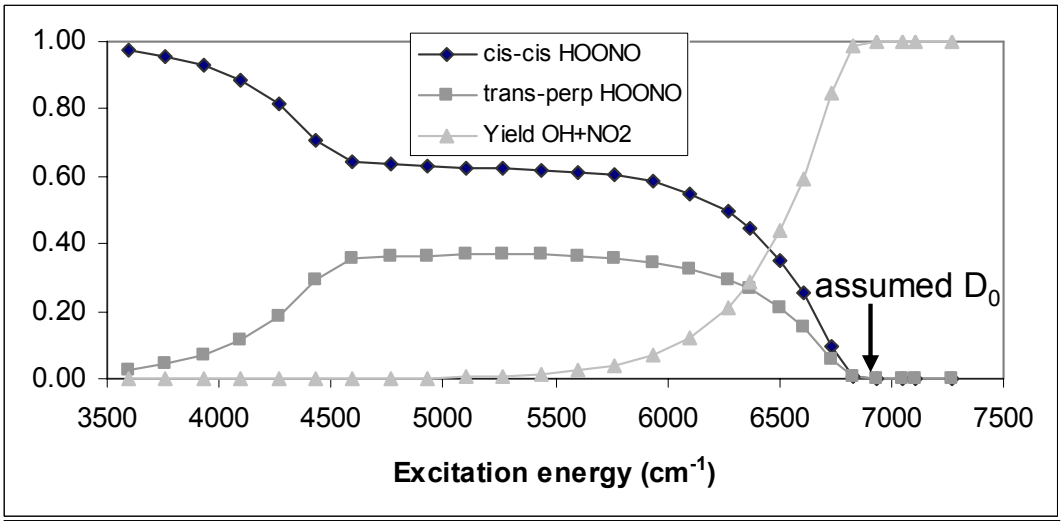
1.00
0.80
0.60
0.40
0.20
0.00
cis-cis HOONO
trans-perp HOONO
Yield OH+NO2
assumed D_0
3500
4000
4500
5000
5500
6000
6500
7000
7500
Excitation energy (cm^{-1})

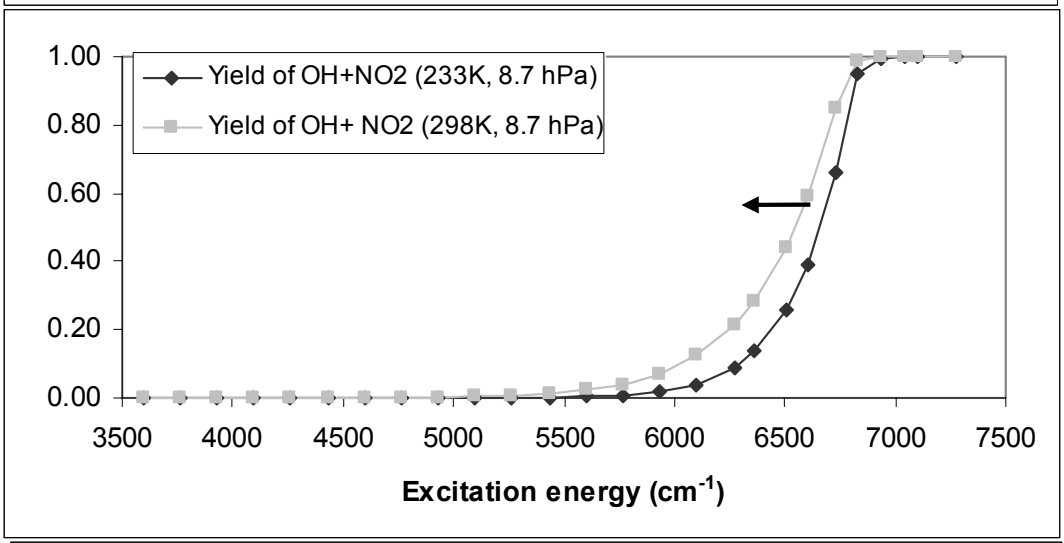
1.00
0.80
0.60
0.40
0.20
0.00
Yield of OH+NO2 (233K, 8.7 hPa)
Yield of OH+ NO2 (298K, 8.7 hPa)
3500
4000
4500
5000
5500
6000
6500
7000
7500
Excitation energy (cm^{-1})

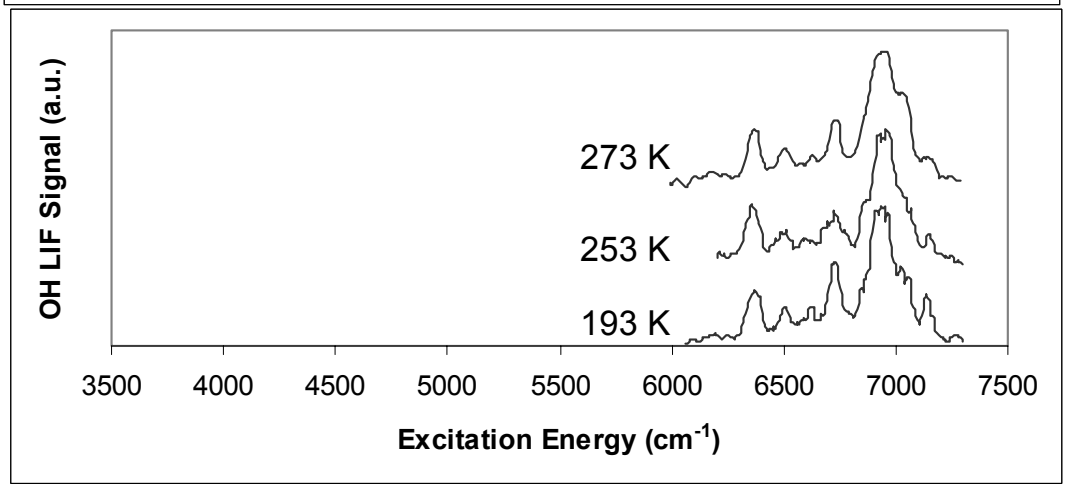
OH LIF Signal (a.u.)
273 K
253 K
193 K
3500
4000
4500
5000
5500
6000
6500
7000
7500
Excitation Energy (cm^{-1})

Figure 3-9. **a)** Simulation of the quantum yield of *cis-cis* HOONO, *trans-perp* HOONO, and OH + NO_2 products, following vibrational excitation of *cis-cis* HOONO at 298 K, as a function of excitation energy. Calculations assume a dissociation energy of D_0(*cis-cis* HOONO) = 83 kJ/mol (6940 cm^{-1}, shown with arrow). A significant yield of *trans-perp* HOONO is predicted after excitation above the isomerization barrier. The onset of dissociation occurs at 5500 cm^{-1}, well below the dissociation threshold. Calculations are run at 8.7 hPa N_2 (equivalent to 13 hPa of the gas mixture used in the above experiments, see text).
b) Photodissociation quantum yield as a function of excitation energy, calculated at 233 K and 298 K. with D_0(*cis-cis* HOONO) = 83 kJ/mol. The quantum yield at the 6365 cm^{-1} peak is predicted to double when the temperature is changed from 233 K to 298 K.
c) Experimentally measured cis-cis HOONO spectrum at three temperatures. The relative strengths of the bands in the *cis-cis* HOONO spectrum do not change appreciably over the temperature range 193 K – 273 K.

Figure 3-9a depicts the fraction of *cis-cis* and *trans-perp* HOONO as well as OH + NO_2 produced as a function of energy added to the system at 298 K. When the system is excited above the isomerization barrier between 4500 and 6000 cm^{-1}, a significant amount of the original *cis-cis* HOONO isomerizes, forming a sizeable fraction of *trans-perp* HOONO products as determined by the density of states at the isomerization barrier energy. Photodissociation products begin to appear at 5500 cm^{-1}, with the yield slowly rising to ≈ 50% at 6600 cm^{-1} (still well below D_0). The quantum yield is predicted to approach unity at 6700 cm^{-1}.

Figure 3-9b compares the OH + NO_2 yield for two temperatures representative of our experimental conditions. Over the frequency range of the observed *cis-cis* HOONO spectrum, we find that the quantum yield for photodissociation increases from 30% to

100% at 298 K, and from 15% to 100% at 233 K. At the 6365 cm^{-1} peak, the quantum yield is predicted to double from 233 K to 298 K. Thus, the simulations predict that the relative intensities of the bands should change markedly as a function of temperature.

Figure 3-9c shows the positions of the *cis-cis* HOONO bands on the scale of the quantum yield predictions, and also illustrates the insensitivity of the spectrum to temperature change. We observe no discernable change in relative integrated peak intensities in the *cis-cis* HOONO spectrum over the range 193 K – 273 K.

3.5.4. Calculated transition strengths of cis-cis and trans-perp HOONO

To estimate the relative concentrations of the *cis-cis* and *trans-perp* HOONO from the observed band intensities, we perform semi-empirical calculations to compute transition strengths for the observed overtone bands of both isomers. We test the validity of our normal mode anharmonic oscillator and Morse oscillator approaches by calculating band intensities of the ν_1 and $2\nu_1$ transition of nitric acid, for which experimentally determined oscillator strengths and further predictions are available.

The method of using *ab initio* dipole moment functions in calculating vibrational band intensities has been demonstrated.[75,76] Vibrational band intensity calculations similar to those reported here have been performed by Kjaergaard, Henry, and others on several molecules using a local mode harmonically coupled anharmonic oscillator model (HCAO)[77-79] and coupled Morse oscillators.[80] For calculation of the OH fundamental and overtone in HOONO described here, we consider only the OH normal mode.

The oscillator strength for a given vibrational transition is given by

$$f_{fi} = \frac{4\pi m_e}{3e^2\hbar} \nu_{fi} \sum_{i=a,b,c} |M_i|^2 \qquad (6)$$

where ν_{fi} is the frequency of the transition and M_i are the matrix elements of the transition dipole moment between the ground and excited vibrational states:

$$M_i = \langle f | \mu_i | i \rangle \qquad (7)$$

The values of the matrix elements M_i for the $v = 0 \rightarrow 2$ overtone transitions are obtained by first computing *ab initio* dipole moment functions along one dimension, the normal mode q_1 (essentially the OH stretch). The vibrational matrix elements are then calculated using two different one-dimensional models, an anharmonic oscillator model with a single cubic perturbation, and the Morse oscillator model, where the parameters for both models are fit using observed vibrational energies.

Dipole moments functions are calculated for both *cis-cis* and *trans-perp* HOONO structures using the Gaussian98 program.[69] Optimized structures for each isomer are first determined at the B3LYP/AUG-cc-pVTZ, MP2/AUG-cc-pVTZ, MP3/AUG-cc-pVDZ and QCISD/AUG-cc-pVDZ levels of theory. The atoms are then displaced in 0.1 amu$^{1/2}$ - Å increments from the optimized geometries along the q_1 normal mode, to generate nine structures along the vibrational mode (+0.4 amu$^{1/2}$ - Å > Δq_1 > - 0.4 amu$^{1/2}$ - Å). This normal mode displacement involves primarily motion of the H-atom along the OH bond, with small concomitant motion of the adjacent O-atom. The dipole moments are computed for each of these nine structures, for each principal axis component (i), at each level of theory. These points are then fit to a Taylor series expansion, truncated after the fifth derivative, to

extract the derivatives of the dipole moment function used in the transition moment calculation:

$$\mu_i = \mu_{0,i} + \sum_{n=1}^{5} \frac{1}{n!} \frac{\partial^n \mu_i}{\partial q^n} q^n = \mu_{0,i} + \sum_{n=1}^{5} c_{i,n} q^n \tag{8}$$

Figure 3-2 lists the $\mu_{0,i}$ and coefficients $c_{i,n}$ at all levels of theory used. Also listed is μ_1, the effective reduced mass of the mode q_1, computed in the Gaussian 98 program at each level of the theory.[81,82]

Table 3-2. Computed dipole moment functions in Debye for *trans-perp* and *cis-cis* conformers of HOONO as a function of normal mode displacement q_1. Taylor series coefficients were derived from the fitting of a fifth order polynomial (see text) to *ab initio* dipole moments at nine points along the q_1 normal mode, computed in 0.1 amu$^{1/2}$ - Å increments in the range -0.4 amu$^{1/2}$ - Å < Δq_1 < +0.4 amu$^{1/2}$ - Å. Coefficients are defined as $c_{i,n} = \frac{1}{n!}\frac{\partial^n \mu_i}{\partial q_1^{\,n}}$, where $i = A,B,C$, the principal axes. Units are D/amu$^{n/2}$ Å^n.

	B3LYP AUG-cc-pVTZ	MP2 AUG-cc-pVTZ	MP3 AUG-cc-pVDZ	QCISD AUG-cc-pVDZ
***Trans-perp* HOONO**				
Reduced mass, amu	1.0686	1.0686	1.0684	1.0685
$\|\mu_{tot}\|$(equil)	1.7330	1.8758	2.0498	1.9724
$\mu_{0,A}$	0.7470	0.6909	1.0488	0.8562
$c_{A,1}$	0.8067	0.9256	0.8837	0.9043
$c_{A,2}$	-0.6961	-0.8855	-0.8046	-0.8230
$c_{A,3}$	-2.6773	-0.3270	-0.2301	-0.2139
$c_{A,4}$	-5.5369	0.0499	-0.0640	-0.0526
$c_{A,5}$	14.9472	0.5069	0.7197	0.6901
$\mu_{0,B}$	-0.3478	-0.6010	-0.5989	-0.6306
$c_{B,1}$	-0.0320	-0.0569	-0.1604	-0.1009
$c_{B,2}$	0.4737	0.2048	0.1460	0.1860
$c_{B,3}$	-0.1344	-0.0882	-0.1097	-0.1006
$c_{B,4}$	-1.9665	-0.0123	-0.0001	0.0150
$c_{B,5}$	0.5710	-0.0568	-0.2200	-0.1946
$\mu_{0,B}$	1.5310	1.6370	1.6557	1.6609
$c_{C,1}$	0.8302	1.1023	1.1150	1.1205
$c_{C,2}$	-0.5782	-0.2726	-0.2353	-0.2249
$c_{C,3}$	-1.1973	-0.7564	-0.7030	-0.6433
$c_{C,4}$	-0.6951	0.1149	0.2032	0.2490
$c_{C,5}$	0.6047	0.5634	0.4862	0.2819

	B3LYP AUG-cc-pVTZ	MP2 AUG-cc-pVTZ	MP3 AUG-cc-pVDZ	QCISD AUG-cc-pVDZ
***Cis-cis* HOONO**				
Reduced mass, amu	1.0643	1.0640	1.0642	1.0641
$\|\mu_{tot}\|$(equil)	0.9618	1.1744	1.1987	1.2276
$\mu_{0,A}$	-0.4042	-0.7435	-0.7513	-0.8604
$c_{A,1}$	-0.5378	-0.7808	-0.7929	-0.8628
$c_{A,2}$	-3.4439	-1.1959	-1.2353	-1.3039
$c_{A,3}$	3.4255	-0.2171	-0.1870	-0.2322
$c_{A,4}$	14.5912	0.0450	-0.1166	-0.0649
$c_{A,5}$	-28.5687	0.2815	0.3832	0.43381
$\mu_{0,B}$	-0.9096	-0.9090	-0.9337	-0.8753
$c_{B,1}$	-0.4418	-1.1157	-1.0871	-1.0676
$c_{B,2}$	-1.3162	-0.0838	-0.0801	-0.0926
$c_{B,3}$	-2.9383	-0.3229	-0.3965	-0.4281
$c_{B,4}$	12.6755	-0.2311	-0.1332	-0.1372
$c_{B,5}$	-2.8530	-0.2012	-0.3487	-0.3588
$\mu_{0,C}$	0	0	0	0
$c_{C,1}$	0	0	0	0
$c_{C,2}$	0	0	0	0
$c_{C,3}$	0	0	0	0
$c_{C,4}$	0	0	0	0
$c_{C,5}$	0	0	0	0

We have found that the dipole moment function predicted by the hybrid DFT B3LYP method does not vary smoothly with q_1. Thus, DFT does not seem to be adequate for calculating the dipole moments of HOONO. The erratic variations in electric moment is evidence of orbital switching and/or configuration mixing in HOONO, which suggests that a single configuration method is inadequate to describe the wavefunctions of either

conformer of HOONO. While the DFT method has been reported to predict dipole moment functions for molecules like H_2O that can be accurately described by a single configuration,[83] it does not seem to predict accurate dipole moments functions for HOONO, particularly in the hydrogen-bonded *cis-cis* conformer. Kjaergaard, et al. have observed the same inadequacy of DFT in determination of electrostatic moments in systems with hydrogen bonding in the case of the water dimer.[84]

Our *ab initio* calculations predict that *trans-perp* HOONO has a larger permanent dipole moment than *cis-cis* HOONO, and one that points predominantly along the *c*-axis of the molecule. The permanent dipole moment in *cis-cis* HOONO roughly bisects the *a*- and *b*- axes in the plane of the molecule and points towards the terminal O with a slightly larger component along the *b*-axis than the *a*-axis. These principal axes are shown in Figure 3-1. The first derivatives of the dipole moment can be used to estimate the transition strength of the ν_1 fundamental band in the harmonic limit, and compared to transition strengths determined from analytical gradients computed at the equilibrium geometry. For both *trans-perp* and *cis-cis* HOONO, at the MP2/AUG-cc-pVTZ, MP3/AUG-cc-pVDZ, and QCISD/AUG-cc-pVDZ levels of theory, our numerical derivatives give transition strengths that are roughly a factor of two larger than those calculated from single-point analytic derivatives. This discrepancy suggests the degree to which the single point methods diverge from an explicit calculation of the dipole moment function over a larger geometry change.

In the first approach to calculating transition strengths, we treat the OH normal mode as an anharmonic oscillator with a single cubic perturbation term, and obtain

anharmonic wavefunctions by fitting the predicted energy levels (diagonalizing the Hamiltonian to v = 12) to observed ν_1 and $2\nu_1$ band positions (Table 3-3). The fundamental of *trans-perp* HOONO has not yet been observed in the gas phase, so we estimate it to be 3574 cm^{-1} from prior *ab initio* predictions,[60] which are consistent with the observed Ar matrix frequency.[64] The $2\nu_1$ transition moments are then obtained by numerical integration over the fitted dipole moment function and anharmonic initial and final state wavefunctions.

Table 3-3. Observed vibrational bands, and fitted harmonic frequencies and anharmonicities (cm^{-1}) for the stable conformers of HOONO.

	ν_1	$2\nu_1$	ω_e	$\omega_e x_e$
***Cis-cis* HOONO**	3306[a]	6365[b]	3548	121
***Trans-perp* HOONO**	3574[c]	6971[d]	3751	88.5

a. Bean et al.[26]
b. Nizkorodv and Wennberg[31] and this work
c. *Ab initio* frequency, Bean et al,[26] and matrix isolation spectrum, Cheng et al.[64]
d. Pollack et al.[62] and this work

In the second approach, we calculate the overtone transition moments assuming the OH stretch could be modeled as a Morse oscillator fit to $\omega_e x_e$ and ω_e parameters derived from observed ν_1 and $2\nu_1$ band positions for *cis-cis* HOONO, and predicted ν_1 and observed $2\nu_1$ band positions for *trans-perp* HOONO. We use expressions for the Morse oscillator transition matrix elements of first, second, and third order given by Gallas.[85]

To examine the validity of these two methods, we compute the oscillator strengths for both the fundamental and first overtone of nitric acid, for which extensive experimental and computational results are available. We compute the dipole moment function for nitric acid at the MP2/AUG-cc-pVTZ level of theory over the same +0.4 amu^{½} - Å > Δq_1 > - 0.4 amu^{½} - Å range.

For the fundamental ν_1 OH transition in nitric acid, Lange et al.[86] find an oscillator strength of $f_{10} = 1.07 \times 10^{-5}$ ($\tilde{\sigma}_{10} = 9.46 \times 10^{-18}$ cm^2 / molecule - cm), while Chackerian et al.[87] obtain $f_{10} = 1.40 \times 10^{-5}$ ($\tilde{\sigma}_{10} = 1.24 \times 10^{-17}$ cm^2 / molecule - cm). Our anharmonic oscillator method gives $f_{10} = 2.60 \times 10^{-5}$, while the Morse oscillator method gives $f_{10} = 5.06 \times 10^{-5}$. A recent single point *ab initio* prediction[26] of the OH fundamental intensity in the double harmonic approximation yielded $f_{10} = 1.69 \times 10^{-5}$ (90 km/mol).

The oscillator strength of the first overtone band of nitric acid is also known experimentally and has been calculated previously. The experimental oscillator strength is $f_{20} = 3.75 \times 10^{-7}$ ($\tilde{\sigma}_{20} = 3.32 \times 10^{-19}$ cm^2 / molecule - cm), as determined by Lange et al.[86] The oscillator strength calculated by the anharmonic oscillator method presented here is $f_{20} = 2.26 \times 10^{-7}$, while the prediction from the Morse oscillator method is $f_{20} = 4.49 \times 10^{-7}$. Other *ab initio* techniques predicted yet higher oscillator strengths for the first overtone of nitric acid. Donaldson et al.[88] compute $f_{20} = 5.96 \times 10^{-7}$ at the QCISD/6-31+G(d.p) level (unscaled). Rong et al. calculate $f_{20} = 7.11 \times 10^{-7}$ at the QCISD/6-311++G(2d,2p) level using an empirical Deng-Fan potential, and $f_{20} = 6.05 \times 10^{-7}$ using a Morse oscillator approach.[89]

The results of both the anharmonic and Morse oscillator approaches for HOONO are given in Table 3-4. The difference in the anharmonic and Morse oscillator results indicate the accuracy of modeling transitions in the lowest vibrational levels. We note that this simple treatment does well at these low vibrational levels. The relative transition strengths of *cis-cis* to *trans-perp* HOONO $2\nu_1$ bands for both methods and all four levels of theory used are listed in Table 3-5. Ratio of $2\nu_1$ overtone oscillator strength for *trans-perp* vs. *cis-cis* HOONO at each level of theory.. In all cases, the B3LYP method does not give reliable single point dipole moments for HOONO, and the resulting transition dipole matrix elements and oscillator strengths deviate significantly from the MP2 and higher level results. We therefore do not use the B3LYP results to compute transition strengths. Both the anharmonic oscillator and the Morse oscillator method predict a stronger $2\nu_1$ transition for *trans-perp* than for *cis-cis* HOONO, by a factor of 3.7:1 and 3.2:1, respectively, at the QCISD/AUG-cc-pVDZ level. The methods agree reasonably well, with the Morse oscillator method predicting consistently higher transition dipole moments and oscillator strengths.

Table 3-4. Calculated values of the transition dipole moment matrix elements M_i, oscillator strengths f, and rovibrational hybrid band types for the $2\nu_1$ overtone transitions of *trans-perp* and *cis-cis* HOONO. Matrix elements were computed by integrating ab initio dipole moment functions using both anharmonic oscillator and Morse oscillator methods. Units of M_A, M_B, and M_C are Debye; units of $|M_{tot}|^2$ are Debye^2.

***Trans-perp* HOONO**				
	B3LYP AUG-cc-pVTZ	MP2 AUG-cc-pVTZ	MP3 AUG-cc-pVDZ	QCISD AUG-cc-pVDZ
Anharmonic Oscillator				
M_A	-1.07×10^{-2}	-1.08×10^{-2}	-1.00×10^{-2}	-1.02×10^{-2}
M_B	2.72×10^{-3}	1.57×10^{-3}	1.75×10^{-3}	1.68×10^{-3}
M_C	-8.84×10^{-3}	-8.01×10^{-3}	-7.80×10^{-3}	-7.77×10^{-3}
$\|M_{tot}\|^2$	2.01×10^{-4}	1.82×10^{-4}	1.64×10^{-4}	1.67×10^{-4}
F	6.59×10^{-7}	5.98×10^{-7}	5.37×10^{-7}	5.48×10^{-7}
Hybrid band *a*-type to *c*-type ratio	1.5:1	1.8:1	1.7:1	1.8:1
Morse Oscillator Method				
M_A	-1.19×10^{-2}	-1.25×10^{-2}	-1.16×10^{-2}	-1.19×10^{-2}
M_B	3.01×10^{-3}	1.61×10^{-3}	2.02×10^{-3}	1.82×10^{-3}
M_C	-1.04×10^{-2}	-1.04×10^{-2}	-1.02×10^{-2}	-1.02×10^{-2}
$\|M_{tot}\|^2$	2.58×10^{-4}	2.66×10^{-4}	2.44×10^{-4}	2.48×10^{-4}
F	8.46×10^{-7}	8.73×10^{-7}	8.00×10^{-7}	8.14×10^{-7}
Hybrid band *a*-type to *c*-type ratio	1.3:1	1.4:1	1.3:1	1.4:1

Cis-cis HOONO				
	B3LYP AUG-cc-pVTZ	MP2 AUG-cc-pVTZ	MP3 AUG-cc-pVDZ	QCISD AUG-cc-pVDZ
Anharmonic Oscillator				
M_A	-1.48×10^{-2}	-2.79×10^{-3}	-3.04×10^{-3}	-2.99×10^{-3}
M_B	-4.26×10^{-3}	6.78×10^{-3}	6.57×10^{-3}	6.36×10^{-3}
M_C	0	0	0	0
$\|M_{tot}\|^2$	2.36×10^{-4}	5.38×10^{-5}	5.24×10^{-5}	4.93×10^{-5}
F	7.07×10^{-7}	1.61×10^{-7}	1.57×10^{-7}	1.48×10^{-7}
Hybrid band a-type to c-type ratio	0.1:1	5.9:1	4.7:1	4.5:1
Morse Oscillator Method				
M_A	-1.34×10^{-2}	-1.52×10^{-4}	-3.18×10^{-4}	-5.50×10^{-5}
M_B	-6.24×10^{-3}	9.78×10^{-3}	9.47×10^{-3}	9.19×10^{-3}
M_C	0	0	0	0
$\|M_{tot}\|^2$	2.19×10^{-4}	9.56×10^{-5}	8.98×10^{-5}	8.44×10^{-5}
F	6.57×10^{-7}	2.86×10^{-7}	2.69×10^{-7}	2.53×10^{-7}
Hybrid band a-type to c-type ratio	0.2:1	b-type only	b-type only	b-type only

Table 3-5. Ratio of $2\nu_1$ overtone oscillator strength for *trans-perp* vs. *cis-cis* HOONO at each level of theory.

	Oscillator strength ratio (*tp*:*cc* ratio)			
	B3LYP/ AUG-cc-pVTZ	MP2/ AUG-cc-pVTZ	MP3/ AUG-cc-pVDZ	QCISD/ AUG-cc-pVDZ
Anharmonic Oscillator Method	0.9:1	3.7:1	3.4:1	3.7:1
Morse Oscillator Method	1.3:1	3.0:1	3.0:1	3.2:1

The QCISD level anharmonic oscillator calculation predicts that the $2\nu_1$ spectrum of *trans-perp* HOONO should be a hybrid band with a ratio 1.8:1 *a*-type to *c*-type. Figure 3-5a shows that a band contour simulation agrees very well with the experimental spectrum. This ratio also agrees with the approximate experimental ratio of 1:1 adopted by Pollack, et al.[62] for the same transition. In the case of *cis-cis* HOONO, no structure is observed on the $2\nu_1$ band in this experiment, hence, there is no experimental test for the QCISD/AUG-cc-pVDZ calculated hybrid band *b*-type to *a*-type ratio of 4.5 to 1. Bean, et al.[26] find that a range of ratios of *b*-type to *a*-type from 1 to 4 provide an acceptable fit to their cavity ringdown spectrum of ν_1(*cis-cis* HOONO). Our anharmonic method predicts a *b*-type to *a*-type ratio of 2 for the fundamental OH stretch of *cis-cis* HOONO, consistent with the experimental bounds.

3.5.5. Relative populations of cis-cis and trans-perp HOONO

In principle, the initial populations of the two isomers of HOONO can be estimated using the computed oscillator strengths, if we assume that all long-lived peaks in the HOONO spectrum belong to *cis-cis* HOONO and derive their intensity from the $2\nu_1$ transition. At the earliest time in the flow cell at which HOONO can be observed, the ratio of the integrated area of the *cis-cis* conformer bands to that of the *trans-perp* bands is about 5:1 at 233 K. With the relative transition strength of *trans-perp* to *cis-cis* HOONO of 3.7:1 and assuming unit photodissociation quantum yield for both species, this leads to an approximate upper bound on the initial *cis-cis* to *trans-perp* HOONO concentration ratio of 19:1. This supports the assumption that no rise in *cis-cis* HOONO signal should be detectable due to isomerization, since $n_{tp} << n_{cc}$.

This estimate is only an upper bound on the true initial *cis-cis* to *trans-perp* HOONO concentration ratio, because there is a sizeable delay between when reaction occurs and when HOONO concentrations are probed. As seen in Figure 3-7, the shortest residence time is 80 ms, based on the estimated flow velocity and injector/laser-interaction region distance. This residence time is on the same order of magnitude as the observed isomerization lifetimes; thus, a significant fraction of *trans-perp* HOONO will have isomerized prior to the laser measurement. However, our estimate of residence time is qualitative. The injector flow velocity is significantly greater than the velocity of background NO_2/N_2 gas mixture entering the flow cell. Thus, it is possible that the formation of OH and subsequent reaction with NO_2 occurs over a range of distances from

the injector inlet. This does not adversely impact our measured isomerization rates, since the *trans-perp* HOONO lifetime data show completely single exponential behavior.

3.6. Discussion

3.6.1. Kinetics scheme for HOONO formation and isomerization

The experimental results and RRKM simulations reported here confirm the kinetics scheme for formation of HOONO, shown in Figure 3-10, developed by Golden, et al.[9]

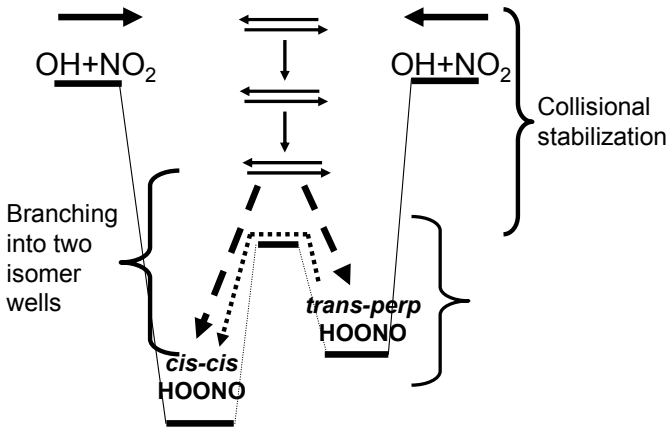

Figure 3-10. Proposed kinetic scheme for OH + NO_2 → HOONO formation. The initially produced HOONO has enough internal energy for a facile isomerization between the *cis-cis* HOONO and *trans-perp* HOONO wells. After a few collisions, the system relaxes into the wells with a comparable yield of both conformers. Slow isomerization from the *trans-perp* HOONO into the *cis-cis* HOONO well then occurs on the millisecond time scale.

Collisional stabilization forms an initially energy-rich HOONO far above the *cis-cis* ↔ *trans-perp* HOONO isomerization barrier (but below the barrier for dissociation back into OH and NO_2). The isomerization rates between the two isomers are substantially faster than the collision rate at 13 hPa; thus the isomers are in microcanonical equilibrium

with relative populations determined by the specific density of states. The two isomers remain in microcanonical equilibrium as they are collisionally relaxed, until the internal energy approaches the barrier height (the two nearly isoenergetic *perp-perp* isomers). Further collisions then relax HOONO below the isomerization barrier, and rapidly form thermalized *cis-cis* and *trans-perp* isomers. This picture is illustrated by our RRKM simulation (Figure 3-9), where we find that if HOONO is placed in either *cis-cis* or *trans-perp* HOONO well at any energy between isomerization and dissociation barriers, the system promptly relaxes below the isomerization barrier into both wells after just a few collisions (at T = 230 K and P = 13 hPa in N_2 buffer).

The initial ratio of the thermalized conformers formed is thus determined by the relative density of states of the two isomers at the *perp-perp* isomer barrier energy, which statistical modeling of the experimentally measured rates predicts to be 40.8 kJ/mol above the *trans-perp* energy. This ratio is predicted to be 2:1 *cis-cis* HOONO to *trans-perp* HOONO using the densities of states from Golden, et al.[9] Thus, the initial population of *trans-perp* HOONO is substantially higher than expected from a Boltzmann distribution (<1%). The high relative abundance of the less stable *trans-perp* isomer arises because the *trans-perp* HOONO density of states rises more rapidly with energy than that of *cis-cis* HOONO. Our own 233 K estimate of this *cis-cis* to *trans-perp* HOONO ratio is 19:1, measured at a distance approximately 80 ms downstream from the discharge inlet in the flow cell. This result confirms that substantial population of *trans-perp* HOONO is formed at temperatures below 233K.

This nonthermal population *trans-perp* HOONO subsequently relaxes to *cis-cis* HOONO by isomerization. Our experiment shows that the HOONO population shifts to the *cis-cis* HOONO well (thermal equilibrium) within 20-100 milliseconds (at 13 hPa), consistent with RRKM modeling.

3.6.2. Spectral assignment of the cis-cis HOONO action spectrum

The room temperature HOONO action spectrum comprises several bands with no resolvable structure. The intensity pattern is also unusual, with the strongest band at 6935 cm^{-1}. Nizkorodov and Wennberg[31] tentatively assigned these bands to three conformers of HOONO: *cis-cis, cis-perp,* and *trans-perp* HOONO. We have found that *all* features in the spectrum observed above 240 K arise from the same conformer. We have also observed that *trans-perp* HOONO cannot give rise to any of these features, since this conformer is observed only transiently at lower temperatures. Finally, recent calculations[9,56] indicate that *cis-perp* HOONO is not a stable isomer.

We therefore propose that these bands be assigned to the $2\nu_1$ overtone and $2\nu_1$–containing combination bands, hot bands, and/or sequence bands of *cis-cis* HOONO. Based on our observations and calculations, we suggest possible new assignments for the *cis-cis* HOONO action spectrum. It must be emphasized that these are tentative assignments.

We assign the first strong peak, at 6365 cm^{-1}, to the origin of the *cis-cis* HOONO overtone ($2\nu_1$). The position, 580 cm^{-1} lower in energy than the $2\nu_1$ origin of nitric acid, is in accord with our expectations for the overtone of the hydrogen-bonded OH stretch in *cis-*

cis HOONO. Bean et al.[26] have observed that the band origin of the fundamental $1\nu_1$ band is red-shifted by ~ 250 cm^{-1} from the free OH stretch of nitric acid. The somewhat larger anharmonic correction, $\omega_e x_e$ = 128 cm^{-1} (Table 3-3), is expected with internal hydrogen-bonding.

This 6365 cm^{-1} band is featureless and appears to be broadened significantly compared to the expected width of the rotational band contour (Figure 3-5b); the other bands in the room temperature spectrum have similar widths. In contrast, the observed band of the *trans-perp* isomer is well fit by the predicted rotational band contour. These observations indicate that the *cis-cis* conformer of HOONO must undergo relatively rapid intramolecular vibrational redistribution (IVR), leading to intrinsic line broadening beyond the width predicted on the basis of the predicted rotational band contour. The rapid IVR may be due to the presence of the intramolecular hydrogen-bond in the *cis-cis* conformer, since hydrogen bonds greatly enhance coupling of the OH stretching vibration to the lower frequency modes.

Computed frequencies provide some guidance in assigning the remaining bands. The highest level theoretical frequencies computed to date are shown in Table 3-1. The four lowest-frequency modes for *cis-cis* HOONO are the two in-plane *a′* modes, the NO stretch (ν_6) and the NOO bend/intermolecular OH···O stretch (ν_7), and the two out-of-plane *a″* modes, the ONOO torsion (ν_8) and the HOON torsion (ν_9). Examination of the normal mode displacements indicates that the two torsional modes are thoroughly mixed.

However, these are harmonic predictions of modes with large amplitude displacements and may have significant uncertainty.

One possible assignment relies on matching the observed band positions to the above *ab initio* frequencies. We then assign $2\nu_1 + \nu_9$ to the 6730 cm^{-1} band, $2\nu_1 + \nu_8$ to the broad 6935 cm^{-1} band, and $2\nu_1 + \nu_6$ to the 7045 cm^{-1} band. Bands at 6180 cm^{-1}, 6505 cm^{-1}, and 6630 cm^{-1}, close to the pure $2\nu_1$ band, would then be assigned as torsional sequence bands of $2\nu_1$.

The difficulty with this assignment is the anomalous intensity pattern of the room temperature *cis-cis* HOONO spectrum. One normally expects the $2\nu_1$ origin to be the strongest band, since the OH stretch is the only expected bright state at this energy. However, the band at 6935 cm^{-1} is ~ 3 times stronger.

The most plausible explanation is that the action spectrum does not reproduce the absorption strengths, because the quantum yield for dissociation is not unity across this wavelength range. Our statistical calculations (Figure 3-9) show that, if the dissociation energy of *cis-cis* HOONO is 83 kJ/mol (6940 cm^{-1}),[50] then the lower frequency bands are suppressed due to non-unity quantum yield. At our assigned origin of the $2\nu_1$ transition frequency, 6365 cm^{-1}, only ≈30% of the *cis-cis* HOONO molecules will dissociate upon photon excitation at room temperature.

However, these calculations also predict that the quantum yield of the origin band will increase significantly (a factor of 2) from 233 K to 298 K, while we observe that all bands in this spectrum scale together over the temperature range 193 – 273 K.

It is possible that a coincidence of two effects leads to this observation. If the higher-energy band(s) around 6935 cm^{-1} are hot bands (v>0) which only have sufficient thermal population of the excited initial state to be observed at higher temperatures, then the intensity of these bands will decrease as the temperature is lowered. The lower-energy bands will decrease with lowering temperature due to the temperature dependence of the quantum yield, and if these two temperature effects coincide, no apparent change in relative band intensity would be observed.

It is also possible that the assumed 83 kJ/mol dissociation energy is too high. Lowering the dissociation energy in the model would simply shift the OH + NO_2 photodissociation yield curve down the frequency axis, and a shift of 5 kJ/mol (indicated by an arrow in Figure 3-9b) would lead to near-unity quantum yield over all bands in the *cis-cis* HOONO spectrum and no temperature dependence of the relative peak intensities. This would give an experimental upper limit on the *cis-cis* HOONO bond dissociation energy of D_0(*cis-cis* HO-ONO) ≤ 78 kJ/mol (6520 cm^{-1}).

If D_0(*cis-cis* HO-ONO) ≤ 78 kJ/mol, the anomalously high intensity of the 6935 cm^{-1} band requires explanation. The intensity of this band may result from strong coupling of the OH stretch with other degrees of freedom, especially the OH torsional mode. The strength of this 6935 cm^{-1} band might be reasonable if it is a superposition of several combination bands of the form $2\nu_1 + n\nu_9$, and the OH – torsion coupling is strong. Multidimensional potential and dipole surfaces, as demonstrated successfully for CH-stretching overtone spectra of methyl rotors,[90] would be required to fully analyze this coupling.

Our experimental evidence is not sufficient to determine the dissociation energy for *cis-cis* HOONO. Direct absorption measurements of *cis-cis* HOONO in the overtone energy regime are currently underway; these measurements would not be subject to quantum yield considerations, and would assist in assigning this spectrum.

3.6.3. Atmospheric implications

Isomerization of *trans-perp* to *cis-cis* HOONO occurs in milliseconds, even at low pressure. As a result, only the *cis-cis* conformer of HOONO will have appreciable concentration in Earth's atmosphere. In addition, the collisional isomerization rate is sufficiently fast that *trans-perp* HOONO will not be present at significant concentrations in gas cell studies near room temperature. For example, Bean et al.[26] have reported cavity ringdown spectroscopy (CRDS) of *cis-cis* HOONO, and determined a branching ratio of reaction 1a and 1b. This branching ratio assumes that all HOONO is present in the *cis-cis* form on the 50-200 ms timescale of the CRDS experiment, since the HOONO yield is determined from the integrated *cis-cis* HOONO band. In CRDS, *trans-perp* HOONO signal would be buried in the extremely strong $HONO_2$ band, and hence difficult to discern. The fast *trans-perp* to *cis-cis* isomerization rates determined here support the assumption made by Bean et al. to derive the HOONO to $HONO_2$ branching ratio.

Our study allows estimation of the *cis-cis* HOONO lifetime in Earth's atmosphere. This lifetime is derived from a calculation similar to that used to predict the HO_2NO_2 near-IR photolysis lifetime.[23] Excitation of $2\nu_1$ and companion bands will be an efficient loss mechanism for HOONO. The average solar radiance at 1.4 μm is 4.90×10^{13} photons cm^{-2}

s^{-1} / cm^{-1}.[91] The predicted oscillator strength of 1.5×10^{-7} gives an integrated band intensity for *cis-cis* HOONO of 1.3×10^{-19} cm^2 molecule cm^{-1}. Assuming unit quantum yield for photodissociation, the resulting photolysis rate of HOONO in the atmosphere due only to IR excitation will be ~6×10^{-6} s^{-1}, leading to an upper limit estimate for the *cis-cis* HOONO lifetime of 1.6×10^5 s (less than 45 daylight hours). Other losses (*e.g.* thermal decomposition, UV photolysis, and reaction with OH) will shorten this lifetime further. For example, using the kinetic parameters from Golden et al.,[49] we predict that HOONO thermal decomposition lifetimes range from a few seconds at the surface to 3×10^6 s (3.5 days) at the tropopause. Thermal decomposition is the dominant removal mechanism in the lower troposphere.

The short lifetime of HOONO suggests that its photochemistry will not be of major importance in Earth's atmosphere. Consider the polar lower stratosphere in summer – a region and time characterized by both fast gas-phase formation of HNO_3 and temperatures that are cold enough to yield a long HOONO thermal lifetime. At 20 km altitude, where [OH] concentrations are ~ 2×10^6 molecules cm^{-3} (1 pptv), the reaction of OH with NO_2 proceeds at a rate of ~1×10^4 molecules cm^{-3} s^{-1}.[92] Assuming a 10% yield of HOONO in this reaction and the maximum HOONO lifetime (1.6×10^5 s), the upper limit for the concentration of HOONO is 1.6×10^8 molecules cm^{-3}, or 80 pptv. This concentration of HOONO may be detectable via remote measurement in the IR or far-IR but we stress this is an upper limit and UV photolysis and reaction with OH will certainly lead to lower abundances. In the troposphere, thermal decomposition will reduce its

concentration further and therefore HOONO is unlikely to influence tropospheric chemistry appreciably. Thus, unless other major sources of HOONO exist, it is unlikely to play a major role in the atmospheric photochemistry.

3.7. Conclusions

We have observed both stable conformers of HOONO, *cis-cis* and *trans-perp,* formed as products in the reaction OH + NO_2 + M in a low pressure discharge flow cell. The two isomers are distinguished by their $2\nu_1$ overtone spectra recorded by action spectroscopy, leading to a new understanding of earlier tentative spectral assignments. The *trans-perp* HOONO $2\nu_1$ band is a sharp feature at 6971 cm^{-1}, observed only at temperatures below 240 K and at a frequency consistent with the spectrum reported by Pollack, et al.[62] We have reassigned all of the bands observed in the room temperature overtone spectrum to *cis-cis* HOONO. We find that under thermal reaction conditions, the *trans-perp* isomer is initially formed at high, non-Boltzmann populations relative to *cis-cis* HOONO; the *trans-perp* HOONO then quickly isomerizes to the more stable *cis-cis* conformer.

We have studied the isomerization of *trans-perp* to *cis-cis* HOONO both experimentally and computationally. From our experimental measurements of the *trans-perp* HOONO decay, we find an isomerization lifetime of 39 ms at 233 K. From the isomerization data over the temperature range 223 – 238 K, we estimate the activation energy for *trans-perp* to *cis-cis* HOONO isomerization to be $E_{act} \sim 33 \pm 12$ kJ/mol, consistent with a strong collision model as shown by statistical modeling. We have performed master equation modeling of the isomerization; we find a barrier height of 40.8

kJ/mol, consistent with experimental data. Finally, we have performed CCSD(T)/cc-pVQZ//CCSD(T)/cc-pVTZ *ab initio* calculations of the *perp-perp* HOONO isomer, the transition state for isomerization. We obtain an activation enthalpy of $\Delta H^{\ddagger 0}_{298} = 41.1$ kJ/mol, in good agreement with both experiment and statistical modeling.

We have calculated the OH + NO_2 photodissociation quantum yield as a function of excitation energy in the near-IR based on the best published *ab initio* and kinetics estimate of D_0(*cis-cis* HOONO) = 83 kJ/mol, and find non-unity quantum yield predicted for some of the observed lower frequency bands of *cis-cis* HOONO. We predict that the quantum yields should be sensitive to temperature, and that the apparent band strengths should change over the temperature range measured; however, we have not observed significant changes in the *cis-cis* HOONO spectrum from 193 – 273 K, suggesting that quantum yield is in fact unity for all bands. It is possible that the relative intensity changes cannot be unambiguously observed with our present signal-to-noise ratios.

We have computed the relative transition strengths of the two isomers, and estimated the abundance of *trans-perp* HOONO relative to *cis-cis* HOONO. Semi-empirical transition strength calculations using QCISD/AUG-cc-pVDZ level *ab initio* dipole moment functions predict that the $2\nu_1$ band of *trans-perp* HOONO absorbs more strongly than the $2\nu_1$ band of *cis-cis* HOONO, with a relative strength of 3.7 calculated using an anharmonic oscillator model and a relative strength of 3.2 calculated using a Morse oscillator model. B3LYP level calculations fail to produce reliable single point calculations of dipole moment functions, while MP2 and MP3 level calculations predict consistent dipole moment functions. Using the calculated relative transition strength of

trans-perp to *cis-cis* HOONO of 3.7 to 1 and assuming unit photodissociation quantum yield for both species, we determine an approximate upper bound on the initial *cis-cis* to *trans-perp* HOONO concentration ratio of 19:1.

The 213 K spectrum of *trans-perp* HOONO can be fit well to the predicted rotational constants, with a hybrid band ratio of 1.8 to 1 *a*-type to *c*-type, consistent with the simulation parameters that fit the Pollack et al.[62] jet-cooled spectrum. We support the assignment by Nizkorodov and Wennberg[31] of the 6365 cm^{-1} band to the origin of the *cis-cis* $2\nu_1$ overtone band. However, this band is broad and featureless, suggesting that *cis-cis* HOONO undergoes much more rapid IVR upon overtone excitation. We cannot make a definitive assignment of the remaining bands observed in the *cis-cis* spectrum.

Based on its calculated $2\nu_1$ transition strength, the more stable *cis-cis* HOONO is predicted to exist in the atmosphere at maximum concentrations of only 1.6×10^8 molecules cm^{-3} (80 pptv), and therefore, will be of limited importance in photochemical processes. For atmospheric chemistry, the most important impact of the formation of the short-lived HOONO reservoir is that radical loss via $OH + NO_2$ is not unity.

CHAPTER 4

THEORY OF *CIS-CIS* HOONO VIBRATIONAL SPECTROSCOPY

This chapter is a brief original description of the work published as:

McCoy, A.B., Fry, J.L., Francisco, J.S., Mollner, A.K., and Okumura, M., "Role of OH-stretch/torsion coupling and quantum yield effects in the first OH overtone spectrum of cis-cis HOONO," Journal of Chemical Physics ***2005,*** *122, 104311.*

This paper is included in its published format as Appendix I.

Chapter 4

4. THEORY OF *CIS-CIS* HOONO VIBRATIONAL SPECTROSCOPY

4.1. Introduction

In Chapter 3, the complex $2\nu_{OH}$ overtone spectrum of *cis-cis* HOONO (Figure 4-1) was introduced and given some speculative assignment, which included the $2\nu_{OH}$ origin band at 6365 cm^{-1} and several "torsional sequence bands." The higher energy bands were tentatively assigned to various combination bands, $2\nu_{OH} + 1\nu_x$, of *cis-cis* HOONO. In this chapter and the attached paper (Appendix I), we show that the physical picture of strong OH-stretch/torsion coupling in the hydrogen-bound ring structure of *cis-cis* HOONO, combined with the nonuniform quantum yield arising from the dissociation energy that falls within the $2\nu_{OH}$ spectrum, does in fact explain almost all features of the *cis-cis* HOONO $2\nu_{OH}$ action spectrum.

Based on this simple OH-stretch/torsion coupling picture, we developed a 2-dimensional *ab initio* model, based upon which the $2\nu_{OH}$ absorption and action spectra of *cis-cis* HOONO are remarkably well predicted. A cavity ringdown direct absorption spectrum of *cis-cis* HOONO in the same $2\nu_{OH}$ region was collected to verify the role of nonuniform quantum yield and to give an additional opportunity for experiment/model comparison.

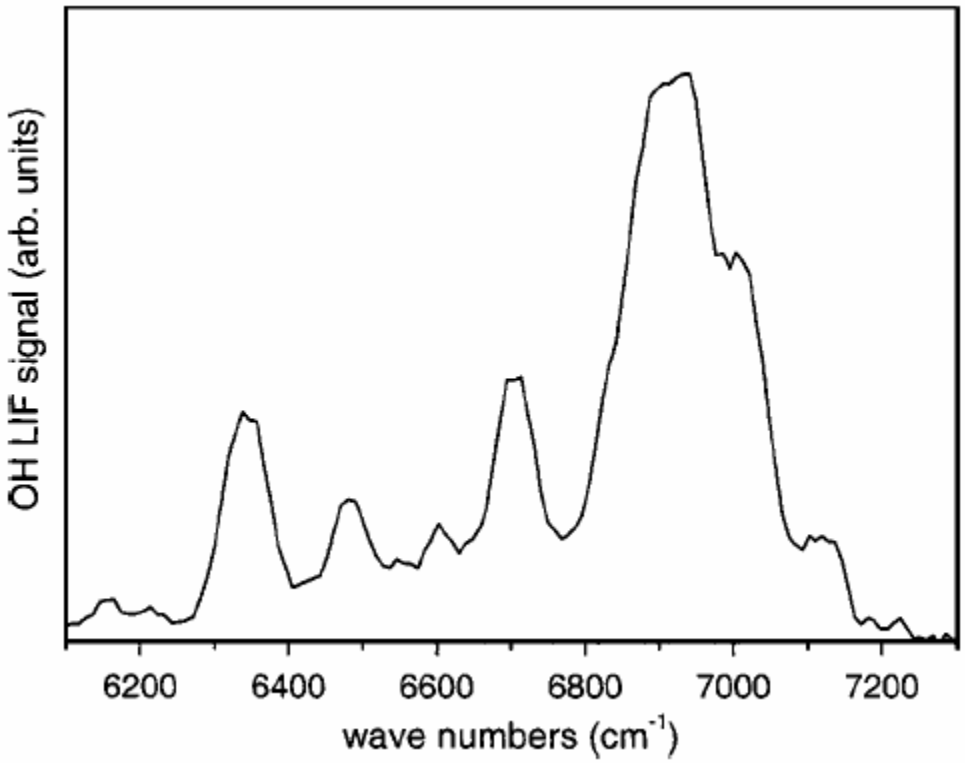

Figure 4-1. Smoothed action spectrum of the $2\nu_{OH}$ band of *cis-cis* HOONO, recorded at room temperature, 10 Torr. Reprinted with permission from McCoy et al.[33] Copyright 2005 American Institute of Physics.

This joint theoretical and experimental investigation was conducted in collaboration with Drs. Anne McCoy (Ohio State University) and Joe Francisco (Purdue University). This fruitful collaboration began after Prof. Mitchio Okumura and I sat with Profs. McCoy and Francisco over an extended lunch at the August 2004 Philadelphia American Chemical Society National Meeting and told them about our physical picture of *cis-cis* HOONO. Prof. Francisco had been working for several months to calculate the torsional potential ($V_{el}(\tau(\text{HOON})$) for *cis-cis* HOONO at CCSD(T)/cc-pVQZ//CCSD(T)/cc-PVTZ, so we built up a 2-D model based on that high-level torsional potential. The primary model

development, realization, and analysis was conducted by Anne McCoy, myself, and Mitchio Okumura. Because the model required a correction for nonuniform quantum yield to match experimental band intensities, we enlisted the cavity ringdown expertise of another Caltech graduate student, Andrew Mollner, who brought his ringdown setup to our spectroscopy lab and worked very hard with me to produce a clean *cis-cis* HOONO direct absorption spectrum for comparison with the model.

The details of the model and experimental verification are given in Appendix I. This chapter briefly outlines the physical picture upon which the model is based, the general computational strategy, selected results, and implications for the HOONO/$HONO_2$ branching ratio.

4.2. Physical picture of *cis-cis* HOONO

The planar equilibrium ring structure of *cis-cis* HOONO (Figure 3-1, p.70) clearly suggests that hydrogen-bonding plays a role in the rich OH vibrational spectroscopy of this molecule. In fact, the fundamental OH stretch band has been observed by cavity ringdown at 3306 cm^{-1};[26] using the expected anharmonicity, this leads to the assignment (made also by Fry, et al.[32]) of the 6365 cm^{-1} band (Figure 4-1) to the *cis-cis* HOONO first overtone, $2\nu_{OH}$. Examining the electronic energy potential and OH stretch frequencies calculated as a function of τ(HOON) (τ(HOON) refers to the HOON dihedral angle, or torsional angle) gives an idea of how the torsional excitation might influence the vibrational spectrum (Figure 4-2).

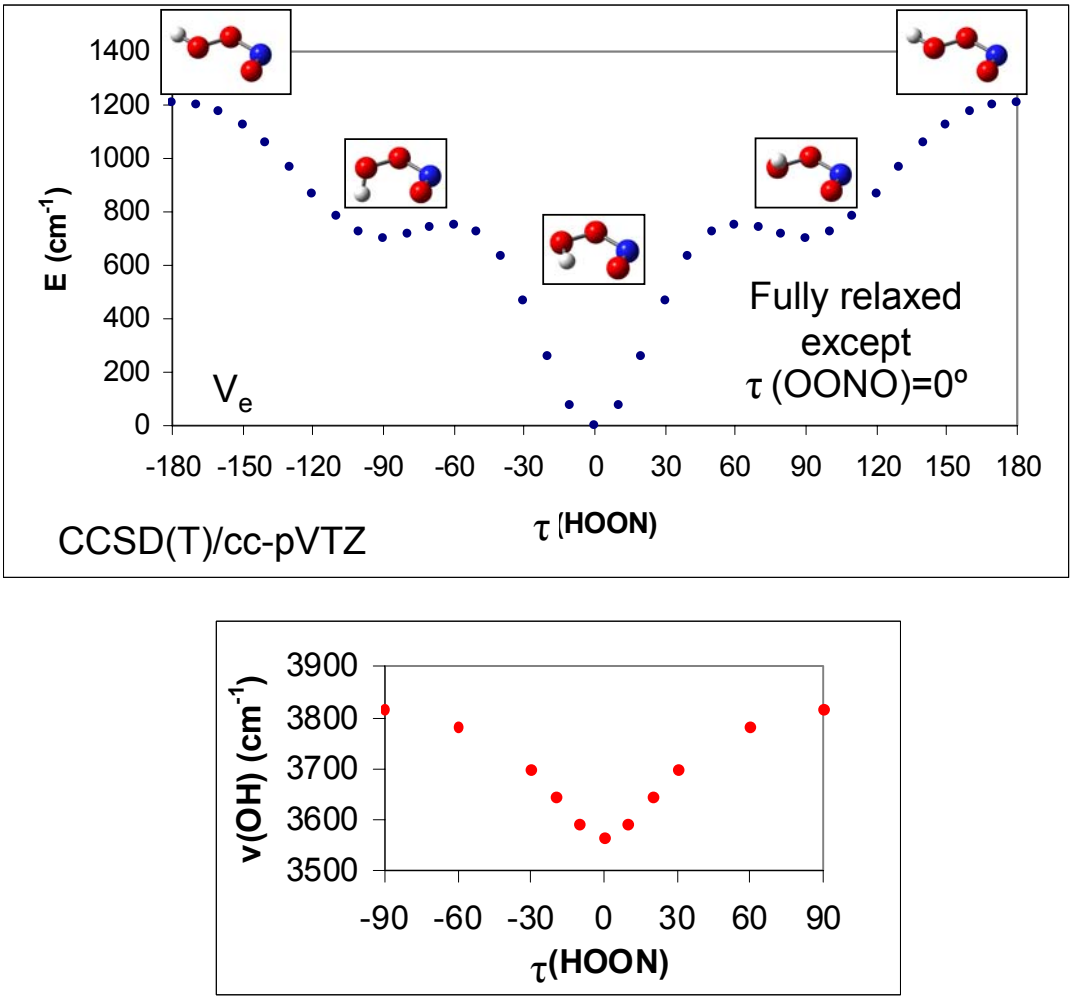

Figure 4-2. Potential and OH stretch frequency as a function of torsional angle (τ(HOON)) showing the coupling of the OH stretch with HOON torsional motion.

The OH stretch frequency is shifted over 200 cm^{-1} from a "free" OH in the *cis-perp* HOONO geometry (τ(HOON) = 90°) to the *cis-cis* HOONO equilibrium structure (τ(HOON) = 0°). This is indicative of very strong coupling between the OH stretch and torsional modes. Based on this, we build up a 2-D model considering only these two modes, which can be used to generate energy levels to simulate the spectrum.

4.3. Computational strategy

4.3.1. Two-dimensional potential and dipole moment surfaces

Building up from the CCSD(T)/cc-pVTZ torsional minimum energy potential , we calculated two-dimensional potential and dipole moment surfaces as functions of *r*(OH) and τ(HOON), with the remaining seven coordinates constrained to their values on the torsional minimum energy potential. A 2-D potential grid of 169 points was generated at the CCSD(T)/AUG-cc-pVTZ level, while the dipole moment surface at the same 169 points was calculated at QCISD/AUG-cc-pVTZ.

Because any *ab initio* calculation is an approximation, scaling factors are often invoked to improve calculated energies. In this case, all points on the potential grid were scaled by a factor based on the ratio of the energy differences between τ and 0° for the cc-pVQZ and cc-pVTZ basis sets:

$$V(r,\tau) = V_{\mathrm{pVTZ}}(r,\tau)\left[\frac{V^{\mathrm{MEP}}_{\mathrm{pVQZ}}(\tau) - V^{\mathrm{MEP}}_{\mathrm{pVQZ}}(0^\circ)}{V^{\mathrm{MEP}}_{\mathrm{pVTZ}}(\tau) - V^{\mathrm{MEP}}_{\mathrm{pVTZ}}(0^\circ)}\right] = V_{\mathrm{pVTZ}}(r,\tau)\sigma(\tau) \qquad (9)$$

This is done because the cc-pVQZ basis set is larger and should better approximate physical reality, but to calculate the entire grid at that higher level is prohibitively computationally expensive. This method allows calculation of the entire potential grid at cc-pVTZ, but extrapolation to the higher level theory. Subsequent discussions of this work with other researchers who have done similar computations[93,94] have lead to the realization that this choice of scaling parameter is somewhat arbitrary. However, the agreement with experiment, while it may be partly due to luck, is encouraging.

From these surfaces, the energies and transition intensities required to simulate the vibrational spectrum were determined using a 2-D discrete variable representation method. This generates frequencies and intensities for an infinite series of $(v',n') \leftarrow (v'',n'')$ transitions. The stick spectra from the $(v' = 2,n') \leftarrow (v'' = 0,n'')$ transitions are used to simulate the experimental $2\nu_{OH}$ spectrum.

4.3.2. Quantum yield

In order to accurately simulate the intensity pattern of the $2\nu_{OH}$ action spectrum, the quantum yield of each transition must also be taken into account. This is done by simply determining the fraction of the *cis-cis* HOONO population at temperature *T* that has enough energy in other modes to be excited above the dissociation threshold with *hv*. For this determination, the dissociation energy used is D_0 = 82.0 kJ/mol = 6860 cm^{-1}, a value estimated by Konen et al.[25] based on measured OH product state distributions for *trans-perp* HOONO photodissociation and the *ab initio* energy difference between *cis-cis* HOONO and *trans-perp* HOONO.

4.4. Predicted *cis-cis* HOONO $2\nu_{OH}$ action spectrum

The predicted $2\nu_{OH}$ spectrum of *cis-cis* HOONO based on this simple two-dimensional model with D_0 the only empirical parameter is shown in Figure 4-3. The stick spectrum underneath represents the output of the model with the quantum yield multiplier, which is convolved with a 70 cm^{-1} FWHM Gaussian to generate the full spectrum. The different quantum yield factors at 300 K and 233 K generate the slightly different intensity patterns in the two spectra.

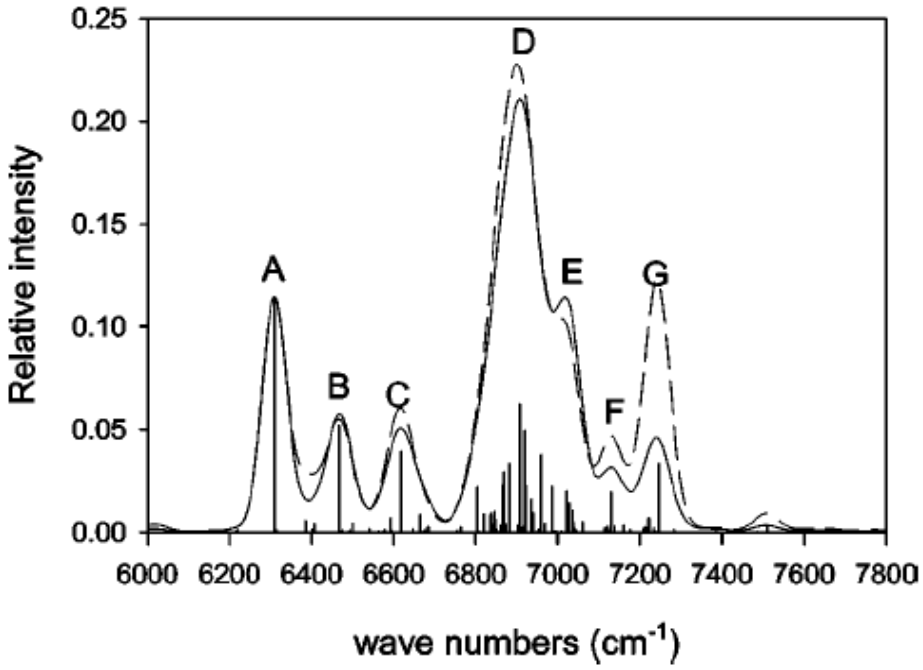

Figure 4-3. Calculated *cis-cis* HOONO $2\nu_{OH}$ action spectrum, at 300K (solid) and 233 K (dashed), from two-dimensional OH-stretch/torsion model with photodissociation quantum yield multiplier based on D_0 = 6860cm^{-1}.

The three lowest energy bands, **A**, **B**, and **C**, are the torsional sequence bands $n = 0 \leftarrow 0$, $n = 1 \leftarrow 1$, and $n = 2 \leftarrow 2$, respectively. The large shifts in the sequence band frequencies are indicative of the strong stretch-torsion coupling which leads to increased energy level spacing of the torsion states in the $v = 2$ manifold relative to $v = 0$. The prominent feature at 6900 cm^{-1} (**D**) is a pileup of multiple transitions, the majority of which are $\Delta n = +1$ lines. These $n'' > 2$ transitions sample the *cis-perp* shelf on the HOONO torsional potential, where the *C* (out-of-plane) component of the dipole moment is maximum. The remaining three bands to the blue, **E**, **F**, and **G**, arise from $\Delta n = +2$ lines.

4.5. Experimental verification with cavity ringdown spectroscopy

To verify that our invocation of quantum yield to explain the intensity pattern of the spectra was founded, we collected a direct absorption spectrum of *cis*-*cis* HOONO for comparison to the model prediction without the quantum yield correction. This spectrum was collected by cavity ringdown spectroscopy. Without the selectivity of the action spectroscopy technique, it is impossible to avoid interfering species. Therefore, our signal-to-noise was severely limited by the subtraction of $HONO_2$ and *cis*-HONO spectra, and we could not collect spectra above 6800 cm^{-1} due to an enormous interference by $HONO_2$. Nevertheless, the obtained direct absorption spectrum is clearly distinct from the experimental action spectrum and matches the model prediction for the absorption spectrum well (Figure 4-4).

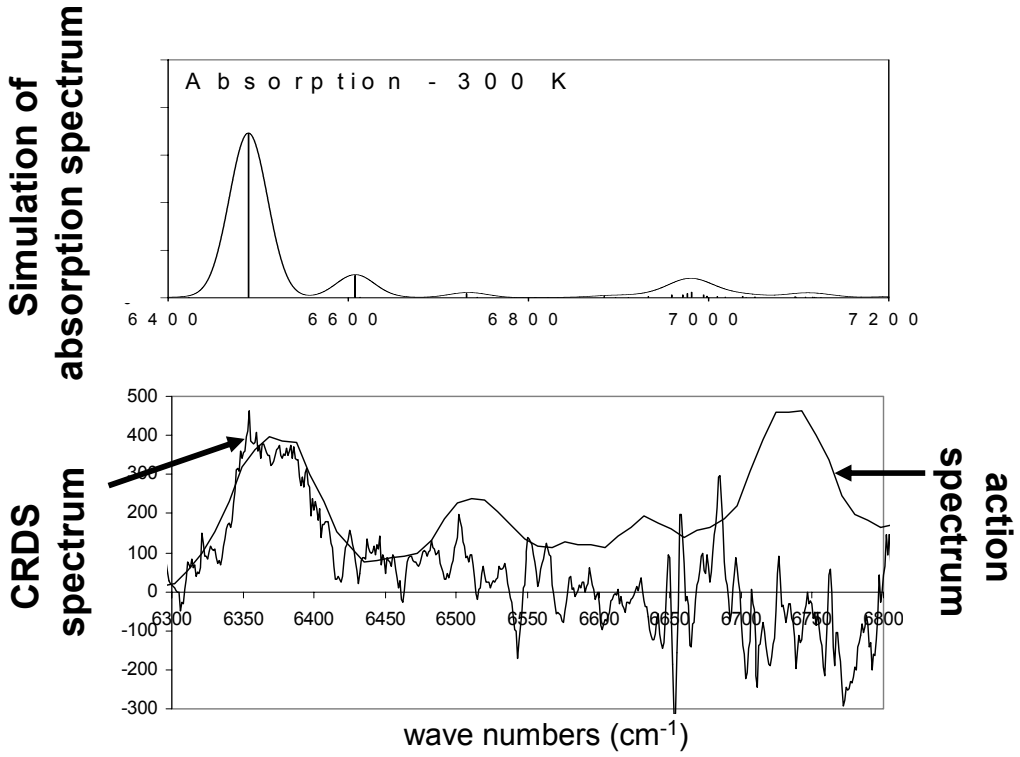

Figure 4-4. Experimental cavity ringdown (direct absorption) spectrum of *cis-cis* HOONO ($HONO_2$ and *cis*-HONO subtracted), shown compared to the smoothed experimental action spectrum (bottom panel) and simulated *cis-cis* HOONO absorption spectrum (top panel).

4.6. Implications for HOONO/$HONO_2$ branching ratio

This new understanding of the vibrational spectroscopy of *cis-cis* HOONO has implications for the laboratory determination of the HOONO/$HONO_2$ branching ratio. As discussed in section 1.2.1, this branching ratio is critical to atmospheric concentrations of HO_x and NO_x radicals. The laboratory determination of this branching ratio is done by the same cavity ringdown technique described in section 4.5, but in the region of the OH stretch fundamental. The integrated *cis-cis* HOONO band (orange) is compared to the

$HONO_2$ band (blue) using the calculated band strengths to determine relative concentrations. The cavity ringdown spectrum of HOONO and $HONO_2$ in the OH stretch fundamental region is shown in Figure 4-5.

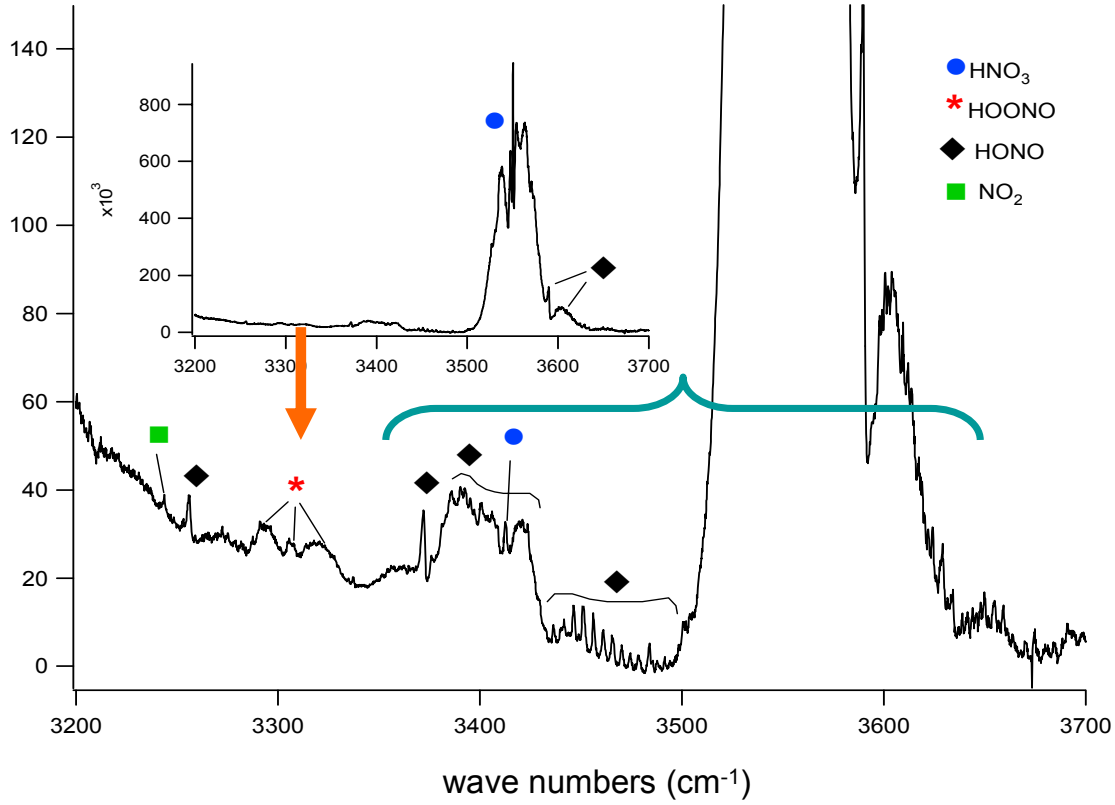

Figure 4-5. Cavity ringdown spectrum of OH + NO_2 products (courtesy Andrew Mollner). The HOONO band measured is indicated in orange, the $HONO_2$ band in blue. The turquoise bracketed region will contain torsionally excited *cis-cis* HOONO bands according to the model described in this chapter.

As shown in chapter 3, only *cis-cis* HOONO needs to be considered in this branching ratio determination because of the timescale of the measurement. However, the new understanding of the *cis-cis* HOONO vibrational spectrum introduced in this chapter

clearly indicates that torsionally excited states are populated at ambient temperatures and contribute to the vibrational spectrum. In the cavity ringdown spectrum shown here, any such torsionally excited bands (turquoise bracketed region) would be swamped by $HONO_2$ signal and hence missed in the calculation of the branching ratio.

Based on the model developed here, the fraction of the *cis-cis* HOONO missed due to absorption features with $n'' \geq 2$ can be determined for the fundamental region. The calculated $1\nu_{OH}$ absorption spectrum is shown in Figure 4-6. This analysis suggests that the branching ratio measurement of 7.5% reported by Bean et al.[26] must underestimate the *cis-cis* HOONO population by about 20%.

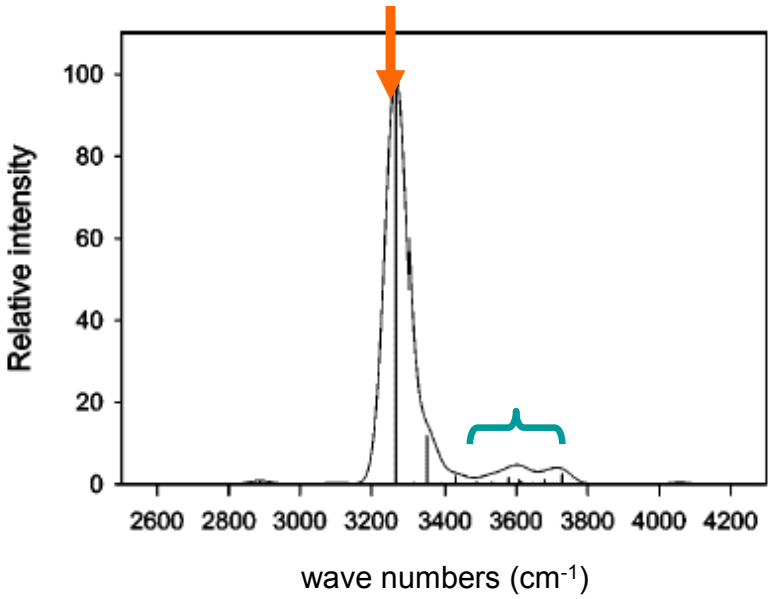

Figure 4-6. Predicted $1\nu_{OH}$ absorption spectrum for *cis-cis* HOONO with origin band observed in the cavity ringdown spectrum indicated in orange and torsionally excited features bracketed in turquoise.

This leads to the tentative conclusion that the HOONO/$HONO_2$ branching ratio should be significantly higher than currently estimated. When coupling to other modes is considered as well, this estimate may increase yet further. A higher HOONO/$HONO_2$ branching ratio means a weaker sink for HO_x and NO_x, since HOONO redissociates thermally to OH and NO_2 relatively quickly (~seconds at 300 K). This in turn would mean that current global models underestimate the concentrations of reactive HO_x and NO_x in the atmosphere.

4.7. Conclusions

A simple two-dimensional OH-stretch/torsion coupling model reproduces the complex experimental *cis-cis* HOONO $2\nu_{OH}$ spectrum remarkably well. The model demonstrates the importance of the *cis-perp* geometry of HOONO, and provides experimental corroboration for the estimated dissociation energy D_0 = 82 kJ/mol = 6860 cm^{-1}. This study suggests that further work accounting for coupling to other modes in *cis-cis* HOONO is required to correctly determine the HOONO/$HONO_2$ branching ratio.

CHAPTER 5

ROTATIONAL SPECTROSOCPY AND DIPOLE MOMENT OF HOONO

This work is in press as:

Fry, J.L., Drouin, B.J., and Miller, C.E., "Rotational spectroscopy and dipole moment of cis-cis HOONO and DOONO," Journal of Chemical Physics ***2005.***

A related earlier paper,

Drouin, B.J., Fry, J.L., and Miller, C.E., "Rotational spectrum of cis-cis HOONO," Journal of Chemical Physics ***2004,*** *120, 5505-5508,*

is included in its published format as Appendix II.

Chapter 5

5. ROTATIONAL SPECTROSCOPY AND DIPOLE MOMENT OF HOONO

5.1. Abstract

The rotational spectrum of *cis-cis* HOONO has been studied over a broad range of frequencies (13 – 840 GHz) using pulsed beam Fourier transform microwave spectroscopy and room temperature flow cell submillimeter spectroscopy. The rotational spectrum of the deuterated isotopomer, *cis-cis* DOONO, has been studied over a subset of this range (84-640 GHz). Improved spectroscopic constants have been determined for HOONO, and the DOONO spectrum is analyzed for the first time. Weak-field Stark effect measurements in the region 84-110 GHz have been employed to determine the molecular dipole moments of *cis-cis* HOONO [μ_a = 0.542(8) D, μ_b = 0.918(15) D, μ = 1.07(2) D] and DOONO [μ_a = 0.517(9) D, μ_b = 0.930(15) D, μ = 1.06(2) D]. The quadrupole coupling tensor in the principal inertial axis system for the ^{14}N nucleus has been determined to be χ_{aa} = 1.4907(25) MHz, χ_{bb} = –4.5990(59) MHz, χ_{ab} = 3.17(147) MHz, and χ_{cc} = 3.1082(59) MHz. Coordinates of the H atom in the center of mass frame have been determined with use of the Kraitchman equations: $|a_H|$ = 0.516 Å and $|b_H|$ = 1.171 Å. The inertial defects of HOONO and DOONO are consistent with a planar equilibrium structure with significant out-of-plane H atom torsional motion. Comparisons of the present results are made to *ab initio* calculations.

5.2. Introduction

The primary loss mechanism for HO_x ($OH + HO_2$) and NO_x ($NO + NO_2$) radicals in the atmosphere is the three-body radical-radical association reaction:

$$OH + NO_2 + M \rightarrow HNO_3 + M \quad \text{(R1)}$$

Knowledge of the rate constant for this reaction is critical to accurate modeling of atmospheric chemistry since catalytic HO_x and NO_x reaction cycles regulate ozone concentrations in the upper troposphere and stratosphere as well as ozone formation and air quality in the lower troposphere. High level *ab initio* calculations have identified *cis-cis* and *trans-perp* peroxynitrous acid as stable minima on the HOONO potential energy surface.[9,26,57,60,95] Experimental measurements of reaction (R1) are thus complicated by the existence of multiple HNO_3 products:

$$OH + NO_2 + M \rightarrow HONO_2 + M \quad \text{(R1a)}$$

$$\rightarrow \textit{cis-cis}\ HOONO + M \quad \text{(R1b)}$$

$$\rightarrow \textit{trans-perp}\ HOONO + M \quad \text{(R1c)}$$

The formation of the stable nitric acid isomer, $D_0(HO\text{-}NO_2) \sim 200$ kJ/mol, via reaction (R1a) sequesters OH and NO_2 radicals in a non-reactive reservoir species. Alternatively, formation of the less stable HOONO isomer, $D_0(HO\text{-}ONO) \sim 80$ kJ/mol, via reactions (R1b) and (R1c) regenerates the OH and NO_2 radicals due to rapid thermal decomposition. In fact, *cis-cis* HOONO measurements provide an effective proxy for the total HOONO yield, (R1b)+(R1c), under atmospheric conditions, since a recent kinetics

study demonstrated that the *trans-perp* conformer isomerizes quickly to the more stable *cis-cis* HOONO (Figure 5-1) at atmospherically relevant temperatures.[32]

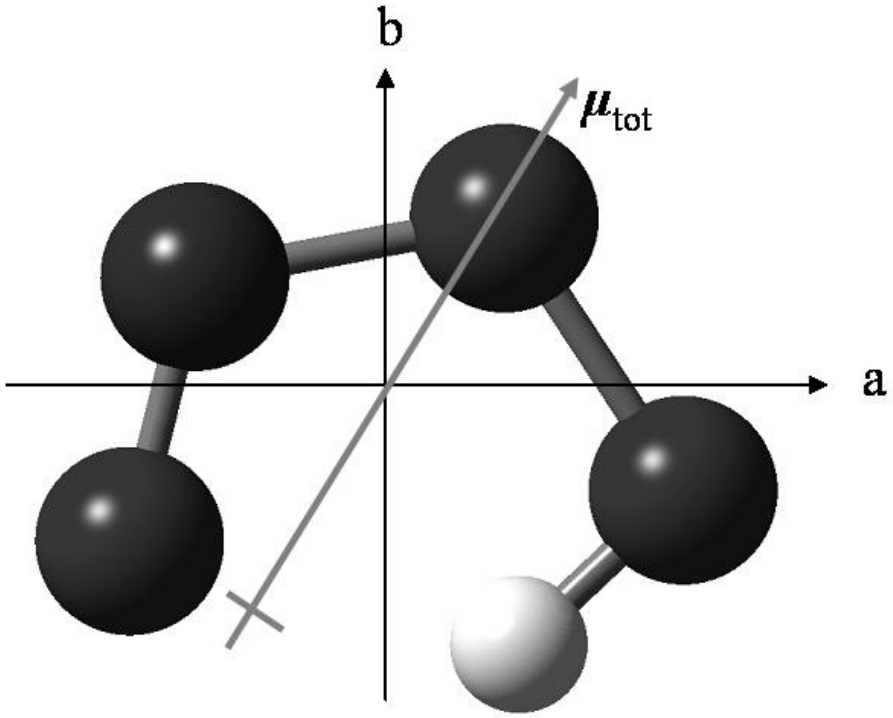

Figure 5-1. Calculated structure of *cis-cis* HOONO in principal axis system. The molecule is planar, with partial H-bonding between the terminal O and H atoms. The total dipole moment vector is shown.

Recent kinetics and spectroscopy experiments have found both direct and indirect evidence for HOONO production in the OH + NO_2 reaction,[26,31,32,54] and the vibrational spectroscopy of HOONO is a subject of continued study.[25,96,97] The current best estimate of the HOONO/$HONO_2$ branching ratio is 0.075 ± 0.020(2σ) at 295 K and 20 Torr.[26] Recent spectroscopic modeling suggests an upward adjustment of this branching ratio by approximately 25%.[33] Ongoing experiments to determine the temperature and pressure

dependence of the branching ratio[98] suggest a larger HOONO/$HONO_2$ branching ratio under atmospheric conditions, consistent with kinetic modeling predictions.[9] All experimental evidence points to a significant rate of HOONO formation in the atmosphere, but it has not been detected in the atmosphere to date.

Our previous work[34] on the pure rotation spectrum of *cis-cis* HOONO provided a potential means for specific atmospheric identification from balloon, aircraft or ground based millimeter and submillimeter spectrometers. An accurate determination of the permanent electric dipole moment is essential to determine the measurement sensitivity required for atmospheric detection or to quantify HOONO concentrations measured in absorption or emission in the laboratory. We have measured Stark shifts of carefully chosen low-J transitions to obtain μ_a, μ_b, and μ_{total}. The results are compared to spectral simulations and *ab initio* calculations for the vibrationally averaged zero point level. Additionally, we report the rotation spectrum and dipole moment of DOONO as well as the substitution coordinates of the hydrogen atom. These center of mass coordinates render the molecular assignment of the spectrum completely unambiguous and allow comparison with *ab initio* structure calculations.

5.3. Experimental methods

The millimeter and submillimeter measurements were carried out at JPL using a 1 m long glass cell in double-pass configuration, with sources and detectors at one end of the cell and a polarization-rotating rooftop reflector at the opposite end (Figure 5-2). The source and detector are mounted at a relative angle of 90º, with a polarized grid at 45º to

pass from the source and reflect to the detector. Specifics of the multipliers and detectors in use on the millimeter and submillimeter spectrometer are given elsewhere.[99] For the Stark effect measurements, two parallel plate electrodes are inserted into the flow cell at an effective separation of d = 2.594(44) cm.

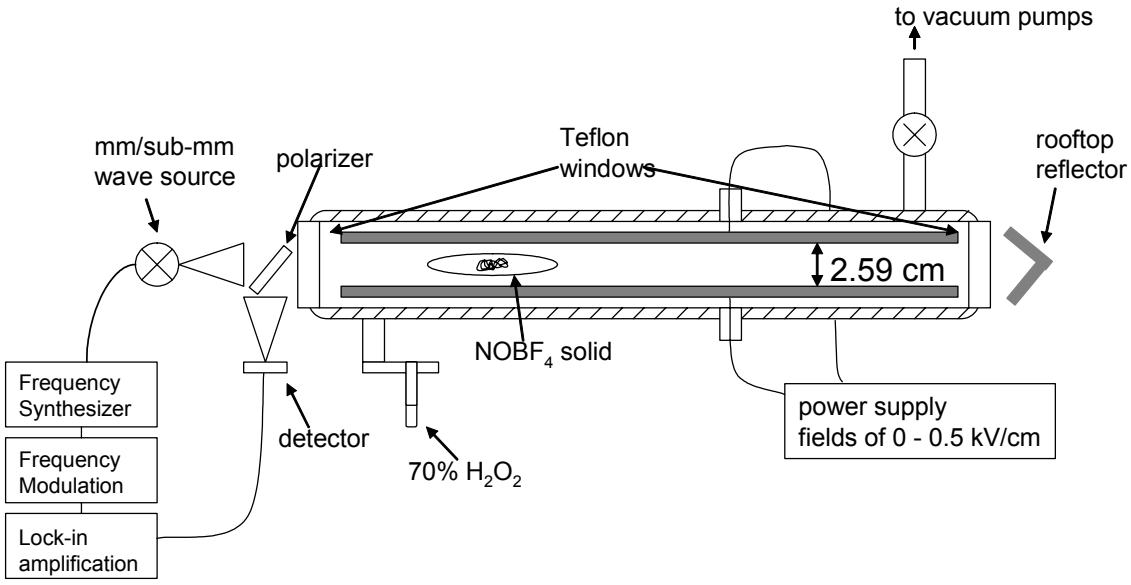

Figure 5-2. Schematic of JPL sub-millimeter experimental apparatus. Microwave radiation makes two passes through the cell with 90º polarization rotation due to the rooftop reflector. Stark plates are at a separation of 2.594(44) cm, and fields of 0 – 1.25 kV are generated across them. $NOBF_4$ solid is placed in boat in the interior of the cell, over which the 70% H_2O_2 flows.

HOONO was generated by reaction of gaseous 70% H_2O_2 in H_2O (FMC Corporation[§]) with solid $NOBF_4$ (Sigma-Aldrich[**]). The $NOBF_4$ solid was placed in a shallow Pyrex boat inside the absorption cell, over which the hydrogen peroxide vapor

[§] FMC Corporation: http://www.fmc.com/.

[**] Sigma-Aldrich Co.: http://www.sigmaaldrich.com/.

flowed from a sidearm port. A slow flow achieved through constriction at the pump port allowed the longest duration of HOONO production. Faster flows reduced the amount of observable byproducts (primarily $HONO_2$, but also HO_2NO_2 and BF_2OH) but increased the frequency of venting the system to refill the boat. D_2O_2 (ICON Isotopes[††]), ~ 50% in D_2O, was substituted for H_2O_2 as the precursor for DOONO. The cell was conditioned with D_2O prior to the DOONO search and discovery. Substantial HOONO was still observable in the deuterated system, perhaps an indication of atmospheric water absorbed in the hygroscopic $NOBF_4$ sample. In all cases the vacuum pump valve was adjusted to optimize the flow rate of H_2O_2 (D_2O_2) for maximum HOONO (DOONO) production.

The low-frequency rotational spectra of HOONO were collected in a supersonic expansion inside the Mark II Flygare-Balle Fourier-transform microwave spectrometer at Caltech.[100] In these experiments the $NOBF_4$ solid is contained behind a wire mesh in a cavity next to the channel of the pulsed valve housing, directly downstream of the poppet. This solid sample holder was designed for the heating of low-volatility solid samples[101] but was used in these experiments at room temperature only. Argon carrier gas is bubbled through a 70% H_2O_2 solution to entrain the reactant H_2O_2 in the gas phase and subsequently pulsed through the sample holder and into the FTMW chamber.

[††] ICON Isotopes: http://www.iconisotopes.com/.

5.4. Results and discussion

5.4.1. Observed spectra and assignment

All spectral fitting and rotational line simulations were performed using Pickett's SPFIT program suite.[102] The DOONO spectrum was predicted by isotopic shifting of the HOONO spectrum. Characteristic spectral signatures were identified within a few hundred MHz of the estimated positions. These transitions were fitted to refine the prediction and the search continued. The transition frequencies were well predicted after 2-3 iterations of this process.

The submillimeter wave rotational spectroscopy of *cis-cis* HOONO has been expanded from the previous assignment of 225 lines in the 179-640 GHz range, fit with a standard deviation of 48.4 kHz,[34] to a current dataset of 480 lines (115 blended lines of 2, 3, or 4 transitions and 174 nonblended lines) in the 13-840 GHz range, fit with a standard deviation of 51.5 kHz. Measured and calculated frequencies and quantum number assignments are found in the JPL millimeter and submillimeter spectral line catalog at http://spec.jpl.nasa.gov/catalog, and the HOONO SPFIT and SPCAT files are included in the online supplemental material.[35] Rotational constants and distortion constants determined from the least-squares fit to this extended data set are shown in Table 5-1.

Cis-cis DOONO scans in the ranges 80-640 GHz resulted in a data set of 246 lines (54 blended lines of 2, 3 or 4 transitions and 103 nonblended lines), up to $J = 42$ and $K_a = 18$ fit, with a standard deviation of 47.5 kHz. Measured and calculated frequencies and quantum number assignments of DOONO are also available in the online supplemental

material in the form of SPCAT and SPFIT files.[35] Spectroscopic constants determined from the least-squares fit to this data set are also shown in Table 5-1.

Table 5-1. Fitted cis-cis HOONO and DOONO Hamiltonian parameters.[a,b]

Parameter	Units	HOONO	DOONO
A	MHz	21406.39252(61)	20245.01569(157)
B	MHz	7948.05526(32)	7913.26701(72)
C	MHz	5791.00077(28)	5685.34813(63)
$-\Delta_J$	kHz	–8.053692(223)	–8.08964(104)
$-\Delta_{JK}$	kHz	16.03416(99)	13.8573(49)
$-\Delta_K$	kHz	–59.98412(32)	–47.067(38)
$-\delta_J$	kHz	–2.472485(77)	–2.529099(257)
$-\delta_K$	kHz	–13.73624(181)	–13.3029(39)
Φ_J	mHz	–14.913(60)	–15.36(44)
Φ_{JJK}	mHz	185.55(50)	165.4(50)
Φ_{JKK}	mHz	–888.16(189)	–729.7(202)
Φ_K	Hz	1.1005(46)	0.729(192)
ϕ_J	mHz	–5.2803(232)	–5.237(142)
ϕ_{JK}	mHz	–53.36(70)	–54.7(36)
ϕ_K	mHz	397.7(43)	298(35)
$1.5\chi_{aa}$	MHz	2.2361(37)	1.498(283)
$¼(\chi_{bb}-\chi_{cc})$	MHz	–1.9268(15)	–1.9163(277)
χ_{ab}	MHz	3.17(147)	3.17[c]
σ_{fit} / # lines	kHz	50.6/480	47.5/246

a. Values in parentheses represent 1σ uncertainties in units of the least significant figure.
b. Transitions below 13-19 GHz have uncertainty 2 kHz, 20-122 GHz have uncertainty 40 kHz,123-640 GHz have uncertainty 50 kHz, 641-847 GHz have uncertainty 70 kHz.
c. Value fixed to that determined for HOONO.

Figure 5-3 shows measured and simulated spectra of HOONO and DOONO near 270 GHz. In the $K_c = 21 – 20$ R-bunch, only the lowest two K_a components are still "bunched," with $K_c = 0,1$ (not shown) collapsed as a degenerate quartet and $K_c = 1,2$ split into quartets with characteristic intensity patterns. Both panels of Figure 5-3 are 20 MHz wide, showing the larger spread of the asymmetry splitting in HOONO. The DOONO quartet is more compact, and a completely separated $HONO_2$ feature is visible within the 20 MHz window. The simulations of each quartet take into account the dipole component measurements, which are different for HOONO and DOONO due to a small principal axes rotation. These dipole components are described in the next section and Figure 5-3 shows the corresponding change in relative intensities of the inner and outer lines in the quartets.

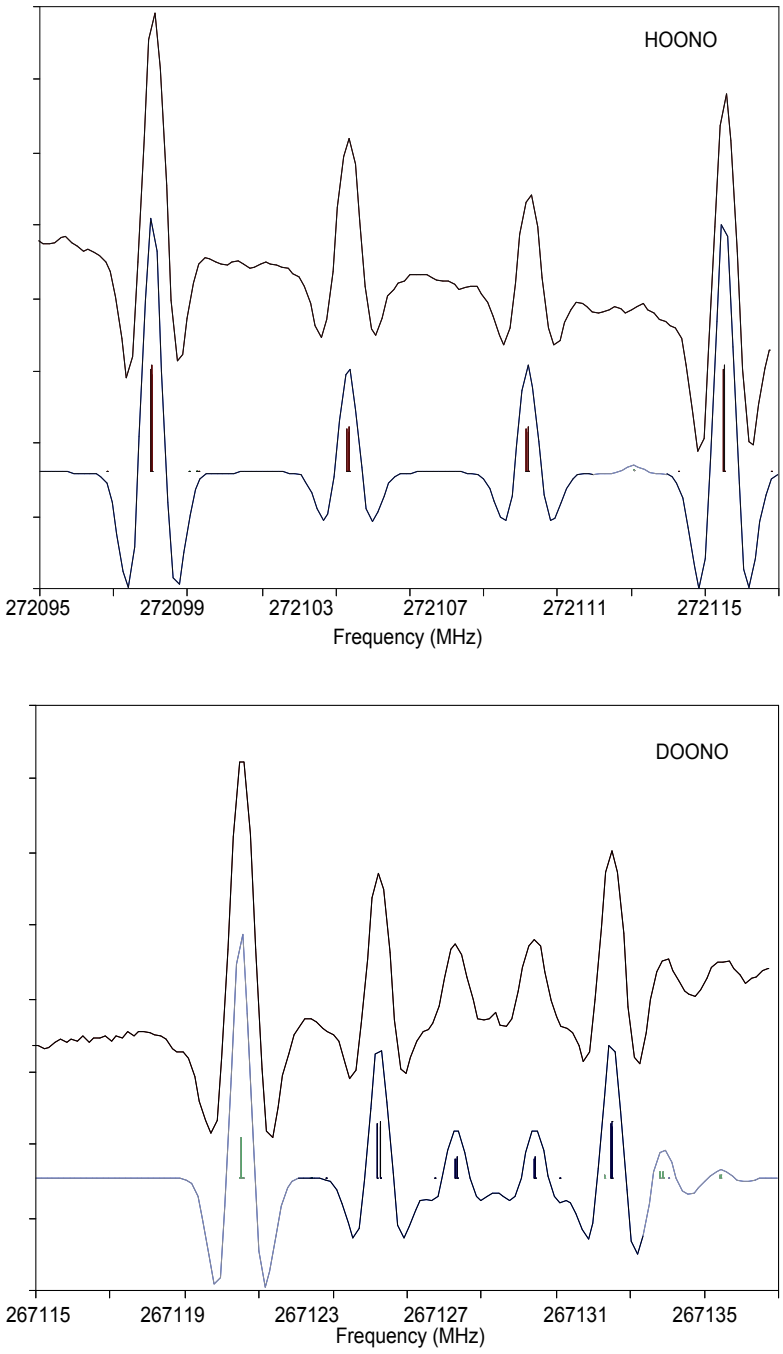

Figure 5-3. The $J = 22 \leftarrow 21$ $K_c = 21 \leftarrow 20$ quartets of HOONO and DOONO. Upper traces are measurement, lower traces are simulations (0.5 MHz FWHM second derivative Gaussian and stick spectra) of predicted HOONO, DOONO (black), and $HONO_2$ (gray) transitions.

5.4.2. Stark effect measurement of dipole moments

The dipole moments of both HOONO and DOONO were determined by examining Stark effect shifts of 10 and 12 rotational transitions, respectively, in the region 84-110 GHz under weak field conditions ($0 \leq V \leq 1.25$ kV). The separation between Stark plates in the spectrometer was found to be $d = 2.594(44)$ cm after calibration (see below). Therefore the maximum applied field strength was $\varepsilon = V/d = 482$ V cm^{-1}.

The weak-field method, described previously by Mueller, et al.,[103,104] measures the second-order Stark shifts of the intensity weighted averages of unresolved M_J Stark components. The shift for an energy level is of the form

$$\Delta E = \varepsilon^2 \left[A + BM_J^2 \right] \tag{10}$$

where A and B are the Stark coefficients and ε is the strength of the electric field. To calculate the shift for a transition, the ΔE for the two levels are subtracted. For a reliable weak field measurement, the combined shifts of the individual Stark components of both the upper and lower levels of each of the M_J substates must be contained within the linewidth of the measurement. This requirement excludes the use of any near-degenerate energy levels that show rapid splitting of the M_J levels due to the first order Stark effect.

The use of a rooftop reflector to rotate the polarization of the millimeter beam radiation by 90º before the second pass of the Stark cell ensured that equal contributions from the $\Delta M_J = 0$ and $\Delta M_J = \pm 1$ components were measured. The intensity weighted average of each transition from each M_J sub-level is a function of the upper and lower state

Stark effect coefficients A', A'', B', and B'' as well as the J' quantum number. This average was calculated for each component, g ($g = a, b$).

$$\frac{\Delta\nu_g}{\varepsilon^2} = (A_g^{'} - A_g^{''}) + (B_g^{'} - B_g^{''})\frac{[8J(J+1)]}{20} \quad for\ \Delta J = 0$$
$$\frac{\Delta\nu_g}{\varepsilon^2} = +[(A_g^{'} - A_g^{''}) + (B_g^{'} - B_g^{''})\frac{J(6J+7)}{20} + B_g^{'}\frac{J+1}{2}] \quad for\ J+1 \leftarrow J \qquad (11)$$
$$\frac{\Delta\nu_g}{\varepsilon^2} = -[(A_g^{'} - A_g^{''}) + (B_g^{'} - B_g^{''})\frac{J(6J+7)}{20} + B_g^{''}\frac{J+1}{2}] \quad for\ J \leftarrow J+1$$

The Stark field strength, ε, was calibrated to account for plate separation as well as inhomogeneity in the overlap of the quasioptical mm-wave beam and the electric field by measuring several Stark shifts for SO_2 (μ = 1.63305(4) D).[105] Stark shifts were measured for 10 SO_2 transitions to yield a corrected plate separation that also inherently calibrated any linear error in the voltage measurement. The transitions were chosen to fall in the same frequency range as those measured for HOONO; this eliminated the need to consider any frequency dependence in the calibration. The calibration factor is d = 2.594(44) cm, yielding measurements with 1.7% accuracy at the 1σ level.

HOONO and DOONO lines were chosen for Stark shift measurements based on predicted signal strength, shifted lineshape, and Stark coefficients. A complete list of the 10 HOONO and 12 DOONO lines used for the Stark analysis is given in Table 5-2, with quantum numbers and zero field frequencies listed for each line. Two different statistical procedures were used to analyze the data to ensure proper treatment of the measurement statistics. Both procedures began with measurements of line center and shifts of the line center as a function of the applied voltage. The zero field line center was measured before

and after measurements with the applied field, and the average frequency was used as the origin for the shift calculation. These before and after zero field measurements differed from each other by less than 15 kHz for each line. In the first statistical method the Stark shifts for each transition were fit as a function of ε^2. Significant deviations from linearity occurred when a transition passed out of the weak field limit. Therefore, measurements for several of the strongest shifts were removed from the analysis to ensure that all data were within the weak field approximation. The largest Stark shifts included in the dipole moment fitting were up to 400 kHz for HOONO and 140 kHz for DOONO. In Method I, the 10 slopes (12 for DOONO) from each regression for each transition were used in a non-linear fit to the dipole moment components:

$$\frac{\Delta\nu}{\varepsilon^2} = C_a \Delta\nu_a + C_b \Delta\nu_b \qquad (12)$$

Fixed values for A', A'', B', and B'' determined with a unitary dipole component (under this condition $C_g = \mu_g$) were used to calculate the $\Delta\nu_g$. The coefficients (C_a and C_b) representing the magnitude of each dipole moment component were then varied to minimize the sum of the squared differences of the measured and calculated slope divided by its uncertainty. The weighted fit was necessary because the measured slopes range over several orders of magnitude. Examples of the individual Stark shift regression measurements are shown in Figure 5-4.

Table 5-2. Complete listing of lines for which Stark effect measurements were conducted.

Stark effect lines measured			
HOONO		**DOONO**	
$J_{Ka,Kc} \leftarrow J_{Ka,Kc}$	Observed Frequency (zero field)	$J_{Ka,Kc} \leftarrow J_{Ka,Kc}$	Observed Frequency (zero field)
$7_{1,7} \leftarrow 6_{0,6}$	89113.199	$7_{1,7} \leftarrow 6_{0,6}$	86985.395
$7_{0,7} \leftarrow 6_{1,6}$	84732.389	$8_{1,7} \leftarrow 7_{1,7}$	96431.690
$8_{0,8} \leftarrow 7_{1,7}$	97226.837	$8_{1,8} \leftarrow 7_{0,7}$	97620.973
$8_{1,8} \leftarrow 7_{0,7}$	99787.057	$8_{0,8} \leftarrow 7_{1,7}$	95784.832
$8_{4,5} \leftarrow 8_{3,6}$	101548.048	$9_{1,9} \leftarrow 8_{1,8}$	107907.758
$8_{4,4} \leftarrow 8_{3,5}$	95377.054	$9_{4,6} \leftarrow 9_{3,7}$	95330.742
$9_{0,9} \leftarrow 8_{1,8}$	109353.886	$9_{4,5} \leftarrow 9_{3,6}$	82232.494
$16_{5,11} \leftarrow 16_{4,12}$	95637.084	$18_{5,13} \leftarrow 18_{4,14}$	83697.383
$18_{5,13} \leftarrow 18_{4,14}$	89262.020	$20_{5,15} \leftarrow 20_{4,16}$	97563.298
$20_{5,15} \leftarrow 20_{4,16}$	95492.054	$21_{6,15} \leftarrow 21_{5,16}$	97547.901
		$22_{6,16} \leftarrow 22_{5,17}$	98866.419
		$23_{6,17} \leftarrow 23_{5,18}$	104287.942

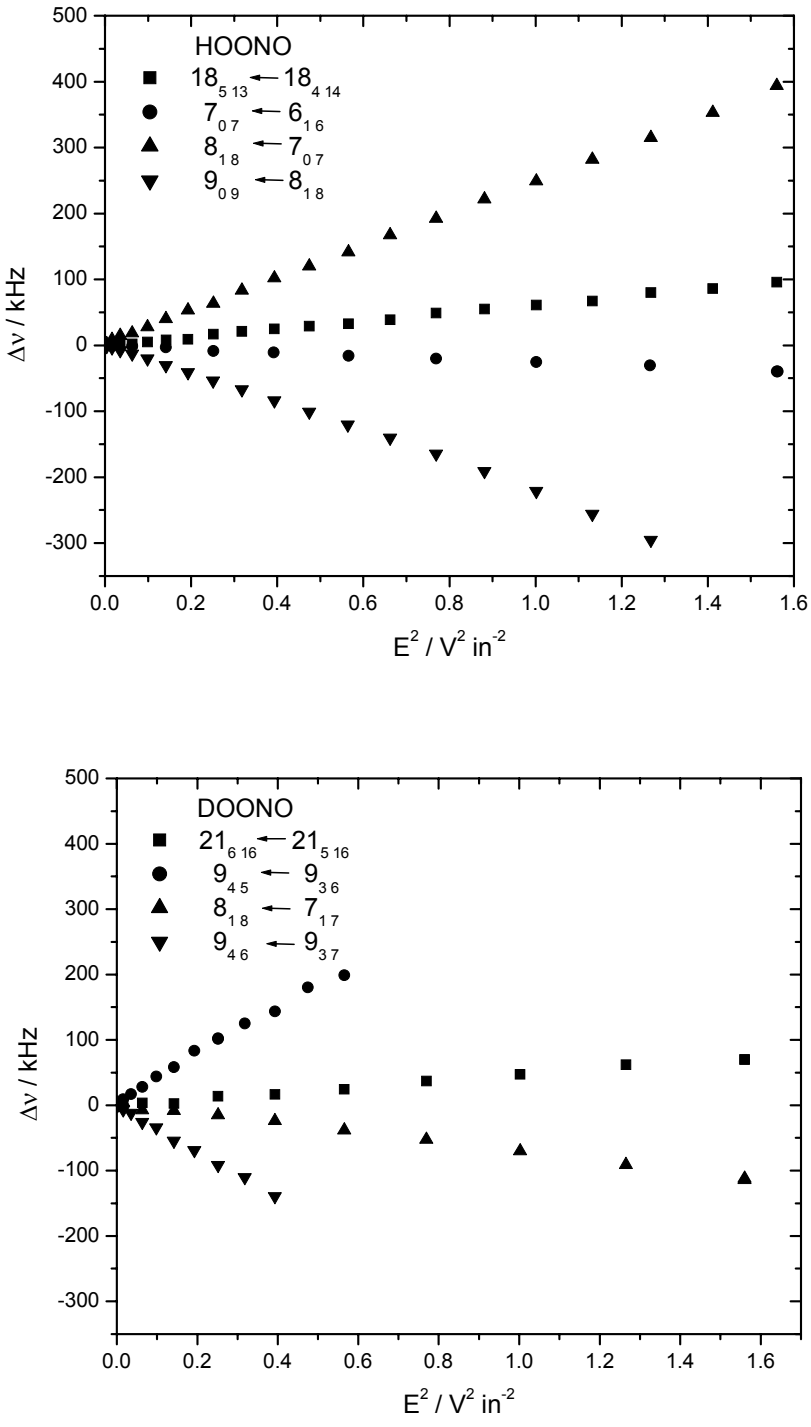

Figure 5-4. Selected Stark effect measurements for *a*-type and *b*-type rotational transitions of HOONO and DOONO.

To check the Method I results, a second independent statistical analysis was performed (Method II) in which all 177 measured HOONO Stark shifts (158 measurements for DOONO) were fit simultaneously to the parameters C_a and C_b using equation 13:

$$\Delta\nu(\varepsilon) = \varepsilon^2 C_a \Delta\nu_a + \varepsilon^2 C_b \Delta\nu_b \tag{13}$$

Both procedures produced precise values for μ_a and μ_b with differences of less than 4% in μ_a and less than 2% in μ_b. Method II weights all transitions only by their inherent center frequency shift and the quality of this measurement, so this method has been chosen as the preferred approach. The resulting dipole moments are shown in Table 5-3. These components are in good agreement (within 3σ) with *ab initio* calculations of the vibrationally averaged components of the dipole moment,[106,‡‡] also shown in Table 5-3.

‡‡ The *ab initio* calculations were performed at the CCSD(T) level with an atomic natural orbital basis set. Vibrationally averaged components of the dipole moment were calculations via the expression:

$$\left\langle \mu^i \right\rangle = \mu_e^i + \sum_k \frac{\partial \mu^i}{\partial q_k}\left\langle q_k \right\rangle + \frac{1}{2}\frac{\partial^2 \mu^i}{\partial q_k^2}\left\langle q_k^2 \right\rangle$$

where the first and second dipole derivatives were calculation *ab initio*, and the expectation values of the normal coordinates were determined using standard second-order perturbation theory. Further details can be found in: X. Zhang, M.R. Nimlos, G.B. Ellison, M.E. Varner, and J.F. Stanton (in preparation), where vibrationally averaged dipole moments of HOONO in the ground and all singly-excited vibrational states are documented.

Table 5-3. Dipole moments (Debye) for cis-cis HOONO and DOONO determined by Stark effect analysis.

	HOONO		**DOONO**	
	Experiment	***ab initio***[b]	**Experiment**	***ab initio***[b]
μ_a	0.542(8)	0.531	0.517(9)	0.520
μ_b	0.918(15)	0.869	0.930(15)	0.874
μ_{total}	1.07(2)	1.018	1.06(2)	1.016
N_{lines}	10		12	

a. Values in parenthesis are 1σ accuracy in the last significant figure derived from the calibration.
b. *Ab initio* dipole moment components are from the vibrationally averaged CCSD(T)/ANO calculations by Stanton et al.[106,*]

The direction of the electric dipole moment in HOONO can be determined unambiguously from a comparison of the differences in the axis rotation that is apparent from the μ_a and μ_b components of the dipole moment for HOONO and DOONO. When the principal axes are defined to place the nitrogen atom in the (–*a*,+*b*) quadrant and hydrogen in the (+*a*,-*b*) quadrant (as in Figure 5-1), the negative pole of the dipole vector is oriented towards the (+*a*,+*b*) quadrant. This orientation is expected since the H-O bond has the largest electronegativity differential in the molecule, and this bond is roughly parallel to the total dipole moment vector (see Figure 5-1). The 1.7% uncertainty (1σ) in the calibration factor *d* dominates the overall accuracy of the dipole moment determination.

5.4.3. Position of H atom in principal axis frame

The rotational constants for HOONO and DOONO reported in Table 5-1 have been converted into moments of inertia, shown in Table 5-4. The moments of inertia have also

been used to determine the substitution coordinates of the hydrogen atom in the principal axis center of mass frame of the molecule using the well-known Kraitchman equations.[107,108] The experimentally determined center of mass H atom coordinates are reported in Table 5-5.

Table 5-4. Cis-cis HOONO and DOONO moments of inertia and inertial defects.[a,b]

	HOONO	**DOONO**
I_{aa} (amu Å^2)	23.6087918(7)	24.963135(2)
I_{bb} (amu Å^2)	63.585248(3)	63.864781(6)
I_{cc} (amu Å^2)	87.269728(4)	88.891489(10)
Δ (amu Å^2)	0.075688865(5)	0.063573434(10)

a. Values in parenthesis are 1σ uncertainties based on the fitted parameters.
b. Correlations among the parameters are minimal and were ignored.

Table 5-5. Comparison of HOONO experimental and *ab initio* H atom coordinates.

	|a|	**|b|**	**|c|**
MP2/6-311G(d,p)[57]	0.637	1.269	0.000
CCSD/6-311++G(d.p)[59]	0.597	1.183	0.000
CCSD(T)/cc-pVTZ[32]	0.590	1.161	0.000
CCSD(T)/ANO[106]	0.535	1.159	0.000
Experiment	0.516	1.171	0.081

The structural parameters calculated in this way represent a ground-state effective structure (r_s), which includes any vibrational effects in the ground state moments of inertia used to determine the structural parameters. This is evidenced by the nonzero out-of plane RMS (root-mean-squared) displacement of the H atom position. In spite of the planarity of

cis-cis HOONO in the r_e structure, zero-point torsional motion results in a nonzero RMS displacement of the H atom out of plane.

This experimental H atom position is compared to the *ab initio* calculated H atom position from several calculations in Table 5-5. The ground state structure of *cis-cis* HOONO was first calculated by McGrath and Rowland at MP2/6-311G(d,p),[57] and later by Tsai et al. at CCSD/6-311++G(d,p),[59] by Fry et al. at CCSD(T)/cc-pVTZ,[32] and by Stanton at CCSD(T)/ANO.[106] This comparison supports the conclusion that high-level CCSD(T) calculations accurately predict the structural parameters of HOONO.

5.4.4. Inertial defect

The out-of-plane RMS displacement of each atom results in a nonzero inertial defect, shown for HOONO and DOONO in Table 5-4. In HOONO, the positive inertial defect decreases upon deuteration. In a number of planar species (H_2O, H_2S, H_2Se and H_2CO) deuterium substitution *increases* the (nominally positive) inertial defect due to dominance of in-plane vibrational motions.[107,108] However, the inertial defect is a balance of in-plane (typically positive) and out-of-plane (typically negative) contributions. The inertial defect for HOONO is smaller than that for $HONO_2$,[109] indicating more contribution in HOONO from all out-of-plane motions. Riveros and Cox[109] measured inertial defects for a series of nitric acid isotopomers and found the largest change in inertial defect (–0.0089 amu-Å^2) with deuterium substitution. This decrease in inertial defect for $HONO_2$ to $DONO_2$ indicates dominance of H atom out-of-plane motion relative to other atoms. The same phenomenon applies in HOONO to DOONO, i.e., the large decrease in inertial defect

for deuterium substitution (–0.0121 amu-Å^2) is consistent with larger amplitude out-of-plane motion of hydrogen than in $HONO_2$.

Calculations of the inertial defects from the *ab initio* force field[106,110] (Δ(HOONO) = 0.0954, Δ(DOONO) = 0.0840 amu-Å^2) show similar decrease with deuterium substitution (0.01141 amu-Å^2) to that observed experimentally. The positive calculated inertial defect indicates the overall dominance of harmonic force field contributions (in-plane), while the change in inertial defect upon deuterium substitution is due mainly to the Coriolis (out-of-plane) components.

5.4.5. Nuclear quadrupole coupling constants

The $I = 1$ spin of the ^{14}N nucleus allowed us to measure nuclear quadrupole splitting on selected transitions. Many of the millimeter wavelength transitions of both HOONO and DOONO with $J < 25$ show characteristic quadrupole splitting patterns. The splittings in Q-branch transitions are resolved enough to determine $\chi_{bb}-\chi_{cc}$ with four significant figures. Furthermore, the high precision measurements attained in the Flygare-Balle Fourier-transform microwave spectrometer helped improve the precision of the nuclear quadrupole coupling parameter, χ_{aa}, for HOONO.

HOONO has C_s symmetry in its ground vibrational state, with the average position of each atom lying in the *ab* plane, leading by symmetry to $\chi_{bc} = \chi_{ac} = 0$, but $\chi_{ab} \neq 0$. In general, the weak coupling of ^{14}N nuclear spin to the rotation of the molecule precludes determination of the full nuclear spin-rotation coupling tensor. However, for *cis-cis* HOONO the 4_{14} and 3_{22} energy levels are accidentally nearly degenerate, and the off-

diagonal quadrupole coupling allows perturbations among the $F = 2,3$ components. A single measured spectral feature, the $3_{22} \leftarrow 2_{11}$ transition in the millimeter range, samples this perturbation and has been used to determine χ_{ab}. Fits which include the χ_{ab} term but do not include the $3_{22} \leftarrow 2_{11}$ transition experience a divergence of the fit until a completely undetermined χ_{ab} value is obtained. The precision of the splitting in this transition dominates the uncertainty in the determination of the principal quadrupole tensor and the determination of the offset angle $|\theta| = 23(+5,-8)$ between the principal inertial axes system and the principal quadrupole axes system. Due to the planar symmetry of this species, this angle necessarily lies in the *ab* plane; however, its sign is not unambiguous without isotopic information.

5.5. Conclusions

This work extends our previous analysis of the rotational spectrum of *cis-cis* HOONO. Rotational spectra for HOONO have been measured over frequencies that include nearly the entire range of thermally populated energy levels. The μ_a and μ_b components of the dipole moment have been determined to an accuracy of 3% using a weak field Stark shift analysis. Low frequency, low-*J* measurements have allowed determination of hyperfine splittings in the rotational spectra due to ^{14}N nuclear quadrupole coupling. These new data enable the search for *cis-cis* HOONO via atmospheric remote sensing.

Additionally, the use of deuterated reactants has enabled us to identify and analyze the rotational spectrum of DOONO for the first time. These measurements, combined with

our HOONO analyses, provide the precise determination of the hydrogen atom coordinates in the principle axis system. A comparison of HOONO and DOONO dipole moments yields the unambiguous determination of the dipole moment vector. Comparisons between experimental and *ab initio* dipole moments and H atom position in the principal axis frame agree well, indicating that high-level theory accurately characterizes *cis-cis* HOONO. Analysis of the inertial defect for HOONO and DOONO is consistent with a planar equilibrium structure with significant out-of-plane H atom torsional motion.

CHAPTER 6

VIBRATIONAL OVERTONE INITIATED PHOTODISSOCIATION OF PEROXYACETYL NITRATE (PAN)

This chapter is original and includes discussion of the work published as:

Nizkorodov, S.A., Crounse, J.D., Fry, J.L., Roehl, C.M., and Wennberg, P.O., "Near-IR photodissociation of peroxy acetyl nitrate," Atmospheric Chemistry and Physics ***2005,*** *5, 385-392.*

This paper is included in its published format as Appendix III.

Chapter 6

6. VIBRATIONAL OVERTONE INITIATED PHOTODISSOCIATION OF PEROXYACETYL NITRATE (PAN)

6.1. Introduction

6.1.1. Large-scale atmospheric transport of NO_x

A very important class of molecules in atmospheric chemistry consists of the oxides of nitrogen, $NO_x = NO + NO_2$. NO_x emissions in urban areas are a major component of photochemical smog, and NO_x limits the production of ground-level ozone. The efficiency of the $OH + NO_2$ reaction also means that NO_2 plays a determining role in the concentration of OH in the troposphere. In the stratosphere, ozone loss is catalyzed by the NO_x cycle:[1]

$$NO + O_3 \rightarrow NO_2 + O_2 \qquad \text{(R11)}$$

$$NO_2 + O \rightarrow NO + O_2 \qquad \text{(R12)}$$

While the most important chemistry involves the radicals NO and NO_2, oxidized nitrogen exists in many other forms in the atmosphere as reservoir species for NO and NO_2. NO_x and its atmospheric oxidation products are grouped together as reactive nitrogen, NO_y. The most abundant NO_y compounds are NO_2, peroxyacetyl nitrate (PAN), nitric acid, and particulate nitrate (NO_3^-).[111] The partitioning among NO_y species determines reactivity, and it varies significantly spatially. The transport of reservoir NO_y species provides sources of NO_x to otherwise unpolluted parts of the atmosphere. For example, the episodic

lifting of Asian pollution outflow into the lower free troposphere (2-5 km) and subsequent westerly propagation ahead of cold fronts is the principal source of pollutants over the western Pacific.[112] Recent studies have indicated a significant increase the concentration of NO_y in the boundary layer (0-2 km) over the last 7 years.[113] An investigation of the photochemistry of NO_y is critical to the understanding of NO_y partitioning and lifetimes.

In the visible and near IR regions of the solar spectrum, Earth's atmosphere is largely transparent. Thus, weakly bound reservoir species with low-lying dissociative states may have lifetimes limited by photolysis. We have an experimental apparatus designed to investigate these near-IR photolysis processes. We have recently completed a study of the molecule HOONO, a weakly-bound ($D_0 \sim 80$ kJ/mol) isomer of nitric acid. Using action spectroscopy combined with a temperature-controlled kinetics flow tube, we were able to distinguish multiple conformers of the HOONO molecule for the first time and observe the isomerization kinetics.[32]

The target molecule described in this chapter is another NO_x reservoir species, peroxyacetyl nitrate (PAN), $CH_3C(O)OONO_2$. PAN has been identified as one of the most abundant reactive nitrogen (NO_y) species. Its concentration exceeds that of HNO_3 in parts of the troposphere, and it plays a major role in the transport of NO_x to unpolluted areas.[114] Since its identification in polluted air in Los Angeles in the 1950s,[115] PAN has been the subject of many field and experimental studies to elucidate its atmospheric importance. Field studies have focused on partitioning of reactive nitrogen (NO_y), where PAN has been found to be the most abundant NO_y species during summer and spring.[116] In theoretical and laboratory work, the weak O-O and N-O bonds in PAN have been shown to lead to a

short thermal lifetime at ambient temperatures and pressures in addition to ultraviolet photolytic and chemical losses (reaction with OH).[47,117]

PAN is formed via three-body recombination in the atmosphere in urban areas where both hydrocarbon and NO_x concentrations are high, by the reaction:

$$CH_3C(O)OO + NO_2 + M \rightarrow CH_3C(O)OONO_2 + M \qquad \text{(R13)}$$

At ground level, with warmer temperatures and higher pressures, thermal decomposition is the major loss of PAN. However, as PAN is convectively transported into the upper troposphere, its lifetime increases and photolysis becomes the major loss process.[47] The UV photolysis of PAN is well-constrained, and the relatively long lifetime of PAN with respect to this sink has lead to the assumption that PAN is essentially inert in the upper troposphere. If, however, photolysis in other spectral regions occurs, PAN may well be a significant source of NO_x in the upper troposphere. The importance of this source of NO_x will be even more dramatic in the high latitudes, where large slant ozone columns result in very little UV photolysis. This photolytic decomposition of PAN in the near – IR is the focus of the experiments described here.

In the case of HOONO, we were able to couple energy into the molecule via the 1st overtone of the OH stretch, a relatively strong absorber. In PAN, we hope to couple energy into the molecule via the overtone of the CH stretch. This absorption is expected to be weaker than the corresponding OH overtone by approximately a factor of 5.[118] The 2nd CH overtone is expected to fall near 8600 cm^{-1}, where dissociation might reasonably occur, since D_0 for PAN is 9500 – 9900 cm^{-1} [27,28] and the molecules will have some internal

energy. In spite of the similar bond energies of the O-O and N-O bonds, it has been determined that O-O bond fissure involves a significant barrier, and thus all photolysis will result in $CH_3C(O)OO$ and NO_2 products.[28]

In the presence of sufficient NO and O_2, it is anticipated that the $CH_3C(O)OO$ fragment will promptly yield OH via the following fast reactions:

$$CH_3C(O)OO + NO \rightarrow CH_3 + CO_2 + NO_2 \quad \text{(R14)}$$

$$CH_3 + O_2 \rightarrow CH_3OO \quad \text{(R15)}$$

$$CH_3OO + NO \rightarrow CH_3O + NO_2 \quad \text{(R16)}$$

$$CH_3O + O_2 \rightarrow CH_2O + HO_2 \quad \text{(R17)}$$

$$HO_2 + NO \rightarrow \mathbf{OH} + NO_2 \quad \text{(R18)}$$

Since we can detect very low concentrations of OH with our LIF detection scheme, this mode of detection is preferred. However, preliminary studies in our laboratory have indicated that OH formation after photolysis may not occur as predicted by this mechanism. For this reason, we also employ a second detection scheme in which we couple our photolysis / flow tube system with a chemical ionization mass spectrometer (CIMS) for detection of peroxy radicals. Our laboratory owns a CIMS spectrometer, used primarily for field studies. Detection of the $CH_3C(O)OO$ radical has been demonstrated with our CIMS.[119] With this detection technique we can determine the amounts of immediate photolysis product and even investigate the subsequent chemical mechanism by adding NO and O_2.

By comparison of the $CH_3C(O)OO$ product yield from near-IR photolysis and UV photolysis, where cross-sections are known, we can estimate absolute quantum yields of the $CH_3C(O)OONO_2 + M \rightarrow CH_3C(O)OO + NO_2 + M$ step. We will also be able to test energy transfer within the molecule. The CH stretches are predicted to be nondegenerate and hence would be spectrally resolved by our action spectroscopic technique. By comparing product quantum yield when exciting on the various CH modes, we can test theories about heterogeneity in absorption cross-section influencing coupling of vibrational energy into the PAN molecule.

6.2. Experimental methods

6.2.1. Action spectroscopy and chemical ionization mass spectrometry

We investigate the spectroscopy and kinetics of weakly-bound species using action spectroscopy. In this method infrared radiation coupled vibrationally into the molecule causes dissociation. In recent experiments, the excitation is the first overtone of the OH stretch vibration in the HOONO molecule ($2\nu_1$), and the detection of the OH fragment is via Laser Induced Fluorescence (LIF). HOONO action spectra obtained in this way are shown in Figure 3-3 and Figure 4-1.

In the proposed PAN experiments we attempt to observe OH formation after PAN photodissociation via reactions R14 – R18. In addition, we replace the LIF detection with another very sensitive technique: chemical ionization mass spectrometry (CIMS). This technique combines molecular selectivity with very high sensitivity; the more stable

species in the flow tube mixture will not dissociate at these near-IR energies, and the CIMS method is sensitive to as few as 10^{10} molecules/cm^3 with one second integration time.

The experimental arrangement for this spectroscopic technique consists of an OPO to produce the pump pulses (IR or UV, depending on which wavelength mixing scheme is used), a flow tube, and chamber with background pressure of ~ 0.1 Torr. Gases are mixed in a 50 cm long jacketed glass flow cell of 25 mm internal diameter. The flow tube has a movable injector port along the interior and is coated with Teflon to minimize the occurrence of heterogeneous chemistry on the walls. PAN is introduced to the flow cell by bubbling N_2 through liquid PAN solution. A schematic of this experiment is shown in Figure 6-1, with both LIF and CIMS detection shown.

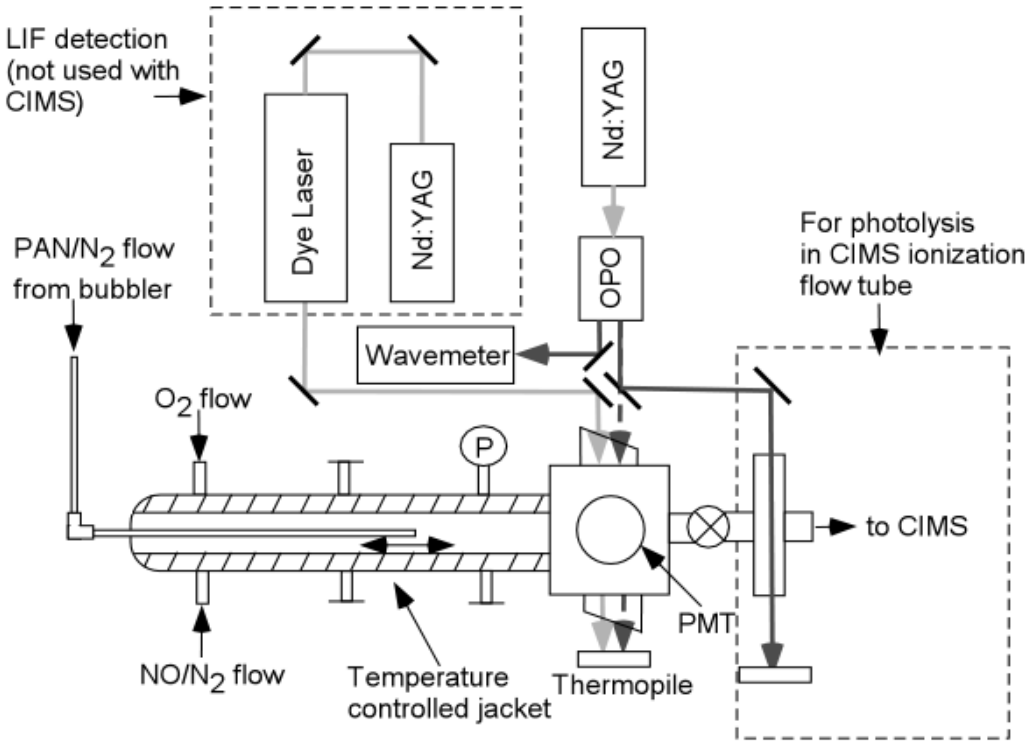

Figure 6-1. Schematic of alternate action spectroscopy and chemical ionization mass spectrometry detection for PAN.

The tunable near-IR is generated in a type-II BBO optical parametric oscillator (OPO) pumped by the 355 nm third harmonic of a pulsed Nd:YAG laser (Coherent Infinity 40-100, 3 cm^{-1} bandwidth). This OPO[39] outputs 2-3 mJ/pulse in the idler beam, tunable in the range 800 nm – 2500 nm (4000 – 12,5000 cm^{-1}) by rotation of the BBO crystals. The frequency of the signal beam is continuously monitored by a Burleigh Instruments, Inc. Pulsed Wavemeter. The wavemeter is calibrated using photoacoustic spectroscopy of the well-established frequencies of water transitions in the 7000 – 7200 cm^{-1} region.[65]

The chemical ionization mass spectrometer (CIMS) will be used to detect the immediate PAN photolysis products, $CH_3C(O)O_2$ and NO_2, and the subsequent reaction products upon addition of O_2 and NO to the gas mixture. The 10 Torr flow tube reactor

described above will be coupled via a glass frit or Teflon valve to a photolysis cell (mTorr) through the inlet of the quadrupole mass spectrometer. The ion source produces SF_6^- ions for which the reaction products and rate coefficients of reaction with $CH_3C(O)O_2$ and NO_2 are known.[120] These ion-molecule reactions occur in the ion flow tube region of the instrument, through which the photolysis laser beam will also travel to eliminate secondary chemistry of the photolysis products. A small fraction of total flow is sampled by a pinhole, and the gas mixture travels through two differentially pumped chambers where ions are sampled and mass analyzed. The employment of ion-molecule reactions reduces background signal on any given mass because only the selected species will react to produce the correct product ion mass. For both $CH_3C(O)O_2$ and NO_2, charge transfer reaction dominates, and the products detected will be $CH_3C(O)O_2^-$ and NO_2^-. A schematic of the CIMS instrument is shown in Figure 6-2.

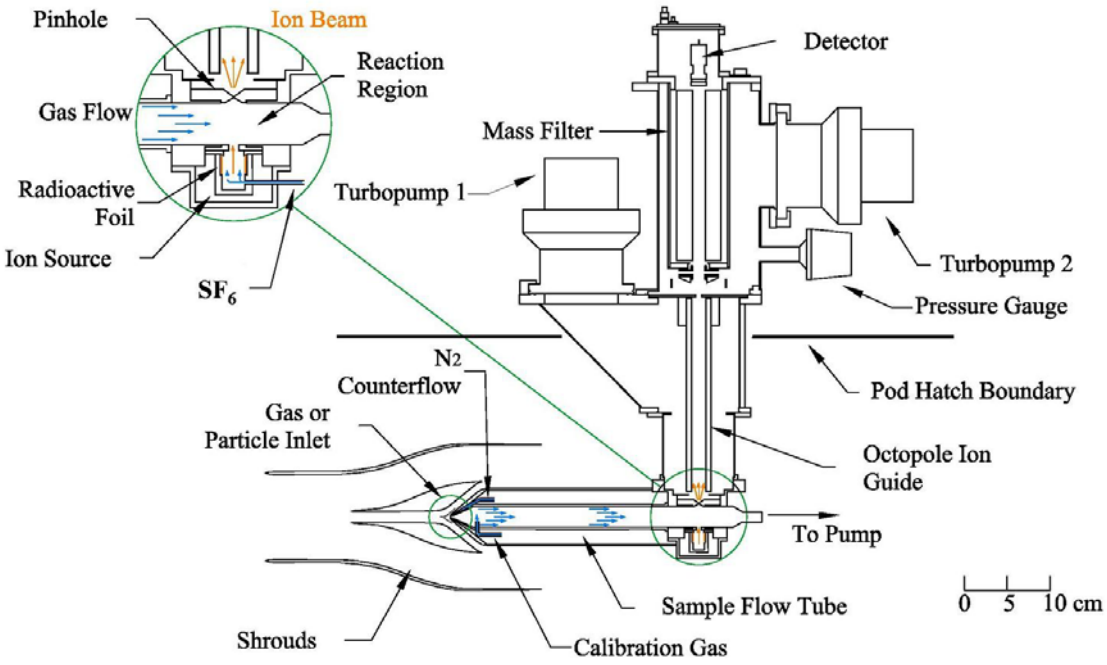

Figure 6-2. Schematic of chemical ionization mass spectrometer (CIMS) inlet and detection.

6.3. Experimental results

Using this coupled Action Spectroscopy – Chemical Ionization Mass Spectrometry technique, we attempted to measure photolysis cross sections of PAN in the near-IR region, where the Earth's atmosphere is transparent and solar actinic flux is high. The goal was to obtain photodissociation yields for the first three overtones of the CH stretch in PAN and possible combination bands in the near-IR. We were also looking to interrogate the subsequent reactions of the photolysis products, $CH_3C(O)O_2$ and NO_2, with O_2 and NO.

These studies would elucidate the importance of the photolytic sink of PAN in determining the total atmospheric lifetime of PAN, the major reservoir species responsible for large-scale transport of the pollutant NO_x.

Unfortunately, photodissociation of PAN via excitation in the C–H overtone region was never successfully detected using either LIF or CIMS detection techniques. This has since been interpreted in light of the large binding energy of PAN and the existence of many vibrational degrees of freedom that make the lowest overtone excitation with appreciable photodissociation yield the $4\nu_{CH}$ band, which has a relatively low absorption cross section. This interpretation is presented in a recent paper,[36] reproduced as Appendix III.

The experimental attempts to observe near-IR photodissociation of PAN were exhaustive. Both $3\nu_{CH}$ and $4\nu_{CH}$ regions were scanned, and a large parameter space of PAN bubbler ballast N_2 flow, PAN bubbler pressure, NO flow, O_2 flow, LIF cell pressure, and PAN solution temperature was sampled. The synthesis of PAN (after Gaffney et al.[46]) was perfected by FTIR analysis of the products, and the FTIR spectrum of PAN is well understood. The FTIR spectrum of the $v' = 1,2$, and 3 CH bands are reported in the Nizkorodov, et al. paper.[36]

The optimum flow and pressure conditions for OH production from PAN dissociation (based on reactions R14 – R18) was found, after several failed attempts to look directly for the near-IR overtone photodissociation at various flows, by photodissociating PAN in the UV. This was successfully demonstrated at $\lambda_{photodiss} \sim 240$ nm. The signal was verified as belonging to PAN because (1) increasing NO flow increased the signal, (2)

without O_2 present, increasing NO *decreased* the signal, and (3) with PAN depleted, increasing NO has *no* effect. The optimum O_2 flow was minimal, as O_2 very efficiently quenches OH* luminescence in the action spectroscopic detection.

To increase the interaction time of the PAN molecules with the excitation radiation, we modified the experimental arrangement to direct the pump laser beam along the length of the kinetics flow tube rather than at a 90° to the gas flow. This modification still did not allow detection of overtone mediated photodissociation.

The failure to experimentally detect overtone mediated PAN dissociation can be understood based on estimated cross sections of the PAN C–H overtones. For the OH LIF detection, we can compare to a successful experiment which observed such dissociation from the $3\nu_{OH}$ band of peroxynitric acid (HO_2NO_2, PNA). This comparison can be made by accounting for the facts that this C–H overtone is approximately a factor of 2 weaker than the PNA O–H overtone, a factor of 5 broader, and that there is approximately a 10% efficiency in the conversion of $CH_3C(O)O_2$ to OH. These factors, along with the best signal-to-noise ratio observed in the $3\nu_{OH}$ band of PNA, give an estimated upper limit on photodissociation from PAN $3\nu_{CH}$ of 10%.[36]

The failure to detect photodissociation products in the CIMS detection arrangement can similarly be rationalized in terms of the upper limit on quantum yield that should have allowed detection. In the CIMS experiment (Figure 6-2), the reagent ion SF_6^- was employed, and the immediate dissociation product NO_2 was detected as NO_2^-. Clear NO_2 signal was observed from both simple thermolysis of the PAN molecule (as a constant NO_2 background) as well as an enhancement in signal with UV photodissociation of PAN.

Hence, similarly to the OH LIF detection experiments, PAN flow was optimized to produce maximum UV photodissociation signal, and then the wavelength was switched to the near-IR to scan over the $3\nu_{CH}$ and $4\nu_{CH}$ regions of the spectrum to search for overtone mediated photodissociation. Again, none was observed.

Given the estimated CIMS sensitivity of 10^{10} molecules/cm^3 with one second integration time, we can calculate the minimum quantum yield that should be detectable given our estimates of the cross section and excitation laser parameters. For a measured concentration of PAN (FTIR) of ~ 10^{14} molecules cm^{-3}, an excitation laser interaction area of 0.2 cm^2 and energy of 2 mJ/pulse, and estimated cross sections for the $3\nu_{CH}$ and $4\nu_{CH}$ bands,[36] the estimated minimum quantum yield that will result in detectable product signal at $3\nu_{CH}$ is 3%, and at $4\nu_{CH}$, 70% (see calculation in Table 6-1).

Table 6-1. Calculation of minimum quantum yield for which photodissociation product signals should be above the CIMS instrument detection limit of 10^{10} counts/s, with experiment run at 100 Hz.

Band	**[PAN] (molec/cm^3)**	**Estimated Cross Section (cm/molec)**	**Beam area (cm^2)**	**Photons/pulse based on 2 mJ/pulse**	**Signal (counts/s) if QY=1, 100 Hz**	**Min QY detectable at 10^{10} counts/s**
$3\nu_{CH}$	10^{14}	1.3×10^{-20}	0.2	1.1×10^{16}	2.9×10^{11}	3%
$4\nu_{CH}$	10^{14}	7.6×10^{-22}	0.2	9.1×10^{15}	1.4×10^{10}	70%

The paper included as Appendix III estimates, by comparison to similar molecules, that the PAN quantum yield on the $3\nu_{CH}$ band is <0.5%. This result suggests that our failure to observe overtone photodissociation at $3\nu_{CH}$ was likely due to the very low efficiency of that process. The failure to detection PAN photodissociation at $4\nu_{CH}$, where

quantum yield should be >80%, is more puzzling. However, the low cross section at this higher overtone means that it is not a process likely to be of importance in the atmosphere. Therefore, we did not pursue these experiments further.

6.4. Estimated PAN photodissociation rate in the near-IR

The published paper on PAN included as Appendix III reports measured integrated absorption cross sections (FTIR) for the PAN ν_{CH}, $2\nu_{CH}$, $3\nu_{CH}$, and an estimated absorption cross section for the $4\nu_{CH}$ band based on comparison to the similar molecules acetone and acetaldehyde. In order to estimate the PAN overtone mediated photodissociation rate, we require an approximate dissociation quantum yield for each of the relevant bands. In this case, the relevant bands are $3\nu_{CH}$ (8550 cm^{-1}) and $4\nu_{CH}$ (11,100 cm^{-1}) because they lie near the dissociation threshold of $D_0(CH_3C(O)O_2–NO_2) \sim 9500 – 9900$ cm^{-1}.[27,28]

The quantum yields for these bands were calculated using the Multiwell suite of statistical master equation modeling programs[73] also demonstrated in Chapter 3 for HOONO. A thermal population of PAN molecules is abruptly shifted upwards by the photon energy, then either dissociates with the microcanonical rate constant or collisionally stabilizes according to a chosen collision model. After thermalization (~10^3 collisions), the fraction which has photodissociated is considered the quantum yield. This quantum yield can be calculated as a function of pressure and temperature to simulate the process in various regions of the atmosphere. Use of this statistical modeling requires choice of collision model parameters and the formalism for calculating the energy-dependent microcanonical dissociation rates. In addition, for density of state calculations the normal

modes and moments of inertia are required. The details of this calculation are described in Appendix III.

With the quantum yields known, photodissociation rates for atmospheric PAN in $3\nu_{CH}$ and $4\nu_{CH}$ bands can be calculated by multiplying cross section by quantum yield by photon flux at each band center. The resulting 24-hour averaged photodissociation rates for atmospheric PAN in $3\nu_{CH}$ and $4\nu_{CH}$ are shown in Figure 6-3, compared to the competing dissociation processes of UV photodissociation and thermal dissociation. In these 24-hour averages, the near-IR channel ($3\nu_{CH}$ and $4\nu_{CH}$) plays a minor role throughout the atmosphere (<10%). However, because UV radiation is much more strongly attenuated in the atmosphere than near-IR radiation, the near-IR photolysis channel could become comparable to the UV photolysis rate at very high solar zenith angle (SZA), providing a contribution to the observed twilight "burst" of HO_x radicals.[121]

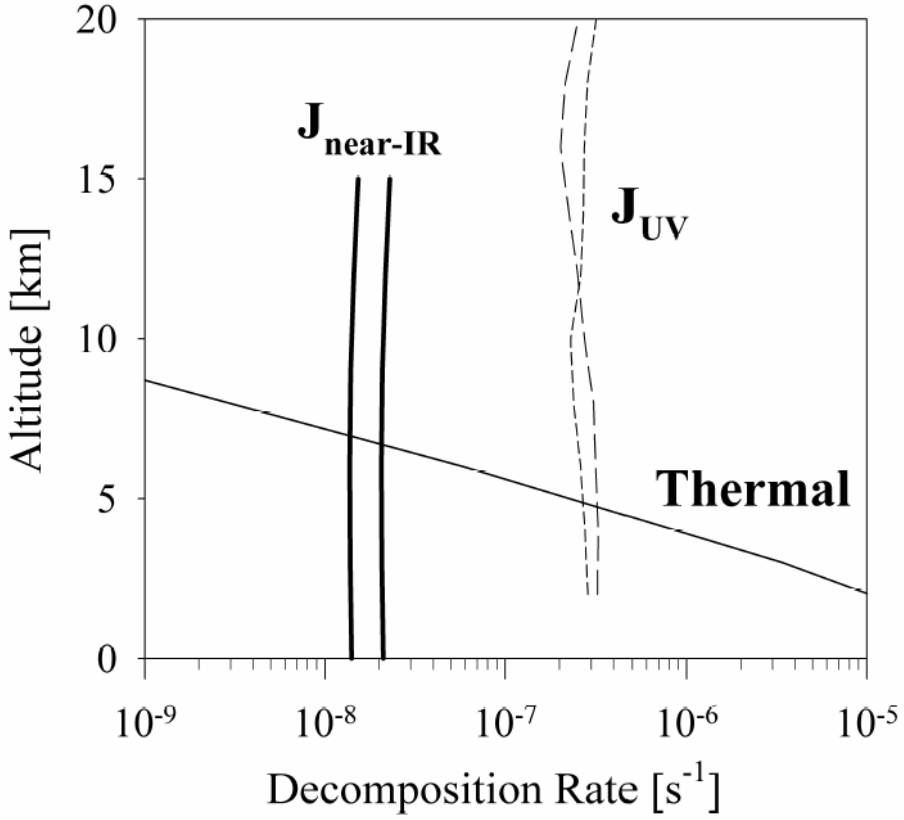

Figure 6-3. 24-hour averaged decomposition rate of PAN with respect to near-IR photodissociation (thick lines, faster decomposition rate is for an 18 hour May day and slower for a 12 hour September day), UV photolysis (dashed lines, calculated for actual conditions at 67°N in May (short dash) and 35°N in September (long dash)), and thermal dissociation (thin line). Reprinted with permission from Nizkorodov et al.[36] Copyright 2005, Authors.

6.5. Conclusions

Combined experimental and theoretical investigation of overtone-induced photodissociation in PAN indicates that this process will not represent a major atmospheric loss process for this atmospheric reservoir molecule. The higher binding energy and larger

number of vibrational modes contribute to making PAN more resistant to near-IR photodissociation than the simpler peroxy nitrates, HO_2NO_2 (PNA), for which $2\nu_{OH}$ and $3\nu_{OH}$ overtone photodissociation are the dominant sink processes in the upper troposphere and lower stratosphere.[21] The near-IR photolysis of PAN is only competitive with UV photolysis at high SZA and is calculated to contribute a maximum of 5-10% of the 24-hour averaged removal of PAN.

CHAPTER 7

UV PHOTODISSOCIATION OF METHYL HYDROPEROXIDE (MHP) AND HYDROXYMETHYL HYDROPEROXIDE (HMHP)

Chapter 7

7. UV PHOTODISSOCIATION OF METHYL HYDROPEROXIDE (MHP) AND HYDROXYMETHYL HYDROPEROXIDE (HMHP)

7.1. Introduction

Organic peroxides are important trace constituents of the atmosphere, acting as sinks and temporary reservoirs for HO_x and RO_x radicals. As discussed in Chapter 1, the transport of these reservoir species can have important regional and even global effects on radical concentrations. The atmospheric lifetimes of peroxides are determined by the rates of the multiple loss processes. Wet and dry deposition are likely to dominate in the lower atmosphere, while reaction with OH and photolysis account for the remainder of loss and will dominate where deposition is not favorable. The atmospheric lifetimes of these peroxides will determine the extent to which they contribute to regional or global transport of pollutants.

The photolytic sink of peroxides is measured in terms of the photolysis rates, which depend on the absorption cross sections at wavelengths longer than the ~305 nm "ozone cutoff," below which ozone absorbs the majority of the solar radiation in the upper atmosphere. Some cross sections of atmospheric peroxide species were listed in Table 1-1, p. 13. UV photolysis generally dominates over overtone photolysis for molecules with moderate binding energies because the quantum yield of photodissociation is small at lower overtones, while it is always unity for excitation of electronic transitions in the UV.

Therefore, the accurate knowledge of UV photolysis cross sections is critical to evaluating the lifetime of reservoir molecules.

This chapter discusses investigation of the UV photodissociation of the two most abundant atmospheric organic hydroperoxides: methyl hydroperoxide (MHP, CH_3OOH) and hydroxymethyl hydroperoxide (HMHP, $HOCH_2OOH$). In these experiments we employ a novel technique for UV cross section measurements based on action spectroscopy developed by Dr. Coleen Roehl in our laboratory and described in a forthcoming publication.[37] Based on these measured absorption cross sections, the total photolysis rate in the UV can be determined for these hydroperoxides for comparison to estimates of the other loss processes.

7.2. Action spectroscopy determination of UV cross sections

The standard method for measurement of absorption cross sections is a simple Beer's Law absorption experiment, where the attenuation of light by a known concentration of molecules is measured directly. In our laboratory, the technique of action spectroscopy has been adapted to the highly sensitive measurement of UV cross sections. In this case, the photodissociation of the hydroperoxide into OH + X (X = CH_3O and $HOCH_2O$ in the cases of the peroxides discussed in this chapter) is measured by laser induced fluorescence (LIF) detection of the OH product. By calibrating this LIF signal either to the photodissociation signal of a species with known UV absorption cross sections, such as H_2O_2, or internally to a known cross section at some wavelength, this method can be rendered quantitative. The advantage of this novel technique is in the high sensitivity of the LIF detection of OH radical, which should allow measurement of lower cross sections

that direct absorption methods. This comparison will be discussed in more quantitative detail in the upcoming publication.[37]

7.2.1. Optical parametric oscillator (OPO) and frequency mixing generation of tunable UV beam

The optical arrangement to generate tunable UV in the range 300 – 360 nm is shown in Figure 7-1. The tunable visible wavelength signal output of our 355 nm pumped type II BBO OPO (described in detail in section 2.2) is overlapped with the 1064 nm output of the same Nd:YAG laser that pumps the OPO in a mixing crystal (type I BBO) to generate tunable UV. The transmitted beam is reflected through a Pellin-Broca prism to spatially separate the wavelength components of the beam (355 nm pump beam, visible OPO signal output, 1064 nm, and the desired UV wavelength) and to compensate for translation of the beam as the mixing crystal is rotated. An aperture is used to reject all beams but the desired UV, and that beam is directed into the photolysis chamber collinearly with the OH LIF probe beam. LIF signal (obtained as described in section 2.3) is collected and converted to quantitative absorption cross section units (cm^2 $molecule^{-1}$) by a calibration process, different for MHP and HMHP, described in the upcoming publication.[37]

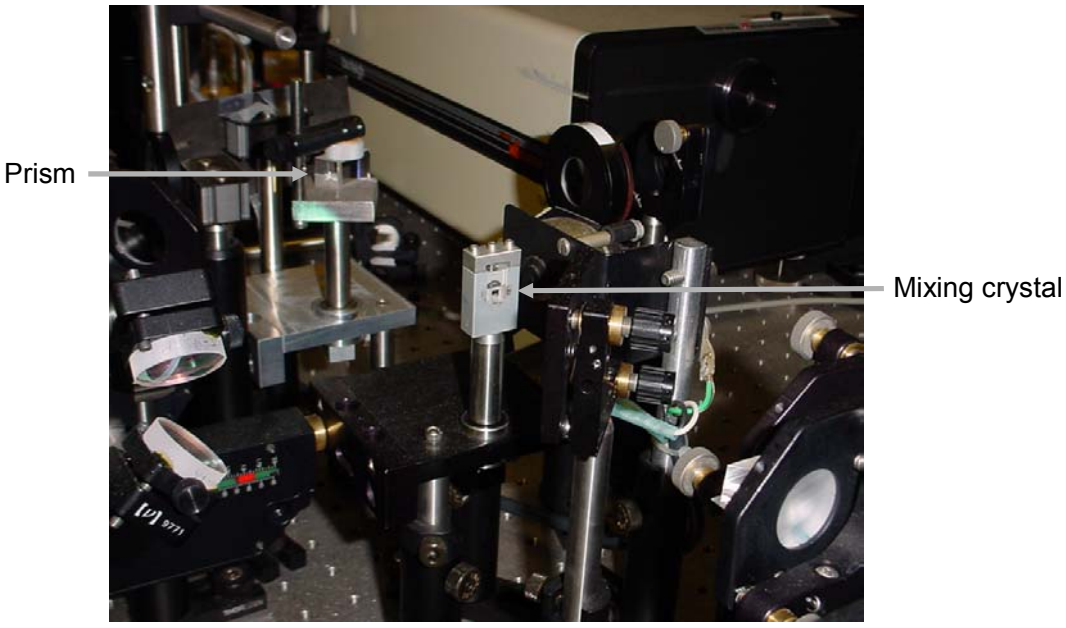

Figure 7-1. Optics for frequency mixing of tunable visible OPO output with 1064 nm to generate tunable UV, 300-360 nm.

7.3. Measured UV photolysis cross sections, 300-360 nm

7.3.1. Methyl hydroperoxide (MHP)

The UV photolysis cross section for MHP as a function of wavelength is shown in Figure 7-2, with data tabulated in Table 7-1. Our work is compared to UV cross sections reported by Vaghjiani and Ravishankara[48] and Matthews et al.[122] In our work and that by Vaghjiani and Ravishankara, extrapolation has been used to determine cross sections at selected wavelengths (in our data set, at 300 and 310 nm and above 350 nm, and in Vaghjiani and Ravishankara's data set, above 365 nm). Extrapolated points are noted in Table 7-1 with an asterisk. This extrapolation is based on the linear dependence observed when plotting the natural logarithm of the absorption cross section versus wavelength for

many molecules.[20] The Matthews, et al. data shows some deviation from a smooth, linear plot. However, the authors suggest that only a single excited singlet electronic state is responsible for the absorption band, so that this irregularity can only be due to measurement noise.

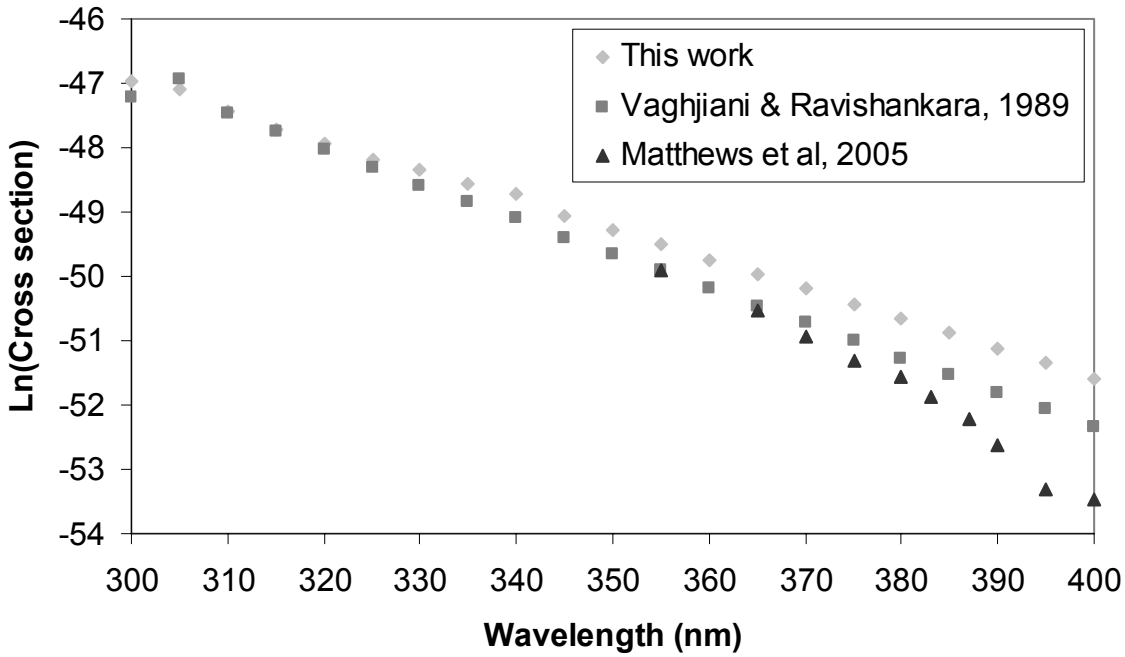

Figure 7-2. Absorption cross sections measured and extrapolated for methyl hydroperoxide (MHP). For this work, experimental data are shown for 305 nm and 315 – 350 nm, with extrapolation at other wavelengths where either signal was too small or residual OH LIF laser overwhelmed the photolysis signal; for Vaghjiani and Ravishankara[48] data are shown up to 365 nm with extrapolation above; and for Matthews et al.[122] only experimental cross sections are shown.

Table 7-1. Absorption cross section as a function of wavelength for methyl hydroperoxide. Extrapolated cross sections are indicated by an asterisk (*).

	Cross section (cm^2 $molecule^{-1}$)		
Wavelength (nm)	**This work**	**Vaghijiani & Ravishankara[48]**	**Matthews et al.[122]**
300	3.95E-21*	3.13E-21	
305	3.50E-21	4.13E-21	
310	2.49E-21*	2.39E-21	
315	1.90E-21	1.82E-21	
320	1.50E-21	1.37E-21	
325	1.20E-21	1.05E-21	
330	1.00E-21	7.90E-22	
335	8.00E-22	6.10E-22	
340	7.00E-22	4.70E-22	
345	5.00E-22	3.50E-22	
350	4.00E-22	2.70E-22	
355	3.15E-22*	2.10E-22	2.10E-22
360	2.50E-22*	1.60E-22	1.14E-22
365	1.99E-22*	1.20E-22	7.50E-23
370	1.58E-22*	9.32E-23*	5.20E-23
375	1.25E-22*	7.11E-23*	4.00E-23
380	9.97E-23*	5.43E-23*	3.00E-23
385	7.92E-23*	4.15E-23*	2.10E-23
390	6.29E-23*	3.16E-23*	1.40E-23
395	5.00E-23*	2.42E-23*	7.00E-24
400	3.97E-23*	1.84E-23*	6.00E-24

Apparent in Table 7-1 is that the cross sections measured and extrapolated here are up to two times higher than those measured by Vaghjiani and Ravishankara, upon which the JPL recommendation is based.[20] The different between our measurements and the previous study increases with increasing wavelength. Our extrapolated cross sections at high wavelengths are also higher than the experimentally measured values of Matthews, et al,[122] but these extremely low cross sections are prone to high measurement uncertainties and are atmospherically of minor importance.

7.3.2. Hydroxymethyl hydroperoxide (HMHP)

Data collection is still underway for the UV cross sections of hydroxymethyl hydroperoxide, and the final analysis will be reported in the upcoming paper.[37] A preliminary result for the cross section as a function of wavelength, with experimentally determined points in the range 315-350 nm and extrapolation above to 400 nm and below to 300 nm, is shown in Figure 7-3 and tabulated in Table 7-2. The present data are compared to a previous study by Bauerle and Moortgat.[123]

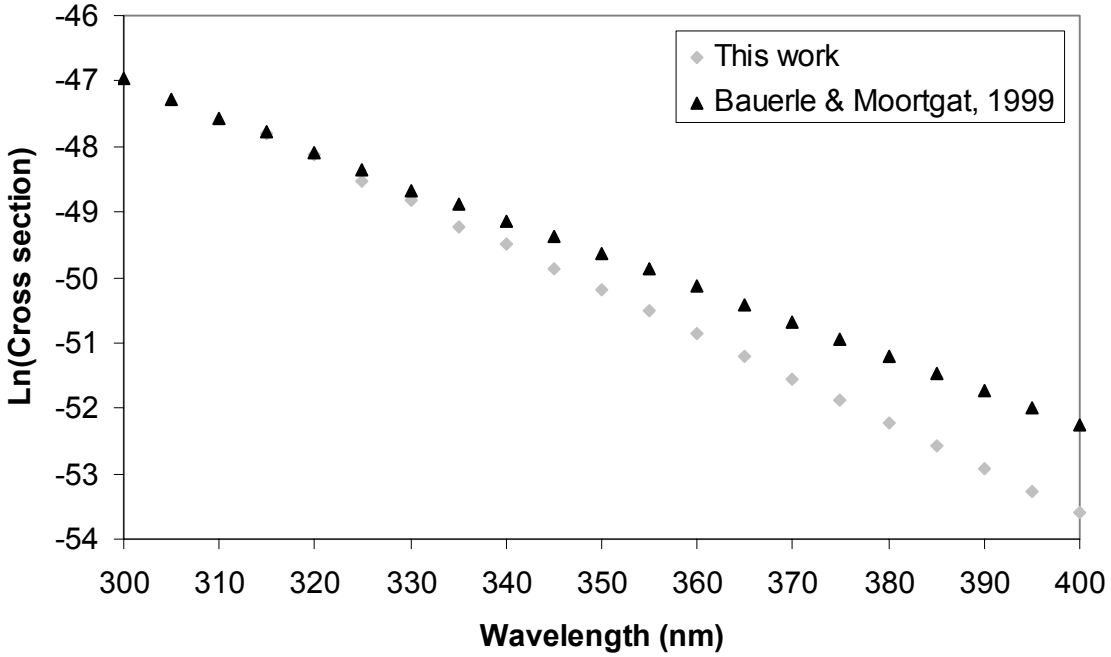

Figure 7-3. Absorption cross sections measured and extrapolated for hydroxylmethyl hydroperoxide (HMHP). For this work, experimental data are shown 315 – 350 nm with extrapolation to 400 nm above and 300 nm below; for Bauerle and Moortgat,[123] data are shown 300 – 360 nm with extrapolation to 400 nm above.

Table 7-2. Absorption cross section as a function of wavelength for hydroxymethyl hydroperoxide. Extrapolated cross sections are indicated by an asterisk (*).

	Cross section (cm^2 $molecule^{-1}$)	
Wavelength (nm)	**This work**	**Bauerle & Moortgat[123]**
300	5.00E-21*	4.00E-21
305	3.55E-21*	2.90E-21
310	2.52E-21*	2.20E-21
315	1.74E-21	1.80E-21
320	1.25E-21	1.30E-21
325	8.30E-22	1.00E-21
330	6.22E-22	7.30E-22
335	4.19E-22	5.90E-22
340	3.18E-22	4.50E-22
345	2.17E-22	3.60E-22
350	1.59E-22	2.80E-22
355	1.15E-22*	2.20E-22
360	8.15E-23*	1.70E-22
365	5.79E-23*	1.25E-22*
370	4.11E-23*	9.61E-23*
375	2.91E-23*	7.40E-23*
380	2.07E-23*	5.69E-23*
385	1.47E-23*	4.38E-23*
390	1.04E-23*	3.38E-23*
395	7.39E-24*	2.60E-23*
400	5.24E-24*	2.00E-23*

In the case of HMHP, our measured and extrapolated cross sections are up to a factor of 2.5 *smaller* than the previous measurement, with the difference in measurements increasing with increasing wavelength. These measurements differences at 400 nm should be taken in context: on the order of 10^{-24} cm^2 molecule^{-1}, they are essentially zero and a factor of four is not very significant (as is apparent in the calculations in section 7.4).

7.4. Extrapolated total UV photolysis rates

In order to evaluate the atmospheric importance of UV photolysis, we determine the ground-level total UV photolysis rate across the 300 – 400 nm window between the ozone cutoff and where the cross sections become small and hence atmospherically negligible. This is an adaptation of equation 1 (p. 14), for the case where quantum yield is unity across the entire band ($\Phi(\lambda)=1$ for all λ). We multiply the experimentally determined cross sections (cm^2 molecule^{-1}) by literature solar spectral actinic fluxes (photons cm^{-2} s^{-1} nm^{-1}) at 0 km for each wavelength (taken from Figure 3.3 of Seinfeld and Pandis[1]) and multiply by the 5 nm bin width to get partial photolysis rates J_λ:

$$J_\lambda = \sigma(\lambda) I(\lambda) d\lambda \quad [\mathrm{s}^{-1}] \tag{14}$$

These partial photolysis rates J_λ are plotted as a function of wavelength in Figure 7-4 and Figure 7-5 and tabulated in Table 7-3 and Table 7-4. A coarse box integration of the band is then calculated by summing all these partial photolysis rates, to derive the integrated band photolysis rate J:

$$J = \sum_\lambda J_\lambda \quad [\mathrm{s}^{-1}] \tag{15}$$

The integrated UV photolysis in the region 300-400 nm is likely to account for most of the UV photolysis of these peroxides. Essentially no light penetrates the atmosphere below 300 nm due to strong absorption by ozone in the stratosphere. Above 400 nm, the absorption cross sections are very small so that partial photolysis rates become negligible.

7.4.1. Methyl hydroperoxide (MHP)

The partial photolysis rates calculated from equation 14 for methyl hydroperoxide are shown as a function of wavelength in Figure 7-4, with our present results compared to results derived from the cross sections of Vaghjiani and Ravishankara[48] and Matthews et al.[122] These calculated partial photolysis rates and the photon fluxes used to calculate them are shown in Table 7-3. Also shown are the calculated (equation 15) total photolysis rates of 8.43×10^{-6} s^{-1} and 6.39×10^{-6} s^{-1}, for the cross sections determined by this work and that of Vaghjiani and Ravishankara, respectively. Hence, our data suggest a 25% increase in the total UV photolytic loss of MHP over previous estimates.

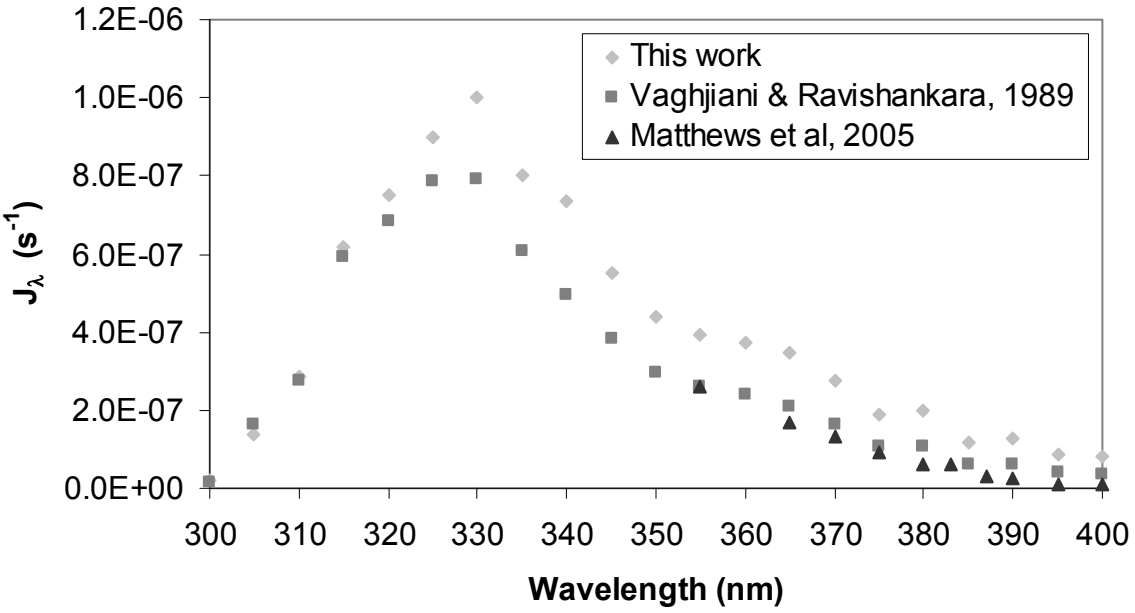

Figure 7-4. Partial photolysis rates for methyl hydroperoxide (MHP) across the region of the UV band where most photolysis occurs.

Table 7-3. Partial photolysis rates (J_λ) for methyl hydroperoxide (MHP). Partial rates are calculated by multiplying MHP cross sections (Table 7-1) by solar flux by bin width (5 nm). Total photolysis rate is the sum of the partial rates.

Wavelength (nm)	Solar spectral actinic flux (photons cm^{-2} s^{-1} nm^{-1})[a]	J_λ (s^{-1}) (Using cross sections from this work)	J_λ (s^{-1}) (Using cross sections from Vaghjiani and Ravishankara)
300	1.00E+12	1.98E-08	1.57E-08
305	8.00E+12	1.40E-07	1.65E-07
310	2.30E+13	2.86E-07	2.75E-07
315	6.50E+13	6.18E-07	5.92E-07
320	1.00E+14	7.50E-07	6.85E-07
325	1.50E+14	9.00E-07	7.88E-07
330	2.00E+14	1.00E-06	7.90E-07
335	2.00E+14	8.00E-07	6.10E-07
340	2.10E+14	7.35E-07	4.94E-07
345	2.20E+14	5.50E-07	3.85E-07
350	2.20E+14	4.40E-07	2.97E-07
355	2.50E+14	3.94E-07	2.63E-07
360	3.00E+14	3.75E-07	2.40E-07
365	3.50E+14	3.48E-07	2.10E-07
370	3.50E+14	2.76E-07	1.63E-07
375	3.00E+14	1.88E-07	1.07E-07
380	4.00E+14	1.99E-07	1.09E-07
385	3.00E+14	1.19E-07	6.22E-08
390	4.00E+14	1.26E-07	6.33E-08
395	3.50E+14	8.75E-08	4.23E-08
400	4.00E+14	7.95E-08	3.69E-08
	$J_{\text{total UV}}$ =	**8.43E-06**	**6.39E-06**

a. Values taken from Figure 3.3 of Seinfeld and Pandis.[1]

7.4.2. Hydroxymethyl hydroperoxide (HMHP)

The partial photolysis rates calculated for hydroxymethyl hydroperoxide are shown as a function of wavelength in Figure 7-5, with our present results compared to results derived from the cross sections of Bauerle and Moortgat.[123] These calculated partial photolysis rates and the photon fluxes used to calculate them are shown in Table 7-4. Also shown are the calculated (equation 15) total photolysis rates of 4.56×10^{-6} s^{-1} and 6.23×10^{-6} s^{-1} for the cross sections determined by this work and that of Bauerle and Moortgat, respectively. In this case, our data suggest a ~ 25% *decrease* in the total UV photolytic loss of HMHP over previous estimates.

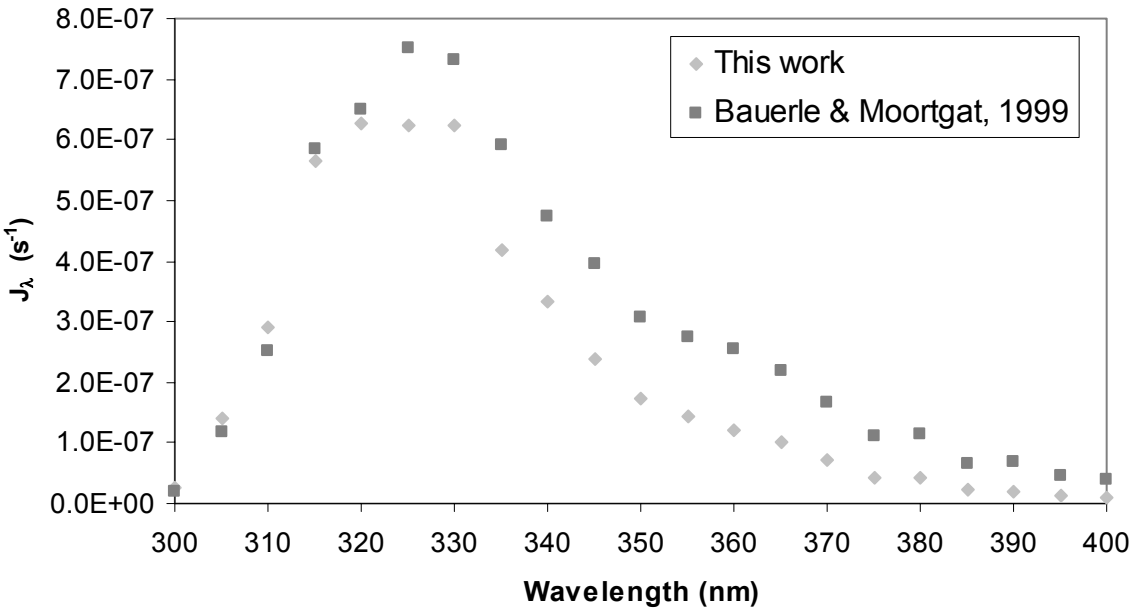

Figure 7-5. Partial photolysis rates for hydroxymethyl hydroperoxide (HMHP) across the region of the UV band where most photolysis occurs.

Table 7-4. Partial photolysis rates (J_λ) for hydroxymethyl hydroperoxide (HMHP). Partial rates are calculated by multiplying HMHP cross sections (Table 7-2) by solar flux by bin width (5 nm). Total photolysis rate is the sum of the partial rates.

Wavelength (nm)	Solar spectral actinic flux (photons cm^{-2} s^{-1} nm^{-1})[a]	J_λ (s^{-1}) (Using cross sections from this work)	J_λ (s^{-1}) (Using cross sections from Bauerle and Moortgat)
300	1.00E+12	2.50E-08	2.00E-08
305	8.00E+12	1.42E-07	1.16E-07
310	2.30E+13	2.90E-07	2.53E-07
315	6.50E+13	5.66E-07	5.85E-07
320	1.00E+14	6.25E-07	6.50E-07
325	1.50E+14	6.23E-07	7.50E-07
330	2.00E+14	6.22E-07	7.30E-07
335	2.00E+14	4.19E-07	5.90E-07
340	2.10E+14	3.34E-07	4.73E-07
345	2.20E+14	2.38E-07	3.96E-07
350	2.20E+14	1.74E-07	3.08E-07
355	2.50E+14	1.44E-07	2.75E-07
360	3.00E+14	1.22E-07	2.55E-07
365	3.50E+14	1.01E-07	2.18E-07
370	3.50E+14	7.19E-08	1.68E-07
375	3.00E+14	4.37E-08	1.11E-07
380	4.00E+14	4.14E-08	1.14E-07
385	3.00E+14	2.20E-08	6.58E-08
390	4.00E+14	2.08E-08	6.75E-08
395	3.50E+14	1.29E-08	4.55E-08
400	4.00E+14	1.05E-08	4.00E-08
	$J_{\text{total UV}}$ =	**4.65E-06**	**6.23E-06**

a. Values taken from Figure 3.3 of Seinfeld and Pandis.[1]

7.4.3. Discussion of UV photolysis rates

The total ground level UV photolysis rates for MHP and HMHP determined here, of 8.43×10^{-6} s^{-1} and 4.56×10^{-6} s^{-1}, respectively, both seem to indicate significant discrepancy from earlier measurements. For MHP, our data suggest an upward adjustment of the UV photolysis rate by about 25%, and for HMHP our data suggest a downward adjustment of the UV photolysis rate, also of about 25%.

It is important to consider the uncertainty introduced by extrapolation. The absorption cross section extrapolation was done using all available data from each dataset; however, any errors in the slope of the available data will be carried through in the extrapolated region (355 – 400 nm for our data, 370 – 400 nm for Vaghjiani and Ravishankara, and 365 – 400 nm for Bauerle and Moortgat). It would be far superior to have experimental cross sections in this region, but cross sections are extremely small. To evaluate the contribution of this extrapolated region to the total photolysis rate, we compare the photolysis rate obtained by summing the experimental data only (300 – 350 nm) to the total rates (300 – 400 nm) reported in Table 7-3 and Table 7-4.

For MHP, the 300 – 350 nm UV photolysis rate is 6.24×10^{-6} s^{-1}, compared to the total rate of 8.43×10^{-6} s^{-1}, using the cross sections from this work. If the 300 – 350 nm UV photolysis rate from our data is compared to the same region using Vaghjiani and Ravishankara's data, the increase in photolysis rate implied by our data is only 18% rather than 25%. However, the general suggestion based on our experimental results is robust; the photolysis rate must be significantly higher than previously believed.

For HMHP, the 300 – 350 nm UV photolysis rate is 4.06×10^{-6} s^{-1}, compared to the total rate of 4.56×10^{-6} s^{-1}, using the cross sections from this work. If we again compare the 300 – 350 nm UV photolysis rate from our data to the same region using Bauerle and Moortgat's data, the decrease in photolysis rate is only 17% rather than 25%. Again, the general conclusion, that the photolysis rate must be significantly lower than previously believed, is robust.

Another important point is that these calculations of photolysis rates are rather crude. We have simply binned the solar spectrum into 5 nm sections and have only considered the average solar irradiation at 0 km altitude. Since our interest in these molecules is motivated by the role they play as reservoir species allowing regional or global transport, we clearly anticipate that they will not be limited to the ground level. A more sophisticated calculation of the UV photolytic lifetime of these peroxides would account for the vertical profile of the solar spectral actinic flux and the albedo of the Earth's surface.

7.5. Conclusions

The present action spectroscopy measurements of methyl hydroperoxide and hydroxymethyl hydroperoxide UV photodissociation cross sections suggest an upward adjustment of the ground level UV photolysis rate of MHP on the order of 25% and a downward adjustment of the ground level UV photolysis rate of HMHP, also on the order of 25%. A more sophisticated photolysis rate calculation, using these cross section data and including vertical resolution and planetary albedo, would provide rates with greater confidence. The adjustments suggested here are significant; however, the atmospheric

importance of these ~ 25% changes in UV photodissociation rates for MHP and HMHP will depend heavily on the relative importance of the UV photolytical sink, rainout and washout, and reaction of these peroxides with OH. Analysis of these competing processes requires more sophisticated atmospheric modeling with meteorological and additional chemical inputs. As such, we leave this in the hands of the global modeling community.

CHAPTER 8

VIBRATIONAL OVERTONE INITIATED PHOTODISSOCIATION OF HYDROXYMETHYL HYDROPEROXIDE (HMHP)

This chapter is soon to be submitted as:

Fry, J.L., Matthews, J.N., Lane, J.R., Roehl, C.M., Sinha, A., Kjaergaard, H.G., and Wennberg, P.O., "OH-stretch vibrational spectroscopy of hydroxymethyl hydroperoxide," to Journal of Physical Chemistry A.

Chapter 8

8. VIBRATIONAL OVERTONE INITIATED PHOTODISSOCIATION OF HYDROXYMETHYL HYDROPEROXIDE (HMHP)

8.1. Abstract

We report measurement and analysis of the photodissociation spectrum of hydroxymethyl hydroperoxide ($HOCH_2OOH$) and its partially deuterated analog, $HOCD_2OOH$, in the OH-stretching region. Spectra are obtained by Fourier transform infrared spectroscopy in the $1\nu_{OH}$ and $2\nu_{OH}$ regions and by laser induced fluorescence detection of the OH fragment produced from dissociation of $HOCH_2OOH$ initiated by excitation of the $4\nu_{OH}$ and $5\nu_{OH}$ overtone regions (action spectroscopy). A one-dimensional local mode model of each OH chromophore is constructed using ab initio calculated OH-stretching potential energy and dipole moment curves at the coupled-cluster level of theory. Major features in the observed absorption and photodissociation spectra are explained by our local mode model. In the $4\nu_{OH}$ region, explanation of the photodissocation spectrum requires a nonuniform quantum yield, which is estimated by assuming statistical energy distribution in the excited state.

8.2. Introduction

Hydroperoxides are important trace constituents of the urban and global atmosphere. They play important roles in oxidation chemistry as both reservoirs and sinks of OH radical and odd oxygen.[15,19,124] Organic peroxides are also oxidants in their own

right, oxidizing SO_2 in clouds, fogs, or rain,[125,126] and are believed to have a toxic effects on plants.[2]

In the gas phase, H_2O_2 and the organic hydroperoxides are formed via recombination reactions of peroxy radicals (HO_2, RO_2). In the troposphere, peroxy radicals are produced primarily by photooxidation of CO and volatile organic compounds (VOCs) by the hydroxyl radicals.[1] Because the peroxy radicals are removed via reactions with NO and NO_2, the production rate of hydroperoxides via this mechanism tends to be lower in polluted atmospheres.[1]

Recent investigations have found that, in the presence of water, the ozonolysis of isoprene and other alkenes can also produce hydroperoxides.[127-132] Although these alkene ozonolysis reactions remain poorly understood, it is thought that they involve the formation of a carbonyl oxide (or Criegee biradical) which subsequently reacts with water to form peroxide. Observations of H_2O_2 and other organic hydroperoxides after sunset, when model calculations showed ozonolysis to be the dominant source of peroxides, provide evidence for this mechanism.[133] The smallest stabilized Criegee biradical, CH_2OO, formed in the ozonolysis of ethene and terminal alkenes, is believed to react with water to form hydroxymethyl hydroperoxide ($HOCH_2OOH$ or HMHP):

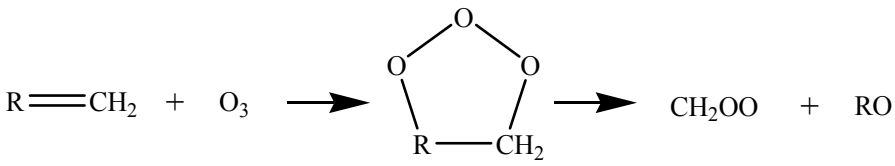

(R19)

$$CH_2OO + H_2O \longrightarrow HOCH_2OOH\ (HMHP) \qquad (R20)$$

Hydroxymethyl hydroperoxide has been positively identified in the atmosphere, but its atmospheric abundance is still quite uncertain.[18,133-146] For example, HMHP values as high as 5 ppbv were reported during photochemical episodes with high ozone and isoprene in the southeastern United States in summer.[138] More recent campaigns have reported smaller concentrations, e.g. a median HMHP value of 1 ppbv during the 1995 Southern Oxidants Study campaign in Nashville, TN;[136] maximum HMHP mixing ratio of 0.2 ppbv during the 1998 BERLIOZ campaign in Pabstthum, Germany;[133] and HMHP undetected during ESCOMPTE (2001) and BOND (2002) campaigns in Marseilles, France.[134] However, some of these results may be spurious because the measurement of these species is challenging and sampling artifacts have been reported.[15]

The atmospheric fate of HMHP and its role in the transport of continental boundary-layer pollutants to more remote environments is determined by the relative rates of the various HMHP loss processes. Photolysis (and to a lesser extent reaction with OH[123]) tends to recycle the radical pool, while wet and dry deposition are permanent sinks of HO_x. Direct measurements of HMHP removal by reaction with OH are very difficult since HMHP is unstable. An estimated 298 K lifetime for reaction with OH of about 2 days is derived from the comparable rate coefficient for reaction of OH with CH_3OOH.[123] Efficient removal of HMHP by wet and dry deposition is expected due to its high solubility.[147] Photolysis rates for HMHP in the UV were first estimated by Su et al.,[148] who observed $HOCH_2OOH$, during experiments on the photooxidation of formaldehyde.

Absorption cross-sections of HMHP vapor were later reported between 205 and 360 nm.[123] Photolysis of HMHP is expected to yield OH and $HOCH_2O$ radical products which react further with atmospheric O_2:

$$HOCH_2OOH + h\nu \rightarrow HOCH_2O + OH \quad \text{(R21)}$$

$$HOCH_2O + O_2 \rightarrow HCOOH + HO_2 \quad \text{(R22)}$$

Thus, photolysis of $HOCH_2OOH$ results in release of two molecules of HO_x from the reservoir peroxide.

In this study we investigate the vibrational overtone photodissociation of HMHP in order to evaluate the importance of this process as a sink of HMHP and a source of HO_x. We make use of a high-power, frequency tunable photolysis laser system that is coupled to sensitive measurements of OH radical products using laser-induced fluorescence (LIF). This technique has proven useful in evaluating the importance of overtone photolysis as an atmospheric HO_x source.[21,32,97,149,150] We study the vibrational overtone initiated decomposition of HMHP excited in the third ($4\nu_{OH}$) and fourth ($5\nu_{OH}$) overtone regions of the OH stretching vibrations. We supplement this study with Fourier transform infrared absorption spectroscopy of the $1\nu_{OH}$ and $2\nu_{OH}$ regions.

To facilitate assignment of the spectra we have calculated the OH stretching transitions using an anharmonic oscillator local mode model with parameters and dipole moment functions obtained from *ab initio* coupled cluster calculations. The local mode model has been successful in the description and analysis of XH-stretching (where X = C, N, O) overtone spectra.[151-153] With the use of experimental local mode parameters and

dipole moment functions calculated at modest *ab initio* levels, relative intensities within a given overtone were obtained.[78] More recently, empirically scaled *ab initio* calculated local mode parameters combined with *ab initio* dipole moment function have been successful in predicting OH stretching spectra of hydrated complexes.[154,155] The advancement in computational methods and hardware now allows high level *ab initio* calculations, which can eliminate the need for empirical scaling of the local mode parameters. Recently, the OH-stretching local mode parameters of the different conformers in ethylene glycol were calculated with impressive agreement to experiment.[156]

8.3. Experiment

The action spectroscopy experimental apparatus has been described previously.[157] In this photodissociation action spectroscopy experiment, HMHP undergoes vibrationally mediated dissociation upon absorption of a near-IR or visible photon, and the resulting OH fragment is probed via LIF.

HMHP (or the partially deuterated analog, HMHP-d_2) is synthesized based on the method originally described by Bauerle and Moortgat.[123] A low flow of N_2 is passed over 5 g paraformaldehyde powder (Aldrich) (or the deuterated analog, paraformaldehyde-d_2, Aldrich) at 100ºC and subsequently bubbled for ~15 hours through a glass vessel containing 7 mL 90-95% H_2O_2 in H_2O at 60ºC. Excess H_2O_2 must be maintained during the synthesis to avoid formation of *bis*-HMHP ($HOCH_2OOCH_2OH$).[158] The synthesis was monitored by FTIR to ensure minimal *bis*-HMHP formation. The HMHP (HMHP-d_2) is generated in the peroxide vessel, never completely consuming the H_2O_2. This liquid sample is immediately placed in a glass U-tube for the experiments. To prevent injury in

case of a peroxide explosion, the sample U-tube is contained in a Plexiglass box. A bulb of water behind a valve is connected to the top of the U-tube above the sample and outside of the sample box, such that after experiments are finished, the peroxide residue can be quenched with water prior to handling. The sample is pumped on at ~20 mTorr for up to 1 hour prior to photolysis experiments to remove remaining H_2O, HCOOH, and H_2O_2 contamination, and then flowed into the photolysis chamber, which is maintained at ~80 mTorr for experiments. **Extreme caution should be exercised when working with concentrated samples of peroxides. The water quenching method is highly recommended; an explosion in our lab occurred when a concentrated HMHP sample was vented to atmospheric pressure.**

Visible and near-IR radiation for excitation of the third or fourth OH overtone region, $4\nu_{OH}$ or $5\nu_{OH}$, is generated by a Nd:YAG (Spectra Physics GCR-270) pumped Lambda Physik Scanmate dye laser, operating in the region of 600-650 nm (Rhodamine 640 + DCM mixture, 40 mJ/pulse) and 720-770 nm (LDS750 + LDS765 mixture, 20 mJ/pulse). The OH photofragments are probed via the *A*-*X* transition at ~308 nm using LIF. The 0.13 cm^{-1} bandwidth probe radiation is provided by frequency doubling the output of a second Nd:YAG (Continuum:HY81-20) pumped dye laser (Continuum: ND60). The pump-probe delay is fixed at 80 ns (20 ns) for the $4\nu_{OH}$ ($5\nu_{OH}$) spectroscopy experiments reported here. The OH fluorescence is collected using an *f*/1 lens system imaged onto an end-on photomultiplier tube (EMI 9813QB). The signal from this PMT is sent to a gated charge integrator (LeCroy, 2249SG analog-to-digital converter) and digitized for computer data collection.

Near and mid-IR absorption spectra are obtained in a 2 meter path length absorption cell using a Nicolet (Magna-IR 560) FTIR spectrometer. A small droplet of the HMHP sample is added to the cell and, after the majority of the HCOOH, H_2O, and H_2O_2 impurity is pumped off, spectra are obtained in the range 1000 cm^{-1} – 11000 cm^{-1} using either an extended KBr or a CaF_2 beamsplitter and an MCT-A detector.

8.4. Theory and calculations

The geometries of the three lowest energy conformers of HMHP are optimized at the hybrid density functional theory, B3LYP,[159-161] quadratic configuration interaction including singles and doubles, QCISD,[162] and coupled cluster singles and double with perturbative triples, CCSD(T)[163-165] levels of theory with a selectively augmented cc-pVTZ (correlation consistent polarized triple zeta)[166-168] basis set. The CCSD(T) theory is known to provide accurate molecular geometries and spectroscopic constants[169] but is computationally demanding. To reduce the computational cost we use the aug-cc-pVTZ basis set for the two hydroxyl groups, while modelling the rest of the molecule with the cc-pVTZ basis set. This form of selective augmentation (labelled aug´-cc-pVTZ) has been shown to accurately model OH-stretching vibrations in ethylene glycol.[156] Harmonic normal mode frequencies were calculated at the QCISD/aug´-cc-pVTZ level for the three stable conformers of HMHP. All *ab initio* energy calculations were run using the computational suite MOLPRO 2002.6.[170]

8.4.1. Vibrational OH stretching model

The oscillator strength, *f*, of a transition from the ground vibrational state $|0\rangle$ to a vibrationally excited state $|\nu\rangle$ is given by:[78,171]

$$f_{v0} = 4.702\times10^{-7}[\text{cm D}^{-2}]\ \tilde{\nu}_{v0}\left|\vec{\mu}_{v0}\right|^2 \tag{16}$$

where $\tilde{\nu}_{v0}$ is the wavenumber of the transition and $\vec{\mu}_{v0} = \langle v|\vec{\mu}|0\rangle$ is the transition dipole moment matrix element in debye (D).

We have used a simple anharmonic oscillator local-mode model to characterize the OH-stretching modes. The Hamiltonian for an isolated OH stretching oscillator can be written as a Morse oscillator:[172]

$$(H - E_{|0\rangle})/hc = v\tilde{\omega} - (v^2 + v)\tilde{\omega}x \tag{17}$$

where $E_{|0\rangle}$ is the energy of the vibrational ground state and $\tilde{\omega}$ and $\tilde{\omega}x$ are the local-mode frequency and anharmonicity, respectively.

The OH-stretching frequency and anharmonicity are obtained from the second (f_{ii}), third (f_{iii}) and fourth (f_{iv}) order derivatives of the potential energy with respect to the OH-stretching coordinate according to:[173,174]

$$\tilde{\omega} = \frac{\sqrt{f_{ii}G_{ii}}}{2\pi c} \tag{18}$$

$$\tilde{\omega}x = \frac{\hbar G_{ii}}{32\pi c f_{ii}}\left(\frac{5f_{iii}^2}{3f_{ii}} - f_{iv}\right) \tag{19}$$

where G_{ii} is the reciprocal of the OH reduced mass.

The dipole moment function is approximated by a series expansion in the internal displacement coordinate q about the equilibrium geometry:

$$\vec{\mu}(q) = \sum_i \vec{\mu}_i q^i \tag{20}$$

where the coefficients $\vec{\mu}$ are given by:

$$\vec{\mu}_i = \frac{1}{i!}\frac{\partial^i \vec{\mu}}{\partial q^i}\bigg|_e \tag{21}$$

The coefficients $\vec{\mu}_i$ are determined from an *ab initio* calculated one-dimensional grid of the dipole moment $\vec{\mu}(q)$.

One-dimensional grids were calculated using QCISD/aug′-cc-pVTZ and CCSD(T)/aug′-cc-pVTZ at their respective optimized geometries by displacing each OH bond from equilibrium by $-0.30 < \Delta q < 0.40$ Å in steps of 0.05 Å for a total of 15 points. The required force constants are found by fitting a 12th order polynomial to the 13 points symmetrically distributed about the equilibrium bond length. The dipole moment expansion coefficients are found from a sixth order polynomial fitted to all 15 grid points. The dipole moment at each grid point was determined analytically for the QCISD level of theory and numerically using a finite field of ± 0.005 a.u. for the CCSD(T) level of theory.

This field size was chosen to ensure numerical stability of the higher order dipole derivatives without perturbing the molecular system significantly.[175]

8.4.2. $HOCH_2O$-OH bond dissociation energy

Ab initio geometry optimizations and energy calculations of HMHP and the two photodissociation fragments, OH and OCH_2OH, at the UCCSD(T)/aug´-cc-pVTZ level were carried out to obtain an estimate of the bond dissociation energy, D_0. Zero point vibrational energy (ZPVE) corrections were calculated with the UQCISD/aug´-cc-pVTZ method.

D_0 was also estimated using a statistical state counting calculation using the HMHP density of states calculated by the MultiWell DenSum program.[73,176] A value for D_0 was found that gives quantum yields for the two major bands in the $4\nu_{OH}$ spectrum that match those determined by comparison of observed relative band intensities and calculated band strengths in the $4\nu_{OH}$ and $5\nu_{OH}$ regions. This estimated D_0 was subsequently used to predict atmospheric pressure quantum yields, and to estimate the atmospheric vibrational overtone photolysis rate for HMHP.

8.5. Results and discussion

Previously, the lowest energy conformers of HMHP had been studied with the B3LYP/6-311++G(2d,2p) method.[177] We further optimized the three lowest energy conformers to the CCSD(T)/aug´-cc-pVTZ level. The optimized structures and relative energies are shown in Figure 8-1and we refer to them as HMHP-A, HMHP-B, and HMHP-C. The complete optimized geometries for these three conformers of HMHP are shown in

the supporting information section 8.7 (Table 8-5). In the lowest energy conformer, HMHP-B, it is the OO─H group which donates the H atom to form a hydrogen bond. In the two higher energy conformers, HMHP-A and HMHP-C, it is the RO─H group that donates the H atom to form a hydrogen bond. With the CCSD(T)/aug´-cc-pVTZ method, HMHP-C and HMHP-A are found to be 76 and 301 cm^{-1} higher in energy than HMHP-B. Including zero-point vibrational energy correction at the QCISD/aug´-cc-pVTZ level, the energy difference becomes 13 and 215 cm^{-1}, respectively, which, assuming a Boltzmann distribution, would give approximately 44% HMHP-B, 41% HMHP-C, and 15% HMHP-A at 300 K.

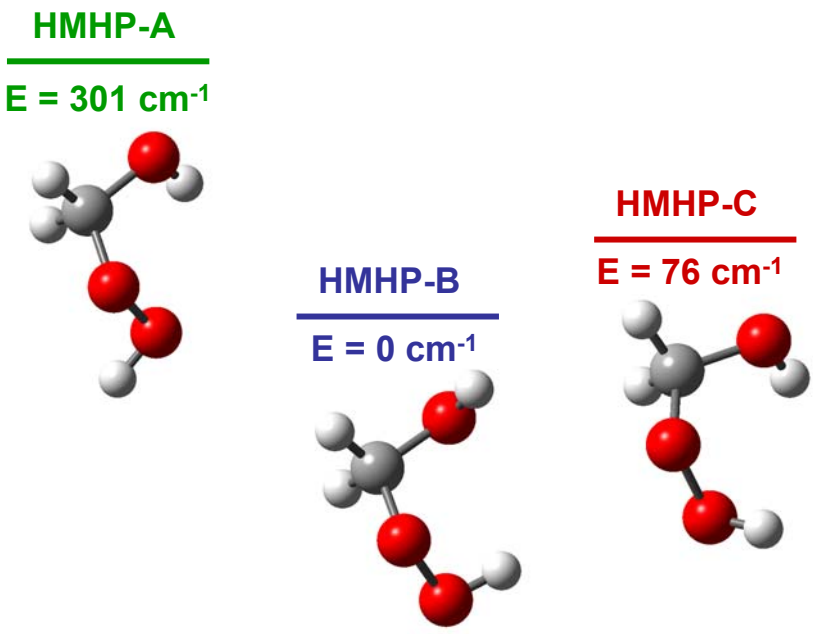

Figure 8-1. Energy level diagram of the relative energies of the three most stable structural conformers of hydroxymethyl hydroperoxide (HMHP), as calculated at the CCSD(T)/aug´-cc-pVTZ level including QCISD/aug´-cc-pVTZ ZPE.

8.5.1. OH stretching spectra

The fundamental (ν_{OH}) and first overtone ($2\nu_{OH}$) OH-stretching regions of the FTIR spectrum are shown in Figure 8-2 and Figure 8-3. The signal-to-noise ratio was not sufficient to detect any bands in the $3\nu_{OH}$ region. The entire FTIR spectrum in the range 1000 – 7500 cm^{-1}; a table of FTIR band positions, relative intensities, and assignments, and the QCISD/aug´-cc-pVTZ calculated normal modes and intensities for the three conformers are given in the supporting information section 8.7 (Figure 8-8, Figure 8-9, Table 8-6, and Table 8-7). Impurities visible in the FTIR spectrum are H_2O_2, H_2O, and CO_2. The action spectra of HMHP in the $4\nu_{OH}$ and of HMHP-d_2 in the $5\nu_{OH}$ overtone regions are shown Figure 8-4 and Figure 8-5, respectively. The observed OH-stretching transitions and measured relative intensities are given in Table 8-1.

Table 8-1. Observed OH band centers (in cm^{-1}), relative peak intensities, and assignments.

Observed band center (cm^{-1})	Relative intensity[a]	Assignment
3598.1	0.70	OO─H, all 3 conformers
3647.8	1.00	RO─H, all 3 conformers
6947.1	0.40	OO─H, HMHP-B
7022.9	0.85	OO─H, HMHP-A/C
7125.4	1.00	RO─H, all 3 conformers
13200	0.05	OO─H, HMHP-B
13330	0.30	OO─H, HMHP-A/C
13480	0.15	unassigned
13550	1.00	RO─H, all 3 conformers
16010	0.30	OO─H, HMHP-B
16220	1.00	OO─H, HMHP-A/C
16400	0.30	unassigned
16550	0.95	RO─H, HMHP-A/B
16600	0.60	RO─H, HMHP-C

a. Measured relative intensities refer to comparison within each spectral region.

The spectra are made complex by the two different OH chromophores and the existence of at least two conformers. To facilitate the assignment of the spectra, we calculated the OH-stretching transitions of the different chromophores in the three lowest energy structures with the anharmonic oscillator local mode model. The CCSD(T) calculated local mode parameters of the different OH oscillators are given in Table 8-2. The calculated band positions and oscillator strengths of the OH stretching local mode transitions are shown in Table 8-3. The results obtained with the QCISD method are similar

to those obtained with CCSD(T) and are not shown. The CCSD(T) frequencies are closer to the experimental band positions than those obtained with the QCISD method, alleviating the usual need for empirical scaling of local mode parameters.[155,156]

Table 8-2. Calculated OH–stretching local mode parameters (in cm^{-1}) compared with experimentally derived values.

Mode	$\tilde{\omega}$	$\tilde{\omega}x$
OOH (HMHP–A) [a]	3769.8 (37)	85.70
ROH (HMHP–A) [a]	3820.6	82.40
OOH (HMHP–B) [a]	3733.8	85.69
ROH (HMHP–B) [a]	3820.1	83.72
OOH (HMHP–C) [a]	3771.1	85.04
ROH (HMHP–C) [a]	3833.6	83.01
Experimental		
OOH (HMHP–A/C) [b]	3779	89.2
OOH (HMHP–B) [b]	3748	90.5

[a] Calculated with the CCSD(T)/aug´-cc-pVTZ method.
[b] Experimental values from Birge-Spooner fit of the $2\nu_{OH}$, $4\nu_{OH}$ and $5\nu_{OH}$ bands.

Table 8-3. Calculated OH–stretching frequencies (in cm^{-1}) and intensities[a]

		HMHP – A		**HMHP – B**		**HMHP – C**	
v		$\tilde{\nu}$	f	$\tilde{\nu}$	f	$\tilde{\nu}$	f
1	OOH	3598.4	5.8×10^{-6}	3562.4	3.9×10^{-6}	3601.0	6.1×10^{-6}
	ROH	3665.8	5.6×10^{-6}	3652.7	4.8×10^{-6}	3667.5	4.8×10^{-6}
2	OOH	7025.5	8.5×10^{-7}	6953.4	5.9×10^{-7}	7031.9	7.7×10^{-7}
	ROH	7146.7	4.3×10^{-7}	7138.0	5.5×10^{-7}	7169.1	4.5×10^{-7}
3	OOH	1028.1	3.1×10^{-8}	10173.0	2.4×10^{-8}	10292.8	2.7×10^{-8}
	ROH	10472.9	1.5×10^{-8}	10455.8	2.0×10^{-8}	10504.6	1.6×10^{-8}
4	OOH	13365.3	1.6×10^{-9}	13221.3	1.4×10^{-9}	13383.5	1.4×10^{-9}
	ROH	13634.2	7.9×10^{-10}	13606.1	9.3×10^{-10}	13674.0	8.0×10^{-10}
5	OOH	16278.2	1.4×10^{-10}	16098.2	1.3×10^{-10}	16304.2	1.3×10^{-10}
	ROH	16630.8	7.1×10^{-11}	16589.1	7.1×10^{-11}	16677.5	7.0×10^{-11}

a. Calculated with the local mode parameters in Table 8-2 and CCSD(T)/aug´-cc-pVTZ dipole moment functions.

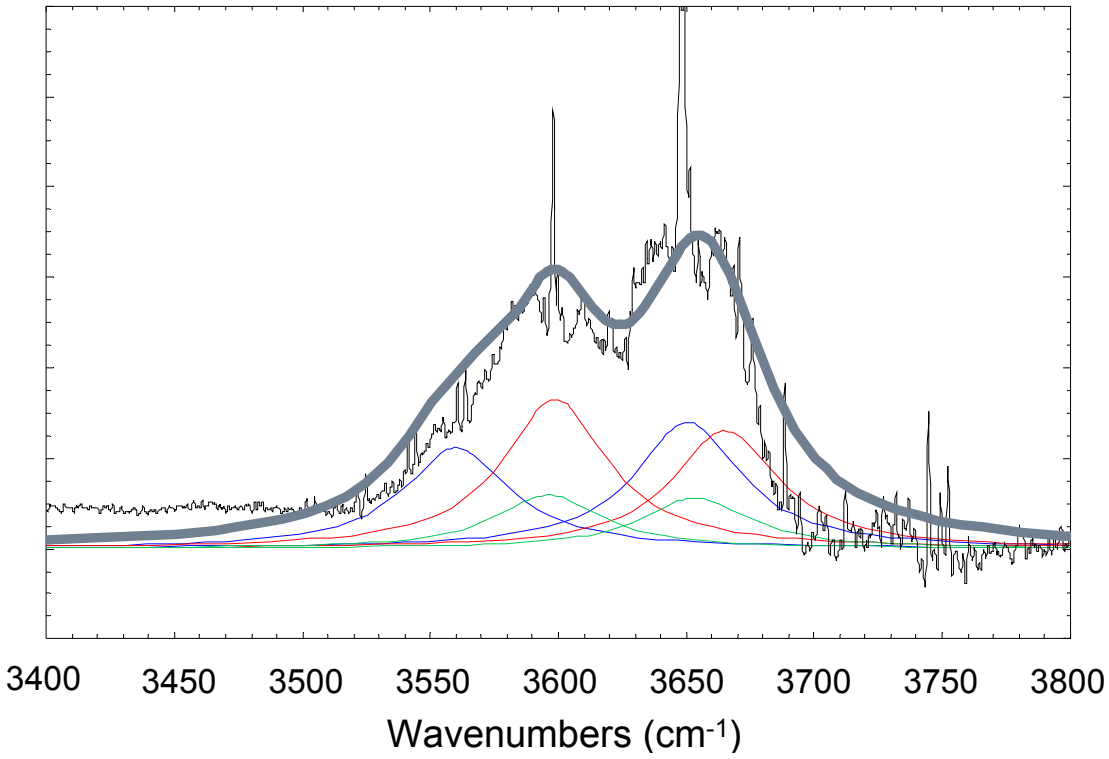

Figure 8-2. Experimental FTIR and simulated spectra in the fundamental ν_{OH} region of HMHP. Experimental spectrum in black; simulated spectra: HMHP-A (green), HMHP-B (blue), HMHP-C (red), and the weighted sum (grey).

In the $1\nu_{OH}$ region (~3600 cm^{-1}) we assign the two bands that are well defined by their Q-branches to the OO–H and RO–H transitions of all conformers. This assignment is made based on our calculations and is consistent with the generally lower vibration frequency of a peroxide OH stretch versus an alcohol OH stretch,[178] and with the Niki et al. assignment.[179] Based on the calculated band center of the RO–H transitions given in Table 8-3, we would not expect the transitions from the various conformers to be resolved. However, the fundamental OO–H stretch of HMHP-B is calculated to be ~ 40 cm^{-1} lower

that those of HMHP-A/C and is perhaps evident as the weak shoulder to the red of the main band.

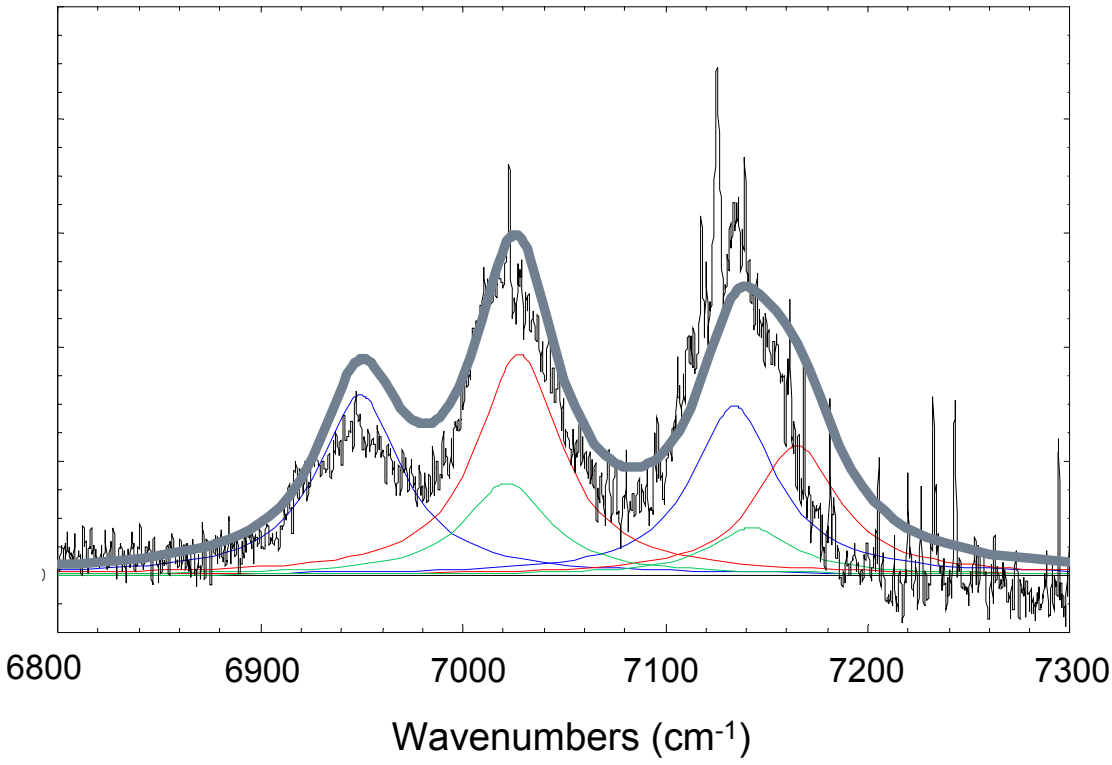

Figure 8-3. Experimental FTIR and simulated spectra in the first overtone $2\nu_{OH}$ region of HMHP. Experimental spectrum in black; simulated spectra: HMHP-A (green), HMHP-B (blue), HMHP-C (red), and the weighted sum (grey).

In the $2\nu_{OH}$ region (~7000 cm^{-1}) region the OO–H stretch transition of HMHP-B appears as a well resolved peak at 6947 cm^{-1}, in excellent agreement with our calculated band center of 6953 cm^{-1}. The OO–H stretch of HMHP-A/C is observed at 7023 cm^{-1}, which is within 7 cm^{-1} of the calculated transitions. The strongest band at 7126 cm^{-1} is assigned to the RO–H transitions of all conformers, which we calculate to lie in the range

from 7138 to 7169 cm^{-1}, possibly indicating that the local mode frequency of HMHP-C is a bit high.

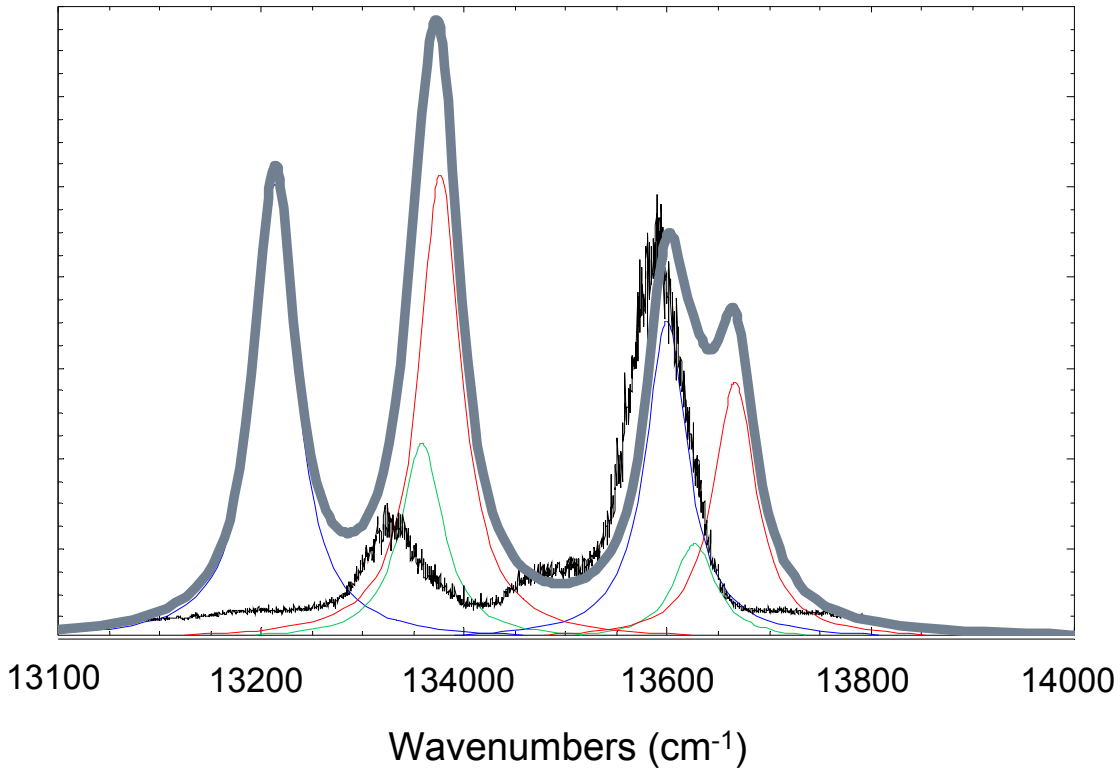

Figure 8-4. Experimental action and simulated spectra in the $4\nu_{OH}$ region of HMHP. Experimental spectrum in black; simulated spectra: HMHP-A (green), HMHP-B (blue), HMHP-C (red), and the weighted sum (grey).

The action spectrum in the $4\nu_{OH}$ region (~13500 cm^{-1}) shown in Figure 8-4 is further complicated by the fact that the dissociation energy of HMHP lies in this region. At excitation energies below the dissociation energy, the quantum yield will be nonuniform since only molecules with sufficient internal energy will dissociate upon excitation by the pump laser. This will suppress the lower energy bands relative to the higher energy bands,

producing a difference between the action spectrum and the absorption spectrum. The dominant band at 13550 cm^{-1} is assigned to the RO–H transitions of all conformers. We assign the weaker band, around 13330 cm^{-1}, to the OO–H transition of HMHP-A/C, with its intensity reduced by the smaller quantum yield. We do not clearly observe the OO–H transition of HMHP-B; it is further to the red and its intensity is significantly reduced by low quantum yield.

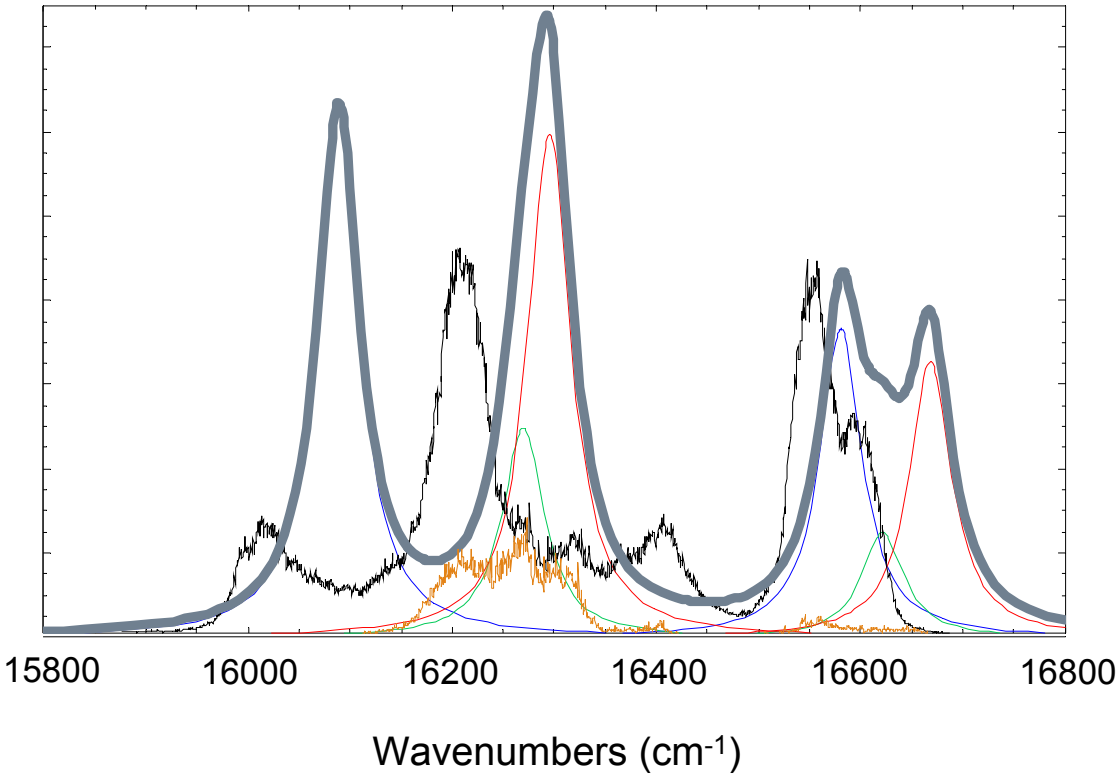

Figure 8-5. Experimental action and simulated spectra in the $5\nu_{OH}$ region of HMHP–d_2. Experimental spectrum in black; simulated spectra: HMHP-A (green), HMHP-B (blue), HMHP-C (red), and the weighted sum (grey).

In Figure 8-5 we show the action spectrum of HMHP-d_2 in the $5\nu_{OH}$ region (~16400 cm^{-1}), which is significantly above the dissociation energy, so that a unity quantum yield can be assumed. We use the HMHP-d_2 spectrum rather than that of HMHP for comparison with the local mode model, because of the existence of a Fermi resonance between OH and CH stretch states, which splits the RO─H stretching transition in the HMHP $5\nu_{OH}$ spectrum into two bands as shown in Figure 8-6. The spectrum of the contaminant species H_2O_2 is shown for reference in this spectral region, since it was not possible to completely remove its contribution. The peaks at 16550 and 16600 cm^{-1} are assigned as the RO─H stretch transitions of HMHP-B and HMHP-A/C, respectively. The separation of these transitions was not observed at the $4\nu_{OH}$ overtone. We assign the other strong transition at 16220 cm^{-1} to the OO–H stretch of HMHP-A/C, with the weaker band to the red at 16010 cm^{-1} assigned to the OO–H stretch transition in HMHP-B.

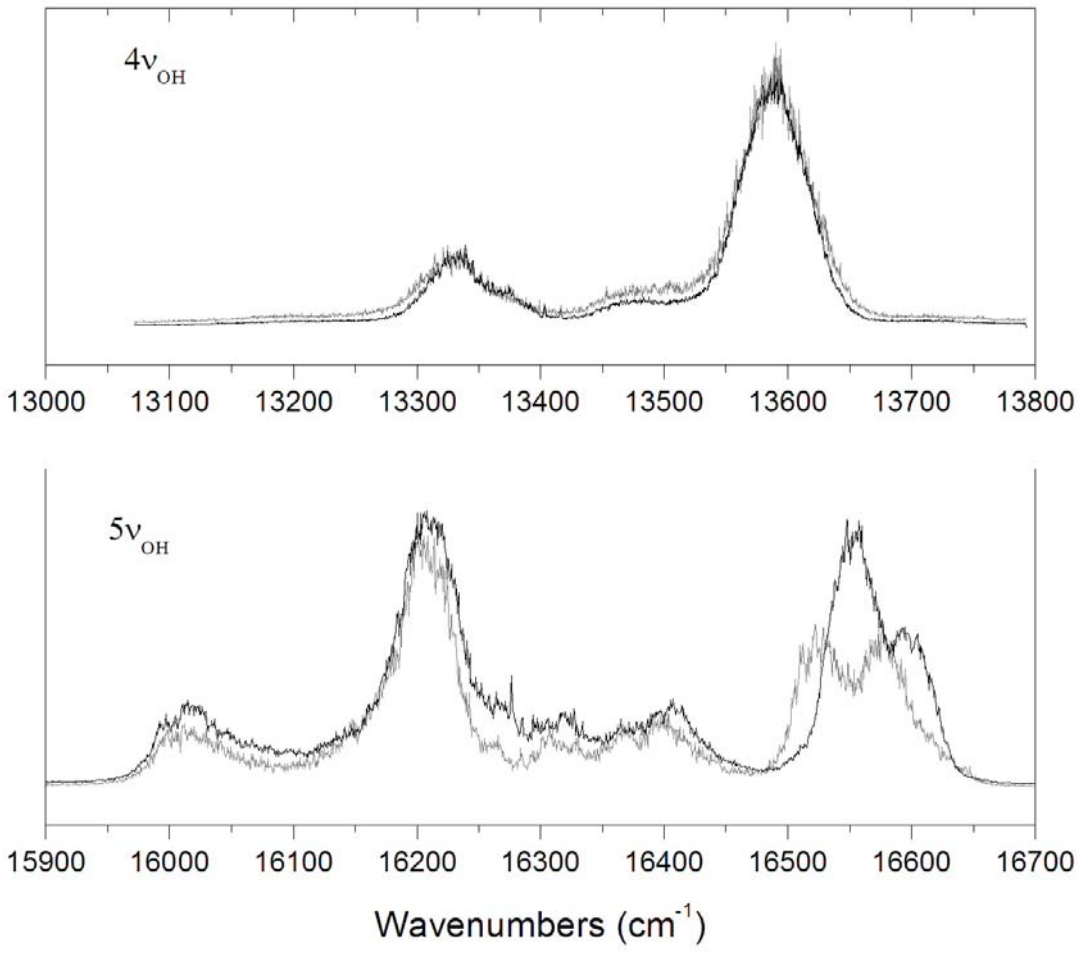

Figure 8-6. Experimental action spectra of HMHP (grey) and HMHP-d_2 (black) in the $4\nu_{OH}$ and $5\nu_{OH}$ region.

The calculated local mode parameters of the different OH-stretching oscillators are compared to experimentally derived parameters from our observed transitions in Table 8-2. The agreement is reasonable with $\tilde{\omega}_{OO-H}$ within 10 cm^{-1} and $\tilde{\omega}x_{OO-H}$ = within 4 cm^{-1} of the calculated values for the OO–H mode in HMHP-A/C. We could not resolve the peaks from the RO–H for HMHP-A/C in more than one overtone and hence no local mode

parameters are derived. The reasonable agreement between these observed and unscaled calculated local mode parameters support our assignment of the peaks.

We have simulated the HMHP absorption spectra in the 1–5ν_{OH} regions. The simulated spectra are obtained by convolving each of our calculated OH-stretching transitions, given in Table 8-3, with a Lorentzian lineshape of full-width at half maximum 50 cm^{-1}. The predicted spectra for the three HMHP conformers are scaled by their relative Boltzmann populations. The simulated absorption bands are shown overlapped with the experimental spectra in Figure 8-2 through Figure 8-5.

The overall agreement in the 1ν_{OH} and 2ν_{OH} regions is excellent. The simulated spectra have reproduced both the positions and intensities of the major features. The agreement in the higher overtone spectra is worse because small errors in the calculated local mode parameters are magnified.[156] In the action spectra the calculated peaks are consistently at slightly higher wavenumbers than the observed peaks. In the 5ν_{OH} region, the calculated relative intensity of the OO–H and RO–H peaks of HMHP-A/C is in good agreement with the experimental HMHP-d_2 spectrum. However, for HMHP-B the intensity of the OO–H peak is overestimated relative to the RO–H peak. Disagreement in spectra can be due to errors in the calculated relative intensities of transitions of the three conformers, errors in the relative energies of the three conformers, or errors in relating action to absorption spectra. A temperature dependence study of the HMHP spectra would help constrain the relative abundance of the conformers. The difference between the calculated absorption spectrum and the observed action spectrum in the 4ν_{OH} region is a clear indication that the dissociation energy (D_0) for HMHP must fall near this region.

The difference in the $5\nu_{OH}$ region of HMHP and HMHP-d_2 spectra (Figure 8-6) suggests significant coupling between the RO–H and CH stretching modes in the HMHP molecule. The dominant peak at 16550 cm^{-1} in the HMHP-d_2 spectrum splits into two strong peaks in the HMHP spectrum. The smaller peak at 16600 cm^{-1} in the HMHP-d_2 is seen as a broad shoulder in the HMHP spectrum. The CH-stretching fundamental is observed in the FTIR spectrum around 2940 cm^{-1}. The combination band $4\nu_{OH} + 1\nu_{CH}$ is therefore ($4\nu_{OH} + 1\nu_{CH} = 16540$ cm^{-1}) near resonant with the $5\nu_{OH}$ band ($5\nu_{OH} = 16550$ cm^{-1}) and significant mixing of states can occur. A similar coupling across bonds has been previously observed in formic acid[180] and in methanol.[181] In both formic acid and methanol, the coupled CH modes are *trans* in configuration to the OH bond. In HMHP, the CH bonds are out of the H–O–C plane, with dihedral angles of 122º for one of the CH stretches, and 55º, 168º, and 43º for the other CH stretch in HMHP-A, -B, and -C, respectively. Only the most stable HMHP-B conformer has a nearly *trans* configuration of the resonant OH and CH modes, and this is conformer for which we see the resonance coupling, consistent with previous studies of coupling across bonds.

The unassigned weak bands around 13480 cm^{-1} and 16400 cm^{-1} in the $4\nu_{OH}$ and $5\nu_{OH}$ overtones may reflect additional conformers of HMHP or combination bands which borrow intensity from the OH stretch bright states. There is some additional discrepancy in the spectra around 16200-16300 cm^{-1}, indicating more H_2O_2 contaminant in the HMHP-d_2 sample than in the HMHP.

8.5.2. Quantum yield and dissociation energy

Comparison of our observed spectrum in the $4\nu_{OH}$ region with the other OH regions, particularly the suppression of the OO-H band, indicates that D_0 is larger than 13300 cm^{-1}. Our UCCSD(T)/aug´-cc-pVTZ calculated dissociation energy D_0, including UQCISD/aug´-cc-pVTZ ZPVE correction, is 14484 cm^{-1} (173.2 kJ/mol). This calculated D_0 value is above the location of the $4\nu_{OH}$ spectrum and would result in very low dissociation quantum yield for all transitions in the $4\nu_{OH}$ region. Previously, D_0 has been calculated to be 13600 cm^{-1} (162.7 kJ/mol) and 15320 cm^{-1} (183.3 kJ/mol) with the CCSD(T)/6-311+G(2d,2p) and CBS-QB3/6-311G(2d,d,p) methods, respectively.[177,182] Both of these calculations included single point energies at the B3LYP/6-31G(d,p) geometry. To date no experimental D_0 has been determined.

We estimate the quantum yield of the bands in the $4\nu_{OH}$ region by comparing the observed and calculated intensities in the $4\nu_{OH}$ and $5\nu_{OH}$ regions. The band intensities are corrected for the difference in pump laser power and for differences in the measured percentage of the total population contained in the probed OH quantum state (~40% in $N = 1$ for $4\nu_{OH}$ and ~20% in $N = 3$ for $5\nu_{OH}$). We apply a further correction to account for the differences in the rate of appearance of OH following the pump laser. We observe essentially instantaneous production (<5 ns) of OH from excitation throughout the $5\nu_{OH}$ region, while for $4\nu_{OH}$ region, OH appears with a time constant that varies from 30-50 ns.[38] Because the spectrum shown in Figure 8-4 was obtained before the complete evolution of the photodissociation in $4\nu_{OH}$, we correct these band intensities by extrapolation to long probe delay time (correction of order 40-50%).

The corrected intensity ratio of the RO─H band in the $4\nu_{OH}$ to $5\nu_{OH}$ region is 2 ± 0.5, where the uncertainty arises primarily from the intensity scaling issues discussed above. The calculated intensity ratio from the local mode model for these transitions is ~12, consistent with the rule of thumb that successive OH overtones differ in intensity by a factor of ~10. Thus, we estimate that the quantum yield at 13550 cm^{-1} is 0.17 ± .05.

The analogous ratio of the integrated intensity of the OO─H band for HMHP-A/C (corrected as discussed above) in the $4\nu_{OH}$ to $5\nu_{OH}$ region is 0.6 ± 0.3. The calculated intensity ratio of these transitions is about 11, hence the quantum yield at 13330 cm^{-1} is 0.05 ± .03. The OO─H transition of HMHP-B is clearly observed in the $5\nu_{OH}$ region but is very weak in the $4\nu_{OH}$ region.

Simple state counting can be used to estimate a dissociation energy (D_0) that is consistent with the observed quantum yields. At 80 mTorr pressure and 80 ns pump-probe delay, this experiment is essentially collision-free, and the total quantum yield can be taken as the fraction of HMHP molecules above D_0 immediately after laser excitation. We estimate a dissociation energy (D_0) by shifting a thermalized (298 K) HMHP internal energy distribution upward by the photon energies 13330 cm^{-1} and 13550 cm^{-1} and determining the value of D_0 required to give the observed quantum yields of Φ(13550 cm^{-1}) = 0.17 ± .05 and Φ(13330 cm^{-1}) = 0.05 ± .03. We use the vibrational frequencies calculated at QCISD/aug´-cc-pVTZ for HMHP-B (Table 8-7) to determine the density of states for the initial thermalized HMHP, using the MultiWell program DenSum.[176]

The dissociation energy found consistent with the experimental quantum yields (Φ) is D_0 = 14050 ± 100 cm^{-1} (168.1 ± 1.2 kJ/mol), and the resulting variation in quantum yield

across the $4\nu_{OH}$ region for experimental conditions is shown in Figure 8-7. It is encouraging that the same D_0 is found consistent with both empirical quantum yields. This indicates that, within the uncertainty of our experimental quantum yield estimates, this simple state-counting model captures the $4\nu_{OH}$ photodissociation of HMHP reasonably well. A more thorough phase space theory (PST) calculation will provide a better constrained experimental estimate of D_0.[38]

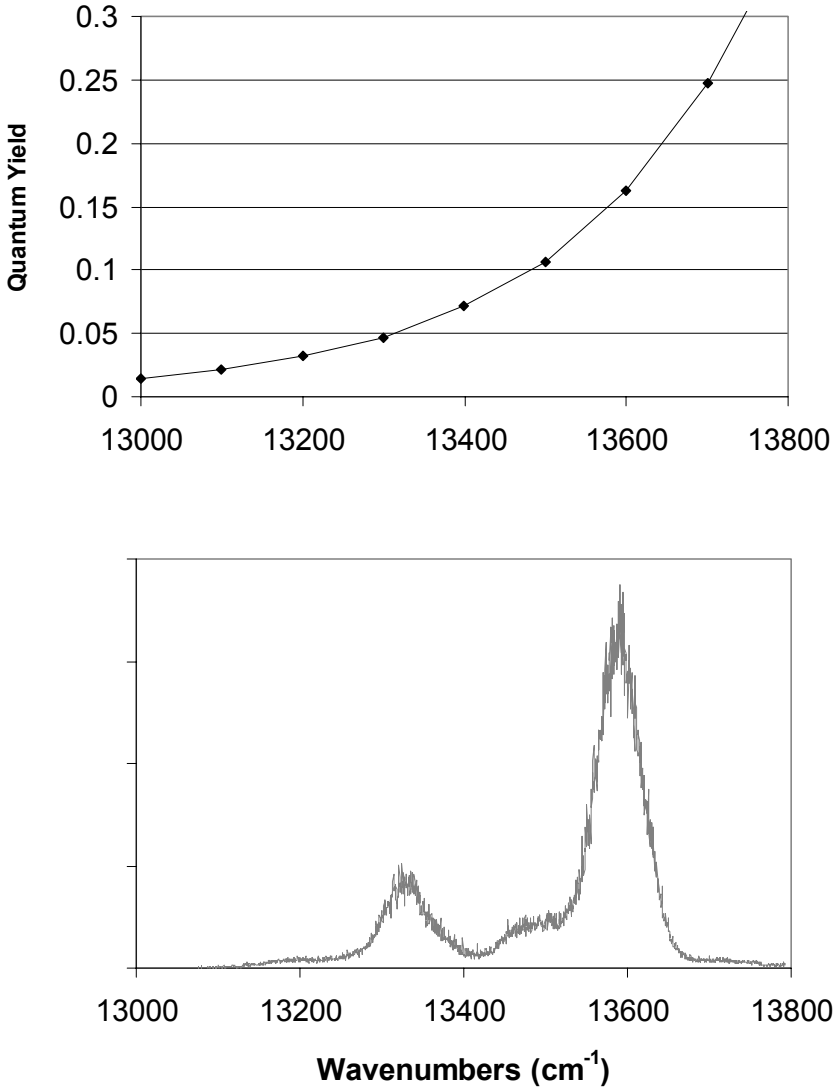

Figure 8-7. Calculated quantum yield (Φ) variation across the $4\nu_{OH}$ spectrum for experimental conditions.

8.5.3. Atmospheric importance of overtone photodissociation

We estimate the clear-sky photolysis rate for HMHP arising from the $4\nu_{OH}$ and $5\nu_{OH}$ transitions from

$$J(\text{HMHP}) = \Phi(\nu)\int \sigma(\nu)I(\nu)d\nu \cong \langle I(\nu)\rangle \int \sigma(\nu)d\nu \qquad (22)$$

where $\Phi(\nu)$ is the estimated quantum yield of photodissociation for atmospheric conditions, $\int \sigma(\nu)d\nu$ is the integrated absorption cross-section, which is related to the calculated oscillator strength by the following relation:[183]

$$\int \sigma(\nu)d\nu = \frac{f}{1.1296\times10^{12}} \Big/ \frac{cm^2}{molecule\ cm^{-1}} \tag{23}$$

and $I(\nu)$ is the frequency-dependent solar spectral actinic flux at the top of the atmosphere. For clear-sky conditions, the atmosphere is essentially transparent at these frequencies, so this is approximately equal to the solar flux at the ground.

Atmospheric quantum yield estimates in the $4\nu_{OH}$ band are estimated based on a comparison of the atmospheric pressure collision rate with observed dissociation rates. The initial percentage of a thermal population above the threshold is only 5% for the 13330 cm^{-1} band and 17% for the 13550 cm^{-1} band, as determined by the quantum yields determined above. Dissociation is observed to be slow, so that at atmospheric conditions, collisional deactivation will dominate the rate of removal of this small above-threshold population by about two orders of magnitude over dissociation. The initial above-threshold population multiplied by the ratio of the dissociation rate to the collision rate is taken as the estimated quantum yield for the two bands in the $4\nu_{OH}$ region.

Results for the four $4\nu_{OH}$ and $5\nu_{OH}$ transitions are given in Table 8-4. The contributions from $4\nu_{OH}$ are negligible due to the very low quantum yields at atmospheric pressure. Integrated cross sections shown are based on the weighted average of the cross sections of the three conformers weighted by their relative contributions. The total overtone

mediated photolysis rate is estimated to be ~ 3.6×10^{-9} s^{-1}. The atmospheric photolysis rate of HMHP via vibrational-overtone excitation is much slower than other loss process for this molecule. By comparison, photolysis in the UV is estimated by Bauerle and Moortgat to be ~ 3×10^{-6} s^{-1} at ground level. The major loss process for HMHP is still likely to be reaction with OH or rainout and deposition.[123]

Table 8-4. Calculated integrated absorption cross sections, dissociation quantum yields, solar spectral actinic flux, and resulting clear sky atmospheric photodissociation rates for overtone bands of HMHP.

	Band center (cm^{-1})	**Integrated cross section[a] (cm^2 $molecule^{-1}$ cm^{-1})**	**Quantum yield**	**Solar flux[b] (photons cm^{-2} s^{-1} / cm^{-1})**	**Photolysis rate (s^{-1})**
$4\nu_{OO\text{-}H}$	13330	1.27×10^{-21}	~0.0002	2.67×10^{13}	$\sim 6.8 \times 10^{-12}$
$4\nu_{RO\text{-}H}$	13550	7.58×10^{-22}	~0.0004	2.58×10^{13}	$\sim 7.8 \times 10^{-12}$
$5\nu_{OO\text{-}H}$	16200	1.17×10^{-22}	1	2.05×10^{13}	2.4×10^{-9}
$5\nu_{RO\text{-}H}$	16550	6.25×10^{-23}	1	1.91×10^{13}	1.2×10^{-9}
				J(total)	**3.6×10^{-9}**

a. Cross sections are weighted averages, based on a population that is 44% HMHP-B, 41% HMHP-C, and 15% HMHP-A.
b. From Seinfeld & Pandis[1] Table 3.1, converted from units of W m^{-2} nm^{-1}.

8.6. Conclusions

The OH vibrational spectroscopy of hydroxymethyl hydroperoxide (HMHP) has been investigated experimentally using FTIR and action spectroscopy and theoretically using *ab initio* predicted structures and a one-dimensional anharmonic oscillator local mode model. With this combined experimental/theoretical approach we have assigned contributions from both OH chromophores (the R–OH and O–OH ends) and from multiple stable conformers of HMHP. The effect of varying quantum yield is also apparent in the

$4\nu_{OH}$ and $5\nu_{OH}$ action spectra. With the aid of statistical state counting we are able to determine the quantum yield as a function of excitation energy and evaluate the atmospheric importance of this overtone-initiated photodissociation process. It is unlikely that the atmospheric lifetime of HMHP will be affected by this process.

8.7. Supporting information

The following tables and figures supply additional detailed information relevant to this chapter. Text (x,y) files of the FTIR spectra shown in Figure 8-8and Figure 8-9 will be available online at http://pubs.acs.org with the publication of this chapter as an article in the Journal of Physical Chemistry A.

Table 8-5. Z-Matrix of optimized geometry of HMHP-A, HMHP-B, and HMHP-C, CCSD(T)/aug'-cc-pVTZ [a]

HMHP-A	**HMHP-B**	**HMHP-C**
O1	O1	O1
C1 1 R2	C1 1 R2	C1 1 R2
H1 1 R3 2 A3	H1 1 R3 2 A3	H1 1 R3 2 A3
H2 2 R4 1 A4 3 D4	H2 2 R4 1 A4 3 D4	H2 2 R4 1 A4 3 D4
H3 2 R5 1 A5 4 D5	H3 2 R5 1 A5 4 D5	H3 2 R5 1 A5 4 D5
O2 2 R6 1 A6 4 D6	O2 2 R6 1 A6 4 D6	O2 2 R6 1 A6 4 D6
O3 6 R7 2 A7 1 D7	O3 6 R7 2 A7 1 D7	O3 6 R7 2 A7 1 D7
H4 7 R8 6 A8 2 D8	H4 7 R8 6 A8 2 D8	H4 7 R8 6 A8 2 D8
Variables:	Variables:	Variables:
R2 = 1.39543173	R2 = 1.40733192	R2 = 1.39940348
R3 = 0.96375469	R3 = 0.96339276	R3 = 0.96255148
R4 = 1.09476547	R4 = 1.08884238	R4 = 1.09317589
R5 = 1.08985693	R5 = 1.09334635	R5 = 1.08958582
R6 = 1.41221324	R6 = 1.40552024	R6 = 1.40998762
R7 = 1.46158782	R7 = 1.45408055	R7 = 1.46081012
R8 = 0.96699084	R8 = 0.96951284	R8 = 0.96704776
A3 = 107.27260324	A3 = 107.90384486	A3 = 107.46217459
A4 = 111.49545679	A4 = 106.40112372	A4 = 111.37328011
A5 = 107.51454293	A5 = 112.30573392	A5 = 107.74235912
A6 = 113.20334702	A6 = 112.27051255	A6 = 113.35758969
A7 = 104.91276565	A7 = 106.33097451	A7 = 105.06243862
A8 = 99.90380078	A8 = 100.88706194	A8 = 99.68649754
D4 = -55.01004630	D4 = 168.82143771	D4 = -43.23496918
D5 = -122.36494810	D5 = -122.68839050	D5 = -122.52535174
D6 = 123.33384465	D6 = 120.89328016	D6 = 123.38100855
D7 = -68.85675108	D7 = -69.80055250	D7 = -70.41308955
D8 = -113.21992691	D8 = 74.84944320	D8 = -246.04086240

a. Bond lengths in Å and angles in degrees.

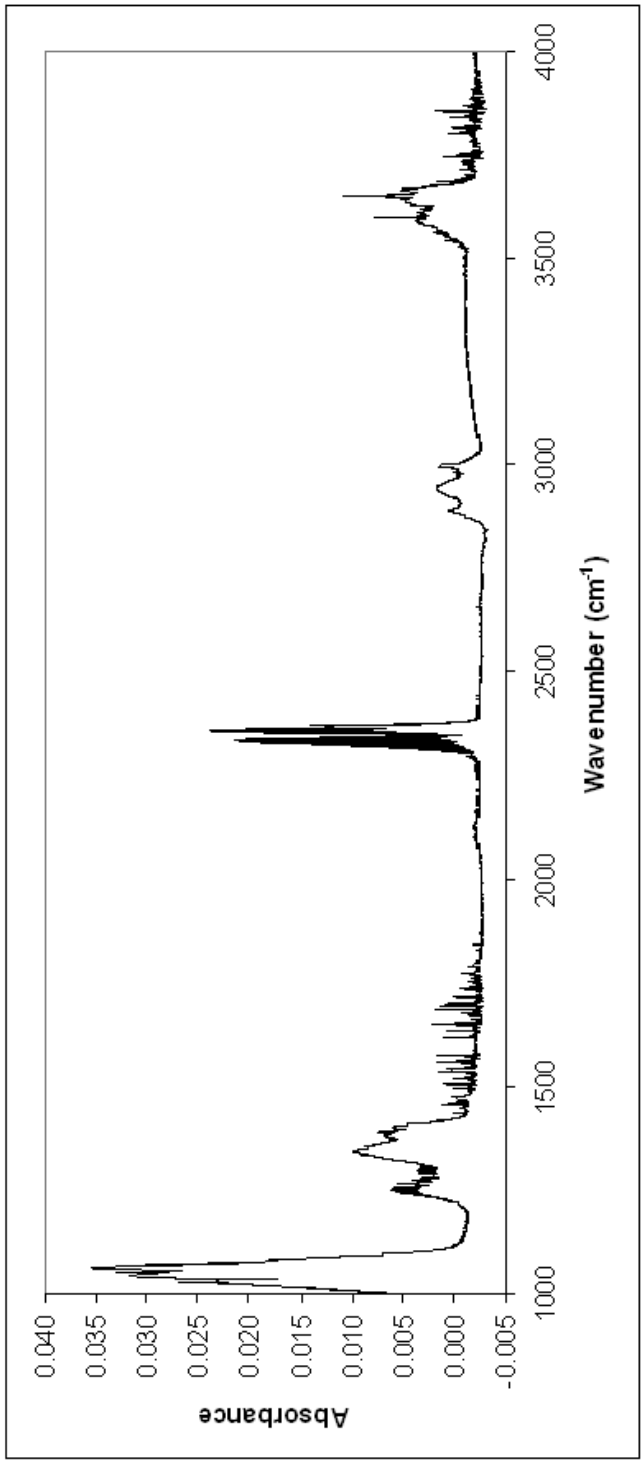

Figure 8-8. FTIR spectrum of HMHP using extended KBR beamsplitter, 1000-4000 cm^{-1}.

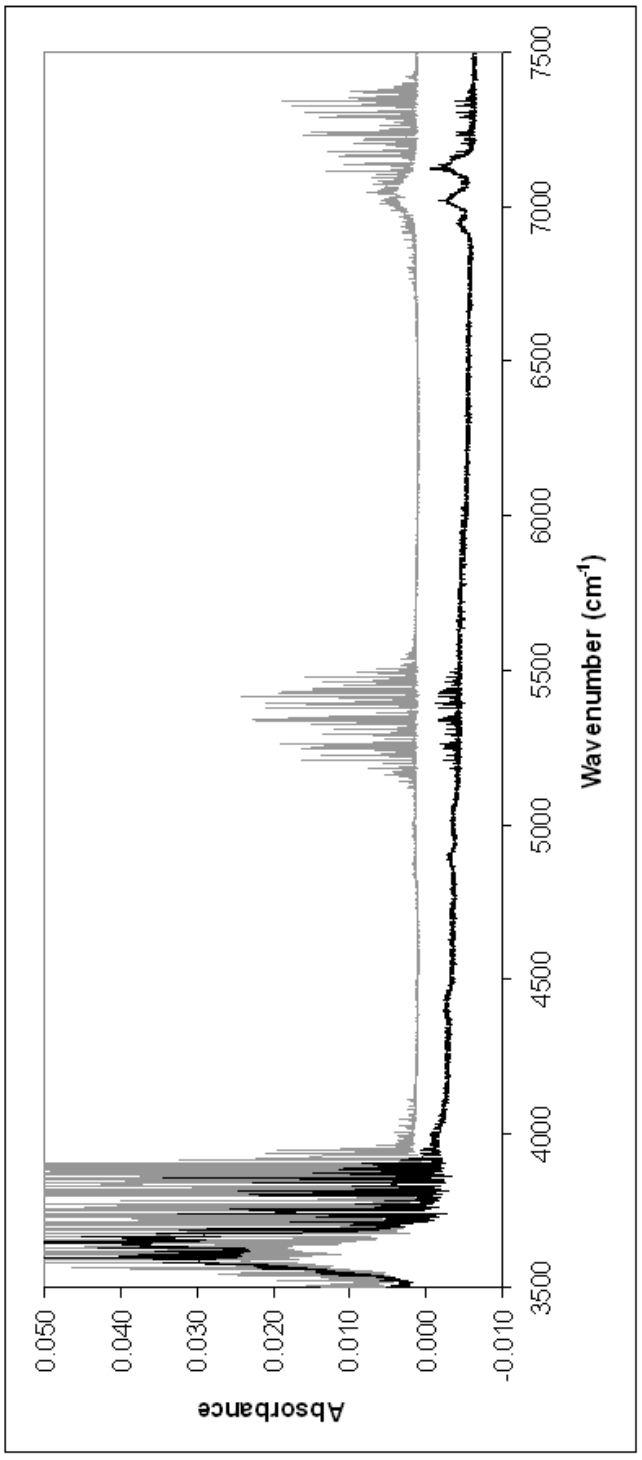

Figure 8-9. FTIR spectrum of HMHP using extended CaF_2 beamsplitter, 3500-7500 cm^{-1} (black). FTIR spectrum of H_2O_2 is shown for reference (grey).

Table 8-6. Observed band positions and relative strengths.

Origin	**Band center from Niki et al.[179] (cm^{-1})**	**Band center (cm^{-1})**	**Relative intensities[a]**
C-O stretch	1050	1049.5	2.7
OO-H bend	1350	1344.9	0.9
C-H stretch	2900	2893.2 2947.2 2999.8	0.4
O**O-H** stretch	3598.1	3598.1	0.7
R**O-H** stretch	3647.8	3647.8	1.0
O-H first overtone region		6947.1	.02
		7022.9	.06
		7125.4	.07

a. Relative intensities are obtained across the entire spectral range by normalizing to the peak height of the RO–H band in the two FTIR spectra. For the 1000 – 4000 cm^{-1} bands, an extended KBr beamsplitter was used, for 4000 – 8000 cm^{-1}, a CaF_2 beamsplitter was used.

Table 8-7. Calculated normal mode frequencies (cm^{-1}) and oscillator strengths for HMHP-A, HMHP-B and HMHP-C.[a]

HMHP-A		**HMHP-B**		**HMHP-C**	
ν	*f*	ν	*f*	N	*f*
169.9	2.27×10^{-7}	172.9	4.55×10^{-6}	178.0	4.17×10^{-6}
248.2	1.44×10^{-5}	311.1	1.42×10^{-5}	221.5	3.46×10^{-5}
352.9	1.69×10^{-5}	391.6	1.58×10^{-5}	385.9	1.78×10^{-6}
462.2	1.23×10^{-5}	437.9	1.29×10^{-5}	450.1	5.82×10^{-6}
615.0	4.51×10^{-6}	634.6	3.72×10^{-6}	623.8	1.99×10^{-6}
893.7	5.29×10^{-6}	907.3	4.13×10^{-6}	900.0	4.92×10^{-6}
1045.6	4.18×10^{-6}	1060.8	1.55×10^{-5}	1056.1	4.93×10^{-6}
1097.0	1.44×10^{-5}	1085.1	7.19×10^{-6}	1086.5	1.48×10^{-5}
1132.2	3.04×10^{-5}	1111.3	2.15×10^{-5}	1118.7	3.00×10^{-5}
1308.5	1.13×10^{-6}	1302.2	4.37×10^{-6}	1302.8	2.67×10^{-6}
1378.5	9.33×10^{-6}	1398.8	9.21×10^{-7}	1399.9	8.49×10^{-6}
1415.8	2.47×10^{-6}	1419.0	1.07×10^{-5}	1414.5	3.29×10^{-6}
1450.7	1.01×10^{-5}	1447.3	6.91×10^{-6}	1444.0	6.31×10^{-6}
1516.6	2.23×10^{-7}	1516.8	6.38×10^{-7}	1517.2	4.78×10^{-7}
3055.6	9.61×10^{-6}	3081.5	6.17×10^{-6}	3074.0	7.40×10^{-6}
3153.6	2.62×10^{-6}	3161.5	2.72×10^{-6}	3159.2	2.46×10^{-6}
3814.4	7.93×10^{-6}	3783.2	5.40×10^{-6}	3815.0	7.90×10^{-6}
3861.9	8.27×10^{-6}	3860.4	7.83×10^{-6}	3875.4	7.56×10^{-6}

a. Calculated at the QCISD/aug′-cc-pVTZ optimized geometry. The frequencies are unscaled.

CHAPTER 9

ATMOSPHERIC SEARCH FOR HOONO

Chapter 9

9. ATMOSPHERIC SEARCH FOR HOONO

9.1. Introduction

In chapters 3 and 4 our current understanding of HOONO's role as a temporary HO_x and NO_x reservoir in the atmosphere was presented. Based on these and other laboratory and theoretical studies of HOONO,[9,25,26,32,33,54,58,62,93,97] we now have a well-defined picture of OH + NO_2 atmospheric chemistry. Detection of HOONO in the atmosphere would be excellent confirmation of our laboratory-based conception of the role it plays in the atmosphere. Because instruments exist to monitor atmospheric concentrations of molecules by measuring rotational transitions in the submillimeter wavelength region, we can apply our knowledge of the rotational spectrum and dipole moment of the atmospherically relevant conformer, *cis-cis* HOONO (presented in chapter 5), to an atmospheric search using existing instrumentation.[§§]

Many scientific efforts and technologies employ transmission or emission and detection in the submillimeter wavelength range (0.3 – 1.0 mm, 300 – 1000 GHz). These efforts include spectroscopy, radar, satellite communications, and the growing scientific field of submillimeter astronomy. These applications have driven the development of a robust series of submillimeter sources and detectors for wavelengths throughout this band which enable highly precise broad band laboratory measurements of the submillimeter

[§§] From this point forward, "HOONO" will refer only to the atmospherically relevant, more stable *cis-cis* HOONO conformer.

spectroscopy of molecules, and subsequent atmospheric measurement using selected strong rotational transitions. Due to the high resolution of these measurements, vertical profiles of trace atmospheric species can be obtained by a retrieval that depends on the pressure-broadening of the lines.

A multitude of instruments for measurement of atmospheric trace gases in the microwave and submillimeter wavelength region were proposed after the initial successful proof of principle by the Upper Atmosphere Research Satellite (UARS) Microwave Limb Sounder in 1991.[184] Later instruments have targeted the shorter submillimeter wavelength range, where the statistical peak in lower-state population occurs for many small atmospheric molecules and radicals. Some of these later-generation submillimeter instruments include the Odin Submillimeter Radiometer (Odin), a joint mission of Sweden, Canada, France, and Finland; the Superconducting Submillimeter-wave Limb-emission Sounder (SMILES) of the Japan Aerospace Exploration Agency; the Compact Scanning Submillimeter-wave Imaging Radiometer (CoSSIR) of NASA Goddard Space Flight Center; Airborne Millimeter- and Submillimeter Observing System (AMSOS) of the University of Bern, Switzerland; the Airborne Submillimeter Radiometer (ASUR) of the University of Bremen; and the Submillimeter Limb Sounder (SLS) of the NASA Jet Propulsion Lab. The latter two will be discussed in greater detail below, as the two target platforms for an atmospheric HOONO search.

Based on the measured dipole moment of HOONO (Chapter 5) and an estimation of the HOONO vertical column (Figure 1-2, p. 8), we can calculate an estimate of the intensity of the atmospheric signal expected from HOONO as viewed by each of the two

selected instruments. This will aid in assessing the viability of an atmospheric search for HOONO by looking for submillimeter emission.

9.2. Targeted instruments for field measurement of HOONO

9.2.1. Choice of HOONO line for atmospheric search

The choice of which HOONO line to search for in the atmosphere is made based on criteria of highest possible line strength with least possible spectral confusion (i.e., as far as possible from neighboring O_3 lines, etc.) in the submillimeter frequency range accessible by available instruments (~605 – 660 GHz). This screening process was accomplished with the aid of Brian Drouin's Submillimeter Analysis Program (SMAP) software[185] for submillimeter spectral simulation. Using this program and known rotational parameters for all the major stratospheric trace constituents, a composite spectrum was generated including HOONO and other atmospheric species. Strong, lone HOONO lines were selected as top candidates. Next, we looked to the available instrumental platforms to compare the candidate HOONO line positions to the regions of the spectrum that are routinely measured.

9.2.2. Airborne submillimeter radiometer (ASUR)

The University of Bremen / Space Research Organization of the Netherlands Airborne Submillimeter Radiometer (ASUR) measures the thermal emission of trace atmospheric gases in the frequency range 604 – 662 GHz.[186-189] It has flown on multiple aircraft based field campaigns, most recently focusing on chemistry in the polar stratosphere[189,190] where HOONO concentrations may be expected to be relatively high due

to the high concentration of HNO_3 prior to denitrification. The accessible altitude range for this uplooking geometry (zenith angle 78°, Figure 9-1) radiometer is approximately 15 – 50 km. ASUR is designed to operate onboard an aircraft flying at an altitude of at least 10 km to avoid tropospheric water vapor absorption and to enable retrieval of vertical profiles of the volume mixing ratio (VMR) of measured species by analysis of the pressure-broadened lineshape.

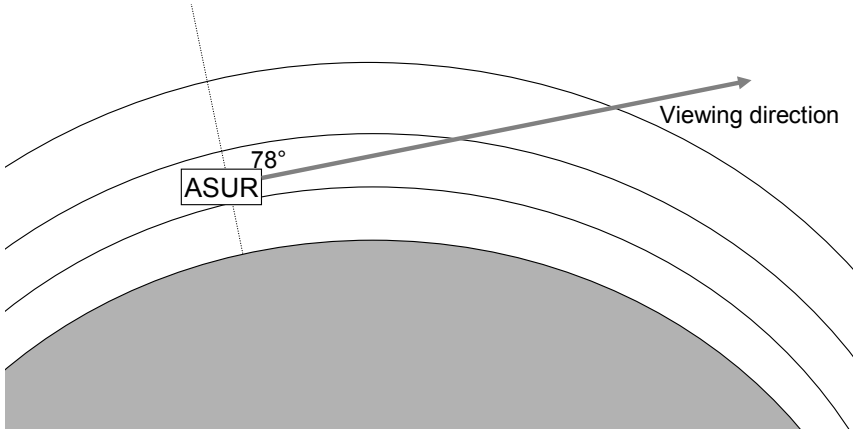

Figure 9-1. Uplooking (ZA = 78°) viewing geometry (not to scale).

The trace gas emission lines routinely measured by the ASUR instrument include HCl, O_3, ClO, N_2O, HNO_3, CH_3Cl, H_2O, BrO, HO_2, HCN, and NO. One of the N_2O line windows used in previous years, a 1.4 GHz wide window centered at 627.288 GHz, fortuitously contains a very strong HOONO line from the list of candidate lines. The HOONO line center is at 627.060 GHz. It is well removed from any ozone or other interfering lines and is the third strongest line in the candidate list. The two stronger HOONO lines would be obscured by O_3 emission.

Because this is a frequency region that has been used before by this spectrometer, calibration to do this window again should be relatively easy. In addition, some archival data exists from field campaigns in 1995, 1996, and 1997 when this region was scanned. It was abandoned for N_2O detection because the spectral feature was not strong enough, and an unanticipated rare O_2 isotopomer line dominates the region, possibly swamping any other trace gas features. Nevertheless, this dataset of approximately 30 spectra from winter Arctic measurements was scoured in search of any sign of HOONO. In fact, in three spectra, a small bump appeared in the spectra at the expected HOONO line position. The spectrum in which this feature is strongest is shown in Figure 9-2, with a zoomed-in view of the HOONO line position in the inset.

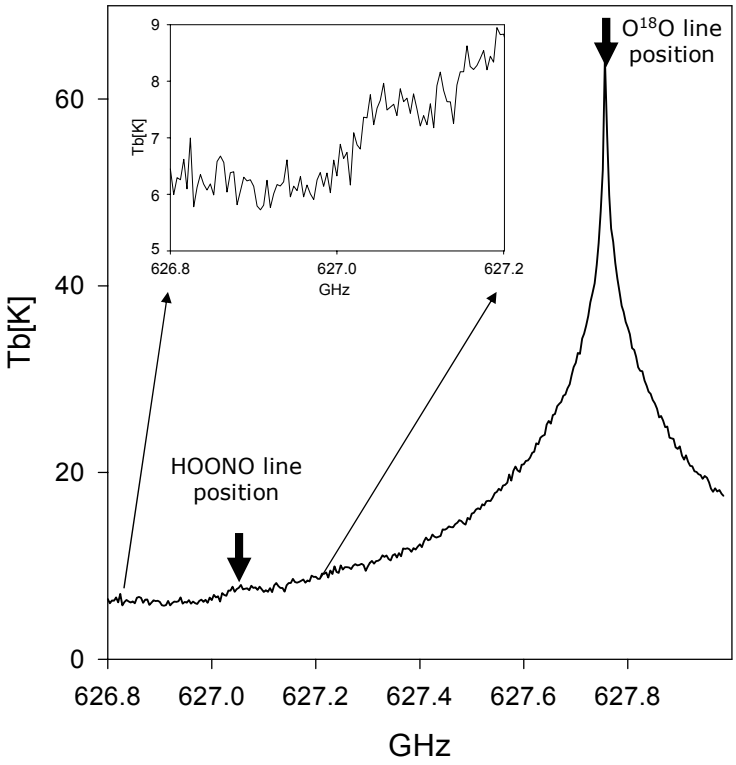

Figure 9-2. ASUR spectrum from flight on Feb 21, 1997 at 71.2°N latitutde, SZA = 83.5, with "bump" at HOONO line position indicated. The major line in this window is an O_2 isotopomer, $O^{18}O$. Inset: Zoomed in spectrum of "bump." Data courtesy of Armin Kleinböhl.

The observation of a feature at the HOONO frequency is enticing, but it was only observed in three discrete spectra in the entire data set of about 50 spectra, so we must be cautious in assigning it to HOONO. The possible detections did all occur at a high SZA, consistent with the expectation that HOONO concentration would be maximized when there is enough light to generate the constituent OH and NO_2 radicals but not enough light to photodissociate HOONO, since its near-IR dissociation is efficient. Still, the signal is

weak and intermittent. A persistent feature would be more convincing. In addition, the intensity of the observed peak, $T_b \sim 0.5$ K, must be compared the expected emission of HOONO in the atmosphere given our best guess vertical profile of HOONO. The calculation of this expected signal is outlined in section 9.3.1.

9.2.3. Submillimeter limb sounder (SLS)

The NASA Jet Propulsion Laboratory Submillimeter Limb Sounder (SLS) is also designed to measure thermal emission of trace atmospheric gases, in this case from a balloon platform that floats at high altitude (~ 30 km) and views emission through the limb of the atmosphere (shown schematically in Figure 9-3). This geometry affords a longer path length, and vertical profiles can be measured directly by varying the viewing direction.

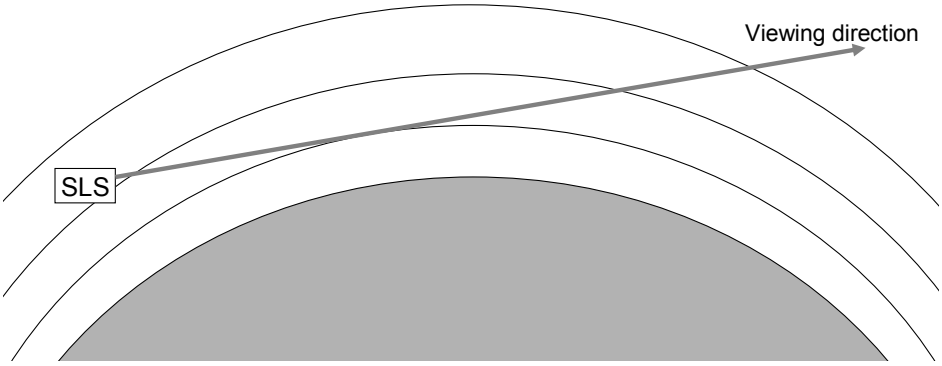

Figure 9-3. Limb sounding viewing geometry (not to scale).

The first generation SLS was demonstrated in 1992 for the measurement of stratospheric ClO, HCl, O_3, and HO_2.[191] It is a heterodyne radiometer measuring thermal emission around 640 GHz, which is designed for operation from a high altitude balloon. At float altitude (~30-40 km), the gondola containing the instrument is stabilized and oriented

using a pointing system so that vertical profiles can be accurately obtained by scanning a flat mirror from +1.0° to –6.0° in 0.2° steps, which correspond to approximately 2 km tangent height intervals.[191,192] This instrument has since been used to measure vertical profiles of HNO_3, N_2O, NO, NO_2, OH, $ClNO_3$, H_2O, CH_4, and N_2O_5 in addition to the species mentioned above.[191-194] In recent years, the instrument has been updated with state-of-the-art technology and very recently completed its first flights with updated hardware. Results are pending from these recent flights, in which the HOONO line at 627.060 GHz was scanned, among others. The manager of the SLS instrument, Robert Stachnik, is currently working on the retrieval of this data.

9.3. Estimate of expected atmospheric HOONO signal strength

The signal in both of these spectrometers is retrieved in terms of brightness temperature (T_b), which is a measure of the strength of emission. Using the known line strengths (due to the known dipole moment) and the estimated column sampled in the atmosphere, this brightness temperature can be quantitatively related to the number of HOONO molecules in that column.

The peak brightness temperature in the limit of local thermal equilibrium, optically thin emission, and a negligible background emission is[101]

$$T_b = \frac{\int_{-\infty}^{\infty} T_b d\nu}{1.064\Delta\nu} = \frac{1}{1.064\Delta\nu}\frac{hc^3}{8\pi k\nu^2} A g_u \frac{N_{tot}}{Q(T_{rot})} e^{-E_u/kT_{rot}} \qquad (24)$$

where 1.064 Δν is the conversion from integrated intensity to peak brightness for a Gaussian transition of FWHM Δν, ν is the transition frequency, N_{tot} is the averaged total column density, A is the rate of spontaneous emission (Einstein A-coefficient), g_u is the upper state degeneracy, $Q(T_{rot})$ is the partition function, T_{rot} is the molecular temperature, and E_u is the upper state energy. The emission rate can be calculated as:[195]

$$Ag_u = \frac{I(\nu)Q(T)\nu^2 2.7964\times10^{-16}}{e^{-E_l/kT} - e^{-E_u/kT}} \text{ sec}^{-1} \quad (25)$$

where $I(\nu)$ is in nm^2 MHz and ν in MHz and E_l and E_u are the lower and upper state energies.

Thus, given our estimated HOONO vertical column (Figure 1-2, p. 8), we can determine what brightness temperature would correspond to our model expectations for the amount of HOONO in the atmosphere. This would serve as a verification of our understanding of the role of HOONO.

9.3.1. Expected ASUR signal

The expected ASUR signal is calculated from the previously calculated HOONO vertical column (Figure 1-2, p. 8) above the flight altitude of 15 km and the simplified idea that at a viewing geometry of 78°, the vertical column observed will be the surface normal vertical column above the flight altitude divided by cos(78°). The total HOONO vertical column 15 km – 60 km is 9.85×10^{14} molecules cm^{-2}. By simple geometry, the slant column at 78° zenith angle has a path length of 216 km and HOONO column of 4.74×10^{15} molecules cm^{-2}.

For the HOONO slant column of 4.74×10^{15} molecules cm^{-2} viewed by ASUR, equations 24 and 25 give $T_b = 0.4$ K. This calculated signal strength is in the range of the signal observed in Figure 9-2, making it possible that this signal was real, but again, the lack of persistence of the signal casts doubt on the assignment. We turn to the SLS instrument, where signal should be stronger because limb viewing geometry results in longer atmospheric path length.

9.3.2. Expected SLS signal

The analogous simple geometrical determination of effective column for the SLS spectrometer depends on viewing angle. We will determine an upper limit by considering a float altitude of 30 km with a viewing angle that is tangent to the surface normal at 20 km, which is equivalent to $\theta = -3.2°$, or ZA = 93.2°. This minimum altitude of 20 km is chosen because at lower altitudes, line broadening decreases the signal strength, in spite of larger HOONO path length. Geometrical considerations show that if we consider up to 60 km altitude (at this altitude the HOONO concentration is negligibly small, so this is sufficient), the path length through the atmosphere at this viewing angle is 1253 km, and the total HOONO column is 2.57×10^{16} molecules cm^{-2}, more than double the column viewed by the ASUR instrument. The corresponding (upper limit) brightness temperature expected is $T_b = 2.3$ K.

This estimate is relatively unsophisticated, however, because it does not take into account any pressure broadening of lines or any detailed radiative transfer. As such, it is to be considered an upper limit for the expected brightness temperature.

A more sophisticated forward model of the expected brightness temperature can be calculated using the modular program ARTS, the atmospheric radiative transfer simulator.[196] Armin Kleinböhl (JPL) kindly ran this forward model for the case of SLS instrument float altitude 30 km, with a series of tangent altitudes (labeled h_T), for a HOONO vertical column that is 10% of HNO_3. This is a crude estimate of the HOONO column, which underestimates the total vertical column (to the best of our knowledge) by ~ 35%. The result of this forward model is shown in Figure 9-4. Using this model, the maximum HOONO signal is predicted to be $T_b = 0.9$ K. Since this model underestimates what we believe the HOONO column to be, this may represent the lower bound of expected HOONO signal. The SLS spectrometer is capable of measuring signals down to $T_b \sim 0.5$ K at this frequency; hence, I am hopeful that the SLS instrument may prove capable of measuring HOONO in the atmosphere.

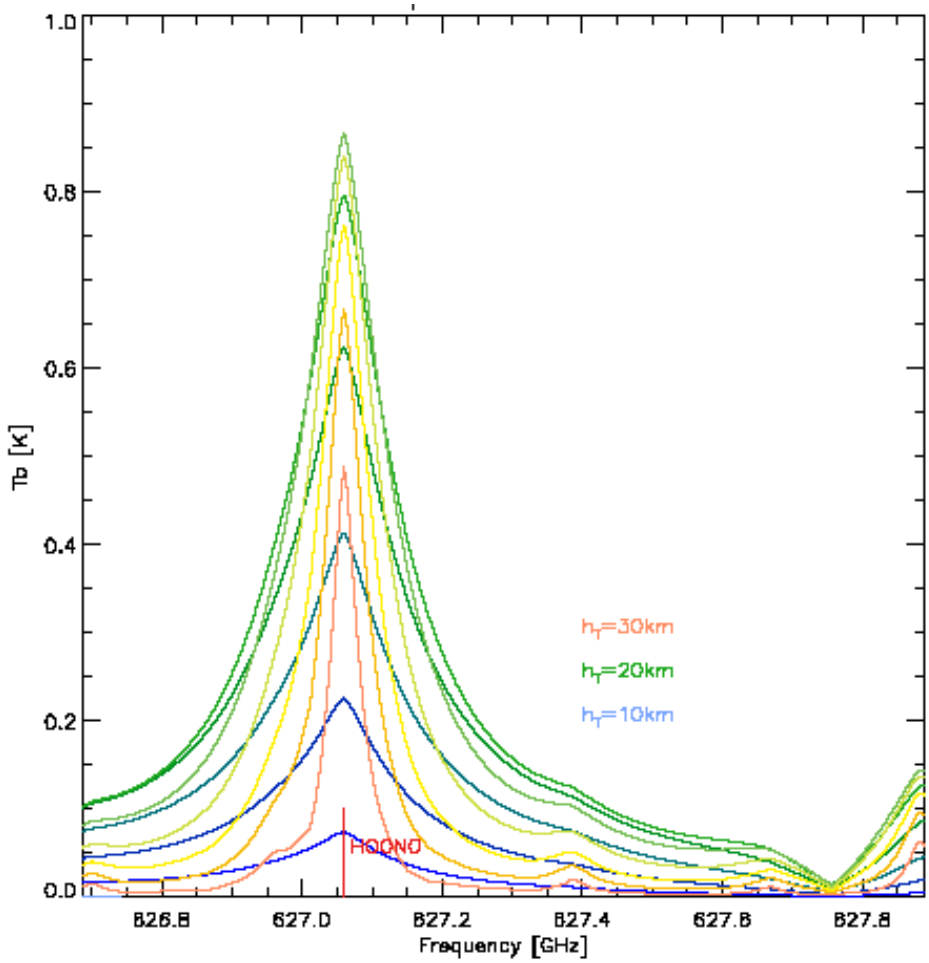

Figure 9-4. ARTS forward model of HOONO signal using SLS instrument. Float altitude, 30 km, tangent altitude of viewing variable, HOONO column fixed to 10% HNO_3 column. Model results courtesy Armin Kleinböhl.

9.4. Outlook

We have looked for HOONO signal in a fortuitously scanned region of the submillimeter spectrum in archival data from the aircraft-based University of Bremen Airborne Submillimeter Radiometer (ASUR) and have initiated a targeted search for the same HOONO line at 627.060 GHz using the balloon-borne JPL Submillimeter Limb

Sounder (SLS). The SLS instrument benefits from a longer atmospheric path length as well as the ability to measure above the pressure-broadening and line confusion of the lower stratosphere. With a predicted HOONO signal strength of 0.9 – 2.3 K for the SLS spectrometer and a detection limit of approximately 0.5 K, it is plausible that this latter HOONO measurement may succeed if our understanding of the role of HOONO in the atmosphere and the resultant predicted vertical profile are correct. With the help of submillimeter field measurement experts Armin Kleinböhl and Robert Stachnik, I hope to have this data analyzed in the near future.

APPENDIX I:
ROLE OF OH-STRETCH/TORSION COUPLING AND QUANTUM YIELD EFFECTS IN THE FIRST OH OVERTONE SPECTRUM OF *CIS-CIS* HOONO

THE JOURNAL OF CHEMICAL PHYSICS **122**, 104311 (2005)

Role of OH-stretch/torsion coupling and quantum yield effects in the first OH overtone spectrum of *cis-cis* HOONO

Anne B. McCoy[a)]
Department of Chemistry, The Ohio State University, Columbus, Ohio 43210

Juliane L. Fry
Arthur Amos Noyes Laboratory of Chemical Physics, California Institute of Technology, Pasadena, California 91125

Joseph S. Francisco
Department of Chemistry, Purdue University, West Lafayette, Indiana 47907

Andrew K. Mollner and Mitchio Okumura[b)]
Arthur Amos Noyes Laboratory of Chemical Physics, California Institute of Technology, Pasadena, California 91125

(Received 24 November 2004; accepted 21 December 2004; published online 11 March 2005)

A joint theoretical and experimental investigation is undertaken to study the effects of OH-stretch/HOON torsion coupling and of quantum yield on the previously reported first overtone action spectrum of *cis-cis* HOONO (peroxynitrous acid). The minimum energy path along the HOON dihedral angle is computed at the coupled cluster singles and doubles with perturbative triples level with correlation consistent polarized quadruple ζ basis set, at the structure optimized using the triple ζ basis set (CCSD(T)/cc-pVQZ//CCSD(T)/cc-pVTZ). The two-dimensional *ab initio* potential energy and dipole moment surfaces for *cis-cis* HOONO are calculated as functions of the HOON torsion and OH bond length about the minimum energy path at the CCSD(T)/cc-pVTZ and QCISD/AUG-cc-pVTZ (QCISD—quadratic configuration interaction with single and double excitation and AUG-augmented with diffuse functions) level of theory/basis, respectively. The OH-stretch vibration depends strongly on the torsional angle, and the torsional potential possesses a broad shelf at ~90°, the *cis-perp* conformation. The calculated electronic energies and dipoles are fit to simple functional forms and absorption spectra in the region of the OH fundamental and first overtone are calculated from these surfaces. While the experimental and calculated spectra of the OH fundamental band are in good agreement, significant differences in the intensity patterns are observed between the calculated absorption spectrum and the measured action spectrum in the $2\nu_{OH}$ region. These differences are attributed to the fact that several of the experimentally accessible states do not have sufficient energy to dissociate to $OH+NO_2$ and therefore are not detectable in an action spectrum. Scaling of the intensities of transitions to these states, assuming $D_0=82.0$ kJ/mol, is shown to produce a spectrum that is in good agreement with the measured action spectrum. Based on this agreement, we assign two of the features in the spectrum to $\Delta n=0$ transitions (where n is the HOON torsion quantum number) that are blue shifted relative to the origin band, while the large peak near 7000 cm^{-1} is assigned to a series of $\Delta n=+1$ transitions, with predominant contributions from torsionally excited states with substantial *cis-perp* character. The direct absorption spectrum of *cis-cis* HOONO (6300–6850 cm^{-1}) is recorded by cavity ringdown spectroscopy in a discharge flow cell. A single band of HOONO is observed at 6370 cm^{-1} and is assigned as the origin of the first OH overtone of *cis-cis* HOONO. These results imply that the origin band is suppressed by over an order of magnitude in the action spectrum, due to a reduced quantum yield. The striking differences between absorption and action spectra are correctly predicted by the calculations. © *2005 American Institute of Physics*. [DOI: 10.1063/1.1859273]

I. INTRODUCTION

Peroxynitrous acid, HOONO, is a weakly bound isomer of nitric acid that is formed as a secondary product of the reaction:

$$OH + NO_2 + M \rightarrow HONO_2 + M, \quad \Delta_{1a}H^0(0) = -204 \text{ kJ/mol}, \tag{1a}$$

$$OH + NO_2 + M \rightarrow HOONO, \quad \Delta_{1b}H^0(0) = -82.0 \text{ kJ/mol}. \tag{1b}$$

Reaction (1a) is a critical radical chain termination step in the atmosphere, as OH and NO_2 combine to form stable

[a)]Author to whom correspondence should be addressed. Electronic mail: mccoy@chemistry.ohio-state.edu
[b)]Author to whom correspondence should be addressed. Electronic mail: mo@caltech.edu

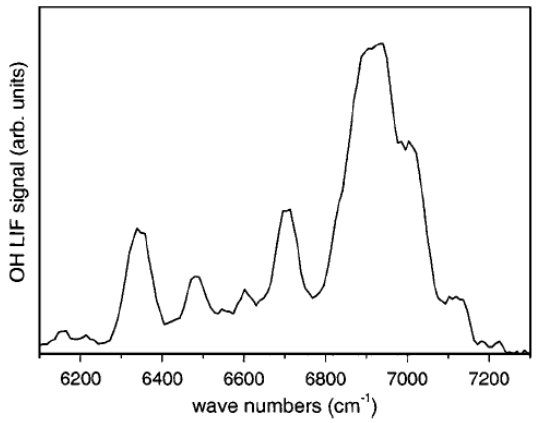

FIG. 1. Smoothed action spectrum of the first overtone of the OH stretch ($2\nu_{OH}$) band in *cis-cis* HOONO, recorded at 10 Torr, 300 K (Refs. 1 and 6).

nitric acid. Channel (1b) reduces the efficacy of reaction (1a) as a sink of HO_x and NO_x radicals, because HOONO rapidly redissociates under atmospheric conditions. HOONO has been the focus of many studies in the past two decades, but only recently has there been direct evidence for its existence and formation in the gas phase under thermal conditions.[1–4]

Theoretical studies establish the stability of HOONO and have identified several minima and transition states. The lowest energy conformer is *cis-cis* HOONO, a planar ring structure in which the OH forms a weak intramolecular hydrogen bond with the terminal O atom. The *trans-perp* conformer, with the heavy atoms in a plane in a *trans* configuration and the OH bond perpendicular to that plane, has been predicted to lie 15.3 kJ/mol (1280 cm^{-1}) higher in energy at the CCSD(T)/cc-pVTZ level of theory.[5,6]

A third postulated minimum corresponds to the *cis-perp* geometry in which the heavy atoms are in a plane in a *cis* configuration and the OH bond is perpendicular to that plane. This conformer was first investigated by McGrath and Rowland at the MP2/6-311+G($3df$,$2p$) (MP2–Møller-Plesset perturbation theory truncated at the second order) level of theory,[7] and has since been studied by several groups at various levels of theory.[4,8–12] The calculations of Golden *et al.* at the QCISD(T)/cc-pVDZ level[5] (QCISD—quadratic configuration interaction with single and double excitation) and Bean *et al.* at the CCSD(T)/cc-pVTZ level[2] demonstrate that higher levels of theory are required for a good description of HOONO. Attempts to locate a *cis-perp* HOONO minimum at the CCSD(T) level have been unsuccessful,[5,6,13] calling into question earlier predictions of a *cis-perp* minimum. In the first spectroscopic detection of HOONO, Lee and co-workers reported matrix-isolation spectra of two of the HOONO isomers, *cis-cis* and *trans-perp* HOONO, but did not observe the *cis-perp* isomer.[14,15]

Recently, Nizkorodov and Wennberg reported the first direct spectroscopic detection of HOONO in the gas phase,[1] reproduced in Fig. 1. In this experiment, excitation of HOONO in the near infrared at the first OH stretch overtone ($2\nu_{OH}$) region was detected by monitoring OH products from vibrational predissociation. The observed spectrum was unusual, with a series of broad peaks from 6300 to 7200 cm^{-1}. A peak at 6365 cm^{-1} was identified as the $2\nu_{OH}$ origin, but the spectrum was dominated by a large, partially blended peak at 6970 cm^{-1}. Nizkorodov and Wennberg tentatively assigned the peaks based on *ab initio* predictions to all three conformers of HOONO, but the lack of observable structure did not allow a definitive assignment.

More recent studies have shown that *trans-perp* HOONO has a spectrum distinct from that shown in Fig. 1,[6,16] and isomerizes quickly to the more stable *cis-cis* conformer (millisecond time scale at room temperature and ~10 Torr).[6] Fry *et al.* therefore attribute all of the bands reported by Nizkorodov and Wennberg to the lowest energy conformer, *cis-cis* HOONO. Matthews *et al.*[17] conclude that the strong 6970 cm^{-1} band is due to *trans-perp* HOONO; however, this is at odds with the experimental observations of Fry *et al.*

The appearance of the action spectrum of HOONO is unusual. A typical overtone spectrum comprises a strong origin band and weaker satellite features; the weak bands are either combination bands (including Fermi Resonances) or hot bands (including sequence bands). The majority of the oscillator strength is typically carried in the local $2\nu_{OH}$ mode. Any assignment of the *cis-cis* HOONO overtone spectrum must explain why this origin band is relatively weak.

One factor that may be important in understanding the anomalous intensity pattern of the overtone action spectrum is the wavelength dependence of the quantum yield. The quantum yield is unity if the photon energy is greater than the dissociation energy D_0. Konen *et al.* now estimate a D_0 for *cis-cis* HOONO of 82.0 kJ/mol (6860 cm^{-1}).[18] All of the bands in the action spectrum that are below the dissociation threshold of 6860 cm^{-1} must be hot bands. Rice–Ramsperger–Kassel–Marcus (RRKM) calculations by Fry *et al.* indicate that the quantum yield falls off rapidly below this limit.[6] Thus, the intensity of bands at frequencies below D_0 would be suppressed.

A second feature of *cis-cis* HOONO that may be responsible for the anomalous intensity patterns is the presence of an intramolecular hydrogen bond, which couples the OH stretch with low-frequency, large amplitude modes near the equilibrium configuration. The internal hydrogen bond causes a redshift in the OH-stretch frequency in *cis-cis* HOONO, with an observed fundamental frequency of 3306 cm^{-1};[2] based on the expected anharmonic correction, the origin of the *cis-cis* HOONO first overtone is the 6365 cm^{-1} band. Torsional motion about the OO bond (the HOON dihedral angle, here referred to as τ) will break the hydrogen bond and lead to a blueshift of the OH bond frequency back to ≈3530 cm^{-1}. The intensity of the OH stretch is predicted to be weaker in the hydrogen-bonded form, by a factor of 1.5 in the double harmonic approximation (QCISD/AUG-cc-pVDZ). Thus, torsionally excited molecules, in which the hydrogen bond is effectively broken, may have absorption bands that are blueshifted and possess larger cross sections than the *cis-cis* HOONO origin.

The above considerations lead to the following hypothesis. The overtone action spectrum observed by Nizkorodov

and Wennberg (Fig. 1) is that of *cis-cis* HOONO, but the relative band intensities deviate significantly from the expected absorption spectrum due to quantum yield effects. The origin and combination bands below D_0 will appear weak, because they have a reduced quantum yield for dissociation. The strong bands at 6970 cm^{-1} arise from hot, torsionally excited molecules for which the internal hydrogen bond has been broken, resulting in a vibrationally averaged frequency of the OH bond close to that of a free OH stretch. The pure absorption spectrum will possess a strong origin band, but will still have significant hot bands and sequence bands with large spectral shifts to the blue that arise from strong coupling between the OH stretch and the low-frequency torsional modes, particularly the HOON torsion.

The present work is a joint theoretical and experimental effort to investigate this hypothesis. We have calculated the absorption and action spectra of *cis-cis* HOONO in the fundamental and first overtone region from first principles, using a two-dimensional model that explicitly treats the OH stretch and HOON torsional degrees of freedom, and experimentally measured the first overtone spectrum of HOONO in direct absorption.

(i) An *ab initio* minimum energy path along the HOON torsional coordinate τ was generated at the CCSD(T)/cc-pVTZ level with the OONO dihedral angle frozen so that the heavy atoms lie in a plane. CCSD(T) energies were also calculated with a cc-pVQZ basis set at the same nuclear geometries. This calculation provides the most accurate prediction to date of the HOON torsional potential, including the *cis-perp* HOONO conformer.

(ii) Electronic energies and the dipole moment components were calculated as functions of the OH stretch coordinate r for fixed HOON angles τ at the CCSD(T)/ccpVTZ and QCISD/AUG-cc-pVTZ level of theory/basis, respectively.

(iii) Two-dimensional quantum mechanical calculations were performed to solve for the torsion-vibration energy levels and transition moments from the resulting surfaces.

(iv) Both absorption and action spectra at 300 K were calculated. The action spectrum was predicted by convoluting the calculated absorption spectrum with a simplified quantum yield. The temperature dependence of this action spectrum was investigated by calculating spectra at 233 and 300 K.

(v) The absorption spectrum was recorded in the region 6300–6800 cm^{-1} by cavity ringdown spectroscopy and compared to the experimental action spectrum and to the theoretical predictions.

II. THEORETICAL AND COMPUTATIONAL METHODS

A. Torsional potential

In order to investigate the role of torsional motion in the *cis-cis* HOONO spectrum in the region of the first overtone, we first calculated a one-dimensional potential surface $V^{\mathrm{MEP}}(\tau)$. This surface is a minimum energy path through the HOONO surface, as a function of the HOON torsion angle τ evaluated at increments of 10°. The OONO dihedral angle was fixed to 0° (the *cis* configuration) and the values of the remaining seven internal coordinates were optimized to minimize the total energy. The potential was calculated using the coupled-cluster method with single and double excitations which incorporated a perturbative estimate of the effects of connected triple excitations [CCSD(T)].[19–21] The Dunning correlation consistent cc-pVTZ basis set was used.[22–24] The Hessian from a quadratic configuration interaction with single and double excitation (QCISD) method[25] optimization of the geometry was used for the geometry optimization at the CCSD(T) level. The energies along the minimum energy path were also calculated at the CCSD(T)/cc-pVQZ level for the geometries previously optimized at the CCSD(T)/cc-pVTZ level of theory and basis set. To distinguish between these two minimum energy paths, we denote them by $V^{\mathrm{MEP}}_{\mathrm{pVTZ}}(\tau)$ and $V^{\mathrm{MEP}}_{\mathrm{pVQZ}}(\tau)$, respectively. The GAUSSIAN98 program[26] was used in all the calculations.

B. Two-dimensional torsion-stretch potential energy and dipole surfaces

To explore further the vibrational states of *cis-cis* HOONO, two-dimensional potential and dipole moment surfaces were evaluated as functions of r and τ, with the remaining seven coordinates constrained to their values on the minimum energy path surface. The potential points were evaluated at the CCSD(T)/cc-pVTZ level of theory/basis set, while the dipole moment surface was evaluated at the QCISD/AUG-cc-pVTZ level of theory/basis set. The potential and dipole surfaces were evaluated for 13 angles and 13 OH distances. The values of r ranged from $r_e(\tau)-0.3$ Å to $r_e(\tau)+0.3$ Å, where $r_e(\tau)$ is the value of the OH bond length along the minimum energy surface at the specified value of τ. The values of τ that were used to construct the two-dimensional surface were 0°, 10°, 20°, 30°, 40°, 60°, 70°, 80°, 90°, 100°, 120°, 150°, and 180°. These points were chosen to span the range of this angle [by symmetry $V(r,\tau)=V(r,-\tau)$] with a higher density of points near the potential minimum and the *cis-perp* conformation.

To correct for the small differences in the energies obtained with the cc-pVQZ and cc-pVTZ basis sets along the minimum energy path, for each value of τ the energies were scaled by $\sigma(\tau)$, the ratio of the energy differences computed by the two basis sets:

$$V(r,\tau)=V_{\mathrm{pVTZ}}(r,\tau)\left[\frac{V^{\mathrm{MEP}}_{\mathrm{pVQZ}}(\tau)-V^{\mathrm{MEP}}_{\mathrm{pVQZ}}(0°)}{V^{\mathrm{MEP}}_{\mathrm{pVTZ}}(\tau)-V^{\mathrm{MEP}}_{\mathrm{pVTZ}}(0°)}\right]$$
$$=V_{\mathrm{pVTZ}}(r,\tau)\sigma(\tau). \quad (2)$$

As $\sigma(\tau)$ is not defined at $\tau=0°$, we extrapolated the scaling from its values at 10°, 20°, and 30° and used $\sigma(0°)=0.943$.

The one-dimensional slices along r through the unscaled cc-pVTZ basis potential at each value of τ were fit to a Morse oscillator,

$$U_{\mathrm{pVTZ}}(r,\tau)=D_e(\tau)[1-\exp(-\alpha(\tau)[r-r_e(\tau)])]^2+U_e(\tau), \quad (3)$$

in order to facilitate extrapolation to a larger range of OH distances. In these fits, all parameters were allowed to vary. Evaluation of the full scaled potential $U(r,\tau)$ was achieved by multiplying $D_e(\tau)$ and $U_e(\tau)$ by the appropriate scaling

factor $\sigma(\tau)$, and using a cubic spline interpolation to evaluate these potential parameters at intermediate angles. The scaled versions of the parameters will be denoted as $D_e^{(s)}(\tau)$ and $U_e^{(s)}(\tau)$ in the discussion that follows. For the spline, the grid was extended to $-360°$ through $360°$ by symmetry in order to avoid unphysical edge effects.

A similar approach was employed to fit the dipole moment surface. Here we first transformed the dipole moment operator into the principal-axis system for the four heavy atoms. We then fit each of the three Cartesian components of the dipole moment to a cubic polynomial in $[r-r_e(\tau)]$. The form of the surface and the resulting intensities will depend on the choice of the embedding of the body-fixed axis system. A principal-axis system was selected in which the three principal axes were determined at each of the 13 geometries along the minimum energy path and the axes are labeled to ensure that the rotational constants obey $A>B>C$. Since the transformation is based on the four heavy atoms, which do not move significantly over the full range of τ, we find that the rotational constants vary by no more than 5%. This is much smaller than the differences between the rotational constants. Evaluation of the vector components of the dipole moment surface was achieved by spline interpolation of the fit parameters.

C. Vibrational energy levels, transition intensities, and spectra

Having obtained a potential and dipole moment surface, the energies and intensities were determined using a two-dimensional discrete variable representation method,[27,28] where both the radial and angular dependences are treated on evenly spaced grids of points with 30 and 75 points, respectively. The value of τ was allowed to vary from $-180°$ to $180°$, while r ranged from 0.500 to 2.225 Å. With these energies and wave functions, the transition strengths of the lines were evaluated using

$$I_{v'',n'';v',n'}(\nu)=\nu|\langle v'n'|\boldsymbol{\mu}(r,\tau)|v''n''\rangle|^2, \tag{4}$$

where ν is the transition wave number in cm^{-1} and $\boldsymbol{\mu}$ is the dipole moment in D, and v and n are the quantum numbers for OH stretch and torsion, respectively. The intensities of lines in the absorption spectrum can then be determined by multiplying the transition strength by a Boltzmann factor $f_{v'',n''}(T)$ accounting for the population of the lower state in the transition,

$$I_{\mathrm{ABS}v'',n'';v',n'}(\nu,T)=C\times f_{v'',n''}(T)\times I_{v'',n'';v',n'}(\nu), \tag{5}$$

where the zero in energy is taken to be the zero-point energy of HOONO, and C is chosen so that the maximum value of $I_{\mathrm{ABS}v'',n'';v',n'}(\nu,T)$ at 300 K is 100.

The above expression gives the absorption intensity for a specific $(v',n')\leftarrow(v'',n'')$ transition. Since the photodissociation product OH is detected in the action spectroscopy experiments, the detection efficiency depends on the quantum yield for dissociation. The dissociation threshold for *cis-cis* HOONO lies 490 cm^{-1} above the $2\nu_{OH}$ overtone band. Therefore, based on harmonic frequencies, the overtone and combination bands involving one quantum of either of the two lowest frequency modes will not have enough energy to dissociate. As such, the intensity of each transition in the OH overtone absorption spectrum was multiplied by the fraction of the population at temperature T that has at least 490 cm^{-1} of vibrational excitation in other modes. This fraction is the estimated quantum yield for photodissociation, $\Phi_{n'}(T)$, which was multiplied by the absorption intensity to determine the action spectrum line intensities,

$$I_{\mathrm{ACTION};n'',v'',n'v'}(\nu,T)=\Phi_{n'}(T)\times I_{\mathrm{ABS};n''v'',n'v'}(\nu,T). \tag{6}$$

III. EXPERIMENT

Cavity ringdown spectroscopy (CRDS) was employed to experimentally obtain the direct absorption spectrum of *cis-cis* HOONO in the overtone region. HOONO was generated in a flow tube reactor at 20–40 Torr, with a gas mixture of 100 SCCM 1% H_2/He mix (SCCM denotes cubic centimeter per minute at STP) and 100 SCCM Ar flowing through a microwave discharge, combining with 200 SCCM 4% NO_2/N_2 (similar to the flow conditions for generating HOONO used in Bean *et al.*[2] and Fry *et al.*[6]). A purge flow of 200 SCCM dry N_2 per mirror was used to prevent destruction of the mirror surfaces. These flows result in a total composition in the cell of 0.125% H_2 and 1.0% NO_2 in bath N_2, Ar, and He.

At these concentrations, the primary reactions were

$$H+NO_2\rightarrow OH+NO, \tag{7}$$

$$OH+NO_2+M\rightarrow HONO_2+M, \tag{1a}$$

$$OH+NO_2+M\rightarrow HOONO+M, \tag{1b}$$

but a key side reaction was

$$OH+NO+M\rightarrow HONO+M. \tag{8}$$

Reference spectra of the two main interfering species, HONO and $HONO_2$, were recorded for spectral subtraction. Both species were generated by bubbling N_2 flow through liquid samples and flowing through the CRDS cell at 40 Torr. The HONO sample was generated by reaction of H_2SO_4 with $NaNO_2$ salt in aqueous solution, and the $HONO_2$ sample was 70% in H_2O, used as purchased from Aldrich.

Spectra were recorded by flowing the relevant gas mixture (discharge products or reference gas) through the center 50 cm long section of a cavity ringdown cell 2 cm in diameter. The optical cavity comprised two highly reflective mirrors (Nova Wave, R=99.995% centered at 1.5 μm) positioned on either end of the cell, spaced 82 cm apart. The mirrors were separated from the central flow region by 16 cm long purge volumes. Resulting empty-cell ringdown times were on the order of 10 μs.

The near-infrared (NIR) radiation, tunable through the range 6000–7000 cm^{-1}, was generated as the idler beam of a optical parametric oscillator (OPO) pumped by a 100 Hz tripled Nd:YAG (355 nm) (YAG—yttrium aluminium garnet) laser. Typical NIR pulse energies were 20 mJ with a laser linewidth of 4 cm^{-1}. Ringdown traces were accumulated with a GaGe Compuscope board (14-bit digitizer).

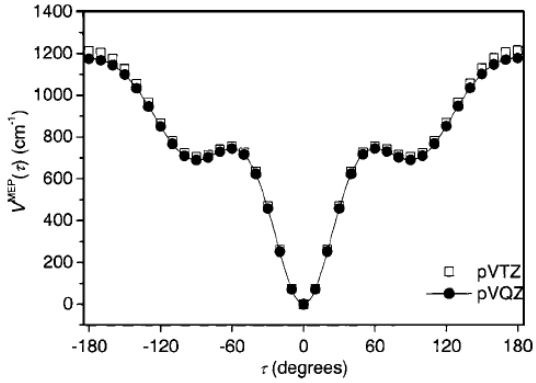

FIG. 2. Calculated torsional minimum energy potential (MEP), as a function of τ with the OONO dihedral angle constrained to 0°. Both potentials were calculated at the CCSD(T) level of theory using the cc-pVTZ (□) and cc-pVQZ (●) basis sets.

Traces from 40 laser shots were averaged before fitting. The averaged traces were fit to exponential functions using the Levenberg–Marquardt algorithm and averaged at each wavelength as the OPO was scanned through the range at a step size of 2 or 4 cm^{-1}. Scans of the full range were repeated in both scanning directions and at various step sizes to ensure that the relative intensities of the peaks were not influenced by slow changes in product concentrations due to fluctuations in the microwave discharge. Absorption spectra were obtained by subtracting the empty-cell ringdown spectra to account for background losses due to the ringdown mirrors.

IV. RESULTS

A. *Ab initio* one-dimensional torsional potential

The CCSD(T)/cc-pVQZ and CCSD(T)/cc-pVTZ torsional minimum energy potential (MEP) functions, $V^{MEP}_{pVTZ}(\tau)$ and $V^{MEP}_{pVQZ}(\tau)$, are plotted in Fig. 2. The energies and optimized structures along τ are reported in Table I of the EPAPS supplemental material for this paper.[29] The potentials that were obtained at these two levels of theory are nearly identical, indicating that the calculation is well converged with respect to basis set. The present results represent the highest level of theory applied to this system to date. Using the cc-pVQZ basis, the barrier for hindered rotation is 14.1 kJ/mol (1180 cm^{-1}), and occurs at τ=180°, the *cis-trans* configuration of HOONO. Near the equilibrium geometry, the potential appears to be fairly harmonic, but there is a plateau in the potential that extends from 50° to 110° that is roughly 8.4 kJ/mol (700 cm^{-1}) above the global minimum. On this surface, there is a slight local minimum at 90°. The depth of this well is sensitive to both the level of theory and basis set. An extensive search for a true local minimum, varying all geometric parameters, was conducted at the CCSD(T)/cc-pVTZ level but failed to find a minimum.

This region of the torsion potential near τ=90° will be referred to as the *cis-perp* configuration of HOONO. The shape of the torsional potential near this geometry also depends on the OH distance r, which was optimized in this calculation, and it is likely that it depends on the OONO torsion angle, which was fixed at 0° in these calculations. As such, we do not ascribe too much significance to the predicted depth (or lack) of the well, although, as we will see, the plateau has important implications for the spectroscopy.

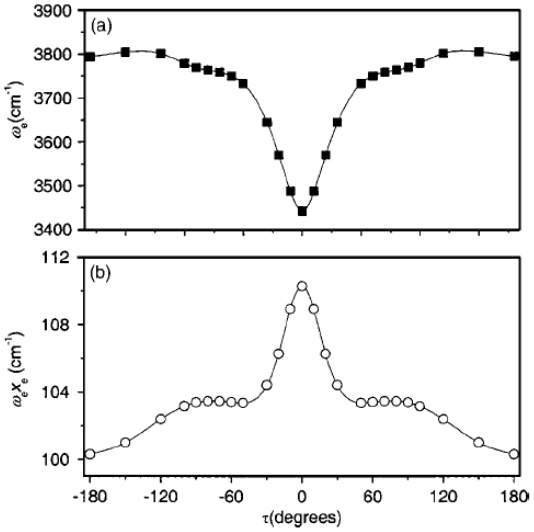

FIG. 3. (a) Harmonic frequency, $\omega_e(\tau)$, and (b) anharmonicity, $\omega_e x_e(\tau)$ for the OH stretch in *cis-cis* HOONO, derived from the parameters in the Morse fits of $U(r,t)$ in Eq. (3), plotted as a function of torsional angle τ.

B. Two-dimensional potential energy surface $U(r,\tau)$ and dipole moment surfaces $\mu(r,\tau)$

The two-dimensional potential energy surface $U(r,\tau)$ was evaluated over the range $r_e(\tau)-0.3$ Å$\leqslant r \leqslant r_e(\tau)+0.3$ Å and $0° \leqslant \tau \leqslant 180°$ by fitting the calculated CCSD(T)/cc-pVTZ points, and introducing scaling factors $\sigma(\tau)$ to correct for differences between the energies calculated using the cc-pVTZ and cc-pVQZ basis sets. This energy surface as a function of τ and r is reported in Table II of the EPAPS supplemental material for this paper.[29] The quality of the fit was tested by comparing the values of $r_e(\tau)$ and $U_e(\tau)$ to the values obtained from electronic structure theory. In all cases, $U_e(\tau)$ is within 12 cm^{-1} of $V^{MEP}_{pVTZ}(\tau)$, or better than 1%. The values of $r_e(\tau)$ agree to better than 0.05% or 0.0005 Å.

The harmonic frequencies $\omega_e^{(s)}(\tau)$ and anharmonicities $\omega_e x_e^{(s)}(\tau)$ for the one-dimensional OH vibration determined from the scaled Morse fits are plotted as a function of τ in Fig. 3 (Morse parameters are reported in Table III of the EPAPS supplemental material for this paper.[29]) Here we use the superscript (s) to indicate that they were calculated using the scaled surface. These quantities depend strongly on the HOON torsional angle, and change most rapidly at small angles. As τ is increased from 0° to 50°, the harmonic OH stretch frequency increases by 300 cm^{-1}, while the anharmonicity decreases sharply. This is consistent with an intramolecular hydrogen-bonding interaction between the OH group and the terminal O atom in the planar *cis-cis* configuration. Such a hydrogen bond softens the OH bond and makes it

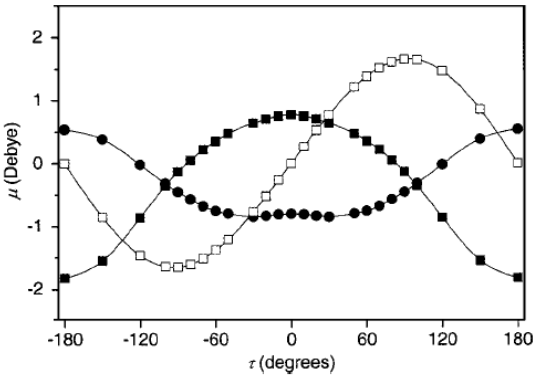

FIG. 4. One-dimensional slices of the dipole moment surface $\mu(r,\tau)$ evaluated at equilibrium OH bond lengths, $r_e(\tau)$, projected onto the three principle axes, defined in the text. μ_A (■), μ_B (●), and μ_C (□). Surface computed at QCISD/AUG-cc-pVTZ level.

more anharmonic, but it is very directional and its effect on the OH vibration weakens quickly as τ is changed.

The two-dimensional surfaces for the three components of the dipole moment were determined at the QCISD/AUG-cc-pVTZ level, at the same values of r and τ that were used to obtain the two-dimensional potential surface. In order to estimate the effects of the size of the basis set on the computed value of the dipole moment, the dipole moment was reevaluated at a subset of the configurations (three values of r at τ=0°, 20°, and 60°) at the QCISD/AUG-cc-pVDZ level. For these points, the dipole moment values computed with the two basis sets differed by less than 3%.

The values of the dipole components along the minimum energy path ($r=r_e(\tau)$) are plotted as a function of r in Fig. 4, and the values of all of the calculated points on the three components of the dipole surface are reported in Tables IV–VI of the EPAPS supplemental material for this paper.[29] The two in-plane components (A and B) are symmetric with respect to τ and are relatively flat over the range $-50° < \tau < 50°$. However, the C (out-of-plane) component has a strong dependence on τ, and is of odd symmetry. The first derivative of this component of the dipole is 0.0258 D/deg at 0°. The differences in the properties of the three components of the dipole moment are consistent with $\Delta n = \pm 1$ transitions carrying significant intensity and having C-type band contours, whereas the $\Delta n = 0$ transitions will have A- and/or B-type band contours. The slices through the dipole moment surface as a function of r for a given τ are fit to a cubic polynomial, centered at $r_e(\tau)$. The raw data and resulting parameters are reported in Tables IV–VII of the EPAPS supplemental material for this paper.[29] Fits to lower and higher order polynomials were also performed and it was found that quadratic through quartic expansions of the dipole moment surface lead to spectra with intensities in near exact agreement.

C. Calculated vibrational energy levels, wave functions, and vibrationally adiabatic potentials

The vibrational energy levels $E(v,n)$ were obtained by solving the two-dimensional Hamiltonian, and are identified

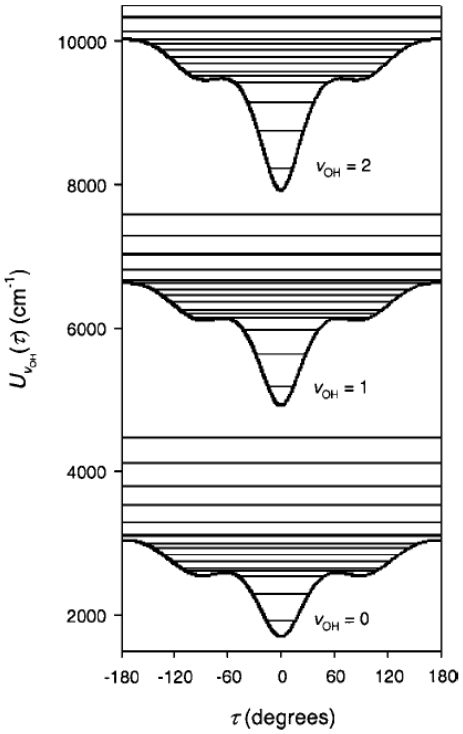

FIG. 5. Vibrationally adiabatic potential energy surfaces $U_{v_{OH}}$ for v_{OH}=0, 1, and 2, plotted as a function of τ. The thin lines on each of the adiabatic potential curves represent the energies $E(v_{OH},n)$ of the torsional states that are associated with the specific v_{OH} quantum level.

by the quantum numbers n for the HOON torsion mode and v for the OH stretch mode. The effect of torsion-stretch coupling is most clearly seen by plotting the vibrationally adiabatic torsion potentials $U_v(\tau)$, obtained by averaging the two-dimensional surface over a specific v state in the OH stretch. This is achieved by evaluating

$$U_v(\tau) = \omega_e^{(s)}(\tau)\left(v+\frac{1}{2}\right) - \omega_e x_e^{(s)}(\tau)\left(v+\frac{1}{2}\right) + U_e^{(s)}(\tau), \quad (9)$$

where the harmonic frequency and anharmonicity are obtained from the scaled potential $U(r,\tau)$, using the standard relationships. These potentials are shown in Fig. 5. In contrast to $V^{\mathrm{MEP}}(\tau)$, which is the bare electronic energy computed along the minimum energy path, $U_v(\tau)$ is the one-dimensional effective potential which includes the vibrational energy of the vth OH stretch state.

As illustrated in Fig. 5, the shape and depth of the adiabatic torsional potentials depend on the amount of OH-stretch excitation. The τ dependence of $\omega_e^{(s)}$ and $\omega_e x_e^{(s)}$, plotted in Fig. 3, illustrates that the OH vibrational energy in Eq. (9) increases sharply with τ. Consequently, the vibrationally adiabatic torsional potentials are deeper than $V_{\mathrm{pVQZ}}^{\mathrm{MEP}}(\tau)$, plotted in Fig. 2, and they become deeper with increasing v.

The first-order effect of the OH-stretch torsion coupling is to increase the barrier height of the hindered rotation, i.e., the energy of *cis-trans* HOONO. The barrier on the scaled

surface increases from 1342 to 1715 cm^{-1} and 2107 cm^{-1} in the $v=0$, 1, and 2 potentials, respectively. This can be compared to the barrier of 1175 cm^{-1} in $V_{pVQZ}^{MEP}(\tau)$. Much of the vibrational dependence of $U_v(\tau)$ is seen at small angles, and the curvature of the torsion potential at the *cis-cis* HOONO minimum is found to increase with increasing OH stretch excitation. This leads to an increase in the difference between the energies of the states with $n=0$ to $n=1$ from 380 cm^{-1} when $v=0$, to 462 cm^{-1} and 537 cm^{-1} when $v=1$ and 2, respectively. Finally, the *cis-perp* HOONO minimum in the one-dimensional surface becomes shallower with increasing OH excitation. The value of the potential in the *cis-perp* configuration ($\tau=90°$), measured relative to the *cis-cis* HOONO minimum, e.g., $U_v(90°)-U_v(0°)$, increases from 848 cm^{-1} for $v=0$ to 1190 cm^{-1} for $v=1$ and 1545 cm^{-1} for $v=2$. This can be compared to the value of the potential along the minimum energy path at the *cis-perp* geometry, where $V_{pVQZ}^{MEP}(90°)=690$ cm^{-1}. The dramatic changes in the torsional potential and frequencies with OH-stretch excitation reflect the large decrease in the OH-stretch frequency in the hydrogen-bonded *cis-cis* configuration.

On each of the one-dimensional adiabatic surfaces, $U_v(\tau)$, in Fig. 5, we plotted the energy of the associated two-dimensional vibrational states. Since we are solving the Schrödinger equation for a two-dimensional system for $v>0$, there will be states with multiple values of v in a given energy range. As such, for a given v, we only showed the energies of, at most, the 20 lowest energy states for which

$$P_v^m = \int_0^{2\pi} d\tau |\langle \psi_v(r)|\Psi_m(r,\tau)\rangle|^2 > 0.75. \tag{10}$$

Here $\psi_v(r)$ represents an eigenstate of the one-dimensional stretch problem, obtained from the one-dimensional slice through our two-dimensional surface at $\tau=0$, while $\Psi_m(r,\tau)$ is a solution to the two-dimensional stretch-torsion Hamiltonian, described above. For these states, we replace the general index m by the combined index v and n, where the value of n is determined by the number of zeros in the integrand.

For $v=0$, the states with $n=0$, 1 and 2 lie below the barrier that separates the *cis-cis* and *cis-perp* HOONO minima and are confined to the *cis-cis* well on the $U_0(\tau)$ adiabatic surface. The highest of these states lies 848 cm^{-1} above the minimum of the $U_0(\tau)$ adiabatic surface and less than 1 cm^{-1} below the *cis-perp* minimum on this surface. There are six additional states that have energies that are at or below the *cis-trans* barrier to free rotation of the OH about the OO bond. In addition, we note that the density of states increases sharply just above the *cis-perp* shelf, because the well opens up rather abruptly at 50°. At energies above the *cis-trans* barrier, the level spacings begin to increase and the states become doubly degenerate as they approach the n^2 dependence of a one-dimensional free rotor. When the OH bond is excited to the $v=1$ or 2 states, the *cis-cis* well deepens and narrows, while the plateau about the *cis-perp* conformer and the *cis-trans* barrier height increase. As a result, for $v=2$, four states have energies below the *cis-perp* shelf, and these states have larger level spacings than those with $v=0$.

In Fig. 6 we plot the projections of the probability densities onto τ for the six lowest energy states ($v=0$) depicted by horizontal lines in $U_0(\tau)$ of Fig. 5. The first four of these states can be best described as a progression of states in the *cis-cis* well with $n=0$–3. There is a sharp increase in the range of the potential sampled by these states and the states with $n>3$. In fact, the $n=4$ state has most of its probability amplitude in the region $45°<|\tau|<120°$ and can be best described as having an anomalously large probability in the *cis-perp* region of the potential. This apparent localization results from the fact that as the potential well opens up near $\tau=90°$, the zero-order description of this motion, e.g., small vibrations about the *cis-cis* HOONO minimum, is no longer valid. As a result of this rapid increase in the range of motion along τ we find that there are two states that are close in energy, one of which is the next state in the progression of vibrational levels from the *cis-cis* HOONO minimum and another which has greater probability amplitude near the *cis-perp* shelf. This is seen in spite of the fact that the well at the *cis-perp* HOONO configuration is quite shallow. While we have not plotted the states for other values of v, the general trends are the same, and the wave functions that correspond to the horizontal lines in Fig. 5 retain their clean nodal structure. The states that have energies lower than the *cis-perp* shelf are localized in regions where $|\tau|<60°$, while the states just above the shelf have anomalously large probability amplitude in the *cis-perp* region of the potential.

D. Calculated absorption and action spectra

Our calculated spectra are shown in Fig. 7. The spectra were generated using the two-dimensional model described above, with a temperature of 300 K. In each of the plots we present a stick spectrum as well as the results a convolution of the stick spectrum by a Gaussian with a full width, half maximum of 70 cm^{-1}, which is chosen to reproduce the observed experimental broadening. In Table I we list some of the most important $(n',v'=2)\leftarrow(n'',v''=0)$ overtone transitions, along with their respective transition frequencies, transition strengths, absorption intensities, and action intensities, as defined in Eqs. (4)–(6).

1. Absorption spectra

The calculated absorption spectra for the fundamental and overtone at 300 K are shown in Figs. 7(a) and 7(b). In both spectral regions, the dominant peak is the origin, and only one transition, the $n=0\leftarrow 0$ band, contributes to its intensity. All of the other bands with significant intensity—combination bands, sequence bands, and hot bands—are shifted to the blue of the origin by 100–600 cm^{-1}. In the convoluted spectra, there is one very broad satellite band in the fundamental region and four narrower satellite bands for the first overtone.

The overtone absorption spectrum is most relevant to the current study. The first two smaller bands adjacent to the $2\nu_{OH}$ origin, **B** and **C**, are approximately 10% and 2% of the intensity of the origin. Each has a single dominant contribution, from $n=1\leftarrow 1$ and $n=2\leftarrow 2$ transitions, respectively. Thus, these levels are "Franck–Condon-like" $\Delta n=0$ se-

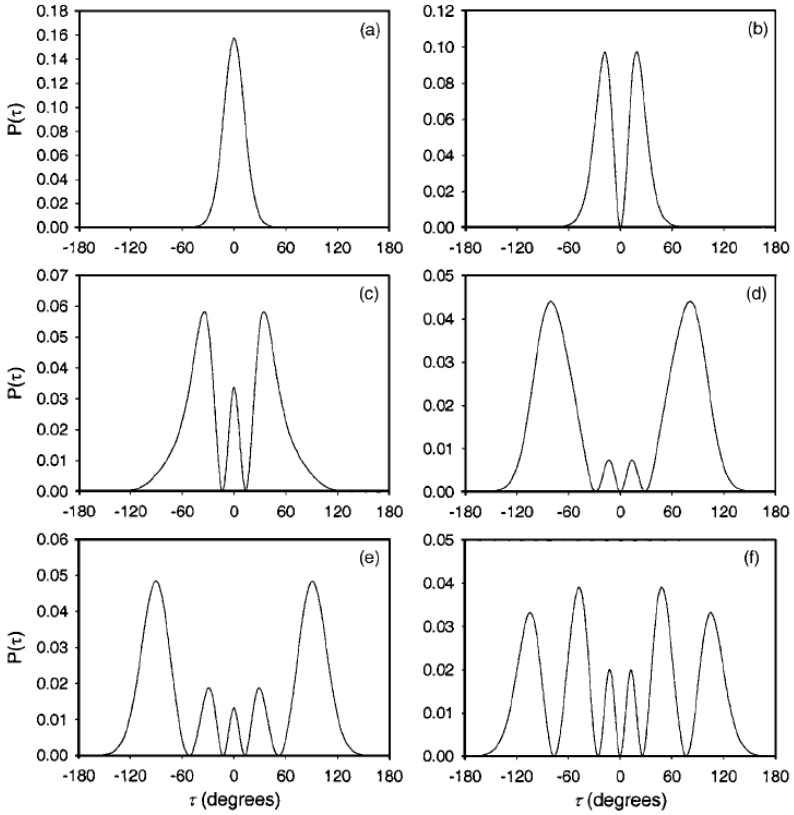

FIG. 6. Probability densities for the six lowest energy states ($v_{OH}=0$, $n=0$–5), projected onto τ.

quence bands. Such large shifts in the sequence band frequencies are a direct result of the stretch-torsion coupling, which leads to the increased energy level spacing of the torsion states in $U_2(\tau)$ versus $U_0(\tau)$, discussed above. These bands are comparable in transition strength to the origin, but appear weak due to their low populations.

The two higher energy bands in the overtone spectrum are pileup bands of several transitions. The third band **D** is ~10% the intensity of the origin. We assign this band to a series of largely unresolved $\Delta n=+1$ *C*-type transitions. The $n=4\leftarrow 3$ transition is the strongest single line, although the transitions with $n''<6$ all carry intensities that are within a factor of 4 of this transition. As such, the main contribution to the overall intensity of the convoluted band comes from the sum of the intensities of transitions with $n''=0$ through 6. As we noted above, the states with $n''\geqslant 3$ have energies above the *cis-perp* plateau, and thus many of the transitions in this band arise from states with significant probability amplitude in the *cis-perp* HOONO geometry. As seen in Table I, the individual $\Delta n=+1$ transitions have large transition strengths for $n''\geqslant 2$, a reflection of the fact that the intensity in this band comes from the *C* component of the dipole vector (e.g., the component that is perpendicular to the OONO plane). It is interesting to note that the states with $n''\geqslant 2$ are at least 628 cm^{-1} higher in energy than the vibrationless level, so that they are expected to be weak based on the Boltzmann factor. However, this decrease in population is compensated by the factor of 50 increase of the transition strength for the $n=4\leftarrow 3$ transition, compared to $1\leftarrow 0$ transition. A fourth weak band, labeled **E**, is another pileup of weak bands with a significant contribution from $\Delta n=+2$ transitions, which appear as a single peak after convolution.

The ν_{OH} fundamental region of the absorption spectrum is similar to the overtone region, although the magnitudes of the blueshifts are less, as expected. Only one satellite band, located 333 cm^{-1} to the blue of the origin, has appreciable intensity (15% of the origin). It arises from the series of $\Delta n=1$ transitions, described above. The $n''=1\leftarrow 1$ and $n''=2\leftarrow 2$ are seen in the stick spectrum with 10% and 2% of the intensity of the most intense transition, the smaller blueshift of these bands leads them to be incorporated as a blue shoulder in the envelope of the most intense transition.

The overtone absorption spectrum at 233 K is shown as a dotted line in Fig. 7(b). The two curves are normalized such that the origin peaks 6310 cm^{-1} have the same intensity. At the lower temperature, the sequence bands and hot bands are approximately three times weaker, due to the lower the Boltzmann factor $f_{v'',n''}(T)$ of the torsionally excited levels.

2. Action spectrum

The primary difference between the absorption and action spectra arises from the fact that the action spectrum

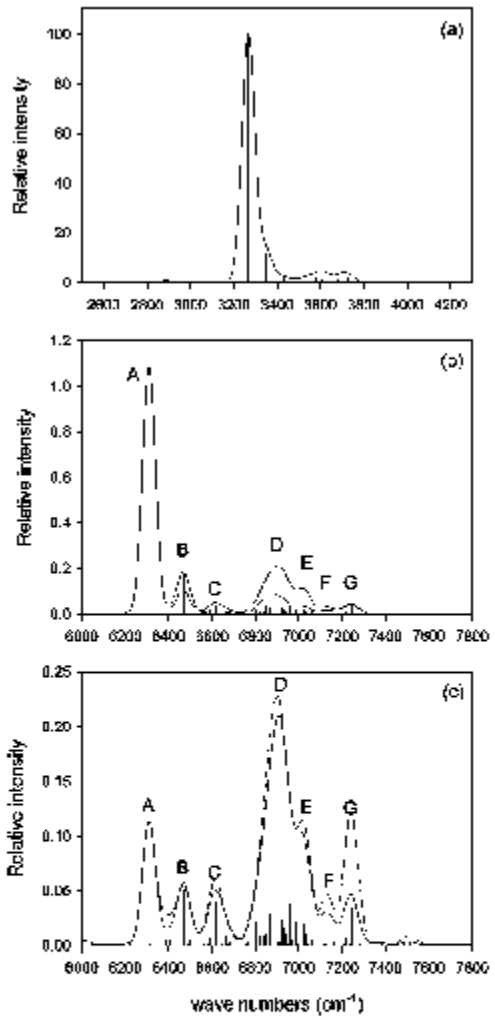

FIG. 7. Spectra, calculated at 300 K (solid) and 233 K (dashed) for the fundamental (top), first overtone (middle), and the first overtone multiplied by the quantum yield for photodissociation given in Eq. (6) (bottom). In all three spectra, the stick spectrum is convoluted with a Gaussian with a full width half maximum of 70 cm^{-1} and all plots at 300 K are normalized so that the maximum value of the stick and convoluted spectra in (a) are 100, while the spectra at 233 K in (b) and (c) are normalized so that the peak maxima at -6300 cm^{-1} have the same relative intensities.

requires that the excited HOONO dissociate to OH+NO_2. We expect that intramolecular vibrational-energy redistribution (IVR) and dissociation will be fast and assume that any excited state above D_0 will predissociate and contribute to the action spectrum. Thus, in our quantum yield calculation we count states that are prepared with energy above D_0.

Experimentally, the $2\nu_{OH}$ state lies 490 cm^{-1} below the dissociation threshold, based on the estimation of D_0(*cis-cis* HOONO) of Konen *et al.*[18] On the other hand, at 300 K hot bands are populated. Therefore, if we neglect off-diagonal anharmonicities between (r,τ) and the seven remaining vibrational modes, we can approximate the action spectrum by weighting the absorption intensity by the fraction of the vibrational partition function that reflects contributions to the intensities of transitions to states with at least 490 cm^{-1} of vibrational energy above the $2\nu_{OH}$ overtone.

The procedure for achieving this is described above. We use the harmonic frequencies obtained at the CCSD(T)/cc-pVTZ level of theory. When we analyzed the vectors associated with the two torsional modes, which had frequencies of 383 and 523 cm^{-1}, we found that they were highly mixed. In fact, when we performed the harmonic analysis making either the mass of hydrogen or the masses of the heavy atoms very large, thereby setting one of the torsion frequencies to zero, we found that the HOON torsion frequency became 439 cm^{-1}, while the OONO torsion frequency became 462 cm^{-1}. This indicated that there is large mixing of the two torsional modes at the harmonic level. As such, we use the average of the two torsion frequencies in place of the calculated OONO frequency. Operationally the above procedure requires us to scale transitions to the $2\nu_{OH}$ state by $\Phi_0(300\text{ K})=0.104$ and transitions to the combination band with 2 quanta in the OH stretch and one in the torsion by $\Phi_1(300\text{ K})=0.288$. At 233 K, we find that the quantum yields have decreased to $\Phi_0(233\text{ K})=0.0352$ and $\Phi_1(233\text{ K})=0.1566$.

The resulting stick and convoluted spectra $I_{ACTION}(\nu,T)$, taking into account the nonunity quantum yield $\Phi_{n'}(300\text{ K})$, is plotted in Fig. 7(c). Action spectrum intensities of specific transitions are listed in Table I.

Comparing the spectra in Figs. 7(b) and 7(c) reveals a dramatic change in the relative band intensities in the overtone spectrum upon inclusion of the quantum yield correction in Eq. (6). The first three bands, **A**, **B**, and **C**, are the same as observed in the absorption spectrum (the $n=0\leftarrow 0$, $n=1\leftarrow 1$, and $n=2\leftarrow 2$ transitions), but the origin is almost ten times weaker, only a factor of 2 to 3 stronger than the next two bands. The most prominent feature in the calculated action spectrum is now the large peak at 6900 cm^{-1} (**D**). This peak has roughly twice the peak intensity of the origin and is substantially broader, indicating that it accounts for more of the total band strength.

As in the absorption spectrum, the **D** band is composed of many transitions, the majority of which are $\Delta n=+1$ lines. This is a reflection of the fact that the intensity in this band comes from the C component of the dipole vector (e.g., the component that is perpendicular to the OONO plane). As is seen in Fig. 4, its value increases from zero in the planar configuration to 1.5 D in the *cis-perp* HOONO configuration. The most intense of these transitions originates from the $n''=3$ state, with significant contributions from states up to $n''=7$. This band is composed of hot bands primarily from states that sample the *cis-perp* HOONO geometry. Additional side bands to the blue of the 6900 cm^{-1} peak, labeled **E**, **F**, and **G**, arise from $\Delta n=+2$ transitions, originating from the ground state (**G**), the state with $n''=1$ (**F**), and a pileup of states with $n''>1$ (**E**).

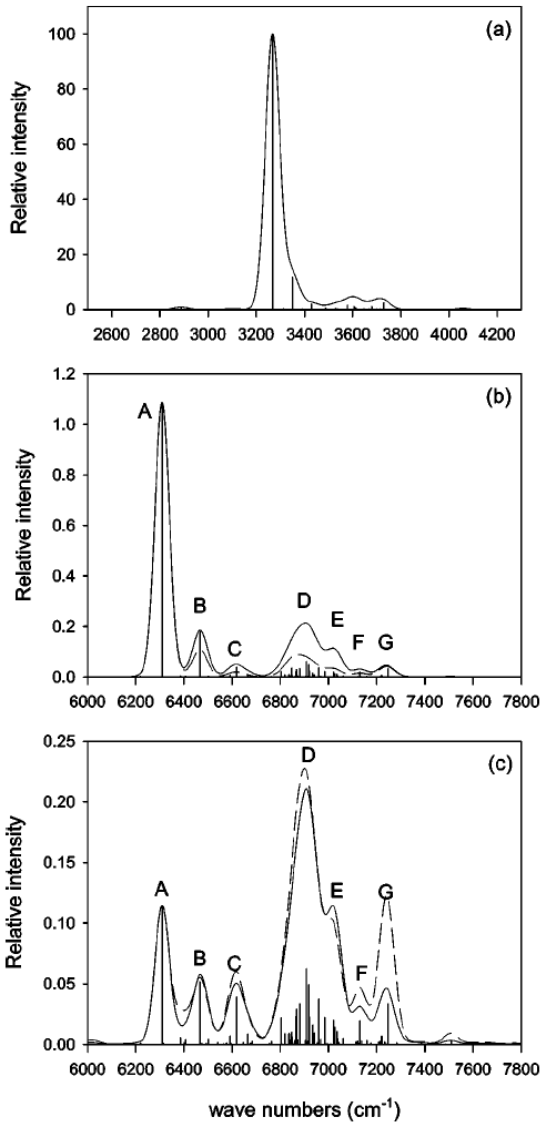

FIG. 7. Spectra, calculated at 300 K (solid) and 233 K (dashed) for the fundamental (top), first overtone (middle), and the first overtone multiplied by the quantum yield for photodissociation given in Eq. (6) (bottom). In all three spectra, the stick spectrum is convoluted with a Gaussian with a full width half maximum of 70 cm^{-1} and all plots at 300 K are normalized so that the maximum value of the stick and convoluted spectra in (a) are 100, while the spectra at 233 K in (b) and (c) are normalized so that the peak maxima at ~6300 cm^{-1} have the same relative intensities.

requires that the excited HOONO dissociate to $OH+NO_2$. We expect that intramolecular vibrational-energy redistribution (IVR) and dissociation will be fast and assume that any excited state above D_0 will predissociate and contribute to the action spectrum. Thus, in our quantum yield calculation we count states that are prepared with energy above D_0.

Experimentally, the $2\nu_{OH}$ state lies 490 cm^{-1} below the dissociation threshold, based on the estimation of D_0(*cis-cis* HOONO) of Konen *et al.*[18] On the other hand, at 300 K hot bands are populated. Therefore, if we neglect off-diagonal anharmonicities between (r,τ) and the seven remaining vibrational modes, we can approximate the action spectrum by weighting the absorption intensity by the fraction of the vibrational partition function that reflects contributions to the intensities of transitions to states with at least 490 cm^{-1} of vibrational energy above the $2\nu_{OH}$ overtone.

The procedure for achieving this is described above. We use the harmonic frequencies obtained at the CCSD(T)/cc-pVTZ level of theory. When we analyzed the vectors associated with the two torsional modes, which had frequencies of 383 and 523 cm^{-1}, we found that they were highly mixed. In fact, when we performed the harmonic analysis making either the mass of hydrogen or the masses of the heavy atoms very large, thereby setting one of the torsion frequencies to zero, we found that the HOON torsion frequency became 439 cm^{-1}, while the OONO torsion frequency became 462 cm^{-1}. This indicated that there is large mixing of the two torsional modes at the harmonic level. As such, we use the average of the two torsion frequencies in place of the calculated OONO frequency. Operationally the above procedure requires us to scale transitions to the $2\nu_{OH}$ state by $\Phi_0(300\ K)=0.104$ and transitions to the combination band with 2 quanta in the OH stretch and one in the torsion by $\Phi_1(300\ K)=0.288$. At 233 K, we find that the quantum yields have decreased to $\Phi_0(233\ K)=0.0352$ and $\Phi_1(233\ K)=0.1566$.

The resulting stick and convoluted spectra $I_{ACTION}(\nu,T)$, taking into account the nonunity quantum yield $\Phi_{n'}(300\ K)$, is plotted in Fig. 7(c). Action spectrum intensities of specific transitions are listed in Table I.

Comparing the spectra in Figs. 7(b) and 7(c) reveals a dramatic change in the relative band intensities in the overtone spectrum upon inclusion of the quantum yield correction in Eq. (6). The first three bands, **A**, **B**, and **C**, are the same as observed in the absorption spectrum (the $n=0\leftarrow 0$, $n=1\leftarrow 1$, and $n=2\leftarrow 2$ transitions), but the origin is almost ten times weaker, only a factor of 2 to 3 stronger than the next two bands. The most prominent feature in the calculated action spectrum is now the large peak at 6900 cm^{-1} (**D**). This peak has roughly twice the peak intensity of the origin and is substantially broader, indicating that it accounts for more of the total band strength.

As in the absorption spectrum, the **D** band is composed of many transitions, the majority of which are $\Delta n=+1$ lines. This is a reflection of the fact that the intensity in this band comes from the C component of the dipole vector (e.g., the component that is perpendicular to the OONO plane). As is seen in Fig. 4, its value increases from zero in the planar configuration to 1.5 D in the *cis-perp* HOONO configuration. The most intense of these transitions originates from the $n''=3$ state, with significant contributions from states up to $n''=7$. This band is composed of hot bands primarily from states that sample the *cis-perp* HOONO geometry. Additional side bands to the blue of the 6900 cm^{-1} peak, labeled **E**, **F**, and **G**, arise from $\Delta n=+2$ transitions, originating from the ground state (**G**), the state with $n''=1$ (**F**), and a pileup of states with $n''>1$ (**E**).

TABLE I. Frequencies, relative absorption and action intensities at 300 K, and absolute transition strengths for the strongest transitions in the calculated *cis-cis* HOONO spectrum, discussed in the text.

n''	n'	ν(cm^{-1})	Band[a]	$I_{\mathrm{ABS}v'',n'';v',n'}$[b]	$I_{\mathrm{ACTION}v'',n'';v',n'}$[b]	$I_{v'',n'';v',n'}$ (cm^{-1} D^2)
0	0	6309	**A**	1.000	0.104	0.3744
1	1	6467	**B**	0.166	0.048	0.3839
2	2	6617	**C**	0.036	0.036	0.2752
3	3	6804		0.020	0.020	0.2219
0	1	6847	**D**	0.032	0.009	0.0121
1	2	6866	**D**	0.021	0.021	0.0491
2	3	6881	**D**	0.031	0.031	0.2342
3	4	6907	**D**	0.058	0.058	0.6353
4	5	6918	**D**	0.043	0.043	0.6077
0	2	7246	**G**	0.031	0.031	0.0115

[a]As identified in Figs. 7(b) and 7(c).
[b]Defined in Eqs. (5) and (6). The values are normalized so that for the $0 \leftarrow 0$ transition in the absorption, the intensity is unity.

The overtone action spectrum at 233 K is shown as a dashed line in Fig. 7(c). We have again normalized the spectra so that the origin peaks at 6310 cm^{-1} have the same intensity. In the action spectrum case, in contrast to the absorption spectrum, there is strikingly little change in the relative band intensities with changing temperature.

E. Experimental results

The cavity ringdown absorption spectrum of products from the discharge reaction H+NO_2 is shown in Fig. 8(a). The spectrum was recorded at 300 K and a total pressure of 40 Torr; the background empty-cell ringdown spectrum has been subtracted. The ordinate is the absorption in units of ppm per pass in the cavity ringdown cell (where the effective pass length is estimated to be about 50 cm). No attempt was made to measure an exact absorption cross section.

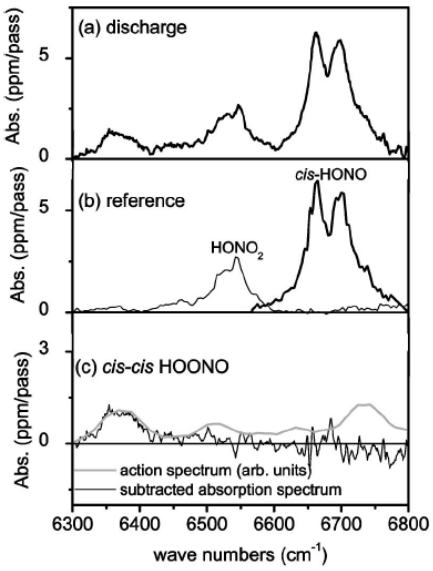

FIG. 8. Direct absorption spectrum of *cis-cis* HOONO recorded by cavity ringdown of OH+NO_2 system, reaction path length $L \approx 50$ cm. (a) Spectrum of products formed in the discharge reaction. (b) Reference spectra of HONO and HNO_3 and scaled to match intensities in (a). (c) Spectrum of *cis-cis* HOONO obtained by subtracting reference spectra from discharge spectrum (curve), compared to the smoothed action spectrum of *cis-cis* HOONO (Ref. 6) in the same spectral region.

Reference spectra of HONO (centered at 6680 cm^{-1}, assigned as the $2\nu_1$ band of *cis*-HONO by Guilmot *et al.*[30]) and $HONO_2$ (centered at 6530 cm^{-1}, assigned as the $2\nu_1-\nu_9$ band by Feierabend *et al.*[31]) are shown in Fig. 8(b). Above 6850 cm^{-1}, the $HONO_2$ $2\nu_1$ band dominates, and no subtraction is possible. The spectra have been scaled in intensity to best fit matching bands in the discharge spectrum.

The subtracted cavity ringdown spectrum, 6300–6800 cm^{-1}, is shown in Fig. 8(c); only one feature remains after subtraction of HONO and $HONO_2$, a band at 6370 cm^{-1}. The subtracted spectrum to the blue of this band, from 6400 to 6800 cm^{-1}, is noisier, primarily due to difficulties with background subtraction and to mirror reflectivity. No additional bands are evident in the absorption spectrum in this region; any absorption bands must have intensities on the order of 10% or less of the origin band. No additional absorption was observed up to 6850 cm^{-1}.

The band at 6370 cm^{-1} is roughly 30–50% of the intensity of the *cis*-HONO band, a result similar to previous observations of *cis-cis* HOONO and *cis*-HONO band intensities in the fundamental region.[2] As this is the only peak observed and has reasonable intensity, we assign this band to the origin of the *cis-cis* HOONO $2\nu_{OH}$ spectrum. This peak has no resolvable structure but has a slightly asymmetric flat-top profile that does not match either Gaussian or Lorentzian line shapes. The bandwidth, 60 cm^{-1} (FWHM), is approximately 50% wider than predicted by a rotational contour simulation for this band.[6]

V. COMPARISON OF CALCULATED AND EXPERIMENTAL SPECTRA

The two-dimensional calculations of the first overtone spectrum of *cis-cis* HOONO predict that the intensity pattern in the action spectrum will differ significantly from the absorption spectrum, due to quantum yield effects. By detect-

ing the CRDS spectrum of this region, we are now in a position to test this prediction and to evaluate the extent to which the coupling of just two modes, the OH stretch and HOON torsion, can account for the previously observed action spectrum.

To compare experimental and calculated spectra, we must shift the absolute frequency scale of the calculated absorption and action spectra by 55 cm^{-1} in order to match the origin in the calculated spectrum with the 6365 cm^{-1} (6370 cm^{-1}) peaks seen in the experimental action (absorption) spectra. Such a shift is well within the uncertainties of the *ab initio* calculation as well as uncertainties stemming from neglect of vibrational couplings with the seven other modes.

In the case of the action spectrum, the strongest feature in the experimental spectrum is the broad band 600 cm^{-1} to the blue of the origin. A band at a similar shift and with large relative intensity (**D**) is also seen in the calculated spectrum. Examining the stick spectrum that underlies this feature, we find that this band has contributions from a series of overlapping $\Delta n=+1$ hot band transitions from torsionally excited molecules. The most intense of these originates from the $n''=3$ state. Transitions originating from states with $n''\leqslant 7$ carry intensities that are at least 15% of the intensity of the most intense band in this progression.

There are two additional features to the blue of the large 6970 cm^{-1} peak in the experimental action spectrum, at 7130 and 7240 cm^{-1}. Similar bands to the blue of the large band are seen in the calculated spectrum (**F** and **G**) and arise from $\Delta n=+2$ transitions from the states with $n''=1$ and 0, respectively. The intensity of the **G** band was observed by Fry *et al.*[6] to increase slightly with decreasing temperature, in agreement with the change seen in the calculated spectra from 300 to 233 K. The remaining features that are seen in both the observed and calculated action spectra are the peaks at 6500 and 6640 cm^{-1}. These are assigned to the $n=1\leftarrow 1$ (**B**) and $n=2\leftarrow 2$ (**C**) sequence bands, respectively.

While many of the peaks in the experimental spectrum are reproduced in the calculated spectrum, there are experimental features that are not found in the calculation. Of the major bands, only the band at 6730 cm^{-1} in Fig. 1 is not reproduced by these reduced dimensional calculations. This band is most likely a combination or sequence band involving one of the seven vibrational modes that are not included in this model. Based on the position of this band and the harmonic frequencies of *cis-cis* HOONO, this band is most likely a combination band that involves another mode.

In contrast to the action spectrum, the calculated absorption spectrum consists of a single strong band at the origin, with the other bands possessing intensities $<5\%$ of the origin. The experimental CRDS absorption spectrum, shown in Fig. 8(c), confirms these predictions, up to 6850 cm^{-1}. In Fig. 8(c), the experimental CRDS absorption spectrum is compared to the previously reported action spectrum. As expected, the absorption spectrum has only one strong band, at 6370 cm^{-1}. This band is nearly identical to the band (**A**) in the action spectrum at essentially the same frequency and is assigned as the origin. None of the features present in the action spectrum at 6505, 6640, or 6730 cm^{-1} are seen in the direct absorption spectrum, within our signal-to-noise. Thus, the intensity patterns of the experimental action and absorption spectra differ qualitatively, in accord with our predictions.

Unfortunately, background absorption by the $2\nu_{OH}$ band of nitric acid at 6944 cm^{-1} overwhelms any signal above 6850 cm^{-1} and prevents us from detecting any HOONO absorption. Consequently, we cannot rule out the presence of the strong 6970 cm^{-1} band seen in the action spectrum. Thus, complete verification by experiment of the effects of quantum yield on the overtone spectrum must await experiments that can observe this band directly.

VI. DISCUSSION

A. Limitations of calculated spectra

Our two-dimensional model captures much of the essential physics of this system through consideration of only the coupling between the HOON torsion and the OH-stretch motions; however, like any reduced dimensional model, it has limitations. Specifically, we know that HOONO has nine degrees of freedom, three of which have relatively low frequencies. Further, just as motion in the HOON torsion will break the intramolecular hydrogen bond in the equilibrium configuration, so will motion along the heavy atom torsion and the in-plane breathing mode. Our calculations indicate that the two torsional modes have the same symmetry and nearly identical frequencies. The lowest torsional levels are thus likely to be highly mixed.

We expect that there will also be significant anharmonic couplings between the OH-stretch vibration and the other two low-frequency vibrational modes. Furthermore, Fermi resonances between the OH stretch and the OOH bend are often evident in overtone spectra. As a result, there are features in the spectrum that cannot be accounted for in this model. We note that parallel to these studies Stanton and co-workers[13] have been using perturbation theory to calculate frequencies and intensities of transitions in the $2\nu_{OH}$ region in the spectrum. The 6730 cm^{-1} band that is not assigned using this two-dimensional model appears to be accounted for as a different combination band in their model.

In addition to missing seven vibrational degrees of freedom, the calculated relative intensities of the action spectrum are also very sensitive to the choice of D_0. The experiment of Konen *et al.*[18] pinpoints D_0 with high precision, but since the dissociation limit falls in the middle of the overtone spectrum, even small shifts in D_0 or in the predicted vibrational frequencies will alter the calculated intensity patterns. Our treatment of the quantum yield is also simple; we consider only which vibrational levels are above or below dissociation. We neglect effects due to dissociation lifetimes and collisional relaxation or excitation, processes which lead to pressure dependent quantum yields that may be important very close to threshold. Finally, we neglect rotations, which couple to the torsion, but also can lead to centrifugal barriers and hence influence dissociation yields.

In spite of the above comments it is quite remarkable how well a two-dimensional model based entirely on *ab initio* energies and frequencies, with the dissociation en-

ergy as the only experimentally constrained parameter, reproduces nearly all of the major features in the recorded action spectrum.

B. Interpretation of the action spectrum

This work clarifies the physical basis for the experimentally observed first overtone action spectrum of *cis-cis* HOONO.[1,6] We find that most of the peaks in the observed action spectrum (Fig. 1) are hot bands, i.e., are transitions from initial states that are vibrationally excited. The first three prominent peaks are $\Delta n=0$ sequence bands. Of these, the $n=0\leftarrow 0$ and $n=1\leftarrow 1$ must arise from hot *cis-cis* HOONO molecules with vibrational excitation in modes other than the OH stretch or the HOON torsion, in order to result in a final state that is above the dissociation threshold. While the photon energy of the broad **D** band exceeds the dissociation energy of 6860 cm^{-1}, this band is also composed of transitions from torsionally excited molecules, primarily $\Delta n=+1$ from higher n'' states.

In previous work, the strength of the 6970 cm^{-1} band was puzzling. We find that several effects contribute to the intensity of this band. First, the intensity of this band does not result from borrowing intensity from the zeroth order $2\nu_{OH}$ state, as is often seen in overtone spectra, e.g., in Fermi resonance states. This is evidenced by the clean nodal patterns in the vibrational wave functions associated with the states that are indicated by the horizontal lines in Fig. 5. As is seen in Table I, the $\Delta n=+1$ transitions from higher level torsional states, e.g., $n=4\leftarrow 3$ and $n=5\leftarrow 4$ actually have larger transition strengths than the origin band. The origin of this enhancement is due in part to the large derivative of the C component of dipole moment with τ. In addition, comparing the states on the adiabatic surfaces with zero and two quanta in the OH stretch, plotted in Fig. 5, we find that the states that are just above the *cis-perp* shelf differ in the number of quanta in the torsion by one. This reflects the deepening of the *cis-cis* well with increasing OH-stretch excitation. This leads to an increase in the magnitude of the matrix elements of the dipole moment operator, and from that the intensities of these $\Delta n=+1$ transitions. Second, there is an unusually high density of states starting at $n''=2$, which stems from the opening of the potential at the *cis-perp* shelf. Thus, while we do not find any states that are truly bound in a *cis-perp* well, the probability density of the states just above this shelf indicates that the vibrationally averaged structure of these molecules is effectively the *cis-perp* geometry. These are the states that predominantly contribute to the **D** band.

The current results also resolve a puzzling discrepancy. Fry *et al.*[6] observed no change in the major features in the experimental action spectrum as they lowered the temperature. However, they expected that bands with photon energies below the dissociation limit D_0 would appear weaker at lower temperatures. Using statistical RRKM calculations, they predicted that the quantum yield would fall off rapidly for $h\nu<D_0$. The origin band intensity was estimated to decrease by over a factor of 2 relative to the **D** band, which lies above D_0.

As seen in Fig. 7(c), the calculated action spectra at 233 K and 300 K show no significant change in relative band intensities with decreasing temperature, demonstrating that the value of $D_0=6860$ cm^{-1} obtained by Konen *et al.*[18] is consistent with the results of Fry *et al.*[6] The surprising similarity of the two plots in Fig. 7(c) can be explained by the observation that the action spectrum is largely due to hot bands of *cis-cis* HOONO. As the temperature is reduced from 300 to 233 K, transitions originating out of the more populous states, $n''=0$ or 1, have smaller quantum yields, while transitions originating out of higher energy torsionally excited states $n''>1$, decrease in intensity as their populations decrease. The reductions in quantum yields for the lower frequency $n''=0$ or 1 transitions nearly exactly match the decrease in the higher frequency bands excited from torsionally hot states. Thus, the overall intensity of the action spectrum decreases almost identically across all bands, and the relative intensities of most of the bands remain unchanged.

There are two notable exceptions to the consistency in band intensity ratios with changing temperature. The **F** and **G** bands in the calculated spectrum are predicted to increase in intensity when the temperature is decreased from 300 to 233 K. The increase in the intensity of these transitions in the calculated spectrum reflect the fact that they are assigned to the $\Delta n=+2$ transition from the $v=1$ and 0 levels and are transitions that have unit quantum yield for dissociation, within our model. The experimental data support this, as the band at 7230 cm^{-1} in the experimental action spectrum also increased in intensity with decreasing temperature from 273 to 193 K.[6] The unassigned band in the experimental action spectrum also showed an increase in intensity with decreasing temperature, consistent with its assignment as a band from the ground state to a combination level of $2\nu_{OH}$ with excitation in at least one of the seven vibrations not included in the present model.

C. Implications for the HOONO yield in the $OH+NO_2$ reaction

Bean *et al.* determined the $HOONO/HONO_2$ yield in reaction (1) by measuring the integrated band intensities of the respective fundamental modes, and converting these to densities using the ratio of CCSD(T)/AUG-cc-pVTZ cross sections computed in the double harmonic approximation for *cis-cis* HOONO.[2] Thus, they made the assumption that all molecules of both species were absorbing in the ν_{OH} band. This is in fact true for $HONO_2$ (the main sequence band is within the envelope of the fundamental). However, the current calculations [Fig. 7(a)] demonstrate that the strong stretch-torsion coupling shifts all of the HOON torsional hot bands (sequence or otherwise) more than 80 cm^{-1} away from the origin of the fundamental band. Thus, integration of the absorption at the origin band excludes states with $n''\geqslant 1$. Based on the harmonic oscillator partition function, the measurement given by Bean *et al.* must underestimate the *cis-cis* HOONO population by $\approx$20%.

These considerations lead us to the tentative conclusion that the low pressure $HOONO/HONO_2$ branching ratio

should be significantly higher than the 7.5% measured by Bean *et al.*[2] (300 K and 13 Torr). To quantify fully this effect, more accurate integrated intensities, taking into account anharmonicity of the OH stretch, must be computed for both HOONO and $HONO_2$. Furthermore, all of the other modes must be included. Coupling with other modes, notably the low-frequency bending/breathing mode ν_7 and OONO torsion ν_8 will alter the frequency shifts. However, if these modes also lead to large shifts in their respective hot bands, then the ratio could be even larger.

D. Mechanism for broadening of the overtone spectrum

The current results shed additional light on the spectral broadening observed in the overtone spectrum of *cis-cis* HOONO. Our CRDS measurement demonstrates that the origin band of the first overtone measured in direct absorption is only slightly narrower than the same band detected by action spectroscopy. Fry *et al.*[6] noted that the width of the $2\nu_{OH}$ overtone origin band in the action spectrum (at 6365 cm^{-1}) is ≈50% broader than a simulated rotational contour. The laser linewidth in both cases was ~4 cm^{-1}. Thus, the width of the $2\nu_{OH}$ overtone origin band at room temperature is intrinsic to absorption in the overtone band and is not a consequence of using action spectroscopy.

Such broadening may have many causes in an action spectrum: dissociation lifetime broadening, inhomogeneous broadening (especially for bands below D_0, which are exclusively hot bands), or IVR. Since we now find that the linewidth is similar in the direct absorption spectrum, we conclude that the $2\nu_{OH}$ origin band of *cis-cis* HOONO is broadened predominantly by IVR processes.

In contrast, for the *trans-perp* HOONO isomer, the action spectrum of the overtone is fit well by a simulated rotational contour.[6] The difference in widths of the *cis-cis* HOONO versus *trans-perp* HOONO overtone bands indicates that IVR is faster in *cis-cis* HOONO. IVR may be facilitated in *cis-cis* HOONO by the presence of the intramolecular hydrogen bond and the strong stretch-torsion coupling. In *trans-perp* HOONO, the OH bond is out of plane and less likely to relax quickly.

VII. CONCLUSIONS

We report the results of a theoretical and experimental investigation of the dynamics that lead to the observed intensity pattern in the OH first overtone action spectrum of *cis-cis* HOONO. We find that coupling of the OH stretch to the HOON torsion and quantum yield effects are primarily responsible for the features seen in the action spectrum.

Theoretical calculated absorption and action spectra, and experimental measurement of the direct absorption spectrum of *cis-cis* HOONO, confirm that the $2\nu_{OH}$ origin band lies below D_0 and is therefore suppressed in the action spectrum.

We are able to account semiquantitatively for most of the features in the action spectrum and their relative intensities, despite the reduced dimensionality of the calculation. Only one major band, at 6730 cm^{-1}, is not predicted and likely involves other vibrations not treated here. Levels with torsional excitation up to $n=6$ contribute to the spectrum, indicating that perturbation theory is unlikely to describe completely the action spectrum.

The *cis-perp* geometry plays an important role in the spectroscopy of *cis-cis* HOONO. A pileup of torsionally excited $\Delta n=+1$ transitions in a *cis-perp*-like geometry, with an effectively free OH stretch and with large intrinsic intensities, accounts for the strongest band near 7000 cm^{-1} in the action spectrum. This is surprising in light of the high energy of the torsionally excited ground states, but is explained in this study as resulting from a combination of effects: a pileup of multiple states at the *cis-perp* geometry, the anomalously large intrinsic intensity of the OH stretch in the *cis-perp* geometry, and the suppression of the origin band which would otherwise dominate the spectrum.

The calculations are highly sensitive to the dissociation energy and are in excellent agreement with the experimental D_0 determined by Konen *et al.*[18] This resolves the apparent inconsistency between this value of D_0 and the finding of Fry *et al.*[6] that the relative intensities of bands in the $2\nu_{OH}$ region of the action spectrum appear to be independent of temperature. As the temperature is lowered, we predict that torsional hot band intensities in the absorption spectrum decrease significantly. In the action spectrum, this decrease in torsional hot band intensities is nearly exactly matched by a drop in the quantum yield for HOONO dissociation of the bands at lower photon energies, which require additional energy in other modes to dissociate.

The quantity of most relevance in atmospheric chemistry is the branching ratio of HOONO relative to $HONO_2$ in reaction (1). This work suggests an upward adjustment of that branching ratio previously reported by Bean *et al.*[2] The reduced dimensionality of this model does not allow a new quantitative estimate of the branching ratio, but does suggest that further work is required to correctly account for coupling to other modes and to assess the integrated cross section of *cis-cis* HOONO in the fundamental region.

ACKNOWLEDGMENTS

This work was supported by the California Air Resources Board (Contract No. 03-333), the National Science Foundation (NSF Grant Nos. CHE-0200968 and ATM-0432377), and the National Aeronautics and Space Administration Upper Atmospheric Research Program (NASA Grant No. NGT-11657). Experiments were performed in the laboratory of Professor Paul O. Wennberg, and the authors gratefully acknowledge his support and interest. J.L.F. and A.K.M. acknowledge support of NSF Graduate Research Fellowships and a NASA Earth System Science Fellowship. The authors thank the NASA Jet Propulsion Laboratory Supercomputing Project for computer time. They thank Stanley P. Sander, John F. Stanton, Amit Sinha, and Marsha I. Lester for helpful discussions and for sharing unpublished results prior to publication.

[1] S. A. Nizkorodov and P. O. Wennberg, J. Phys. Chem. A **106**, 855 (2002).
[2] B. D. Bean, A. K. Mollner, S. A. Nizkorodov, G. Nair, M. Okumura, S. P. Sander, K. A. Peterson, and J. S. Francisco, J. Phys. Chem. A **107**, 6974 (2003).

[3]H. Hippler, S. Nasterlack, and F. Striebel, Phys. Chem. Chem. Phys. **4**, 2959 (2002).
[4]N. M. Donahue, R. Mohrschladt, T. J. Dransfield, J. G. Anderson, and M. K. Dubey, J. Phys. Chem. A **105**, 1515 (2001).
[5]D. M. Golden, J. R. Barker, and L. L. Lohr, J. Phys. Chem. A **107**, 11057 (2003).
[6]J. L. Fry, S. A. Nizkorodov, M. Okumura, C. M. Roehl, J. S. Francisco, and P. O. Wennberg, J. Chem. Phys. **121**, 1432 (2004).
[7]M. P. McGrath and F. S. Rowland, J. Phys. Chem. **98**, 1061 (1994).
[8]H. H. Tsai, T. P. Hamilton, J. H. M. Tsai, M. van derWoerd, J. G. Harrison, M. J. Jablonsky, J. S. Beckman, and W. H. Koppenol, J. Phys. Chem. **100**, 15087 (1996).
[9]K. N. Houk, K. R. Condroski, and W. A. Pryor, J. Am. Chem. Soc. **118**, 13002 (1996).
[10]R. D. Bach, M. N. Glukhovtsev, and C. Canepa, J. Am. Chem. Soc. **120**, 775 (1998).
[11]K. Doclo and U. Rothlisberger, Chem. Phys. Lett. **297**, 205 (1998).
[12]R. S. Zhu and M. C. Lin, J. Chem. Phys. **119**, 10667 (2003).
[13]J. F. Stanton (private communication).
[14]B. M. Cheng, J. W. Lee, and Y. P. Lee, J. Phys. Chem. **95**, 2814 (1991).
[15]W. J. Lo and Y. P. Lee, J. Chem. Phys. **101**, 5494 (1994).
[16]I. B. Pollack, I. M. Konen, E. X. J. Li, and M. I. Lester, J. Chem. Phys. **119**, 9981 (2003).
[17]J. Matthews, A. Sinha, and J. S. Francisco, J. Chem. Phys. **120**, 10543 (2004).
[18]I. M. Konen, I. B. Pollack, E. X. J. Li, M. I. Lester, M. E. Varner, and J. F. Stanton, J. Chem. Phys. (to be published).
[19]G. Purvis and R. Bartlett, J. Chem. Phys. **76**, 1910 (1982).
[20]K. Raghavachari, G. W. Trucks, J. A. Pople, and M. Head-Gordon, Chem. Phys. Lett. **157**, 479 (1989).
[21]J. D. Watts, J. Gauss, and R. J. Bartlett, J. Chem. Phys. **98**, 8718 (1993).
[22]T. H. Dunning, J. Chem. Phys. **90**, 1007 (1989).
[23]R. A. Kendall, T. H. Dunning, and R. J. Harrison, J. Chem. Phys. **96**, 6796 (1992).
[24]D. E. Woon and T. H. Dunning, J. Chem. Phys. **98**, 1358 (1993).
[25]J. A. Pople, M. Head-Gordon, and K. Raghavachari, J. Chem. Phys. **87**, 5968 (1987).
[26]M. J. Frisch, G. W. Trucks, H. B. Schlegel *et al.*, GAUSSIAN 98, Revision A.9, 1998.
[27]D. T. Colbert and W. H. Miller, J. Chem. Phys. **96**, 1982 (1992).
[28]Z. Bacic and J. C. Light, Annu. Rev. Phys. Chem. **40**, 469 (1989).
[29]See EPAPS Document No. E-JCPSA6-122-009510 for parameters of the potential energy and dipole surfaces. A direct link to this document may be found in the online article's HTML reference section. The document may also be reached via the EPAPS homepage (http://www.aip.org/pubservs/epaps.html) or from ftp.aip.org in the directory /epaps/. See the EPAPS homepage for more information.
[30]J. M. Guilmot, M. Godefroid, and M. Herman, J. Mol. Spectrosc. **160**, 387 (1993).
[31]K. J. Feierabend, D. K. Havey, and V. Vaida, Spectrochim. Acta, Part A **60**, 2775 (2004).

APPENDIX II:
ROTATIONAL SPECTRUM OF *CIS-CIS* HOONO

JOURNAL OF CHEMICAL PHYSICS VOLUME 120, NUMBER 12 22 MARCH 2004

Rotational spectrum of *cis–cis* HOONO

Brian J. Drouin
California Institute of Technology, Jet Propulsion Laboratory, Pasadena, California 91109

Juliane L. Fry
California Institute of Technology, Department of Chemistry, Pasadena California 91125

Charles E. Miller
California Institute of Technology, Jet Propulsion Laboratory, Pasadena, California 91109

(Received 15 January 2004; accepted 28 January 2004)

The pure rotational spectrum of *cis–cis* peroxynitrous acid, HOONO, has been observed. Over 220 transitions, sampling states up to $J'=67$ and $K_a'=31$, have been fitted with an rms uncertainty of 48.4 kHz. The experimentally determined rotational constants agree well with *ab initio* values for the *cis–cis* conformer, a five-membered ring formed by intramolecular hydrogen bonding. The small, positive inertial defect $\Delta=0.075667(60)$ amu Å^2 and lack of any observable torsional splittings in the spectrum indicate that *cis–cis* HOONO exists in a well-defined planar structure at room temperature. © *2004 American Institute of Physics.* [DOI: 10.1063/1.1687311]

The radical–radical association reaction

$$OH+NO_2+M\rightarrow HONO_2+M$$

terminates several key HO_x and NO_x catalytic free-radical chain reactions in the lower atmosphere and sequesters the reactants into the reservoir species nitric acid, $HONO_2$. The rate of this reaction directly affects ozone concentrations in the stratosphere and photochemical smog production in the troposphere. Thus, detailed knowledge of the $OH+NO_2+M$ mechanism and rate under all atmospherically relevant conditions is critical for accurate modeling of atmospheric photochemistry. An intensive investigation of discrepancies between low- and high-pressure values of the rate led several groups to propose that a secondary channel

$$OH+NO_2+M\rightarrow HOONO+M$$

competes with the primary reaction channel at higher total pressures.[1–7] Despite the kinetics evidence, detection of gas-phase HOONO eluded several concentrated detection efforts[2,4,5] and its production as a stable species in the $OH+NO_2+M$ reaction remained controversial until very recently.

Peroxynitrous acid, HOONO, has long been known as a short-lived intermediate in aqueous solutions, although its spectroscopic characterization in solution has been limited to a broad UV absorption feature.[8–10] In the early 1990s Lee and co-workers identified HOONO infrared spectra after photodissociating $HONO_2$ in cryogenic Ar and N_2 matrices.[11–13] The vibrational frequencies, H/D and $^{14}N/^{15}N$ isotopic shifts, and band intensities recorded in these studies provided the information to distinguish *trans–perp* and *cis–cis* HOONO conformers. The dynamics of $OH+NO_2$ recombination in the matrix sites favored the production of *trans–perp* HOONO; *cis–cis* HOONO was observed only after $HONO_2$ photodissociation at 193 nm.[13]

In 2002 Nizkorodov and Wennberg reported the detection of gas-phase HOONO by recording the vibrational overtone photodissociation spectrum in the $2\nu_1$ region (6000–7200 cm^{-1}) with ~2 cm^{-1} resolution.[14] They observed a rich vibrational structure with at least seven overlapping HOONO bands. These features were tentatively assigned to both the *cis–cis* and *trans–perp* conformers; however, a reanalysis of this spectral assignment indicates that only *cis–cis* HOONO is present at room temperature, while significant concentrations of *trans–perp* HOONO are observed only below 240 K under moderate flow rates due to rapid isomerization.[15] A number of additional features in this spectrum are assigned to combinations of $2\nu_1$ with the ν_9 torsional mode, indicating a large degree of structural floppiness in HOONO.

This work was followed in rapid succession by detection of the *cis–cis* ν_1 fundamental by Bean *et al.* using cavity ringdown spectroscopy[16] and a high-resolution study of the *trans–perp* $2\nu_1$ band in a supersonically cooled molecular beam by Pollack *et al.*[17] Rotational contour simulations in both studies yielded rotational constants consistent with *ab initio* values. The resolution of individual rotational transitions was not possible due to laser bandwidth limitations in the study of Bean *et al.* and because of dissociative line broadening in the case of the work of Pollack *et al.*

Ab initio calculations have helped guide much of the spectral characterization of HOONO. McGrath *et al.* found stable structures associated with the *cis–cis*, *cis–perp*, and *trans–perp* conformers at the HF/6-31G* and MP2/6-31G* levels of theory.[18] The vibrational frequencies and intensities calculated in this study enabled Lee and co-workers[11,13] to distinguish between the *trans–perp* and *cis–cis* conformers in their matrix IR spectra. McGrath and Rowland subsequently used G2, G2(MP2), QCISD(T)/6-311G(d,p), and MP2 calculations with basis sets up to 6-311+G(3df,2p) to improve characterization of the relative energetics of the three stable conformers.[19] Bean *et al.* found that the *cis–perp* conformer was not a true stationary point at the QCISD(T)/cc-pVTZ or CCSD(T)/cc-pVTZ levels of theory.[16] Bean *et al.* also reported rotational constants and vibrational fre-

quencies for *cis–cis* and *trans–perp* HOONO for QCISD and CCSD(T) calculations. At the CCSD(T)/cc-pVTZ level of theory, the *cis–cis* conformer was found to be 3.4 kcal/mol more stable than the *trans–perp* conformer (including zero-point correction) (Ref. 16) with a best estimate of $D_0(\mathrm{HO–ONO})_{cis-cis} = 18.3$ kcal/mol at the CCSD(T)/CBS level of theory.[20]

There now exists an abundance of convincing spectroscopic evidence supporting a significant HOONO channel in the gas-phase reaction of $OH + NO_2$.[14–17] However, the lack of rotationally resolved spectra in any of these studies has hampered efforts to provide an unambiguous assignment of the observed spectral features or to quantify the relative yields of *cis–cis* and *trans–perp* HOONO produced under different experimental conditions. Our past success in producing, detecting, and analyzing the pure rotational spectra of free radicals and reactive intermediates with the JPL submillimeter spectrometer[21–25] prompted us to initiate a search for HOONO. Submillimeter spectroscopy provides several advantages over the techniques that have previously been used to characterize HOONO: excellent detection sensitivity, superb spectral resolution, and unequivocal molecular specificity for assigned transitions. Additionally, molecular concentrations can be accurately measured from the intensities of pure rotational transitions once the molecular dipole moment is known. Here we report an analysis of the *cis–cis* HOONO submillimeter spectrum.

The JPL submillimeter spectrometer has been described in detail previously.[26] Spectra were recorded by flowing the vapors from a 70% hydrogen peroxide solution (FMC Corporation) over a sample of solid $NOBF_4$ (Aldrich) placed in a shallow Pyrex boat in the bottom of the absorption cell. The hydrogen peroxide flow rate was adjusted to maximize the *cis–cis* HOONO signal. Typical cell pressures were 15–20 mtorr. Small amounts of nitric acid ($HONO_2$) (Ref. 27), peroxynitric acid ($HOONO_2$) (Ref. 27), and hydroxyfluoroborane (BF_2OH) (Ref. 28) were observed as side products. The chemistry used in this study has the advantage of selectively generating *cis–cis* HOONO without large interferences from $HONO_2$.

All spectral fitting and simulations were performed using Pickett's SPFIT program suite.[29] An illustration of the *cis–cis* HOONO molecular structure in its principal axis system is given in Fig. 1. Simulations of the *cis–cis* HOONO rotational spectrum, based on *ab initio* rotational constants and dipole moments,[16] predicted the presence of characteristic asymmetry doublets of both *a*- and *b*-type transitions (i.e., quartets) for low-K_a *R*-type transitions near 400 GHz. Survey scans in the 399–454 GHz region revealed quartet patterns consistent with the *cis–cis* HOONO simulations. The compact origins of several patterns are shown in Fig. 2. Termed "*R* bunches," these patterns occur for oblate limit transitions at intervals of $2C$ (~11.5 GHz) with $J + K_a = \text{const}$. The initial assignments for *R* bunches with $K_a < 5$ were used to refine the spectroscopic parameters and generate new predictions. New transitions were assigned and the fitting process iteratively repeated. Additional spectra were recorded in the 179–183, 269–284, and 627–640 GHz regions to extend the J and K_a range of transitions in the data

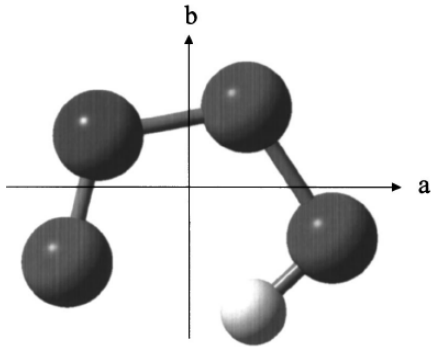

FIG. 1. *cis–cis* HOONO depicted in its principal axis system. The *c* axis is perpendicular to the molecular plane. The structure is taken from the CCSD(T)/cc-pVTZ calculations of Bean *et al.* (Ref. 16).

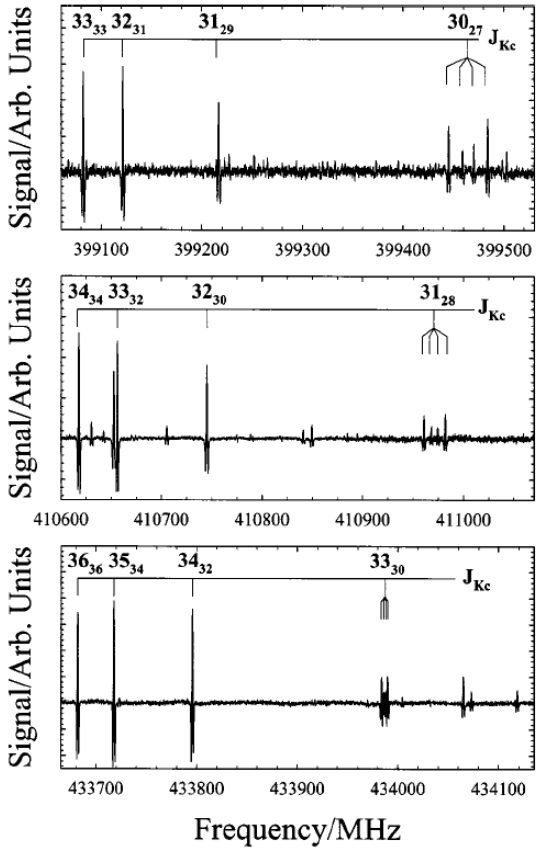

FIG. 2. Submillimeter spectra of *cis–cis* HOONO *R*-bunch origins in the 400 GHz region displaying the characteristic pattern used to make the initial identification. The separation of the first resolved quartet from the first transition of each sequence and the splitting within the quartet both decrease with increasing frequency. The approximate intensity ratio within each quartet reflects the relative magnitudes of $\mu_b^2 : \mu_a^2 : \mu_a^2 : \mu_b^2$. The unmarked features in these spectra are due to $HONO_2$, $HOONO_2$, or other *cis–cis* HOONO transitions.

TABLE I. Fitted *cis–cis*-HOONO Hamiltonian parameters.[a]

Parameter	Units	Value
$(B+C)/2$	MHz	6869.52786(32)
$A-(B+C)/2$	MHz	14536.8651(10)
$(B-C)/4$	MHz	539.26307(12)
$-\Delta_J$	kHz	−8.05340(26)
$-\Delta_{JK}$	kHz	16.0335(11)
$-\Delta_K$	kHz	−59.9854(46)
δ_J	kHz	−2.47179(11)
δ_K	kHz	−13.7320(20)
Φ_J	mHz	−15.005(68)
Φ_{JJK}	mHz	184.55(53)
Φ_{JKK}	mHz	−883.1(21)
Φ_K	Hz	1.0996(56)
ϕ_J	mHz	−5.385(29)
ϕ_{JK}	mHz	−55.11(76)
ϕ_K	mHz	388.7(46)
σ_{fit}/No. lines	kHz	48.4/225

[a]Values in parentheses represent 1σ uncertainties in units of the least significant figure.

set. The final data set included 225 transitions sampling states with J up to 67 and K_a up to 31. The least-squares fit yielded an rms uncertainty of 48.4 kHz and accurately predicted all ground-state *cis–cis* HOONO features with sufficient intensity to be identifiable in the spectra recorded.

Measured and calculated frequencies and quantum number assignments can be found in the JPL millimeter and submillimeter spectral line catalog online at http://spec.jpl.nasa.gov/catalog. Rotational constants and distortion constants up to sixth order were determined using the Watson A reduction. The parameters determined in the least-squares fit are given in Table I.

The A, B, and C rotational constants were determined from the fitted Hamiltonian parameters. These values are given in Table II along with the rotational constants determined from the optimized CCSD(T)/cc-pVTZ structure reported by Bean *et al.*[16] The inertial defect $\Delta = I_{cc} - I_{aa} - I_{bb}$ is 0.076 amu Å^2, consistent with the small, positive inertial defects that have been observed for planar ring molecules such as furan and pyrrole.[30] This evidence indicates that *cis–cis* HOONO is a planar molecule with small out-of-plane deformations caused by zero-point vibrational motion. The lack of any observed torsional splittings in the submillimeter spectrum of the vibrational ground state further suggests that intramolecular hydrogen bonding prevents any significant large-amplitude motion.

TABLE II. *cis–cis* HOONO rotational constants, moments of inertia, and inertial defect.[a]

Parameter	Experiment	CCSD(T)/cc-pVTZ Ref. 16
A (MHz)	21406.3930(10)	21310
B (MHz)	7948.05399(43)	8081
C (MHz)	5791.00173(35)	5859
I_{aa} (amu Å^2)	23.6087915(11)	23.715
I_{bb} (amu Å^2)	63.5852588(34)	62.54
I_{cc} (amu Å^2)	87.2697149(53)	86.26
Δ (amu Å^2)	0.0756646(64)	0.00

[a]Values in parentheses represent 1σ uncertainties in units of the least significant figure.

Our findings of well-defined planarity in *cis–cis* HOONO contrast with the significant levels of torsional excitation that Nizkorodov and Wennberg observed in the $2\nu_1$ region and their conclusion that HOONO exhibits a large degree of structural floppiness.[14] The most likely reasons for this discrepancy lie in the experimental measurements: the submillimeter spectrum detects molecules near the minimum of the potential energy surface while the Nizkorodov–Wennberg experiment detects exclusively molecules that have undergone vibrational photodissociation. HOONO molecules with internal energies above the HO–ONO dissociation threshold might be expected to display significant torsional excitation as they dissociate. Torsional excitation may even enhance the dissociation rate near D_0(HO–ONO) and thermal excitation of torsional vibrations can promote dissociation for molecules nominally excited below D_0(HO–ONO). The variation of the rigidity of the planar structure as a function of vibrational-mode excitation and total internal energy as well as how the deviation from planarity affects the near-threshold dissociation dynamics are clearly areas for further investigation.

The intensities of the various observed rotational transitions can be used to estimate the relative values of the μ_a and μ_b dipole moment components. The $J_{Kc} = 30_{27}$, 31_{28}, and 33_{30} quartets shown in Fig. 2 are especially useful for this since the two central components in each quartet are a-type transitions while the highest- and lowest-frequency transitions in each quartet are b-type transitions. After removal of the J- and K-dependent matrix elements, the relative intensities of the quartets suggest that $\mu_b^2/\mu_a^2 \sim 3$. Simulations using $\mu_a = 0.66$ D and $\mu_b = 1.14$ D produced good agreement with comparable *cis–cis* HOONO transition intensities.

Experiments to measure selected lower-J transitions at millimeter wavelengths to determine μ_a, μ_b, and μ_{tot} are under way. Once experimental values for μ_a, μ_b, and μ_{tot} have been determined, millimeter and submillimeter spectroscopy will provide an excellent method for accurately quantifying *cis–cis* HOONO number densities. This will enable us to quantify the $OH + NO_2 \rightarrow cis\text{–}cis$ HOONO yields under atmospherically relevant conditions. A combined submillimeter and infrared experiment could also be used to quantify the band strengths of the infrared transitions.[14,16,17]

This research was performed at the Jet Propulsion Laboratory (JPL), California Institute of Technology, under contract with the National Aeronautics and Space Administration. This material is based upon work supported under a National Science Foundation Graduate Research Fellowship (J.L.F.) and supported by NSF's Atmospheric Chemistry Program (Grant No. ATM-0094760). The authors thank S. P. Sander (JPL), P. O. Wennberg (Caltech), and M. Okumura (Caltech) for insightful discussions, J. S. Francisco (Purdue) for communicating the results of his *ab initio* calculations, and D. T. Petkie (Wright State) for unpublished HOOH and $HONO_2$ excited state constants.

[1] J. S. Robertshaw and I. W. M. Smith, J. Phys. Chem. **86**, 785 (1982).
[2] J. B. Burkholder, P. D. Hammer, and C. J. Howard, J. Phys. Chem. **91**, 2136 (1987).
[3] D. M. Golden and G. P. Smith, J. Phys. Chem. A **104**, 3991 (2000).
[4] T. J. Dransfield, N. M. Donahue, and J. G. Anderson, J. Phys. Chem. A **105**, 1507 (2001).
[5] N. M. Donahue, R. Mohrschladt, T. J. Dransfield, J. G. Anderson, and M. K. Dubey, J. Phys. Chem. A **105**, 1515 (2001).
[6] J. Troe, Int. J. Chem. Kinet. **33**, 878 (2001).
[7] H. Hippler, S. Nasterlack, and F. Striebel, Phys. Chem. Chem. Phys. **4**, 2959 (2002).
[8] K. Gleu and P. Hubold, Z. Anorg. Allg. Chem. **223**, 305 (1935).
[9] M. Anbar and H. Taube, J. Am. Chem. Soc. **76**, 6243 (1954).
[10] M. Gratzel, A. Henglein, and S. Taniguchi, Ber. Bunsenges. Phys. Chem. **74**, 3445 (1970).
[11] B. M. Cheng, J. W. Lee, and Y. P. Lee, J. Phys. Chem. **95**, 2814 (1991).
[12] W. J. Chen, W. J. Lo, B. M. Cheng, and Y. P. Lee, J. Chem. Phys. **97**, 7167 (1992).
[13] W. J. Lo and Y. P. Lee, J. Chem. Phys. **101**, 5494 (1994).
[14] S. A. Nizkorodov and P. O. Wennberg, J. Phys. Chem. A **106**, 855 (2002).
[15] J. L. Fry, M. Okumura, S. Nizkorodov, C. M. Roehl, and P. O. Wennberg, J. Chem. Phys. (to be published).
[16] B. D. Bean, A. K. Mollner, S. A. Nizkorodov, G. Nair, M. Okumura, S. P. Sander, K. A. Peterson, and J. S. Francisco, J. Phys. Chem. A **107**, 6974 (2003).
[17] I. B. Pollack, I. M. Konen, E. X. J. Li, and M. I. Lester, J. Chem. Phys. **119**, 9981 (2003).
[18] M. P. McGrath, M. M. Francl, F. S. Rowland, and W. J. Hehre, J. Phys. Chem. **92**, 5352 (1988).
[19] M. P. McGrath and F. S. Rowland, J. Phys. Chem. **98**, 1061 (1994).
[20] D. A. Dixon, D. Feller, C. G. Zhan, and J. S. Francisco, J. Phys. Chem. A **106**, 3191 (2002).
[21] B. J. Drouin, C. E. Miller, E. A. Cohen, G. Wagner, and M. Birk, J. Mol. Spectrosc. **207**, 4 (2001).
[22] B. J. Drouin, C. E. Miller, H. S. P. Muller, and E. A. Cohen, J. Mol. Spectrosc. **205**, 128 (2001).
[23] C. E. Miller and E. A. Cohen, J. Chem. Phys. **115**, 6459 (2001).
[24] H. S. P. Muller, C. E. Miller, and E. A. Cohen, J. Chem. Phys. **107**, 8292 (1997).
[25] C. E. Miller and E. A. Cohen, J. Chem. Phys. **118**, 6309 (2003).
[26] B. J. Drouin, J. Fischer, and R. R. Garnache, J. Quant. Spectrosc. Radiat. Transf. **83**, 63 (2004).
[27] H. M. Pickett, R. L. Poynter, E. A. Cohen, M. L. Delitsky, J. C. Pearson, and H. S. P. Muller, J. Quant. Spectrosc. Radiat. Transf. **60**, 883 (1998).
[28] H. Takeo and R. F. Curl, J. Chem. Phys. **56**, 4314 (1972).
[29] H. M. Pickett, J. Mol. Spectrosc. **148**, 371 (1991).
[30] W. Gordy and R. L. Cook, *Microwave Molecular Spectra*, 3rd ed. (Wiley-Interscience, New York, 1984).

APPENDIX III:
NEAR-IR PHOTODISSOCIATION OF PEROXYACETYL NITRATE (PAN)

Atmos. Chem. Phys., 5, 385–392, 2005
www.atmos-chem-phys.org/acp/5/385/
SRef-ID: 1680-7324/acp/2005-5-385
European Geosciences Union

Atmospheric Chemistry and Physics

Near-IR photodissociation of peroxy acetyl nitrate

S. A. Nizkorodov[1], J. D. Crounse[2], J. L. Fry[2], C. M. Roehl[3], and P. O. Wennberg[3]

[1]Department of Chemistry, University of California at Irvine, Irvine, CA 92697, USA
[2]Division of Chemistry and Chemical Engineering, California Institute of Technology, Pasadena, CA 91125, USA
[3]Division of Geological and Planetary Sciences and Division of Engineering and Applied Science, California Institute of Technology, Pasadena, CA, 91125, USA

Received: 4 February 2004 – Published in Atmos. Chem. Phys. Discuss.: 1 March 2004
Revised: 28 April 2004 – Accepted: 7 May 2004 – Published: 10 February 2005

Abstract. Measurements of the C-H overtone transition strengths combined with estimates of the photodissociation cross sections for these transitions suggest that near-IR photodissociation of peroxy acetyl nitrate (PAN) is less significant ($J_{near-IR} \approx 3 \times 10^{-8}\ s^{-1}$ at noon) in the lower atmosphere than competing sinks resulting from unimolecular decomposition and ultraviolet photolysis. This is in contrast to the photochemical behavior of a related peroxy nitrate, pernitric acid (PNA), that undergoes rapid near-IR photolysis in the atmosphere with $J_{near-IR} \approx 10^{-5}\ s^{-1}$ at noon (Roehl et al., 2002). This difference is attributed to the larger binding energy and larger number of vibrational degrees of freedom in PAN, which make $4\nu_{CH}$ the lowest overtone excitation with a high photodissociation yield (as opposed to $2\nu_{OH}$ in PNA).

1 Introduction

Atmospheric photochemistry is normally driven by electronic state excitations in the ultraviolet range of the solar spectrum. However, photodissociation processes resulting from near-IR direct overtone excitations within the ground electronic state can also be significant in special cases (Donaldson et al., 2003). Donaldson et al. (1997) examined several atmospheric molecules featuring small binding energies and strong overtone transitions, and identified HO_2NO_2 (pernitric acid or PNA) as the most likely candidate for an efficient overtone photodissociation. They argued that the dissociation energy threshold for PNA, $D_0(HO_2\text{-}NO_2)$=7970±280 cm^{-1} (Zabel, 1995), is sufficiently low to permit its overtone photolysis via the second OH stretching overtone transition at $E(3\nu_{OH})$=10 090 cm^{-1}. Subsequent experimental study of near-IR photodissociation cross sections of PNA by Roehl et al. (2002) showed that PNA overtone dissociation is even more important than Donaldson et al. (1997) initially surmised. Roehl et al. (2002) found that PNA can photolyze with a substantial yield not only upon $3\nu_{OH}$ but also upon $2\nu_{OH}$ excitation at 6900 cm^{-1}, which lies as much as 1070 cm^{-1} below the PNA formal dissociation energy threshold. These striking results have recently been independently confirmed by Sinha's research group (Matthews et al., 2004). Such efficient under-threshold photolysis can be attributed to the collisional activation and internal energy contributions to the dissociation process, just as in the well-known cases of ultraviolet photodissociation of NO_2 (Pitts et al., 1964; Roehl et al., 1994) and O_3 (Finlayson-Pitts and Pitts, 2000), and overtone dissociation of nitric acid (Sinha et al., 1990). The combined $2\nu_{OH}$ and $3\nu_{OH}$ PNA atmospheric photodissociation rate amounts to $\approx 10^{-5}\ s^{-1}$, making near-IR photolysis the dominant sink process for PNA in the upper troposphere and lower stratosphere (Roehl et al., 2002).

This letter examines possible atmospheric significance of near-IR photolysis for another important peroxy nitrate, $CH_3C(O)OONO_2$ (peroxy acetyl nitrate or PAN). PAN is a key odd-nitrogen component of photochemical smog (Finlayson-Pitts and Pitts, 2000), and it serves both as a temporary reservoir and as a global transporter for NO_x. PAN often accounts for the largest fraction of all odd-nitrogen compounds (NO_y) in the atmosphere, especially at high latitudes (Ridley et al., 2003; Stroud et al., 2003). The primary known sinks for PAN include unimolecular decomposition, which is the dominant channel in the lower atmosphere, and ultraviolet photolysis, which becomes prevalent in the colder upper tropospheric layers. Reaction of PAN with OH is too slow to be of relevance (DeMore et al., 1997). Similar to other peroxy nitrates (Kirchner et al., 1999; Zabel, 1995), PAN has a low dissociation energy, $D_0(CH_3C(O)OO\text{–}NO_2)$=9820±240 cm^{-1} (Bridier et al., 1991; Zabel, 1995), which falls between the $3\nu_{CH}$ ($E \approx 8550\ cm^{-1}$) and $4\nu_{CH}$ ($E \approx 11\,100\ cm^{-1}$) vibrational states of the molecule. To

Correspondence to: S. A. Nizkorodov
(nizkorod@uci.edu)

evaluate the efficiency of near-IR photochemistry of PAN, knowledge of both the intensity of the CH stretching overtones and photodisssociation quantum yields are required. Although the strength of CH stretching overtone transitions are well-known for many hydrocarbons (Hanazaki et al., 1985; Kjaergaard et al., 1991; Nakagaki and Hanazaki, 1986), no information on the cross sections and photodissociation quantum yields for PAN is presently available. In what follows, we show that these quantities can be estimated from statistical models and comparisons with experimental data on related molecules, and we use them to predict the near-IR photodissociation rates for PAN under typical atmospheric conditions.

2 Results and discussion

2.1 Definitons and units

Subject to the approximations described below, band-specific atmospheric photodissociation rates, J_{band}, can be calculated in the following way:

$$J_{\text{band}} = \int_{\text{band}} F(\bar{\nu})\sigma(\bar{\nu})\phi(\bar{\nu})d\bar{\nu} \approx \langle F(\bar{\nu})\rangle \times S_{\text{band}} \times \phi_{\text{band}} \quad (1)$$

$F(\bar{\nu})$ is the frequency-dependent solar flux measured in $\frac{\text{photons}}{\text{cm}^2\,\text{s}\,\text{cm}^{-1}}$, $\langle F(\bar{\nu})\rangle$ is the average value of $F(\bar{\nu})$ over the absorption band, $\sigma(\bar{\nu})$ is base-e molecular absorption cross section in cm^2/molecule, $\phi(\bar{\nu})$ is photodissociation quantum yield, $\bar{\nu}$ is wave number in cm^{-1}, and $S_{\text{band}} = \int_{\text{band}} \sigma(\bar{\nu})d\bar{\nu}$ is the integrated absorption cross section (in cm/molecule) for the band in question. The last equality applies only if $F(\bar{\nu})$ varies weakly with frequency, which is usually a good approximation for the narrow near-IR bands unless they are close to strong water or carbon dioxide absorptions. The quantity ϕ_{band} is best interpreted as the ratio between the integrated photodissociation and absorption cross sections for the band. The paragraphs below deal with estimation of S and ϕ for the CH stretching overtone transitions of PAN.

2.2 PAN overtone absorption cross-sections

Integrated absorption cross sections for PAN fundamentals have been reported by Gaffney et al. (1984). However, their analysis has subsequently been questioned and corrected by Tsalkani and Toupance (1989) for the four strongest infrared bands of PAN below 2000 cm^{-1}. To resolve the resulting ambiguity of the intensity data for the remaining bands not considered by Tsalkani and Toupance (1989), we have measured relative intensities of the CH stretching fundamental and overtone transitions and determined absolute transition intensities by relation to Tsalkani and Toupance (1989) data for NO stretching vibrations of PAN. Pure gaseous PAN samples were synthesized as described by Gaffney et al. (1984), and gas-phase spectra of PAN were recorded with an FTIR spectrometer at 1 cm^{-1} resolution (Fig. 1). Depending on the examined spectral range, we used either a single-pass 20 cm cell containing 0.1–1 Torr partial pressure of PAN, or a multipass cell with an effective path length of 360 cm containing the equilibrium vapor pressure of PAN at room temperature (about 4.5 Torr). The multipass configuration was required to observe the second CH stretching overtone with an acceptable signal-to-noise ratio (Fig. 1).

The ratios of PAN band strengths were obtained from multiple spectra. The absorbances (A=$\sigma(\bar{\nu})\times$[PAN]$\times$pathlength) for the bands in question were always kept small to avoid deviations from the Beer-Lambert law. For very weak transitions like CH-overtones there is no reason to believe that their integrated absorbances should deviate from a linear dependence on PAN concentration. For the stronger fundamental transitions, deviations from linearity are certainly possible, but we measured the ratio of the integrated absorbances at multiple partial pressures of PAN and always obtained the same result. This is an indirect proof that Beer-Lambert law was obeyed for these transitions under our experimental conditions. The value of $S(\nu_{\text{CH}})$ was measured relative to the band strengths of NO_2 stretches reported by Tsalkani and Toupance (1989). Our value, $S(\nu_{\text{CH}})$=1.57×10^{-18} cm/molecule, is 40% lower than that reported by Gaffney et al. (1984). This agrees with the conclusions of Tsalkani and Toupance (1989), who showed that data from Gaffney et al. (1984) overestimated band intensities of PAN by 5 to 35%. The CH stretching overtone band strengths were always measured relative to the closest available CH stretching transition at lower frequency. Our results $S(2\nu_{\text{CH}})/S(\nu_{\text{CH}})$=0.096±0.015 and $S(3\nu_{\text{CH}})/S(2\nu_{\text{CH}})$=0.085±0.030 are consistent with the generally observed trend of the 10-fold drop of overtone intensity per vibrational quantum (we define $S(2\nu_{\text{CH}})$ and $S(3\nu_{\text{CH}})$ as the total integrated absorption cross section for the 5600–6300 cm^{-1} and 8300–9000 cm^{-1} ranges, respectively).

Integrated intensity for the $4\nu_{\text{CH}}$ overtone of PAN could not be reliably determined from our FTIR spectra, but it can be deduced from comparison with spectra of other molecules bearing an acetyl group. Indeed, the observed spectra of the first and second CH overtones of PAN (Fig. 1) closely resemble the spectra of acetone and acetaldehyde (Hanazaki et al., 1985). The orientational site splitting pattern arising from the inequivalence of CH bonds in the methyl group (Hanazaki et al., 1985; Kjaergaard et al., 1991) is similar for all three molecules. The integrated intensities (per methyl group) for the ν_{CH} fundamental, $2\nu_{\text{CH}}$ first overtone, and $3\nu_{\text{CH}}$ second overtone bands are also quite similar (Table 1). Assuming that the PAN overtone intensity decreases with vibrational quantum number by the same factors as the average of the corresponding acetone and acetaldehyde values, S($4\nu_{\text{CH}}$)/ S($3\nu_{\text{CH}}$)=0.059, we can estimate $S_{PAN}(4\nu_{\text{CH}})$ as 7.6×10^{-22} cm/molecule. Based on the good uniformity of

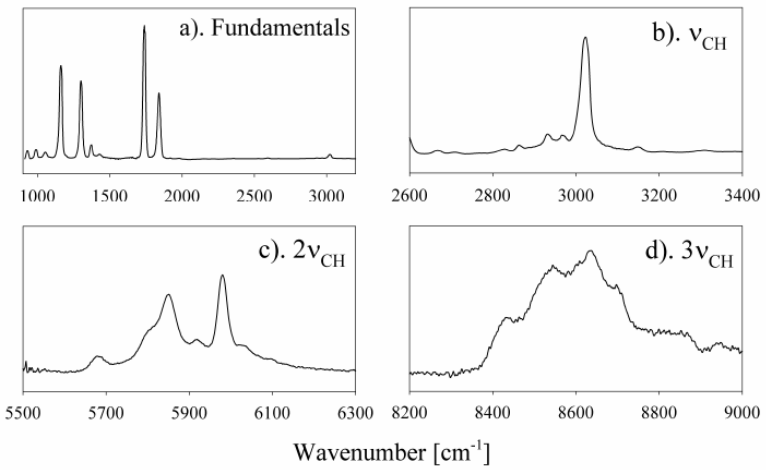

Fig. 1. IR spectrum of PAN recorded in this work: **(a)** fundamental range displaying well-known PAN bands; **(b)** CH stretching fundamental range; **(c)** first CH stretching overtone range; d) second CH stretching overtone range. The CH-stretching overtones have a complicated band structure resulting from the inequivalence of CH bonds in the methyl group. Experimentally measured ratios between integrated absorption cross sections are $S(\nu_{CH}):S(2\nu_{CH}):S(3\nu_{CH})$ = 1:0.096:0.0082. $S(\nu_{CH})$ is measured to be 1.57×10^{-18} cm/molecule (base e) in this work.

the experimentally available band strength ratios for these three molecules, we do not expect the estimated value of $S_{PAN}(4\nu_{CH})$ to deviate from the true band strength by more than a factor of two.

2.3 Photodissociation quantum yields

Photodissociation quantum yields for CH overtone excitations of PAN have been calculated with the Multiwell suite (Barker, 2001) using a statistical approach. The calculation involves shifting the Boltzmann internal energy distribution of the molecule upward by the photon energy, and solving the coupled master equations for discretized internal energy states. Excited molecules can undergo either a unimolecular decomposition with the microcanonical rate constant $k_{uni}(E)$ or collision-induced internal energy change with the rate that depends on pressure and internal energy. The fraction of molecules that end up decomposing by the time internal energy in the surviving molecules is nearly thermalized ($\approx10^3$ collisions) is taken as the photodissociation yield.

The quantum yield calculation presented here is based on the assumptions that: i) the internal energy can exchange freely between different vibrational degrees of freedom (K-rotor states are also counted towards the total available energy); ii). The transition strengths for sequence (hot) bands originating from the low- frequency vibrational states and building upon CH overtones are the same as for the corresponding overtones themselves. The high frequency CH vibrations are known to couple quite weakly with the low-frequency vibrational modes. Therefore, the second assumption is likely to hold, whereas the first one may in principle break down leading to non-statistically long lifetimes of the vibrationally excited molecules. At finite pressures, the dissociation quantum yield may be reduced by these non-statistical effects. The yields we are predicting will therefore represent an upper limit to the actual photodissociation yields.

The exponential collision model built into the Multiwell was used, with the probability of downward collisions taken as $e^{(E_{final}-E_{initial})/\Delta}$, where Δ=45 cm^{-1}+0.005$\times E_{initial}$, a weak collision model (Barker, 2001). Vibrational

Table 1. Experimental integrated absorption cross sections (base e) for the CH-stretching overtones of acetone, acetaldehyde, and PAN. The units of S(band) are cm^2/molecule cm^{-1} (1 cm^{-2} atm^{-1} at 298 K=4.063×10^{-20} cm/molecule). The integrated absorption cross sections are given per CH_3 group; i.e. the acetone values have been divided by 2.

Band	Acetone/2[a]	Acetaldehyde[a]	PAN
(ν_{CH})	3.04E-18	2.02E-18	1.57E-18
2(ν_{CH})	1.28E-19	1.51E-19	1.51E-19[b]
3(ν_{CH})	1.60E-20	1.63E-20	1.28E-20[c]
4(ν_{CH})	1.09E-21	8.21E-22	7.56E-22[d]

[a] From Hanazaki et al. (1985).
[b] Measured to be 9.6% of $S(\nu_{CH})$ in this work.
[c] Measured to be 8.5% of $S(2\nu_{CH})$ in this work.
[d] Assumed value based on comparison with acetone and acetaldehyde (5.9% of $S(3\nu_{CH})$).

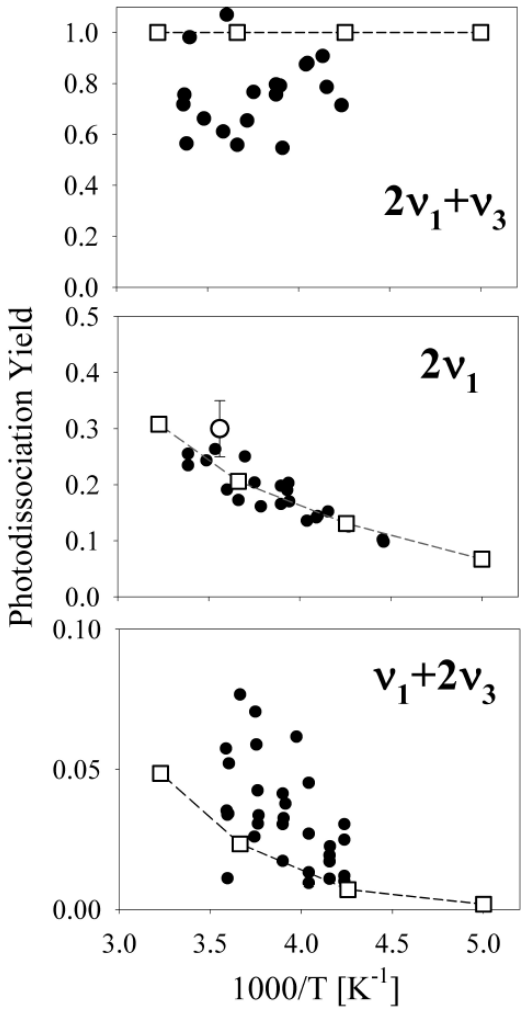

Fig. 2. Experimental photodissociation quantum yields for different vibrational overtone excitations of PNA measured by Roehl et al. (2002) (filled circles) compared to the statistical simulation results (open squares) of this work. Both simulations and data correspond to P=5 Torr. The open circle point in the $2\nu_1$ panel comes from Matthews et al. (2004) and it corresponds to T=298 K, P=0.1 Torr. Parameters for our statistical simulation were chosen to reproduce the $2\nu_1$ photodissociation yields.

frequencies for PAN were taken from Miller et al. (1999). Lennard-Jones collision parameters were the same as used by Bridier et al. (1991). The NO_2 and –C-O-O moieties were treated as hindered rotors in the transition state. The CH_3 group was treated as a free rotor for both reactant and transition state. The initially-selected RRKM parameters were fine-tuned to reproduce i) high pressure limit of the experimental unimolecular decomposition rate (Bridier et al., 1991; Zabel, 1995); ii) the equilibrium constant for PAN decomposition (Bridier et al., 1991) at all experimentally available temperatures. The final choice of parameters for the calculation could reproduce both experimental data sets within 30%.

The predictive power of the calculation was first tested on PNA because photodissociation quantum yields have already been measured for this molecule (Roehl et al., 2002). Figure 2 compares the experimental results with our statistical calculations for the $\nu_{OH}+2\nu_{OOH}$ combination band, $2\nu_{OH}$ overtone, and $2\nu_{OH}+\nu_{OOH}$ combination band of PNA (listed here in the order of increasing excitation energy). Required RRKM parameters for PNA were taken from experiment and from Chen and Hamilton (1996) and Zabel (1995). The simulation reproduces both the magnitude and the temperature dependence of the photodissociation quantum yields with good accuracy. To achieve this level of agreement, we had to reduce the dissociation energy threshold of PNA by 200 cm^{-1} from the accepted experimental value, which is well within the error bars for $D_0(HO_2–NO_2)$=7970±280 cm^{-1} (Zabel, 1995). Staikova et al. (2002) also reported a lower dissociation energy for PNA.

A curious side result of this simulation is the prediction of unity quantum yield for the $2\nu_{OH}+\nu_{OOH}$ excitation of PNA. The experimental data suggest a yield that is slightly below unity for this transition. This discrepancy may be a reflection of not entirely statistical behavior of PNA at these excitation energies. It may also reflect deficiencies of the chosen weak collision model. However, the experimental data for $2\nu_{OH}+\nu_{OOH}$ and $\nu_{OH}+2\nu_{OOH}$ bands are relatively noisy (Fig. 2) making it difficult to draw more definite conclusions. Matthews et al. (2004) assumed a photodissociation quantum yield of one for the $2\nu_{OH}+\nu_{OOH}$ band in their work.

The predicted dissociation yields for PAN excitation at 8700 cm^{-1} (i.e. within the blue wing of the $3\nu_{CH}$ band) are shown in Fig. 3 for several atmospherically relevant temperatures. The most interesting observation is that the photodissociation yields for PAN display a remarkably broad pressure dependence. In contrast, the photodissociation yield for the $2\nu_{OH}$ overtone transition of PNA is fairly constant below P=1 atm. This important difference can be attributed to the substantially larger number of vibrational degrees of freedom and larger binding energy in PAN resulting in lower microcanonical decomposition rates. The collisional deactivation and excitation rates can, therefore, easily compete with unimolecular decomposition even when the system is placed above the dissociation energy. In fact, the calculated PAN dissociation yields do not reach unity under typical atmospheric pressures even for excitation lying as much as 1000 cm^{-1} above the dissociation threshold (Fig. 4). In contrast, PNA is predicted to fall apart with 100% efficiency when excited so high above the dissociation energy threshold at pressures below one atmosphere.

Table 2. Calculated photodissociation quantum yields for PAN overtone transitions under representative atmospheric conditions. The $J_{near-IR}$ column lists the total near-IR photodissociation rates ($J_{3\nu CH}+J_{4\nu CH}$) calculated from the integrated absorption cross sections from Table 1 and a solar flux of 5×10^{14} photons cm^{-2} s^{-1} nm^{-1}. The last column is the fractional contribution of under-threshold dissociation via $3\nu_{CH}$ to the total rate (i.e. $J_{3\nu CH}/J_{near-IR}$).

Altitude (km)	T (K)	P (Torr)	$\phi(3\nu_{CH})$	$\phi(4\nu_{CH})$	$J_{near-IR}$ (s^{-1})	$3\nu_{CH}$ contribution (%)
0	288	760	0.0041	0.80	2.8E-8	14.8
3	269	526	0.0027	0.82	2.8E-8	9.3
6	249	354	0.0016	0.85	2.7E-8	5.5
9	230	230	0.0009	0.88	2.8E-8	3.0
12	217	143	0.0007	0.92	2.9E-8	2.2
15	217	90	0.0011	0.97	3.1E-8	3.1

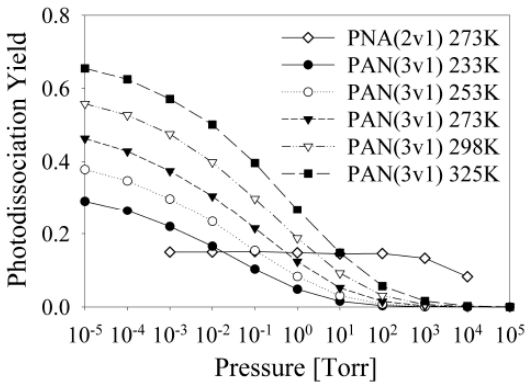

Fig. 3. Pressure dependence of the predicted photodissociation quantum yields for 8700 cm^{-1} excitation of PAN (representative of the $3\nu_{CH}$ excitation) at different temperatures. Calculated photodissociation yields for $2\nu_{OH}$ band of PNA at 273 K are also shown for comparison. In contrast to the PNA case, photodissociation quantum yields for PAN photolysis at 8700 cm^{-1} strongly depend on pressure under typical atmospheric conditions.

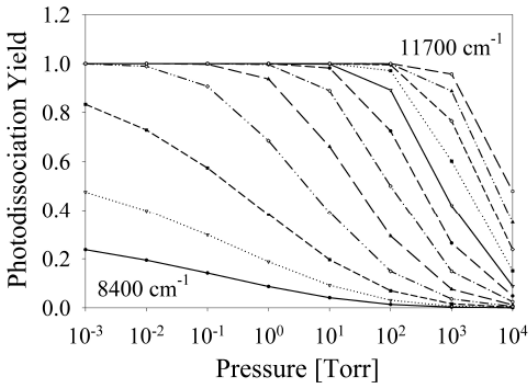

Fig. 4. Pressure dependence of the predicted photodissociation quantum yields of PAN at 298 K at different excitation frequencies. The frequencies cover the range 8400 cm^{-1} (bottom curve) to 11 700 cm^{-1} (top curve) in 300 cm^{-1} increments. Even at the highest excitation energy, the yield is still noticeably different from unity at typical atmospheric pressures.

2.4 near-IR photodissociation rates for atmospheric PAN

Simulated PAN photodissociation yields for a standardized atmosphere are given in Table 2. The effective photodissociation yield for $3\nu_{CH}$ band (estimated as an average of yields calculated for 8450, 8550, and 8650 cm^{-1} excitations) is very small compared to the $4\nu_{CH}$ yield (corresponding to 11 100 cm^{-1} excitation). Using the transition strength data from Table 1 and a typical near-IR solar flux of 5×10^{14} photons cm^{-2} s^{-1} nm^{-1} (Finlayson-Pitts and Pitts, 2000), we estimate the total near-IR photodissociation rate for PAN as $J_{near-IR}\approx3\times10^{-8}$ s^{-1} with a fairly weak altitude dependence (Table 2).

Because of the very low contribution of the $3\nu_{CH}$ band of PAN to the total near-IR photolysis rate (<5% above 6 km), the predicted rate is relatively insensitive to the calculated photodissociation yields. For example, an order of magnitude increase in $\phi(3\nu_{CH})$ would translate to less than 50% increase in the total photolysis rate. The $\phi(4\nu_{CH})$ values are already above 0.8; adjusting them to the maximal value of unity would only produce a marginal increase in the rate. The confidence in the predicted rate is, therefore, dominated by the uncertainty in $S(4\nu_{CH})$ believed to be accurate to within a factor of two (Table 1). Given these uncertainties, a very conservative upper limit for the near-IR PAN photodissociation rate under typical atmospheric conditions can be set at $J_{near-IR}(PAN) < 10^{-7}$ s^{-1}. Using similar reasoning, one can also show that $J_{near-IR}$ is insensitive to poor atmospheric transmittance at wavelengths corresponding to $3\nu_{CH}$ transition (the $4\nu_{CH}$ spectral range is clean).

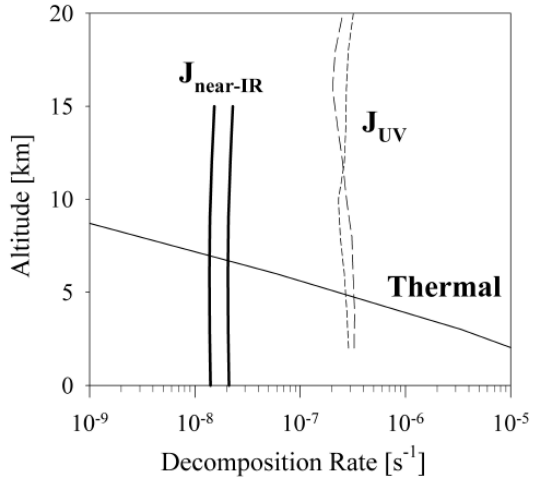

Fig. 5. Dependence of the predicted 24 hour-averaged near IR photodissociation rates (thick solid lines), UV photolysis rates (dashed lines), and unimolecular decomposition rate (thin solid line) on altitude. The UV photolysis rates were calculated for actual conditions of 8 May, 67° N (short dash) and 25 September, 35° N (long dash). Two near IR photolysis curves correspond to 18-hour (8 May) and 12-hour (25 September) day lengths with an average solar flux of 5×10^{14} photons cm^{-2} s^{-1} nm^{-1}. The near IR channel is seen to play a minor role (<10%) at all altitudes.

This limit is to be contrasted with a characteristic near-IR photolysis rate for PNA, $J_{near-IR}(PNA)\approx10^{-5}$ s^{-1}, which is higher by two orders of magnitude. The large difference in the photodissociation rates for PAN and PNA reflects the disparity in absorption cross sections for the overtone excitations responsible for their near-IR photodissociation activity. Whereas the under-threshold $2\nu_{OH}$ excitation accounts for the major fraction of $J_{near-IR}(PNA)$, the $3\nu_{CH}$ band of PAN is but a minor contributor (<5% above 6 km) to $J_{near-IR}(PAN)$. Because the overtone absorption strengths go down by roughly one order of magnitude with each vibrational quantum, the jump in two vibrational quanta between the primary photolytic excitations in PAN($4\nu_{CH}$) and PNA($2\nu_{OH}$) can be held responsible for the observed difference in the $J_{near-IR}$ values. In addition, CH_3 overtone intensities in acetyl groups are known to be systematically lower than those of other kinds of CH_3 groups (Nakagaki and Hanazaki, 1986). They are also considerably lower than intensities of typical OH stretching overtones (e.g. compare $S_{PNA}(2\nu_{OH})=(9.5\pm1.9)\times10^{-19}$ cm/# (Roehl et al., 2002) with $S_{PAN}(2\nu_{CH})=1.51\times10^{-19}$ cm/#).

Although the predicted near-IR photodissociation rate of PAN is quite low (the 24-h average of 1.5×10^{-8} s^{-1} translates into an atmospheric lifetime of 770 days), it becomes strongly competitive with the thermal decomposition rate (Zabel, 1995) above 6 km (Table 2 and Fig. 5). It is also higher than the upper limit for the rate of OH+PAN reaction ($k_{OH+PAN}[OH]<10^{-8}$ s^{-1} for the troposphere; DeMore et al., 1997). Comparison with the UV photolysis rate of PAN is less straightforward because UV radiation is attenuated by the atmosphere to a much greater extent than near-IR at high solar zenith angle (SZA). For example, at 15 km altitude , J_{UV}(PAN) $\approx6\times10^{-7}$ s^{-1} at SZA=0° but it drops to $\approx6\times10^{-8}$ s^{-1} at SZA=86° (solar fluxes for this calculation are taken from Finlayson-Pitts and Pitts, 2000 and PAN absorption cross sections are from DeMore et al., 1997). On the contrary, the estimated near-IR photolysis rate ($\approx3\times10^{-8}$ s^{-1}) is reduced by only 35% upon this SZA change. Consequently, the near-IR photolysis of PAN can potentially become comparable to the UV photolysis rate at very high SZA, providing a small contribution to the twilight production of HO_x radicals at high altitudes (Wennberg et al., 1999).

Figure 5 displays 24-hour averaged rates of UV photolysis, near-IR photolysis, and thermal decomposition for PAN. The UV photolysis rates correspond to conditions found at high and middle latitudes near equinox as described in Salawitch et al. (2002) (8 May 1997 with latitudes between 65° N and 70° N and 25 September 1993 at 35° N). Near-IR rates are estimated by assuming day lengths of 18 h and 12 h, respectively, and a near-IR solar flux of 5×10^{14} photons cm^{-2} s^{-1} nm^{-1}. The thermal decomposition rate for PAN is calculated from data of Zabel (1995). Figure 5 shows that $< J_{near-IR}(PAN)>$ is approximately 5–10% of $<J_{UV}(PAN)>$ at high tropospheric altitudes. At lower altitudes, both photolysis channels are dwarfed by the thermal decomposition. We conclude that near-IR photolysis is not likely to significantly affect the average atmospheric lifetime of PAN. Given that it is hard to quantify the uncertainties of the predicted photodissociation yields and absorption cross sections of PAN, however, the near-IR photolysis of PAN in the atmosphere cannot be completely discounted at this stage. More experimental research in this area is clearly needed.

2.5 Experiments on near-IR photolysis of PAN

We have attempted to measure photodissociation cross sections of PAN in the $3\nu_{CH}$–$4\nu_{CH}$ range using the action spectroscopy approach similar to that used for PNA by Roehl et al. (2002). PAN/N_2 mixture at 1–5 Torr and 250–300 K was irradiated with a tunable pulsed near-IR laser in the presence of a small amount of NO and O_2. A dye laser was employed in a fluorescence scheme to monitor the OH produced in the mixture following the photolysis laser pulse. If the near-IR laser were to photolyze PAN molecules in the gas flow, a momentary increase in the OH fluorescence signal would be observed assuming that the following reaction sequence runs to completion:

$$PAN + h\nu(near{-}IR) \rightarrow CH_3C(O)O_2 + NO_2$$

$$CH_3C(O)O_2 + NO \rightarrow CH_3 + CO_2 + NO_2$$

$$CH_3 + O_2 \rightarrow CH_3O_2$$

$$CH_3O_2 + NO \rightarrow CH_3O + NO_2$$

$$CH_3O + O_2 \rightarrow CH_2O + HO_2$$

$$HO_2 + NO \rightarrow OH + NO_2.$$

Despite numerous attempts under various reaction conditions, we have not been able to observe any near-IR laser induced increase in the OH signal. Detailed kinetic simulations of our experimental conditions predict a signal-to-noise ratio reduction of $\approx 10^2$ for $3\nu_{CH}$ band of PAN compared to $3\nu_{OH}$ band of PNA (which could be successfully observed in this apparatus, Roehl et al., 2002) assuming unity photodissociation yield in both cases. This large penalty is comprised of i) a factor of 2 reduction in the integrated absorption cross section; ii) factor of 5 increase in the effective band width for the CH_3 vs. OH second overtone; iii) a factor of $\sim$10 reduction in the efficiency of conversion of $CH_3C(O)O_2$ into OH in the chemical sequence above, as opposed to that of HO_2 into OH in the case of PNA photodissociation. The signal-to-noise ratio in our best $3\nu_{OH}$ photodissociation spectrum of PNA ($\approx 10^3$, Roehl et al., 2002) allows us to place an upper limit of 10% on the photodissociation yield of the $3\nu_{CH}$ state of PAN at 1–5 Torr and 250–300 K, which is in rough agreement with simulations presented here. The predicted signal-to-noise ratio for the $4\nu_{CH}$ band of PAN is <0.5, consistent with the failure to experimentally detect it.

We are currently designing an experiment that will allow us to measure $CH_3C(O)O_2$ following pulsed near IR laser excitation of PAN/N_2 mixtures using a CIMS (chemical ionization mass spectrometry) technique. Preliminary tests show positive results using UV photons to dissociate PAN. The results of this work will be published elsewhere.

3 Conclusions

Due to its unique combination of binding energy and molecular size, PNA may well turn out to be the only peroxy nitrate that is controlled by near-IR photolysis (Roehl et al., 2002) in the atmosphere. The larger binding energies and higher degrees of molecular complexity make peroxy acetyl nitrates, like PAN, considerably more resistant to direct overtone photolysis in the near-IR range of the solar spectrum. Specifically, our analysis predicts a near-infrared photodissociation rate of $\approx 3\times10^{-8}\,s^{-1}$ for PAN at noon, largely independent of altitude. The near-IR photolysis of PAN can become competitive with UV photolysis under twilight illumination conditions, but even in the coldest upper tropospheric layers it is calculated to contribute only 5–10% to the 24-hour averaged removal rate of PAN.

Acknowledgements. This work was funded in part by NASA's Atmospheric Effects of Aviation Program and the Atmospheric Chemistry program of the National Science Foundation. SAN thanks the Camille and Henry Dreyfus Foundation for financial support during his postdoctoral research at Caltech. The authors thank R. Salawitch (JPL) for providing 24-averaged UV-photolysis rates of PAN used in Fig. 5 and A. Sinha (UCSD) for a preprint of Ref. (Matthews et al., 2004).

Edited by: J. Abbatt

References

Barker, J. R.: Multiple-well, multiple-path unimolecular reaction systems. I. Multiwell computer program suite, Int. J. Chem. Kinetics, 33, 232–245, 2001.

Bridier, I., Caralp, F., Loirat, H., Lesclaux, R., Veyret, B., Becker, K.H., Reimer, A. and Zabel, F.: Kinetic and theoretical studies of the reactions $CH_3C(O)O_2$+NO_2+M $\leftrightarrow$ $CH_3C(O)O_2NO_2$+M between 248 K and 393 K and between 30 Torr and 760 Torr, J. Phys. Chem., 95, 9, 3594–3600, 1991.

Chen, Z. and Hamilton, T. P.: Ab initio study of pernitric acid: comparison with experimental spectra, J. Phys. Chem., 100, 39, 15 731–15 734, 1996.

DeMore, W. B., Sander, S. P., Golden, D. M., Hampson, R. F., Kurylo, M. J., Howard, C. J., Ravishankara, A. R., Kolb, C. E., and Molina, M. J.: Chemical kinetics and photochemical data for use in stratospheric modeling: Evaluation number 12. Jet Propulsion Laboratory, Pasadena, 1997.

Donaldson, D. J., Frost, G. J., Rosenlof, K. H., Tuck, A. F., and Vaida, V.: Atmospheric radical production by excitation of vibrational overtones via absorption of visible light, Geophys. Res. Lett., 24, 21, 2651–2654, 1997.

Donaldson, D.J., Tuck, A.F. and Vaida, V.: Atmospheric Photochemistry via vibrational overtone absorption, Chem. Rev., 103, 12, 4717–4729, 2003.

Finlayson-Pitts, B. J. and Pitts, J. N.: Chemistry of the upper and lower atmosphere: theory, experiments, and applications, Academic Press, 1040, 2000.

Gaffney, J. S., Fajer, R., and Senum, G. I.: An improved procedure for high purity gaseous peroxyacyl nitrate production: use of heavy lipid solvents, Atmos. Environ., 18, 1, 215–18, 1984.

Hanazaki, I., Baba, M., and Nagashima, U.: Orientational site splitting of methyl C-H overtones in acetone and acetaldehyde, J. Phys. Chem., 89, 26, 5637–5645, 1985.

Kirchner, F., Mayer-Figge, A., Zabel, F., and Becker, K. H.: Thermal stability of peroxynitrates, Int. J. Chem. Kinetics, 31, 2, 127–144, 1999.

Kjaergaard, H. G., Henry, B. R., and Tarr, A. W.: Intensities in local mode overtone spectra of dimethyl ether and acetone, J. Chem. Phys., 94, 9, 5844–5854, 1991.

Matthews, J., Sharma, R., and Sinha, A.: Photodissociation of vibrationally excited pernitric acid: HO_2NO_2 ($2v_{OH}$) + 390 nm, J. Phys. Chem. A, 108, 39, 8134–8139, 2004.

Miller, C. E., Lynton, J. I., Keevil, D. M., and Francisco, J. S.: Dissociation pathways of peroxyacetyl nitrate (PAN), J. Phys. Chem., 103, 51, 11 451–11 459, 1999.

Nakagaki, R. and Hanazaki, I.: Overtone spectroscopy of acetyl compounds. Inequivalent carbon-hydrogen (CH) oscillators and

substituent effects of the carbonyl group, Chem. Phys. Lett., 128, 4, 432–438, 1986.

Pitts Jr., J. N., Sharp, J. H., and Chan, S. I.: Effects of wavelength and temperature on primary processes in the photolysis of nitrogen dioxide and a spectroscopic-photochemical determination of the dissociation energy, J. Chem. Phys., 40, 12, 3655–3662, 1964.

Ridley, B. A., Atlas, E. L., Montzka, D. D., Browell, E. V., Cantrell, C. A., Blake, D. R., Blake, N. J., Cinquini, L., Coffey, M. T., Emmons, L. K., Cohen, R. C., DeYoung, R. J., Dibb, J. E., Eisele, F. L., Flocke, F. M., Fried, A., Grahek, F. E., Grant, W. B., Hair, J. W., Hannigan, J. W., Heikes, B. J., Lefer, B. L., Mauldin, R. L., Moody, J. L., Shetter, R. E., Snow, J. A., Talbot, R. W., Thornton, J. A., Walega, J. G., Weinheimer, A. J., Wert, B. P., and Wimmers, A. J.: Ozone depletion events observed in the high-latitude surface layer during the TOPSE aircraft program, J. Geophys. Res. D, 108, D4, TOP 4/1-TOP 4/22, 2003.

Roehl, C. M., Nizkorodov, S. A., Zhang, H., Blake, G. A., and Wennberg, P. O.: Photodissociation of peroxynitric acid in the near-IR, J. Phys. Chem. A, 106, 15, 3766–3772, 2002.

Roehl, C. M., Orlando, J. J., Tyndall, G. S., Shetter, R. E., Vazquez, G. J., Cantrell, C. A., and Calvert, J. G.: Temperature dependence of the quantum yields for the photolysis of NO_2 near the dissociation limit, J. Phys. Chem., 98, 32, 7837–7843, 1994.

Salawitch, R. J., Wennberg, P. O., Toon, G. C., Sen, B., and Blavier, J.-F.: Near IR photolysis of HO_2NO_2: implications for HO_x, Geophys. Res. Lett., 29, 16, 9/1–9/4, 2002.

Sinha, A., Vander Wal, R.L. and Crim, F.F.: State-resolved unimolecular reactions: the vibrational overtone initiated decomposition of nitric acid, J. Chem. Phys., 92, 1, 401–10, 1990.

Staikova, M., Donaldson, D.J. and Francisco, J.S.: Overtone-induced reactions on the HO_2NO_2 potential surface, J. Phys. Chem. A, 106, 12, 3023–3028, 2002.

Stroud, C., Madronich, S., Atlas, E., Ridley, B., Flocke, F., Weinheimer, A., Talbot, B., Fried, A., Wert, B., Shetter, R., Lefer, B., Coffey, M., Heikes, B., and Blake, D.: Photochemistry in the arctic free troposphere: NO_x budget and the role of odd nitrogen reservoir recycling, Atmos. Environ., 37, 24, 3351–3364, 2003.

Tsalkani, N. and Toupance, G.: Infrared absorptivities and integrated band intensities for gaseous peroxyacetyl nitrate (PAN), Atmos. Environ., 23, 8, 1849–1854, 1989.

Wennberg, P. O., Salawitch, R. J., Donaldson, D. J., Hanisco, T. F., Lanzendorf, E. J., Perkins, K. K., Lloyd, S. A., Vaida, V., Gao, R. S., Hintsa, E. J., Cohen, R. C., Swartz, W. H., Kusterer, T. L., and Anderson, D. E.: Twilight observations suggest unknown sources of HO_x, Geophys. Res. Lett., 26, 10, 1373–1376, 1999.

Zabel, F.: Unimolecular Decomposition of Peroxynitrates, Z. Phys. Chem., 188, 119–142, 1995.

APPENDIX IV:
LIST OF PAPERS PUBLISHED IN CONJUNCTION WITH THIS THESIS

(1) Drouin, B.J., Fry, J.L., and Miller, C.E., "Rotational spectrum of *cis-cis* HOONO," Journal of Chemical Physics **2004**, *120*, 5505-5508.

(2) Fry, J.L., Nizkorodov, S.A., Okumura, M., Roehl, C.M., Francisco, J.S., and Wennberg, P.O., "*Cis-cis* and *trans-perp* HOONO: Action spectroscopy and isomerization kinetics," Journal of Chemical Physics **2004,** *121*, 1432-1448.

(3) Nizkorodov, S.A., Crounse, J.D., Fry, J.L., Roehl, C.M., and Wennberg, P.O., "Near-IR photodissociation of peroxyacetyl nitrate (PAN)," Atmospheric Chemistry and Physics **2005**, *5*, 385-392.

(4) McCoy, A.B., Fry, J.L., Francisco, J.S., Mollner, A.K., Okumura, M., "Role of OH-stretch/torsion coupling and quantum yield effects in the first OH overtone spectrum of *cis-cis* HOONO," Journal of Chemical Physics **2005**, *122*, 104311.

(5) Fry, J.L., Drouin, B.J., and Miller, C.E., "Rotational spectroscopy and dipole moment of *cis-cis* HOONO," submitted to Journal of Chemical Physics, October 2005.

(6) Fry, J.L., Matthews, J.N., Lane, J.R., Roehl, C.M., Sinha, A., Kjaergaard, H.G., and Wennberg, P.O., "OH-stretch vibrational spectroscopy of hydroxymethyl hydroperoxide," in preparation.

(7) Drouin, B.J., Miller, C.E., Fry, J.L., Petkie, D.T., Helminger, P., and Medvedev, I., "Submillimeter measurements of isotopes of nitric acid," in preparation.

(8) Roehl, C.M., Marka, Z., Fry, J.L., and Wennberg, P.O., "Near-UV photolysis cross sections of CH_3OOH and HOCH2OOH determined via action spectroscopy," in preparation.

(9) Matthews, J.N. et al, "Unimolecular dissociation and product state distributions in hydroxymethyl hydroperoxide," in preparation.

REFERENCES

References

(1) Seinfeld, J. H.; Pandis, S. N. *Atmospheric Chemistry and Physics*; John Wiley & Sons, Inc.: New York, NY, 1998.

(2) Streitwieser, A.; Heathcock, C. H.; Kosower, E. M. *Introduction to organic chemistry*, 4th ed.; Macmillan Publishing Company: New York, NY, 1992.

(3) Ravishankara, A. R., guest editor. Atmospheric chemistry: long-term issues; Chemical Reviews, 2003; Vol. 103 (12).

(4) IUPAC. Summary of Evaluated Kinetic and Photochemical Data for Atmospheric Chemistry, 2005.

(5) Jenkin, M. E.; Saunders, S. M.; Pilling, M. J. *Atmospheric Environment* **1997**, *31*, 81.

(6) Saunders, S. M.; Jenkin, M. E.; Derwent, R. G.; Pilling, M. J. *Atmospheric Environment* **1997**, *31*, 1249.

(7) Heard, D. E.; Pilling, M. J. *Chemical Reviews* **2003**, *103*, 5163.

(8) Jaegle, L.; Steinberger, L.; Martin, R. V.; Chance, K. *Faraday Discussions* **2005**, *130*, 407.

(9) Golden, D. M.; Barker, J. R.; Lohr, L. L. *Journal of Physical Chemistry A* **2003**, *107*, 11057.

(10) Kleinbohl, A., Private communication.

(11) Jacob, D. J. *Atmospheric Environment* **2000**, *34*, 2131.

(12) Ridley, B. A.; Atlas, E. L.; Montzka, D. D.; Browell, E. V.; Cantrell, C. A.; Blake, D. R.; Blake, N. J.; Cinquini, L.; Coffey, M. T.; Emmons, L. K.; Cohen, R. C.; DeYoung, R. J.; Dibb, J. E.; Eisele, F. L.; Flocke, F. M.; Fried, A.; Grahek, F. E.; Grant, W. B.; Hair, J. W.; Hannigan, J. W.; Heikes, B. J.; Lefer, B. L.; Mauldin, R. L.; Moody, J. L.; Shetter, R. E.; Snow, J. A.; Talbot, R. W.; Thornton, J. A.; Walega, J. G.; Weinheimer, A. J.; Wert, B. P.; Wimmers, A. J. *Journal of Geophysical Research-Atmospheres* **2003**, *108*.

(13) Stroud, C.; Madronich, S.; Atlas, E.; Ridley, B.; Flocke, F.; Weinheimer, A.; Talbot, B.; Fried, A.; Wert, B.; Shetter, R.; Lefer, B.; Coffey, M.; Heikes, B.; Blake, D. *Atmospheric Environment* **2003**, *37*, 3351.

(14) Moxim, W. J.; Levy, H.; Kasibhatla, P. S. *Journal of Geophysical Research-Atmospheres* **1996**, *101*, 12621.

(15) Reeves, C. E.; Penkett, S. A. *Chemical Reviews* **2003**, *103*, 5199.

(16) Jaegle, L.; Jacob, D. J.; Wennberg, P. O.; Spivakovsky, C. M.; Hanisco, T. F.; Lanzendorf, E. J.; Hintsa, E. J.; Fahey, D. W.; Keim, E. R.; Proffitt, M. H.; Atlas, E. L.;

Flocke, F.; Schauffler, S.; McElroy, C. T.; Midwinter, C.; Pfister, L.; Wilson, J. C. *Geophysical Research Letters* **1997**, *24*, 3181.

(17) Prather, M. J.; Jacob, D. J. *Geophysical Research Letters* **1997**, *24*, 3189.

(18) Hewitt, C. N.; Kok, G. L. *Journal of Atmospheric Chemistry* **1991**, *12*, 181.

(19) Lee, M. H.; Heikes, B. G.; O'Sullivan, D. W. *Atmospheric Environment* **2000**, *34*, 3475.

(20) Sander, S. P.; Friedl, R. R.; Ravishankara, A. R.; Golden, D. M.; Kolb, C. E.; Kurylo, M. J.; Huie, R. E.; Orkin, V. L.; Molina, M. J.; Moortgat, G. K.; Finlayson-Pitts, B. J. "Chemical Kinetics and Photochemical Data for Use in Atmospheric Studies, Evaluation Number 14," JPL Publication 02-25, 2003.

(21) Roehl, C. M.; Nizkorodov, S. A.; Zhang, H.; Blake, G. A.; Wennberg, P. O. *Journal of Physical Chemistry A* **2002**, *106*, 3766.

(22) Zhang, H.; Roehl, C. M.; Sander, S. P.; Wennberg, P. O. *Journal of Geophysical Research-Atmospheres* **2000**, *105*, 14593.

(23) Salawitch, R. J.; Wennberg, P. O.; Toon, G. C.; Sen, B.; Blavier, J. F. *Geophysical Research Letters* **2002**, *29*, art. no.1762.

(24) Donaldson, D. J.; Tuck, A. F.; Vaida, V. *Chemical Reviews* **2003**, *103*, 4717.

(25) Konen, I. M.; Pollack, I. B.; Li, E. X. J.; Lester, M. I.; Varner, M. E.; Stanton, J. F. *Journal of Chemical Physics* **2005**, *122*.

(26) Bean, B. D.; Mollner, A. K.; Nizkorodov, S. A.; Nair, G.; Okumura, M.; Sander, S. P.; Peterson, K. A.; Francisco, J. S. *Journal of Physical Chemistry A* **2003**, *107*, 6974.

(27) Bridier, I.; Caralp, F.; Loirat, H.; Lesclaux, R.; Veyret, B.; Becker, K. H.; Reimer, A.; Zabel, F. *Journal of Physical Chemistry* **1991**, *95*, 3594.

(28) Zabel, F. Unimolecular Decomposition of Peroxynitrates, 1995; pp 119.

(29) Matthews, J.; Sinha, A.; Francisco, J. S. *Journal of Chemical Physics* **2005**, *122*.

(30) Fry, J. L.; Lane, J.; Roehl, C. M.; Matthews, J. N.; Sinha, A.; Kjaergaard, H. G.; Wennberg, P. O. *submitted to J. Phys. Chem. A* **2005**.

(31) Nizkorodov, S. A.; Wennberg, P. O. *Journal of Physical Chemistry A* **2002**, *106*, 855.

(32) Fry, J. L.; Nizkorodov, S. A.; Okumura, M.; Roehl, C. M.; Francisco, J. S.; Wennberg, P. O. *Journal of Chemical Physics* **2004**, *121*, 1432.

(33) McCoy, A. B.; Fry, J. L.; Francisco, J. S.; Mollner, A. K.; Okumura, M. *Journal of Chemical Physics* **2005**, *122*.

(34) Drouin, B. J.; Fry, J. L.; Miller, C. E. *Journal of Chemical Physics* **2004**, *120*, 5505.

(35) Fry, J. L.; Drouin, B. J.; Miller, C. E. *in press, J. Chem. Phys.* **2005**.

(36) Nizkorodov, S. A.; Crounse, J. D.; Fry, J. L.; Roehl, C. M.; Wennberg, P. O. *Atmospheric Chemistry and Physics* **2005**, *5*, 385.

(37) Roehl, C. M.; Marka, Z.; Fry, J. L.; Wennberg, P. O. *manuscript in preparation* **2005**.

(38) Matthews, J. N., et al. *manuscript in preparation* **2005**.

(39) Wu, S.; Blake, G. A.; Sun, Z. Y.; Ling, J. W. *Applied Optics* **1997**, *36*, 5898.

(40) Wu, S.; Blake, G. A.; Sun, S. N.; Ling, J. *Optics Communications* **2000**, *173*, 371.

(41) Zhang, H. Ph.D. Thesis, California Institute of Technology, 2001.

(42) Cheng, L. K.; Bosenberg, W. R.; Tang, C. L. *Applied Physics Letters* **1988**, *53*, 175.

(43) Wennberg, P. O.; Cohen, R. C.; Hazen, N. L.; Lapson, L. B.; Allen, N. T.; Hanisco, T. F.; Oliver, J. F.; Lanham, N. W.; Demusz, J. N.; Anderson, J. G. *Review of Scientific Instruments* **1994**, *65*, 1858.

(44) Aloisio, S.; Francisco, J. S. *Journal of the American Chemical Society* **2000**, *122*, 9196.

(45) Belair, S. D.; Kais, S.; Francisco, J. S. *Molecular Physics* **2002**, *100*, 247.

(46) Gaffney, J. S.; Fajer, R.; Senum, G. I. *Atmospheric Environment* **1984**, *18*, 215.

(47) Talukdar, R. K.; Burkholder, J. B.; Schmoltner, A. M.; Roberts, J. M.; Wilson, R. R.; Ravishankara, A. R. *Journal of Geophysical Research-Atmospheres* **1995**, *100*, 14163.

(48) Vaghjiani, G. L.; Ravishankara, A. R. *Journal of Physical Chemistry* **1989**, *93*, 1948.

(49) Golden, D. M.; Smith, G. P. *Journal of Physical Chemistry A* **2000**, *104*, 3991.

(50) Hippler, H.; Nasterlack, S.; Striebel, F. *Physical Chemistry Chemical Physics* **2002**, *4*, 2959.

(51) Matheu, D. M.; Green, W. H. *International Journal of Chemical Kinetics* **2000**, *32*, 245.

(52) Troe, J. *International Journal of Chemical Kinetics* **2001**, *33*, 878.

(53) Fulle, D.; Hamann, H. F.; Hippler, H.; Troe, J. *Journal of Chemical Physics* **1998**, *108*, 5391.

(54) Donahue, N. M.; Mohrschladt, R.; Dransfield, T. J.; Anderson, J. G.; Dubey, M. K. *Journal of Physical Chemistry A* **2001**, *105*, 1515.

(55) Robertshaw, J. S.; Smith, I. W. M. *Journal of Physical Chemistry* **1982**, *86*, 785.

(56) Dixon, D. A.; Feller, D.; Zhan, C. G.; Francisco, J. S. *Journal of Physical Chemistry A* **2002**, *106*, 3191.

(57) McGrath, M. P.; Rowland, F. S. *Journal of Physical Chemistry* **1994**, *98*, 1061.

(58) Jin, H. W.; Wang, Z. Z.; Li, Q. S.; Huang, X. R. *Journal of Molecular Structure-Theochem* **2003**, *624*, 115.

(59) Tsai, H. H.; Hamilton, T. P.; Tsai, J. H. M.; vanderWoerd, M.; Harrison, J. G.; Jablonsky, M. J.; Beckman, J. S.; Koppenol, W. H. *Journal of Physical Chemistry* **1996**, *100*, 15087.

(60) Li, Y. M.; Francisco, J. S. *Journal of Chemical Physics* **2000**, *113*, 7976.

(61) Hippler, H.; Krasteva, S.; Nasterlack, S.; Striebel, F. *personal communication* **2004**.

(62) Pollack, I. B.; Konen, I. M.; Li, E. X. J.; Lester, M. I. *Journal of Chemical Physics* **2003**, *119*, 9981.

(63) Zhu, R. S.; Lin, M. C. *Journal of Chemical Physics* **2003**, *119*, 10667.

(64) Cheng, B. M.; Lee, J. W.; Lee, Y. P. *Journal of Physical Chemistry* **1991**, *95*, 2814.

(65) Rothman, L. S.; Rinsland, C. P.; Goldman, A.; Massie, S. T.; Edwards, D. P.; Flaud, J. M.; Perrin, A.; Camy-Peyret, C.; Dana, V.; Mandin, J. Y.; Schroeder, J.; McCann, A.; Gamache, R. R.; Wattson, R. B.; Yoshino, K.; Chance, K. V.; Jucks, K. W.; Brown, L. R.; Nemtchinov, V.; Varanasi, P. *Journal of Quantitative Spectroscopy & Radiative Transfer* **1998**, *60*, 665.

(66) Judge, R. H.; Clouthier, D. J. *Computer Physics Communications* **2001**, *135*, 293.

(67) Kenley, R. A.; Trevor, P. L.; Lan, B. Y. *Journal of the American Chemical Society* **1981**, *103*, 2203.

(68) Kliner, D. A. V.; Farrow, R. L. *Journal of Chemical Physics* **1999**, *110*, 412.

(69) Frisch, M. J.; Trucks, G. W.; Schlegel, H. B.; Scuseria, G. E.; Robb, M. A.; Cheeseman, J. R.; Zakrzewski, V. G.; J. A. Montgomery, J.; Stratmann, R. E.; Burant, J. C.; Dapprich, S.; Millam, J. M.; Daniels, A. D.; Kudin, K. N.; Strain, M. C.; Farkas, O.; Tomasi, J.; Barone, V.; Cossi, M.; Cammi, R.; Mennucci, B.; Pomelli, C.; Adamo, C.; Clifford, S.; Ochterski, J.; Petersson, G. A.; Ayala, P. Y.; Cui, Q.; Morokuma, K.; Malick, D. K.; Rabuck, A. D.; Raghavachari, K.; Foresman, J. B.; Cioslowski, J.; Ortiz, J. V.; Baboul, A. G.; Stefanov, B. B.; Liu, G.; Liashenko, A.; Piskorz, P.; Komaromi, I.; Gomperts, R.; Martin, R. L.; Fox, D. J.; Keith, T.; Al-Laham, M. A.; Peng, C. Y.; Nanayakkara, A.; Challacombe, M.; Gill, P. M. W.; Johnson, B.; Chen, W.; Wong, M. W.; Andres, J. L.; Gonzalez, C.; Head-Gordon, M.; Replogle, E. S.; J. A. Pople. *Gaussian 98, Revision A.9* **1998**.

(70) Raghavachari, K.; Trucks, G. W.; Pople, J. A.; Head-Gordon, M. *Chem. Phys. Lett.* **1989**, *157*, 479.

(71) Dunning, T. H., Jr. *J. Chem. Phys.* **1989**, *90*, 1007.

(72) Kendall, R. A.; Dunning, T. H., Jr.; Harrison, R. J. *J. Chem. Phys.* **1992**, *96*, 6796.

(73) Barker, J. R. *International Journal of Chemical Kinetics* **2001**, *33*, 232.

(74) Donahue, N. M.; Dubey, M. K.; Mohrschladt, R.; Demerjian, K. L.; Anderson, J. G. *Journal of Geophysical Research-Atmospheres* **1997**, *102*, 6159.

(75) Kjaergaard, H. G.; Bezar, K. J.; Brooking, K. A. *Molecular Physics* **1999**, *96*, 1125.

(76) Kjaergaard, H. G.; Daub, C. D.; Henry, B. R. *Molecular Physics* **1997**, *90*, 201.

(77) Kjaergaard, H. G.; Henry, B. R.; Tarr, A. W. *Journal of Chemical Physics* **1991**, *94*, 5844.

(78) Kjaergaard, H. G.; Yu, H. T.; Schattka, B. J.; Henry, B. R.; Tarr, A. W. *Journal of Chemical Physics* **1990**, *93*, 6239.

(79) Turnbull, D. M.; Kjaergaard, H. G.; Henry, B. R. *Chemical Physics* **1995**, *195*, 129.

(80) Kjaergaard, H. G. *Journal of Physical Chemistry A* **2002**, *106*, 2979.

(81) Ochterski, J. W. *Gaussian White Paper* **1999**.

(82) Wilson, E. B.; Decius, J. C.; Cross, P. C. *Molecular Vibrations*; McGraw-Hill: New York, 1955.

(83) Choi, C. H.; Kertesz, M. *Journal of Physical Chemistry* **1996**, *100*, 16530.

(84) Kjaergaard, H. G.; Low, G. R.; Robinson, T. W.; Howard, D. L. *Journal of Physical Chemistry A* **2002**, *106*, 8955.

(85) Gallas, J. A. C. *Physical Review A* **1980**, *21*, 1829.

(86) Lange, K. R.; Wells, N. P.; Plegge, K. S.; Phillips, J. A. *Journal of Physical Chemistry A* **2001**, *105*, 3481.

(87) Chackerian, C.; Sharpe, S. W.; Blake, T. A. *Journal of Quantitative Spectroscopy & Radiative Transfer* **2003**, *82*, 429.

(88) Donaldson, D. J.; Orlando, J. J.; Amann, S.; Tyndall, G. S.; Proos, R. J.; Henry, B. R.; Vaida, V. *Journal of Physical Chemistry A* **1998**, *102*, 5171.

(89) Rong, Z. M.; Kjaergaard, H. G.; Sage, M. L. *Molecular Physics* **2003**, *101*, 2285.

(90) Rong, Z.; Howard, D. L.; Kjaergaard, H. G. *Journal of Physical Chemistry A* **2003**, *107*, 4607.

(91) Allen, C. W. *Allen's Astrophysical Quantities*; Springer-Verlag: New York, 2000.

(92) Hanisco, T. F.; Lanzendorf, E. J.; Wennberg, P. O.; Perkins, K. K.; Stimpfle, R. M.; Voss, P. B.; Anderson, J. G.; Cohen, R. C.; Fahey, D. W.; Gao, R. S.; Hintsa, E. J.; Salawitch, R. J.; Margitan, J. J.; McElroy, C. T.; Midwinter, C. *Journal of Physical Chemistry A* **2001**, *105*, 1543.

(93) Schofield, D. P.; Kjaergaard, H. G. *Journal of Physical Chemistry A* **2005**, *109*, 1810.

(94) Schofield, D. P.; Kjaergaard, H. G.; Matthews, J.; Sinha, A. *Journal of Chemical Physics* **2005**, *123*.

(95) Doclo, K.; Rothlisberger, U. *Chemical Physics Letters* **1998**, *297*, 205.

(96) Matthews, J.; Sinha, A.; Francisco, J. S. *Journal of Chemical Physics* **2004**, *120*, 10543.

(97) Matthews, J.; Sinha, A. *Journal of Chemical Physics* **2005**, *122*.

(98) Okumura, M., Private communication.

(99) Drouin, B. J.; Maiwald, F. W.; Pearson, J. C. *Review of Scientific Instruments* **2005**, *76*, 093113.

(100) Balle, T. J.; Flygare, W. H. *Review of Scientific Instruments* **1981**, *52*, 33.

(101) Widicus Weaver, S. L. Ph.D. Thesis, California Institute of Technology, 2005.

(102) Pickett, H. M. *Journal of Molecular Spectroscopy* **1991**, *148*, 371.

(103) Muller, H. S. P.; Cohen, E. A.; Christen, D. *Journal of Chemical Physics* **1999**, *110*, 11865.

(104) Muller, H. S. P.; Miller, C. E.; Cohen, E. A. *Journal of Chemical Physics* **1997**, *107*, 8292.

(105) Patel, D.; Margolese, D.; Dyke, T. R. *Journal of Chemical Physics* **1979**, *70*, 2740.

(106) Stanton, J. F., Private communication.

(107) Kraitchman, J. *American Journal of Physics* **1953**, *21*, 17.

(108) Gordy, W.; Cook, R. *Microwave Molecular Spectra*, 3 ed.; John Wiley & Sons, Inc.: New York, 1984.

(109) Cox, P.; Riveros, J. M. *Journal of Chemical Physics* **1965**, *42*, 3106.

(110) Mills, I. M. In *Molecular Spectroscopy: Modern Research*; Rao, K. N., Matthews, C. W., Eds.; Academic Press: New York, NY, 1972; pp 115.

(111) Keim, E. R.; McKeen, S. A.; Gao, R. S.; Donnelly, S. G.; Wamsley, R. C.; Del Negro, L. A.; Fahey, D. W.; Hanisco, T. F.; Lanzendorf, E. J.; Proffitt, M. H.; Margitan, J. J.; Hintsa, E. J.; Jaegle, L.; Webster, C. R.; May, R. D.; Scott, D. C.; Salawitch, R. J.; Wilson, J. C.; McElroy, C. T.; Atlas, E. L.; Flocke, F.; Bui, T. P. *Geophysical Research Letters* **1999**, *26*, 51.

(112) Bey, I.; Jacob, D. J.; Logan, J. A.; Yantosca, R. M. *Journal of Geophysical Research-Atmospheres* **2001**, *106*, 23097.

(113) Russo, R. S.; Talbot, R. W.; Dibb, J. E.; Scheuer, E.; Seid, G.; Jordan, C. E.; Fuelberg, H. E.; Sachse, G. W.; Avery, M. A.; Vay, S. A.; Blake, D. R.; Blake, N. J.; Atlas, E.; Fried, A.; Sandholm, S. T.; Tan, D.; Singh, H. B.; Snow, J.; Heikes, B. G. *Journal of Geophysical Research-Atmospheres* **2003**, *108*.

(114) Singh, H. B.; Condon, E.; Vedder, J.; Ohara, D.; Ridley, B. A.; Gandrud, B. W.; Shetter, J. D.; Salas, L. J.; Huebert, B.; Hubler, G.; Carroll, M. A.; Albritton, D. L.; Davis, D. D.; Bradshaw, J. D.; Sandholm, S. T.; Rodgers, M. O.; Beck, S. M.; Gregory, G. L.; Lebel, P. J. *Journal of Geophysical Research-Atmospheres* **1990**, *95*, 10163.

(115) Stephens, E. R.; Hanst, P. L.; Doerr, R. C.; Scott, W. E. *Industrial and Engineering Chemistry* **1956**, *48*, 1498.

(116) Zellweger, C.; Forrer, J.; Hofer, P.; Nyeki, S.; Schwarzenbach, B.; Weingartner, E.; Ammann, M.; Baltensperger, U. *Atmospheric Chemistry and Physics* **2003**, *3*, 779.

(117) Miller, C. E.; Lynton, J. I.; Keevil, D. M.; Francisco, J. S. *Journal of Physical Chemistry A* **1999**, *103*, 11451.

(118) Fang, H. L.; Meister, D. M.; Swofford, R. L. *Journal of Physical Chemistry* **1984**, *88*, 410.

(119) Crounse, J. D.; Wennberg, P. O., Private Communication.

(120) Villalta, P. W.; Howard, C. J. *Journal of Physical Chemistry* **1996**, *100*, 13624.

(121) Wennberg, P. O.; Salawitch, R. J.; Donaldson, D. J.; Hanisco, T. F.; Lanzendorf, E. J.; Perkins, K. K.; Lloyd, S. A.; Vaida, V.; Gao, R. S.; Hintsa, E. J.; Cohen, R. C.; Swartz, W. H.; Kusterer, T. L.; Anderson, D. E. *Geophysical Research Letters* **1999**, *26*, 1373.

(122) Matthews, J.; Sinha, A.; Francisco, J. S. *Proceedings of the National Academy of Sciences of the United States of America* **2005**, *102*, 7449.

(123) Bauerle, S.; Moortgat, G. K. *Chemical Physics Letters* **1999**, *309*, 43.

(124) Gunz, D. W.; Hoffmann, M. R. *Atmospheric Environment Part a-General Topics* **1990**, *24*, 1601.

(125) Lind, J. A.; Lazrus, A. L.; Kok, G. L. *Journal of Geophysical Research-Atmospheres* **1987**, *92*, 4171.

(126) Zhou, X. L.; Lee, Y. N. *Journal of Physical Chemistry* **1992**, *96*, 265.

(127) Becker, K. H.; Brockmann, K. J.; Bechara, J. *Nature* **1990**, *346*, 256.

(128) Gab, S.; Hellpointner, E.; Turner, W. V.; Korte, F. *Nature* **1985**, *316*, 535.

(129) Horie, O.; Neeb, P.; Limbach, S.; Moortgat, G. K. *Geophysical Research Letters* **1994**, *21*, 1523.

(130) Neeb, P.; Sauer, F.; Horie, O.; Moortgat, G. K. *Atmospheric Environment* **1997**, *31*, 1417.

(131) Sauer, F.; Schafer, C.; Neeb, P.; Horie, O.; Moortgat, G. K. *Atmospheric Environment* **1999**, *33*, 229.

(132) Hasson, A. S.; Orzechowska, G.; Paulson, S. E. *Journal of Geophysical Research-Atmospheres* **2001**, *106*, 34131.

(133) Grossmann, D.; Moortgat, G. K.; Kibler, M.; Schlomski, S.; Bachmann, K.; Alicke, B.; Geyer, A.; Platt, U.; Hammer, M. U.; Vogel, B.; Mihelcic, D.; Hofzumahaus, A.; Holland, F.; Volz-Thomas, A. *Journal of Geophysical Research-Atmospheres* **2003**, *108*.

(134) Francois, S.; Sowka, I.; Monod, A.; Temime-Roussel, B.; Laugier, J. M.; Wortham, H. *Atmospheric Research* **2005**, *74*, 525.

(135) Moortgat, G. K.; Grossmann, D.; Boddenberg, A.; Dallmann, G.; Ligon, A. P.; Turner, W. V.; Gab, S.; Slemr, F.; Wieprecht, W.; Acker, K.; Kibler, M.; Schlomski, S.; Bachmann, K. *Journal of Atmospheric Chemistry* **2002**, *42*, 443.

(136) Weinstein-Lloyd, J. B.; Lee, J. H.; Daum, P. H.; Kleinman, L. I.; Nunnermacker, L. J.; Springston, S. R. *Journal of Geophysical Research-Atmospheres* **1998**, *103*, 22361.

(137) Staffelbach, T.; Neftel, A.; Blatter, A.; Gut, A.; Fahrni, M.; Stahelin, J.; Prevot, A.; Hering, A.; Lehning, M.; Neininger, B.; Baumle, M.; Kok, G. L.; Dommen, J.; Hutterli, M.; Anklin, M. *Journal of Geophysical Research-Atmospheres* **1997**, *102*, 23345.

(138) Lee, J. H.; Leahy, D. F.; Tang, I. N.; Newman, L. *Journal of Geophysical Research-Atmospheres* **1993**, *98*, 2911.

(139) Lee, M.; Heikes, B. G.; Jacob, D. J.; Sachse, G.; Anderson, B. *Journal of Geophysical Research-Atmospheres* **1997**, *102*, 1301.

(140) Sauer, F.; Schuster, G.; Schafer, C.; Moortgat, G. K. *Geophysical Research Letters* **1996**, *23*, 2605.

(141) Sauer, F.; Limbach, S.; Moortgat, G. K. *Atmospheric Environment* **1997**, *31*, 1173.

(142) Jackson, A. V.; Hewitt, C. N. *Atmospheric Environment* **1996**, *30*, 819.

(143) Kok, G. L.; McLaren, S. E.; Staffelbach, T. A. *Journal of Atmospheric and Oceanic Technology* **1995**, *12*, 282.

(144) Tremmel, H. G.; Junkermann, W.; Slemr, F. *Journal of Geophysical Research-Atmospheres* **1993**, *98*, 1083.

(145) Fels, M.; Junkermann, W. *Geophysical Research Letters* **1994**, *21*, 341.

(146) Hellpointner, E.; Gab, S. *Nature* **1989**, *337*, 631.

(147) Osullivan, D. W.; Lee, M. Y.; Noone, B. C.; Heikes, B. G. *Journal of Physical Chemistry* **1996**, *100*, 3241.

(148) Su, F.; Calvert, J. G.; Shaw, J. H.; Niki, H.; Maker, P. D.; Savage, C. M.; Breitenbach, L. D. *Chemical Physics Letters* **1979**, *65*, 221.

(149) Matthews, J.; Sharma, R.; Sinha, A. *Journal of Physical Chemistry A* **2004**, *108*, 8134.

(150) Roehl, C. M.; Fry, J. L.; Marka, Z.; Wennberg, P. O. *manuscript in preparation* **2005**.

(151) Henry, B. R. *Accounts of Chemical Research* **1987**, *20*, 429.

(152) Henry, B. R. *Accounts of Chemical Research* **1977**, *10*, 207.

(153) Child, M. S.; Halonen, L. *Advances in Chemical Physics* **1984**, *57*, 1.

(154) Kjaergaard, H. G.; Low, G. R.; Robinson, T. W.; Howard, D. L. *Journal of Physical Chemistry A* **2002**, *106*, 8955.

(155) Low, G. R.; Kjaergaard, H. G. *Journal of Chemical Physics* **1999**, *110*, 9104.

(156) Howard, D. L.; Kjaergaard, H. G. *to be submitted* **2005**.

(157) Dutton, G.; Barnes, R. J.; Sinha, A. *Journal of Chemical Physics* **1999**, *111*, 4976.

(158) Marklund, S. *Acta Chemica Scandinavica* **1971**, *25*, 3517.

(159) Becke, A. D. *Physical Review A* **1988**, *38*, 3098.

(160) Becke, A. D. *Journal of Chemical Physics* **1993**, *98*, 1372.

(161) Lee, C. T.; Yang, W. T.; Parr, R. G. *Physical Review B* **1988**, *37*, 785.

(162) Pople, J. A.; Headgordon, M.; Raghavachari, K. *Journal of Chemical Physics* **1987**, *87*, 5968.

(163) Purvis, G. D.; Bartlett, R. J. *Journal of Chemical Physics* **1982**, *76*, 1910.

(164) Raghavachari, K.; Trucks, G. W.; Pople, J. A.; Headgordon, M. *Chemical Physics Letters* **1989**, *157*, 479.

(165) Watts, J. D.; Gauss, J.; Bartlett, R. J. *Journal of Chemical Physics* **1993**, *98*, 8718.

(166) Dunning, T. H. *Journal of Chemical Physics* **1989**, *90*, 1007.

(167) Kendall, R. A.; Dunning, T. H.; Harrison, R. J. *Journal of Chemical Physics* **1992**, *96*, 6796.

(168) Woon, D. E.; Dunning, T. H. *Journal of Chemical Physics* **1993**, *98*, 1358.

(169) Helgaker, T.; Ruden, T. A.; Jorgensen, P.; Olsen, J.; Klopper, W. *Journal of Physical Organic Chemistry* **2004**, *17*, 913.

(170) Amos, R. D.; Bernhardsoon, A.; Berning, A.; Celani, P.; Cooper, D. L.; Deegan, M. J. O.; Dabbyn, A. J.; Eckert, F.; Hampel, C.; Hetzer, G.; Knowles, P. J.; Korona, T.; Lindh, R.; Lloyd, A. W.; McNicholas, S. J.; Manby, F. R.; Meyer, W.; Mura, M. E.; Nicklass, A.; Palmieri, P.; Pitzer, R.; Rauhut, G.; Schütz, M.; Schumann, U.; Stoll, H.; Stone, A. J.; Tarroni, R.; Thorsteinsson; Werner, H.-J. MOLPRO, a package of *ab initio* programs designed by H.-J. Werner and P.J. Knowles; 2002.6 ed.

(171) Atkins, P. W. *Molecular Quantum Mechanics*, 2nd ed.; Oxford University Press: New York, 1983.

(172) Kjaergaard, H. G.; Turnbull, D. M.; Henry, B. R. *Journal of Chemical Physics* **1993**, *99*, 9438.

(173) Herzberg, G. *Molecular Spectra and Molecular Structure I. Spectra of Diatomic Molecules*; D. Van Nostrand Company, Inc.: Princeton, NY, 1950.

(174) Kjaergaard, H. G. *unpublished work*.

(175) Pecul, M.; Saue, T.; Ruud, K.; Rizzo, A. *Journal of Chemical Physics* **2004**, *121*, 3051.

(176) Barker, J. R. MultiWell 1.2.1 software, 2002.

(177) Crehuet, R.; Anglada, J. M.; Bofill, J. M. *Chemistry-a European Journal* **2001**, *7*, 2227.

(178) Herzberg, G. *Molecular Spectra and Molecular Structure Volume II: Infrared and Raman Spectra of Polyatomic Molecules*; Krieger Publishing Company: Malabar, Florida, 1945.

(179) Niki, H.; Maker, P. D.; Savage, C. M.; Breitenbach, L. P. *Chemical Physics Letters* **1980**, *75*, 533.

(180) Howard, D. L.; Kjaergaard, H. G. *Journal of Chemical Physics* **2004**, *121*, 136.

(181) Boyarkin, O. V.; Lubich, L.; Settle, R. D. F.; Perry, D. S.; Rizzo, T. R. *Journal of Chemical Physics* **1997**, *107*, 8409.

(182) Hasson, A. S.; Chung, M. Y.; Kuwata, K. T.; Converse, A. D.; Krohn, D.; Paulson, S. E. *Journal of Physical Chemistry A* **2003**, *107*, 6176.

(183) Bernath, P. F. *Spectra of Atoms and Molecules*, 2nd ed.; Oxford University Press: New York, 2005.

(184) Barath, F. T.; Chavez, M. C.; Cofield, R. E.; Flower, D. A.; Frerking, M. A.; Gram, M. B.; Harris, W. M.; Holden, J. R.; Jarnot, R. F.; Kloezeman, W. G.; Klose, G. J.; Lau, G. K.; Loo, M. S.; Maddison, B. J.; Mattauch, R. J.; McKinney, R. P.; Peckham, G. E.; Pickett, H. M.; Siebes, G.; Soltis, F. S.; Suttie, R. A.; Tarsala, J. A.; Waters, J. W.; Wilson, W. J. *Journal of Geophysical Research-Atmospheres* **1993**, *98*, 10751.

(185) Drouin, B. J. Submillimeter Analysis Program, 2005.

(186) Mees, J.; Crewell, S.; Nett, H.; Delange, G.; Vandestadt, H.; Kuipers, J. J.; Panhuyzen, R. A. *Ieee Transactions on Microwave Theory and Techniques* **1995**, *43*, 2543.

(187) Wehr, T.; Crewell, S.; Kunzi, K.; Langen, J.; Nett, H.; Urban, J.; Hartogh, P. *Journal of Geophysical Research-Atmospheres* **1995**, *100*, 20957.

(188) von Konig, M.; Bremer, H.; Kleinbohl, A.; Kullmann, H.; Kunzi, K. F.; Goede, A. P. H.; Browell, E. V.; Grant, W. B.; Burris, J. F.; McGee, T. J.; Twigg, L. *Journal of Geophysical Research-Atmospheres* **2002**, *107*.

(189) Kleinbohl, A.; Bremer, H.; Kullmann, H.; Kuttippurath, J.; Browell, E. V.; Canty, T.; Salawitch, R. J.; Toon, G. C.; Notholt, J. *Geophysical Research Letters* **2005**, *32*.

(190) Kleinbohl, A.; Bremer, H.; von Konig, M.; Kullmann, H.; Kunzi, K. F.; Goede, A. P. H.; Browell, E. V.; Grant, W. B.; Toon, G. C.; Blumenstock, T.; Galle, B.; Sinnhuber, B. M.; Davies, S. *Journal of Geophysical Research-Atmospheres* **2002**, *108*.

(191) Stachnik, R. A.; Hardy, J. C.; Tarsala, J. A.; Waters, J. W.; Erickson, N. R. *Geophysical Research Letters* **1992**, *19*, 1931.

(192) Engel, A.; Schmidt, U.; Stachnik, R. A. *Journal of Atmospheric Chemistry* **1997**, *27*, 107.

(193) Osterman, G. B.; Salawitch, R. J.; Sen, B.; Toon, G. C.; Stachnik, R. A.; Pickett, H. M.; Margitan, J. J.; Blavier, J. F.; Peterson, D. B. *Geophysical Research Letters* **1997**, *24*, 1107.

(194) Stachnik, R. A.; Salawitch, R.; Engel, A.; Schmidt, U. *Geophysical Research Letters* **1999**, *26*, 3093.

(195) Pickett, H. M.; Poynter, R. L.; Cohen, E. A.; Delitsky, M. L.; Pearson, J. C.; Muller, H. S. P. *Journal of Quantitative Spectroscopy & Radiative Transfer* **1998**, *60*, 883.

(196) Buehler, S. A.; Eriksson, P.; Kuhn, T.; von Engeln, A.; Verdesa, C. *Journal of Quantitative Spectroscopy & Radiative Transfer* **2005**, *91*, 65.